12-1-2015

Testing Established Models of Hydrothermal Fluid Distribution Around Porphyry Deposits: The Application of Fluid Inclusion Research to Porphyry Deposit Exploration

Wyatt Moyer Bain
University of Nevada, Las Vegas, bainw1@unlv.nevada.edu

TESTING ESTABLISHED MODELS OF HYDROTHERMAL FLUID DISTRIBUTION AROUND PORPHYRY DEPOSITS: THE APPLICATION OF FLUID INCLUSION RESEARCH TO PORPHYRY DEPOSIT EXPLORATION

By

Wyatt M. Bain

Bachelor of Science – Geology and Geophysics
University of Wisconsin, Madison
2011

A thesis submitted in partial fulfillment
of the requirements for the

Masters of Science – Geoscience

Department of Geoscience
College of Science
The Graduate College

University of Nevada, Las Vegas
December 2015

UNLV | GRADUATE COLLEGE

Thesis Approval

The Graduate College
The University of Nevada, Las Vegas

August 6, 2015

This thesis prepared by

Wyatt M. Bain

entitled

Testing Established Models of Hydrothermal Fluid Distribution around Porphyry Deposits: The Application of Fluid Inclusion Research to Porphyry Deposit Exploration

is approved in partial fulfillment of the requirements for the degree of

Master of Science – Geoscience
Department of Geosciences

Jean S. Cline, Ph.D.
Examination Committee Chair

Kathryn Hausbeck Korgan, Ph.D.
Graduate College Interim Dean

Rodney V. Metcalf, Ph.D.
Examination Committee Member

Minghua Ren, Ph.D.
Examination Committee Member

Barbara Luke, Ph.D.
Graduate College Faculty Representative

ABSTRACT

Testing Established Models of Hydrothermal Fluid Distribution Around Porphyry Deposits: The Application of Fluid Inclusion Research to Porphyry Deposit Exploration

By

Wyatt M. Bain

Dr. Jean S. Cline, Examination Committee Chair

Professor

University of Nevada, Las Vegas

The Kabba porphyry copper prospect in northwestern Arizona contains two zones of porphyry style mineralization and alteration, which are spatially separated by a north-south trending normal fault. These two zones are referred to as the Kabba footwall and hanging wall and are hypothesized to represent the root and intermediate depth levels of the same porphyry-like hydrothermal system, respectively. If this hypothesis is correct, then fluid inclusions found in the hanging wall and footwall should have the physical and chemical characteristics of fluid inclusions in the root and intermediate depth levels of other known porphyry deposits.

Vein and alteration petrography, fluid inclusion petrography and microthermometry, and Raman and LA-ICP-MS analyses of individual fluid inclusions from Kabba footwall and hanging wall samples lead to the following observations: 1) the textures and paragenetic sequence of alteration and mineralization in the Kabba hanging wall is almost identical to the textures and paragenetic sequence of alteration and mineralization in the footwall, 2) the mineralization and alteration in

the Kabba prospect is consistent with the footwall and hanging wall having formed in the deep roots and intermediate zones to a porphyry-like hydrothermal system, respectively, 3) the distribution of fluid inclusion types in the footwall and hanging wall broadly matches the distribution of fluid inclusion types in the deep roots and intermediate zones of other porphyry systems, 4) the chemical and physical conditions of fluid inclusions in the Kabba system are very similar to the chemical and physical conditions of fluid inclusions in the Butte porphyry system in Montana, 5) Cu concentrations in fluid inclusions from Kabba are highest in inclusions with the lowest Sr, Rb, and Ba, and 6) Cu concentrations were consistently high in vapor-rich fluid inclusions. These observations strongly suggest that the mineralization and alteration in the Kabba system formed at great depth in a porphyry-like hydrothermal system, and that the hanging wall and footwall represent the root and intermediate depth levels of that system. Based on the microthermometric behavior of fluid inclusions from the hanging wall and footwall it is interpreted that, 1) the mineralization and alteration in the Kabba system formed via 5 episodes of hydrothermal fluid flux through the footwall and hanging wall, 2) immiscibility may have played a role in forming the mineralization in the hanging wall, 3) fluids went from being H_2O- to CO_2-rich over time, 4) the Kabba footwall and hanging wall formed at pressures between 2500-3000 bars (10-12 km) and 1500-2000 bars (6-8 km), respectively, 6) fluids in the footwall and hanging wall were trapped between <300-545°C and <300-525°C, respectively, and 7) additional drilling in the Kabba prospect should focus on the hanging wall area, around the flanks of the aeromagnetic anomaly to the northeast and northwest of drill hole K-10, as this area is in indicated to contain the mineralized portion of a porphyry-like hydrothermal system.

TABLE OF CONTENTS

LIST OF TABLES

LIST OF FIGURES

CHAPTER 1

INTRODUCTION

Porphyry deposits are the source of ~60% of the world's copper (John et al., 2010), and a major source of the world's lead, zinc, tungsten, tin, gold, and silver. Because of their status as a major source of mineral resources, these deposits are critically important to supplying the raw material needed to grow and sustain global economies, and their discoveries create economic opportunities in many regions around the world. The American cordillera is one such region, being particularly well-endowed with these deposits (Figure 1), and the southwestern United States, particularly Arizona, is a premier region for porphyry exploration in North American (Figure 2). Exploration and production from porphyry deposits in Arizona is a major source of income and economic opportunity in the Southwestern US and this underscores the importance of understanding how these mineral resources form and developing techniques which can efficiently locate and characterize these deposits in the Earth's crust.

Fluid inclusion research is an important method for understanding how porphyry and other ore systems formed and evolved through time. By examining ancient hydrothermal fluids trapped in fluid inclusions in porphyry environments we can identify patterns of pressure, temperature, and ore fluid chemistry across hydrothermal systems and characterize how the hydrothermal fluids evolved as they migrated from depth and into the shallow crust of the Earth. In the past 20 years our ability to analyze fluid inclusions has grown dramatically with the advent of sophisticated analytical techniques, particularly LA-ICP-MS (Ulrich et al, 2011), that allow us to quantify the compositions of fluids in fluid inclusions. Recent research has combined LA-ICP-MS analysis with detailed fluid inclusions petrography and microthermometry, and this work has led to the development of fluid inclusion distributions models that show typical three-

dimensional patterns of fluid inclusion compositions and distributions throughout porphyry systems (Reynolds and Beane, 1985; Ulrich et al., 2001; Rusk et al., 2008; Landtwing et al., 2010). These patterns involve fluids evolving from high temperature, pressure, and density at depth, to low temperature, pressure, and density as they move upward and outward through a porphyry system. Because this pattern is common to many porphyry systems, fluid inclusion distribution models should have predictive capabilities applicable to resource exploration. If these fluid inclusion distribution models can be successfully applied to porphyry exploration, then fluid inclusion research and established fluid inclusion distribution models will constitute an additional tool that can aid exploration geologists as they search for new mineral resources.

The thesis presented herein tests the predictive power of established fluid inclusion distribution models by using them to understand the Kabba porphyry copper prospect in Northwestern Arizona. This prospect contains two structurally separated areas of porphyry style alteration and mineralization, which are hypothesized to represent the deep roots and intermediate depth zones of a single porphyry system. If this hypothesis is correct, and if Kabba represents a porphyry system, then fluid inclusions found in these areas of porphyry-style alteration and mineralization should have the physical and chemical characteristics of fluid inclusions found in the root and intermediate depth zones of other known deposits, as predicted by the models. In order to test this hypothesis, vein and alteration petrography, fluid inclusion petrography and microthermometry, and Raman and LA-ICP-MS analyses of individual fluid inclusions were integrated and compared to established fluid inclusions distribution models. Based on this comparison, the alteration, mineralogy, and fluid inclusions types found in the Kabba system are consistent with the presence of a porphyry system and do support the faulted porphyry system hypothesis. These results and the data collected from the Kabba prospect are presented and

discussed in the following chapters.

CHAPTER 2

BACKGROUND

Porphyry Deposits

Porphyry deposits are large concentrically zoned systems of hydrothermally altered igneous rock that contain abundant sulfide and oxide minerals which are rich in base and precious metals (Lowell and Guilbert, 1970; Gustafson and Hunt, 1975; Hedenquist and Lowenstern, 1994; Sillitoe 2010) (Figure 3 A). Most porphyry deposits are hosted by intrusive igneous rocks that typically range in character from intermediate to felsic, and typical porphyry systems have a genetic association with intermediate calc-alkaline porphyritic rocks. Most models of porphyry deposit formation describe a process which begins with a reservoir of andesitic magma forming above a subduction zone and rising into a highly-fractured zone in the upper crust, such as a pull-apart jog or a restraining bend in a transform fault (Figure 3 B), where it begins to slowly cool and crystalize at depth (Lowell and Guilbert, 1970; Guilbert, 1986; Sillitoe, 2010; Cloos and Sepiie, 2013). As the andesitic magma cools it forms a water-saturated carapace around its outer margins and becomes saturated in volatiles including H_2O and minor amounts of CO_2 (Figure 3 C). These volatiles, particularly H_2O, can contain high concentrations of ions such as Cl^- and HS^-, which complex with metal ions such as Cu^+, Mo^+, Zn^+, Pb^+, and Sn^+ and, as the volatiles become saturated in the melt, the complexing ions efficiently extract metal ions from the parental andesitic magma (Cline and Bodnar, 1991). After the andesitic magma becomes saturated in hot, metal-rich fluids it buoyantly rises and forms an elevated dome-shaped cupola of H_2O-saturated magma under the roof of the magma chamber (Figure 3 B, C), (Cloos and Sepiie, 2013). Eventually the cupola will become over pressured and will rupture, causing the hot metal-rich fluids to exsolve from the magma and vent upward and outward into the

igneous country rock above the magma chamber. As the fluids move away from the magma chamber they are focused into low pressure pathways in the subsurface, such as faults, and the fluid pressure on the country rock above the magma chamber increases. This increased fluid pressure causes the formation of hydraulic fractures in the country rock. As the fluids in hydraulic fractures continue to rise, the metal-rich fluids cool, depressurize, react with the country rock, and precipitate sulfide, oxide, and silicate minerals. As the minerals fill fractures they form abundant veins, which are common in porphyry systems, and as the fluids react with the wall rocks, they form the concentric zones of alteration that are the hallmark of porphyry deposits around the world (Lowell and Guilbert, 1970; Guilbert, 1986; Sillitoe, 2010; Cloos and Sepiie, 2013).

Three vein types are commonly found in porphyry systems: A, B, and D veins (Gustafson and Hunt, 1975; Sillitoe, 2010) (Figure 4). A veins are filled with granular quartz, typically have an irregular, discontinuous, or segmented appearance, and commonly have sinuous boundaries (Gustafson and Hunt, 1975; Sillitoe, 2010) (Figure 4). The irregular or sinuous morphology of A veins stems from the fact that they form early in the development of porphyry systems when the system is at its highest temperatures and the host rocks within the systems from ductile fractures, forming sinuous fractures rather than straight, brittle fractures. Their early formation in porphyry environments means that A veins are commonly cut by B and D veins which form later. Alteration that is most commonly associated with A veins is high temperature potassic alteration and A veins commonly have potassic alteration selvedges composed of variable amounts of perthitic K-feldspar, shreddy biotite, anhydrite, bornite and chalcopyrite (Sillitoe, 2010).

B veins typically occur as continuous, planar structures with parallel walls, and have sulfide filled centerlines (Gustafson and Hunt, 1975) (Figure 4). B veins form after A veins and

after the porphyry system has cooled enough to allow for the formation of straight, brittle fractures. The centerlines of B veins form as the result of reopening of these veins or incomplete filling of the veins originally, along their long axis followed by precipitation of younger generations of quartz, sulfides, or alteration minerals (Gustafson and Hunt, 1975). Where filled with sulfides, the center lines typically contain chalcopyrite and pyrite. Also, phyllic, propylitic, and/or moderate potassic alteration selvedges are commonly observed around the margins of B veins.

D veins are typically narrow (<2-20 mm in width), continuous, systematically oriented structures filled entirely with sulfides (Figure 4). The dominant sulfide found in D veins is pyrite, but D veins commonly also contain minor chalcopyrite, bornite, enargite, sphalerite and galena. D veins form along with B veins and can commonly crosscut, or be crosscut by B veins. Conversely, D veins cut A veins but are typically not cut by A veins. D veins can be associated with alteration and commonly have selvedges composed of phyllic alteration minerals or sericite-chlorite.

The typical types of alteration associated with porphyry deposits (potassic, propylitic, phyllic, and argillic) occur in a roughly "light bulb" shaped or telescoping pattern in which different alteration types occur along side or partly overlapping one another (Lowell and Guilbert, 1970; Gustafson and Hunt, 1975; Hedenquist and Lowenstern, 1994; Seedorff et al., 2008; Sillitoe, 2010) (Figure 4). The spatial distribution of alteration types relative to one another in a porphyry system is controlled by pressure and temperatures and chemical gradients, which form around the igneous source of the hydrothermal fluids involved in the formation of the porphyry deposit. As a result the different types of alteration found around porphyry deposits

will occur in relatively predictable locations, and this is an important aspect of porphyry deposits because the recognition of alteration zones can be used to vector to sulfide ore in these systems. Potassic alteration is found in the deep core of porphyry systems (Figure 3 A), is associated with the highest temperature fluids, and is an early alteration type to form. This alteration is characterized by alkali exchange, primarily K^+ for Ca^+ and Na^+, and the replacement of primary plagioclase with potassium feldspar, and primary pyroxene and amphibole with shreddy secondary biotite (Sillitoe 2010). This alteration typically occurs as selvedges along the outer margins of quartz veins and veinlets, and zones with this alteration are typically highly fractured and commonly contain abundant chalcopyrite and bornite, with minor amounts of diginite, and pyrite (Lowell and Guilbert, 1970; Seedorff et al.; 2008; Sillitoe, 2010).

Propylitic alteration is found on the periphery of porphyry systems, and is associated with lower temperature, relative to potassic alteration, volatiles such as H_2O and CO_2 (Seedorff et al., 2008) on the cooler outer edge of the system. This alteration type is associated with the replacement of primary minerals with chlorite, epidote, and albite, and rocks that are propylitically altered typically have a green color. The formation of propylitic alteration occurs at the same time as potassic alteration, and potassic alteration typically grades outward overprinting earlier propylitic alteration until the magmatic system begins to cool, at which time propylitic alteration encroaches on and overprints potassic alteration towards the system center (Lowell and Guilbert, 1970; Seedorff et al., 2008; Sillitoe, 2010).

Phyllic alteration commonly consists of an assemblage of quartz, sericite, and pyrite (QSP), which typically overprints the highly fractured boundary between the propylitic and potassic alteration zones, or is found directly above the potassic zone and grades upward into argillic alteration. Phyllic alteration results from decreasing hydrothermal fluid temperature and

pH as the porphyry hydrothermal system cools, and is most abundant in areas with high fracture densities. As fluids related to phyllic alteration cool below about 400°C, precipitation of copper sulfide minerals (Lowell and Guilbert 1970; Seedorff et al., 2008; Sillitoe, 2010) occurs forming ore zones within the phyllic alteration zone or along its contact between potassic and phyllic alteration.

Phyllic alteration is also commonly associated with chlorite-sericite alteration, which results from primary host rock plagioclase and biotite altering to chlorite, sericite, illite, and hematite (Sillitoe et al., 2010). These alteration styles are closely related to each other, can commonly be intermixed or form discrete zones adjacent to one another, and typically constitute some or all of the ore zones found in porphyry systems (Sillitoe, 2010).

Advanced argillic alteration typically forms at the top of porphyry systems, distal from the core of the system, and is characterized by the conversion of host rock plagioclase to kaolinite, dickite, and pyrophyllite, the formation of a vuggy quartz lithocap, and the precipitation of alunite at the top of porphyry systems. The presence of this alteration type in porphyry systems is variable and is related to the formation of low temperature H^+-rich vapor that leaches the shallowest portions of porphyry systems.

Greisen alteration forms in the deepest parts of porphyry systems, commonly from 4-12 km depth to the base of major ore zones or below the potassic alteration zone, and is characterized by the conversion of primary potassium feldspar and plagioclase to coarse-grained, grey muscovite. This alteration type commonly occurs as selvedges of coarse muscovite along the outer margins of quartz veins and occurs with or overprints deep potassic alteration (Stavast, 2006; Seedorff et al., 2008; Maher, 2008). Greisen is a hallmark of major feeder zones or large hydrothermal conduits in the deepest parts of porphyry systems, through which voluminous

quantities of hydrothermal fluids pass as they rise into the upper crust (Stavast, 2006; Seedorff et al., 2008; Maher 2008).

All models of porphyry deposit formation more or less outline how hydrothermal fluids derived from magmas evolve and move up through the crust. To better understand this process many studies have examined fluid inclusions associated with porphyry alteration and mineralization. These studies, first, group fluid inclusions into assemblages based on common spatial association and similar phase ratios indicating that they were all trapped at about the same time (Goldstein and Reynolds, 1994), and then characterize inclusion assemblages relative to the porphyry deposit in terms of their spatial distribution throughout the porphyry system. Resulting fluid inclusion assemblage (FIA) distribution models have described porphyry systems that formed at various paleodepths including shallow systems such as Santa Rita (Reynolds and Beane, 1985) and Refugio (Muntean and Einaudi, 2000), intermediate depth systems such as Bingham Canyon (Landtwing et al., 2010), Bajo de la Alumbrera (Ulrich et al., 2001), and Far Southeast (Hedenquist et al., 1998), and deep systems such as Butte (Rusk et al., 2008) and Endako (Selby et al., 2000) (Figure 5). These models are important to our understanding of fluid evolution in porphyry systems and they illustrate a common pattern in the spatial distribution of various types of FIAs relative to a system's barren core and ore zones. This pattern is characterized by a transition from high temperature and pressure, high salinity, aqueous inclusions in the core of a porphyry system, to low temperature and pressure, moderate to low salinity, vapor-rich inclusions in the intermediate and high level periphery of the system (Reynolds and Beane, 1985; Hedenquist et al., 1998; Muntean and Einaudi, 2000; Selby et al., 2000; Ulrich et al., 2001; Rusk et al., 2008; Landtwing et al., 2010). This pattern is described in general below.

In the deep core of some typical porphyry systems, aqueous, low salinity fluids with ~20-30% vapor dominate (Rusk et al., 2008). These fluids are not always encountered because they reside in the deepest levels of porphyry systems and recorded the highest temperatures and pressures in a porphyry environment. Because of their abundance in the deep levels of porphyry systems, these fluids are widely recognized as parental fluids that exsolved from a magma, and are thought to evolve into the fluids that are commonly found in the shallower levels of porphyry environments.

Above the deep core of typical porphyry systems, at mid system levels, halite-saturated inclusions coexist with vapor-rich inclusions, resulting from fluid immiscibility at ~400 – 700°C and ~350 to 950 bars pressure. Salinities range from ~35 – 70 wt.% NaCl equivalent in halite-bearing inclusions to ~1 – 19 wt.% NaCl equivalent salinity in vapor-rich inclusions (Ulrich et al., 2001). Though mostly dominated by coexisting halite-saturated and vapor inclusions, the intermediate depth portions of typical porphyry systems also contain minor aqueous inclusions, which have salinities between 0.2-25 wt% NaCl equiv, record temperatures between 200-330°C, and record pressures <100 bars (Ulrich et al., 2001).

The shallow upper regions in a typical porphyry system are dominated by vapor-rich inclusions, which commonly appear similar to vapor-rich inclusions found in the intermediate depth portions of typical porphyry systems, but commonly record lower pressures and temperatures. Also, veins in the shallow depth areas in a typical porphyry system also contain small amounts of the aqueous, 0.2-25 wt% NaCl equivalent inclusions.

Though the general pattern of fluid inclusions recording high temperatures and pressures in the core of porphyry systems and lower temperatures and pressures in the shallow periphery of porphyry systems is common for most porphyry deposits, patterns in various porphyries differ.

This variation arises from differences in depth of formation, the chemistry and physical conditions of the fluids that exsolved from their parental magma, and the country rocks that the fluids moved through as they rose through the crust. For example, the porphyry deposit at Butte, Montana formed between 8-10 km depth, and is one of the most deeply-formed porphyry deposits ever mined and studied (Figure 5) (Rusk et al., 2008). Fluid inclusions in veins in drill core from the deepest available part of the Butte porphyry deposit are dominated by two types of liquid-rich, CO_2-bearing fluid inclusions: B35 and B60 (Rusk et al., 2008). B35 inclusions are two-phase inclusions containing ~35 vol% vapor that contains 3-8 mol% CO_2 and a liquid with a salinity of ~1-8% wt% NaCl equiv.; these inclusions homogenized to liquid between 330-400°C. B60 inclusions are two-phase inclusions containing ~60 vol% vapor that contains ~3-9 mol% CO_2, and a liquid with a salinity of ~1-7 wt% NaCl equiv.; these inclusions homogenized to liquid between 360-400°C. Similar to other porphyry systems, veins in the deep root zone of the Butte porphyry deposit contain few vapor-rich inclusions. However, unlike other porphyry systems, moderate amounts of halite-saturated inclusions were found, and the B35 and B60 inclusions that dominate at depth contain CO_2, although only two inclusions that contain liquid CO_2 were observed. In the shallow part of the Butte system, B60 inclusions dominate along with vapor-rich B85 inclusions, which contain ~70-85% vapor with 10-20 mol% CO_2 and 0-3 wt% NaCl equiv., and have homogenization temperatures between 370-520°C (Rusk et al., 2008). Along with these B60 inclusions and B85 inclusions, a moderate proportion of B15H inclusions, which contain ~15% vapor, liquid, and a halite daughter crystal, and homogenize by halite melting between 175-415°C, are also present in the shallow portions of Butte. The B60 and B85 inclusions that dominate the shallow part of the Butte systems are similar to other porphyry systems; however, the presence of CO_2 in the B60 and B85 inclusions, the moderate rather than

abundant evidence for boiling and related halite-bearing inclusions, and the great depth of formation (8-10 km) are unusual (Rusk et al., 2008).

The distribution of fluid inclusions in the Butte porphyry deposit shows that productive porphyry systems can vary from typical patterns of many porphyry systems. However, the general pattern of fluid inclusions in the upper part of a porphyry system containing lower density fluids and having formed at lower pressure and temperature than inclusions found in the core of the system is present at Butte even though the populations of fluid inclusions found at Butte are distinct from inclusion patterns in typical porphyry systems. This illustrates the fact that even though there are variations in the types of fluid inclusions found in some porphyry deposits, the general patterns described by established fluid inclusions distribution models can be applied to most porphyry deposits.

The Kabba Prospect

This thesis focuses on the Kabba hydrothermal system. The Kabba system is comprised of the Kabba prospect, which is located approximately 19 miles southeast of Kingman, Arizona, directly east of the Hualapai Mountains, and the historic Maynard mining district, which is west of the Kabba prospect and encompasses the eastern foothills of the Hualapai mountains (Figure 6, 7). The Kabba prospect and the Maynard mining district are adjacent to one another and lie on a mineral trend with the Bagdad and Mineral Park porphyry copper deposits, located 73 miles to the southeast and 31 miles to the northwest, respectively (Anderson, 1955; Lang and Eastoe, 1988; Titley and Anthony, 1989) (Figure 8).

The Maynard district, which contains abundant surface outcrops of intrusive granites, granodiorites, monzonites, quartz monzonites, gneiss, and porphyry-style mineralization and alteration, has been interpreted to be separated from the Kabba prospect by a north-south tending

Hualapai fault (Vuich, 1975; Bell Copper Corp. 43-101 report, 2013), and the Maynard district is referred to here after as “the Kabba footwall” or simply, “the footwall”(Figure 7, 9). The granites, granodiorites, monzonites, and quartz monzonites are mostly on the eastern side of the Maynard district, and range in age from mid-Triassic to late Cretaceous (Vuich, 1975; Bell Copper Corp. 2013). The gneisses are adjacent to the igneous intrusive rocks, are located on the western side of the Maynard district, extend westward into the Hualapai Mountains, and are Precambrian in age (Vuich, 1975; Bell Copper Corp. 2013).

The igneous and metamorphic rocks in the footwall contain many of the hallmarks of typical porphyry systems including abundant quartz veining, pyritic, sericitic, and potassic alteration halos along that margins mineralized quartz veins, subtle propylitic and argillic alteration disseminated throughout the country rock, sub-economic Cu and Mo mineralization disseminated in the country rocks and in the quartz veins (Vuich, 1974), and many historic mining claims that cluster around the flanks of a large aeromagnetic anomaly located in the northern half of the footwall (Figure 10) (Bell Copper Corp. 2013). The primary host rocks for the Cu and Mo mineralization and porphyry-style alteration in the footwall are the mid-Triassic to late Cretaceous granites, granodiorites, monzonites, and quartz monzonites. However, the adjacent Precambrian gneisses also contain moderate porphyry-style alteration and Cu-Mo mineralization, and host porphyry dikes of an unknown age (Vuich, 1974; Bell Copper Corp, 2013).

The presence of porphyry-style mineralization and alteration in the footwall has attracted the attention of prospectors and geologists since the early 1800s, and mining of marginally economic quantities of gold, silver, copper, molybdenum, lead, tungsten, and vanadium (Vuich, 1974) took place from the late 1800s until the mid-1950s. Following the decline of active mining

in the Maynard district (i.e. the footwall area) in the mid 1950s, several companies including Bear Creek Exploration, Union Carbide, Conoco, Kerr-McGee, AMAX, Cerromin, and Noranda operated significant diamond drilling exploration programs investigating the mid-Triassic to late Cretaceous granites, granodiorites, monzonites, and quartz monzonites in the area. These exploration activities failed to discover a productive resource but did identify abundant porphyry-style alteration and local areas of high copper and molybdenum in the sub-surface. Drilling in this area continues to this day, but an economic resource has yet to be discovered (Bell Copper Corp, 2013).

The Kabba prospect is located at the northern end of the valley to the east of the Hualapai fault, south of Interstate 40, and west of US Highway 93 (Figure 6, 7). The valley that contains the Kabba prospect and the surrounding area is referred to hereafter as the "Kabba hanging wall," or simply as the "hanging wall". The hanging wall region is mostly covered by Quaternary gravels and has few bedrock outcrops. However, small outcrops of granites and granodiorites with abundant quartz veins are present where ephemeral streams have cut through the valley gravels, and historic small-scale gold, silver, lead, and zinc deposits dot the valley (Figure 7). The hanging wall also contains a large areomagnetic anomaly, the southern end of which runs through the northern end of the Kabba prospect (Figure 10), and seismic data collected by Bell Copper Corp. from the hanging wall shows that several fault blocks, which have moved northeast along the Hualapai normal fault, reside below the Quaternary gravels present at the surface in the hanging wall area (Figure 11).

The aeromagnetic anomaly in the hanging wall is similar to the aeromagnetic anomaly present in the footwall in terms of its diameter and the fact that small-scale mines in the hanging wall align around its flanks. Also, the hanging wall aeromagnetic anomaly is ~8 km northeast of

the footwall aeromagnetic anomaly. This ~8 km northeast offset between the hanging wall and footwall anomalies is consistent with the inferred offset of the fault blocks along the Hualapai fault characterized using seismic data. Based on these patterns, Bell Copper Corp has hypothesized that the hanging wall and footwall aeromagnetic anomalies represent a single anomaly now offset by faulting.

Though the hanging wall area contains abundant small-scale mines, a large aeromagnetic anomaly, and surface outcrops of granites and granodiorites with abundant quartz veins, no porphyry-style alteration is exposed at the surface and the only mineralization present at the surface has been removed by historic mining. In 2005 the Bell Copper Corporation acquired 8031 acres of contiguous claims covering this area now known as the Kabba prospect (Figure 7) and has been conducting an exploration and drilling program on this prospect to the present day (Bell Copper Corp, 2013).

In 2011, Bell Copper Corp drilled diamond drill hole K-10 into the southern flank of the aeromagnetic anomaly on the northern part of the Kabba prospect, and intersected pervasive quartz veining, green mica, potassic alteration, and chalcopyrite-molybdenite-galena-sphalerite-pyrite mineralization. Based on the mineralization and alteration found in the K-10 drill core, the Bell Copper Corporation interpreted that the K-10 drill hole may have pierced the periphery of a porphyry-like hydrothermal system. To test this interpretation, Bell Copper Corporation plans to drill additional holes north and northeast of the K-10 drill hole in search of major Cu-Mo mineralization. This drilling is set to commence in the summer of 2015 (Bell Copper Press Release, 2015).

Exploration in the hanging wall and footwall areas has led to the hypothesis that the hanging wall and footwall contain two distinct zones of porphyry-style mineralization and

alteration that were once part of the same system, but have since been separated by the north-south trending Hualapai normal fault (Figures 9) (Vuich, 1974; Bell Copper Corp, 2013). If this hypothesis is correct, then it follows that the mineralization and alteration in the hanging wall and footwall were formed at the same time, and, owing to their separation by a normal fault, the mineralization and alteration in the footwall formed at a greater depth than the mineralization and alteration in the hanging wall. This means that the mineralization and alteration found in the footwall and hanging wall might represent two distinct zones that formed at different depths as part of a single porphyry system.

The objective of this study is to test the faulted porphyry system hypothesis by 1) characterizing the mineralization, alteration, and vein types found in the hanging wall and footwall, and comparing these features to the mineralization, alteration, and vein types in other porphyry systems, 2) characterizing the physical and chemical characteristics and spatial distribution of fluid inclusion assemblages (FIAs) trapped in veins in the hanging wall and footwall, and comparing these data to the established FIA distribution models for economic porphyry systems. If the hanging wall and footwall area were previously part of a single porphyry system and each formed at different depths and conditions, then it follows that 1) the paragenetic sequence of mineralization and alteration types associated with veins in the hanging wall and footwall should be related to one another, 2) the mineralization and alteration in each location should have formed from the same hydrothermal fluids and therefore the fluid inclusions found in the hanging wall and footwall should have related patterns in enrichment and depletion of various elements, and 3) the distribution of fluid inclusion types in the footwall and the hanging wall should show related patterns of decreasing fluid pressure, temperature, and density with decreasing depth, similar to patterns in economic porphyry systems.

CHAPTER 3

METHODS

Sample Selection and Field Work: Hanging wall

Samples collected from drill core were supplied by Bell Copper Co. and came from drill hole K-10 (Figure 7, 12, 13), which was collared in the Kabba hanging wall in alluvial cover that fills the valley east of the Hualapai Mountains (249595E 3890992N, UTM 12). The drill hole has a total depth of 1346 meters, including 996 meters of alluvium and 349 meters of moderately mineralized igneous and metamorphosed country rock. This is the only hole drilled by Bell Copper Co. that encountered significant sulfide mineralization and alteration. Core samples chosen from K-10 contain a variety of sulfide minerals, alteration, host rocks, and cross-cutting relationships, and sampling focused on quartz veins that hosted sulfide mineralization, exhibited well-developed alteration selvedges adjacent to veins, and had the potential to host fluid inclusions related to mineralization and alteration and suitable for analysis. In total, 67 core samples were collected from drill hole K-10. Samples selected from drill hole K-10 and the analysis carried out on each sample are listed in Appendix A.

Sample Selection and Field Work: Footwall

Fieldwork in the footwall focused on areas mapped by Vuich (1974), which are known to contain variable amounts of Cu and Mo sulfide mineralization and alteration typical of porphyry systems (Sillitoe, 2010) (Figure 12 C, 13 B-E). The primary objective of fieldwork in the footwall was to collect samples representative of the local mineralization and suitable for detailed petrographic and fluid inclusion analysis, and to gather information on the mineralogy, texture, abundance, and spatial distribution of quartz and sulfide veins. In order to put footwall

samples in temporal context with one another, veins and cross-cutting relationships in footwall outcrops were characterized in detail.

Samples were collected from outcrops of quartz veins that hosted sulfide mineralization and porphyry-style alteration. Barren and mineralized veins were collected in order to document the variation in vein types and associated alteration and mineralization present in the footwall. A total of 85 samples for fluid inclusion analysis were selected from historic mines and prospect pits that are distributed throughout the footwall area. These samples represent areas with abundant Cu and Mo mineralization and were the most likely candidates for hosting fluid inclusion that trapped ore forming fluids. Samples selected from the Kabba footwall and the analyses carried out on each sample are listed in Appendix B.

Doubly Polished Thick Section Sample Selection

A total of 25 footwall and 15 hanging wall samples that showed particularly well developed alteration selvedges, abundant sulfide mineralization, and clear quartz veins with a thickness >0.5 cm were selected to be made into thick sections for petrographic and fluid inclusion analysis. Billets for sections were ground to a thickness of ~100 μm and doubly polished for fluid inclusion analyses. Descriptions of footwall and hanging wall samples prior to cutting and polishing can be found in appendix C and D.

Conventional Petrographic Analysis

Doubly polished thick sections were studied using both transmitted and reflected light to characterize ore and alteration mineralogy, textures, and crosscutting relationships. Microscopic observations were used to establish the paragenetic sequence of ore and alteration minerals in

and associated with quartz veins in each sample. This paragenetic sequence was then used to identify assemblages of fluid inclusions with consistent liquid to vapor ratios that indicate synchronous trapping of past hydrothermal fluids related to specific generations of vein minerals and alteration (Goldstein and Reynolds, 1994). These fluid inclusion assemblages or "FIAs" are important to this study because they indicate the presence of fluid inclusions that have not been modified since trapping. Thus, they can provide an accurate record of pressure, temperature, and chemical (P-T-X) conditions of the fluids involved in alteration and mineralization.

Scanning Electron Microscope-Energy Dispersive Spectroscopy (SEM-EDS)/Cathodoluminescence (SEM-CL) Analysis

Semi-quantitative SEM-EDS analysis was carried out using the JEOL-5600 Scanning Electron Microscope (SEM) located in the Electron Microanalysis and Imaging Laboratory (EMiL) at the University of Nevada, Las Vegas (UNLV). This analysis was used to confirm mineral identifications and paragenetic relationships observed during conventional microscope analysis. Beam conditions for SEM-EDS analysis were 15 KeV acceleration voltage, 40 µm spot size, aperture 2, and a 20 mm working distance

SEM-CL analysis was used to distinguish between successive generations of quartz and characterize crosscutting relationships and quartz textures that are not visible with conventional transmitted and reflected light microscopy. SEM-CL images were collected with a Centaurus CL detector with 185 to 850 nM spectral range, and the optimum beam conditions for SEM-CL imaging were 15 KeV acceleration voltage, 42-46 µm spot size, aperture 2, and a 14-18 mm working distance. Images were recorded in greyscale and, thus, CL intensities for target material are referred to as "CL-bright" and "CL-dark", and are further defined by their texture. This

analysis links discrete areas of quartz and included fluid inclusions to particular paragenetic stages, which is key for distinguishing different fluid inclusion groups from one another.

Microthermometry

Ice melting, clathrate melting, and homogenization temperatures were collected for individual groups of fluid inclusions using a Linkam THMSG 600 stage mounted on an Olympus BX60 petrographic microscope. The Linkam stage was calibrated using synthetic fluid inclusions produced by Synflinc. Using the synthetic inclusions, temperatures measured within this stage were compared to the known temperatures of CO_2 melting at -56.6 ±0.01°C, pure ice melting at 0.0°C, and the liquid-vapor homogenization of pure H_2O at the critical point of 374.2°C. The accuracy of ice melting temperatures are +/- 0.1°C and homogenization temperature accuracy is estimated at ~5°C. Calculation of P-T-X conditions for analyzed groups of fluid inclusions was accomplished using the MacFlincor program (Brown, 1989; Brown and Hagemann, 1995). MacFlincor yielded bulk compositions, salinities, and isochors for analyzed inclusions.

Raman Analysis

The density of CO_2 in select inclusions was determined using microRaman spectroscopy at the University of Bern, Switzerland. Measurements were performed with a Jobin Yvon LabRAM-HR800 system with an integrated Raman microprobe consisting of an Olympus BX41 confocal microscope coupled to an 800 mm focal-length spectrograph. All measurements were gathered using a 100x objective on the Olympus microscope and a frequency-doubled Nd-YAG continuous-wave laser with an excitation wavelength of 532.12 nm (green) that was used to excite the samples. Acquisition times ranged from 15 to 30 seconds and acquisitions were

repeated 3 times per inclusion. This analysis was used to characterize the composition and distribution of CO_2-bearing fluid inclusions.

Laser Ablation – Inductively Coupled Plasma – Mass Spectrometry (LA-ICP-MS)

LA-ICP-MS analysis was used to quantify major and minor trace element compositions of selected fluid inclusions. The LA-ICP-MS system used consisted of a 193-nm ArF Excimer laser system with a fast-washout, rhomb-shaped ablation cell with a volume of $1cm^3$ coupled to an ELAN 6100 DRC quadruple mass spectrometer. The instrument was tuned to high sensitivity while keeping the ThO/Th-ratio below 0.5%. Carrier gas flow rate was 1.1 L/min He + 5 ml/min H_2 (Guillong and Heinrich, 2007), and laser repetition rate was 10 Hz. Element concentration ratios were determined using NIST glass standard SRM-610. Data reduction was done using SILLS software (Guillong et al., 2008), and Na concentrations (salinities) derived from microthermometric measurements were used to correct for variance in measured element concentrations caused by contributions from other cations.

CHAPTER 4

VEINS AND ALTERATION

Footwall and hanging wall samples selected for analysis typically contained > 0.5 cm thick quartz veins that host sulfide and oxide minerals and display the variety of alteration types and mineralization found in drill core and outcrop in the hanging wall and footwall areas. Below is a detailed description of footwall and hanging wall host rocks, veins, alteration, and mineral assemblages present in the veins.

Host Rocks: Footwall

The host rocks in the footwall were collected from surface outcrops along dry washes in the footwall area, and are comprised of moderately to heavily altered intrusive phaneritic rocks of late Cretaceous age (Vuich, 1974) (Figure 12 C, 13 B-E). These intrusive rocks are commonly composed of ~45-70% euhedral to subhedral plagioclase, ~20-45% subhedral to anhedral quartz, and ~5-10% euhedral biotite with minor white micas, and plot in the quartz monzonite and granodiorite fields on a quartz-plagioclaes-alkili-foid (QPAF) diagram. The degree of alteration in host rock outcrops and hand samples increases with increasing quartz vein density and, where quartz vein density was highest, the original texture of the host rocks is partly to completely obscured. These rocks are described in detail by Vuich, 1974.

Vein Assemblages: Footwall

The minerals found in footwall veins tend to occur in consistent and discrete groups that are referred to as assemblages. Four mineral assemblages were identified in the footwall and the minerals within each assemblage are consistently intergrown with one another, have similar

textures and temporal range, and, with the exception of assemblage 4_F, which is described below, are associated with a single generation of quartz. The textures and occurrences of many of the minerals from each assemblage are, in many cases, the same as those found in the hanging wall. As a result, many of the sulfide and oxide minerals found in the footwall share the same abbreviation as their analogues in the hanging wall. However, footwall and hanging wall mineral assemblages are described separately from one another below.

Each footwall assemblage is described below and in Table 1. All footwall assemblages are identified by a number, which signifies temporal order relative to other assemblages in the footwall. The subscript "F" signifies "footwall" and is used to differentiate between hanging wall samples, which do not have a subscript.

Assemblage 1_F: This assemblage is associated with quartz that has a bright white color and a mottled or growth-zoned pattern in cathodoluminescence (Figure 14) and is referred to hereafter as CL-bright quartz. Individual crystals of this quartz range in size between 100-900 µm, have rounded edges and euhedral growth-zoned or mottled cores, and are light to moderately fractured. The sulfide minerals in assemblage 1_F include anhedral chalcopyrite (Cpy_1) and pyrrhotite (Po) that occur as 5-50 µm wide inclusions in subhedral pyrite (Py_2) (Figure 15 A, B), and molybdenite (Mo_1) (Figure 15 C) that occurs as masses of elongate, subhedral-euhedral, lath-shaped crystals that range in size from 100-800 µm. Cpy_1 and Po inclusions in pyrite occur as individual anhedral inclusions or as individual inclusions of adjacent Cpy_1 and Po crystals. Cpy_1 also occurs in minor amounts as anhedral-subhedral inclusions in magnetite (Figure 15 D, E). However, Cpy_1 does not occur with Po in magnetite, and no Po inclusions are found in any magnetite crystals.

Masses of abundant euhedral Mo_1 crystals are typical and are commonly intergrown with CL-bright quartz. Rarely, Mo_1 is partly rimmed by magnetite (Mt), chalcopyrite (Cpy_2) (Figure 15 C) and pyrite (Py_2) crystals, but is never intergrown with these minerals. Also, Mo_1 is much less abundant than Cpy_1 in assemblage 1_F

Assemblage 2_F: Assemblage 2_F, as well as assemblage 3_F, is associated with quartz that has a flat black color under cathodoluminescence, ranges in size between 5-500 µm, fills fractures in and crosscuts CL-bright quartz, and is referred to here after as CL-dark cathodoluminescence (Figure 14 A, B, C). CL-dark quartz fills fractures in sulfide and oxide minerals in assemblage 1_F, commonly contains rounded inclusions of CL-bright quartz, is associated with white muscovite, and is typically associated with the bulk of the sulfide mineralization in the footwall.

The sulfide and oxide minerals in assemblage 2_F include subhedral pyrite (Py_2) that ranges in size between 100-1000µm and contains inclusions of Cpy_1 and Po (Figure 15 A, B), masses of euhedral-subhedral magnetite (Mt) crystals that range in size between 100-800µm (Figure 15 E, G), and anhedral rutile (Ru) (Figure 15 H, F) that ranges in size from 10-200µm and commonly occur within and adjacent to masses of coarse, euhedral white muscovite (Figure 15 H, I) that range in size from 20-500µm. Py_2 and Mt in this assemblage commonly occur as individual crystals or as masses of individual crystals intergrown with CL-dark quartz. Rarely, Mt also occurs as anhedral inclusions in Py_2 alongside Cpy_1 and Po. Where occurring as an inclusion in Py_2, Mt crystals commonly are euhedral to subhedral (Figure 15 F). Also, individual Mt crystals in this assemblage contain minor anhedral-subhedral Cpy_1. Cpy_1 inclusions in Mt are similar to the Cpy_1 inclusions in Py_2, but differ in that individual Cpy_1 inclusions in Mt have a more euhedral shape (Figure 15 E). Rutile-bearing coarse white muscovite is included in

assemblage 2 and also in assemblage 3, and occurs as masses of anhedral-subhedral crystals, which form along the outer boundaries of CL-dark quartz or in fractures in CL-bright quartz (Figure 15 H, I).

Assemblage 3_F: Assemblage 3_F includes anhedral-subhedral chalcopyrite (Cpy_2), which ranges in size from 20-500µm (Figure 15 C, D, K, J), and elongate, euhedral, lath-shaped molybdenite crystals (Mo_2) (Figure 15 L) that range in size from 50-100µm, and both of these minerals are typically intergrown with CL-dark quartz and coarse white muscovite.

$Chalcopyrite_2$ occurs in only minor amounts and is always intergrown with CL-dark quartz, filling fractures in Cl-bright quartz or fractures in sulfide phases in assemblages 1_F and 2_F. Cpy_2 crystals also commonly have a rough or "pitted" surface (Figure 15 K).

$Molybdenite_2$ crystals in this assemblage always occur within or adjacent to masses of rutile-bearing coarse white muscovite, which are lined by or intergrown with CL-dark quartz. Rarely, masses of rutile-bearing coarse white muscovite also include Cpy_2. Also, Mo_2 is much less abundant than Cpy_2 in assemblage 3_F and Cpy_1 in assemblage 1_F, but is much more abundant than Mo_1 in assemblage 1_F.

Assemblage 4_F: This assemblage is characterized by hematite (Figure 15 E, G), which is not associated with quartz. Hematite forms anhedral crystals that are typically <2 µm and that rim magnetite and rutile.

Veins: Footwall

Based on size and morphology, two types of veins were identified in the granites and quartz monzonites exposed in the footwall: A_B and A_{NB} veins (Tables 2 and 3). A_B veins are >2cm wide commonly and are composed of multiple vertical bands of quartz that are parallel to

one another (Figure 16 A, B). These veins are always found in prospect pits and are referred to herein as A_B veins, wherein "B" signifies banded. Within an A_B vein, each band has straight margins and commonly exhibits discontinuous bands of coarse sulfides or coarse phyllosilicates, which are aligned parallel to the vein margins. Coarse muscovite associated with these bands fills vein centerlines or rims the outer margins of individual bands of CL-dark quartz (Figure 16 A). A_B veins also commonly contain host rock fragments within or in-between individual bands and elongated parallel to vein margins (Figure 16 B).

A_{NB} veins range in size from <0.5-2cm and are analogous to individual quartz bands in the A_B veins, but occur as single veins (Figure 16 C, D). These veins are commonly found throughout the footwall area and are referred to hereafter as A_{NB} veins, wherein "NB" signifies "non-banded." A_{NB} veins have moderately sinuous boundaries, and are very similar to the individual bands in A_B veins in that they host the same mineral assemblages, exhibit the same mineral textures and alteration types, and contain host rock fragments. These smaller veins typically don't have sulfide or mica filled centerlines, and rarely host sulfides, oxides, and coarse phyllosilicates along their margins. However, when filled with CL-dark quartz, A_{NB} veins commonly have coarse mica alteration selvedges. ANB veins also commonly contain large masses of magnetite, which are absent from A_B veins (Figure 16 C).

A_B and A_{NB} veins generally contain the same sulfide and oxide minerals and quartz types. However, minor differences exist between A_B and A_{NB} veins in terms of the abundances and textures of the sulfide and oxide mineral phases found in the veins, particularly Mo_1, Mo_2, CPy_2, Py_2, and Mt (Tables 2 and 3).

Host rocks: Hanging wall

The host rocks for vein samples from drill hole K-10 (Figure 7, 12 B, 13 A) that penetrated hanging wall rocks are variably altered igneous porphyritic and phaneritic rocks. The phaneritic rocks found in the hanging wall typically contain ~10-30% euhedral to subhedral potassium feldspar, ~20-50% euhedral to anhedral plagioclase, ~20-30% subhedral to anhedral quartz, and ~2-5% subhedral to euhedral biotite, and plot in the granite field on a QPAF diagram. The porphyritic rocks found in the hanging wall typically contain phenocrysts of euhedral plagioclase (~60-70%), anhedral potassium feldspar (10-20%) anhedral quartz (~20-30%), euhedral biotite (2-5 %), and euhedral to subhedral amphibole (~2%) in a fine plagioclase- and quartz-rich ground mass. These rocks plot in the granodiorite field on a QPAF diagram. All the hanging wall samples were collected from drill core and are not available in outcrop. However, surface outcrops to the west of the hanging wall field area are of late Cretaceous and Precambrian age; thus, it's possible that hanging wall host rocks are from this age range (Vuich, 1974).

Vein Assemblages: Hanging Wall

Vein minerals in the hanging wall occur in 5 discrete assemblages based on textural and crosscutting temporal relationships. The minerals from each assemblage are commonly intergrown with one another and are described generally below, and in detail in Table 4.

Assemblage 1: Assemblage 1 minerals are intergrown with CL-bright quartz, which has a growth-zoned or mottled appearance in cathodoluminescence (Figure 14 A, B, C). Individual crystals of this quartz commonly range in size between 100-900 µm, have rounded edges and euhedral growth-zoned or mottled cores, are commonly highly fractured, and are crosscut by later quartz generations. This quartz is identical to the CL-bright quartz found in the footwall.

Sulfide and oxide minerals in assemblage 1 include pitted euhedral, non-inclusion-bearing pyrite (Py_1) that ranges in size between 50-200µm (Figure 17 A), anhedral galena (Gl) that ranges in size between 50-600µm (Figure 17 A, B), and anhedral sphalerite (Sp) that encloses anhedral chalcopyrite and ranges in size between 50-500µm (Figure 17 A, B). This assemblage also includes grey, very fined-grained (<2 µm) masses of anhedral calcite (Cc), which are intergrown with Sp and Gl along with CL-bright quartz (Figure 16 F).

Assemblage 2: The sulfide minerals in assemblage 2 are also intergrown with CL-bright quartz, and fill or partially fill cracks in assemblage1 sulfides. Assemblage 2 sulfides include anhedral chalcopyrite (Cpy_1) and pyrrhotite (Po) that occur as 5-50 µm wide inclusions in euhedral pyrite (Py_2) crystals (Figure 17 C), and euhedral-anhedral molybdenum (Mo_1) that ranges in size between 50-100µm (Figure 17 D) and commonly forms along vein margins or fills fractures in assemblage 1 sulfides. Chalcopyrite and pyrrhotite inclusions in pyrite are identical to the chalcopyrite and pyrrhotite in footwall assemblage 1 and thus, share the Cpy_1 and Po abbreviation, respectively. However, footwall Cpy_1 and hanging wall Cpy_1 differ in that hanging wall Cpy_1 does not occur as inclusions in Mt.

$Molybdenite_1$ in this assemblage is similar to $molybdenite_1$ in footwall assemblage 1 and also shares the Mo_1 abbreviation. However, masses of Mo_1 in the hanging wall tend to be smaller in size 100-500 µm, less abundant, and contain more euhedral crystals than footwall Mo_1. Mo_1 masses in the hanging wall are also never encompassed by magnetite (Mt), chalcopyrite (Cpy_2), or pyrite (Py_2) crystals.

Assemblage 3: Unlike assemblages 1 and 2, the sulfide, oxide and silicate minerals in assemblage 3 are intergrown with or adjacent to fine-grained CL-dark quartz crystals, which range in size between 5-500 µm and are identical to CL-dark quartz found in the footwall (Figure

14 A, B, C). This quartz fills fractures in and crosscuts CL-bright quartz, fills fractures in sulfide and oxide phases associated with assemblages 1 and 2, contains rounded inclusions of CL-bright quartz, and is typically associated with the bulk of the sulfide mineralization in the hanging wall.

Assemblage 3 sulfides and oxides include euhedral pyrites (Py_2) that range in size between 100-1000 µm and contain Cpy_1 and Po inclusions (Figures 17 C, D, E), euhedral magnetite (Mt), which ranges in size between 100-800µm and occurs as individual crystals intergrown with CL-dark quartz or Py_2 (Figure 17 E), and anhedral masses of rutile which range in size between 10-200µm and occur adjacent to or within masses of green mica (Figure 17 G, K) or as inclusions in Py_2 (Figure 17 F). Rutile-bearing green micas (GM) are also included in this assemblage, and occur as masses of anhedral-subhedral crystals, which range in size between 50-200 µm and are intergrown with CL-dark quartz or fill fractures in CL-bright quartz (Figure 17 G).

Cpy_1 and Po inclusion-bearing pyrites in the hanging wall are identical to Py_2 found in the footwall and share its abbreviation. Magnetite and rutile in the hanging wall are also identical to Mt and Ru found in footwall assemblage 3 and share the Mt and Ru abbreviations, respectively. However, one key difference between the Ru found in the hanging wall and in the footwall is that hanging wall Ru is associated with green mica rather than coarse white muscovite. Also, as in the footwall, hanging wall Mt commonly occurs as inclusions in Py_2, but these inclusions typically are euhedral. Furthermore, Mt crystals in the hanging wall that occur by themselves and are not inclusions in Py_2, never contains Cpy_1 inclusions similar to the Cpy_1 inclusions in Py_2.

Assemblage 4: All sulfide phases in assemblage 4 are intergrown with CL-dark quartz and green mica, and fill fractures in assemblages 1, 2 and 3 minerals. Assemblage 4 sulfides include anhedral chalcopyrite (Cpy_2) that ranges in size between 20-500µm and occurs adjacent

to or fills fractures in Py_2 (Figure 17 H), subhedral to euhedral molybdenum (Mo_2) that ranges in size between 50-100µm and occurs within masses of green mica (Figure 17 I), and anhedral bornite (Bn), which ranges in size between 10-50µm and forms rims round chalcopyrite (Figure 17 J).

Cpy_2 in the hanging wall is identical to Cpy_2 found in the footwall, and shares the Cpy_2 abbreviation. Likewise, Mo_2 in assemblage 4 is identical to Mo_2 in the footwall, but is associated with green mica rather than coarse white muscovite. Never the less, molybdenum from assemblage 4 shares the Mo_2 abbreviation with the molybdenite$_2$ in hanging wall assemblage 3 because of its similar texture and occurrence within and around a phyllosilicate mineral.

Green micas (GM), which host masses of anhedral rutile, are also included in this assemblage and occur as masses of anhedral-subhedral crystals that rim CL-dark quartz or fill fractures in CL-bright quartz (Figures 17 G). Rutile-hosting green micas form green alteration selvedges adjacent to the veins.

Assemblage 5: Assemblage 5 is identical to assemblage 4 in the footwall and contains hematite, which is not associated with quartz. Hematite in the hanging wall occurs as very fine-grained anhedral crystals that rim individual magnetite and rutile crystals, and commonly also forms splays of elongate, lath-shaped crystals that range in size between 5-150µm (Figure 17 E, K). Given its general similarity to hematite found in the footwall, hematite in hanging wall assemblage 5 shares the "Hem" abbreviation with hematite in footwall assemblage 4.

Veins: Hanging Wall

A Veins: A veins (Table 2) are the second most common vein type occurring in the hanging wall, are found in ~29% of hanging wall samples, have sinuous or jagged boundaries,

commonly branch off to form multiple veins, never have centerlines, contain sulfides along their margins, and are similar to "A" veins described by Gustafson and Hunt (1975) (Figure 16 G). A veins are commonly crosscut by B veins that have straight, well-defined margins, and such A veins are overprinted by alteration and mineralization associated with cross-cutting B veins (Figures 16 G). However, A veins are never crosscut by sphalerite- and galena-rich B veins with moderately sinuous boundaries.

The abundance and variety of minerals present in A veins is variable and A veins commonly contain both assemblage 1 and 2 minerals, which are consistently related to CL-bright quartz, and assemblage 3 and 4 minerals which are consistently related to CL-dark quartz (Table 5). However, typical A veins are composed of 75-80% CL-bright quartz, 5-10% CL-dark quartz, 1-1.5% Py_1, 0.5-1% Sp; 1-2% Cpy_1, 0.5-1% Po, 1-2% Mo_1; 2-7% Py_2, 2-4% Ru; 2-4% Cpy_2, 2-5% Bn; and 1-5% Hem. Typically, CL-bright quartz is the dominant quartz in A-veins but individual CL-bright quartz crystals are commonly crosscut by multiple sets of fractures filled with CL-dark quartz. Py_1, Sp, Gl, and assemblage 2 Mo_1 occur as scattered masses of anhedral to subhedral crystals within veins along the vein margins, and are intergrown with CL-bright quartz. Assemblage 3 Mt and Py_2 containing assemblage 2 Cpy_1 and Po inclusions occur in masses within A veins, along the vein margins, or in the center of the veins as a centerline, and are only observed where CL-bright quartz is cut by CL-dark quartz-filled fractures. Assemblage 4 Cpy_2, Ru, and Bn all occur as scattered masses of fine crystals throughout the A veins and are always adjacent to CL-dark quartz. Hematite in A veins mostly occurs as elongate lath-shaped crystals in A-veins, but also forms well-defined rims around masses of anhedral rutile crystals. These observations demonstrate that assemblage 1 and 2 minerals are consistently related to CL-

bright quartz, and assemblage 3 and 4 minerals are consistently related to CL-dark quartz (Table 5).

Fragments of host rock granites and granodiorites that contain plagioclase and orthoclase phenocrysts and groundmass are also common in A veins (Figure 17 L). These host rock fragments range in size from 0.8-3mm and are typically rimmed by sulfide minerals from assemblages 1, 2, and 3 (Figure 17 L).

Potassic alteration is the most abundant alteration typically associated with A veins, which are never temporally related to green mica alteration or alteration selvedges composed of green mica. However, A veins are locally overprinted by green mica alteration where A veins are cut by B veins (Figure 16 G).

B Veins: B veins (Table 2) are the most common hanging wall vein type, are found in 65% of hanging wall granite and granodiorite samples, have straight to moderately sinuous vein boundaries, commonly contain sulfide or calcite filled centerlines, and are similar to the "B" veins described by Gustafson and Hunt (1975) (Figure 16 E, F, H)**.** Of all examined B veins in the hanging wall, ~75% have straight, well-defined vein margins and commonly contain disseminated sulfides or sulfides filling a centerline. The remaining ~25% of B veins have moderately sinuous boundaries, small masses of disseminated sulfides and/or sulfide filled centerlines, calcite bands, and a high ratio of CL-bright to CL-dark quartz.

Like A veins, B veins commonly also contain both assemblage 1 and 2 minerals, which are consistently related to CL-bright quartz, and assemblage 3 and 4 minerals which are consistently related to CL-dark quartz (Table 5). However, B veins are typically composed of 40-55% CL-bright quartz, 30-50% of cross-cutting CL-dark quartz, 0-10% calcite, 0-5% Py_1, 10-

20% Py_2, 0-15% Sp, 0-15% Gl, 2-7% Mt, 2-5% Ru, 1-5% Hem, 1-5% Cpy_2, 1-5% Mo_2, 1-3% Cpy_1, 1-3%Mo_1, 1-2% Po, and 1-2% Py_1. CL-bright quartz in B veins commonly forms along the outer margin of the vein in contact with the host rock and commonly has abundant fractures, which are filled with CL-dark quartz. The density of CL-dark quartz-filled fractures in CL-bright quartz increases from the margins of the quartz veins to their centers, with CL-bright quartz near vein margins having few fractures (Figure 14 D, E), and CL-bright quartz in the interior of the vein having abundant fractures (Figure 14 F). B vein centerlines are primarily filled with highly fractured assemblage 3 Cpy_1 and Po inclusion-bearing Py2, which is rimmed by CL-dark quartz. Rutile-bearing green micas in B veins are commonly intergrown with centerline sulfides and CL-dark quartz, or fill fractures in CL-bright quartz. Fractures in centerline Py_2 are typically filled by assemblage 4 Mo_2 and Cpy_2 along with CL-dark quartz and rutile-bearing green micas. B veins also commonly contain fragments of host rock granites and granodiorites that range in size from 0.5-3 mm and are commonly rimmed by assemblage 1, 2, and 3 sulfide minerals.

The ~25% of B veins with moderately sinuous boundaries contain a greater abundance of assemblage 1 Py_1, Sp, and Gl than B veins with straight boundaries, tend to contain the largest euhedral CL-bright quartz crystals (500 µm-2.5 mm), commonly contain calcite bands along their margins that are intergrown with Py_1, Sp, and Gl (Figure 16 F), and are never cut by, nor crosscut, A veins. In contrast, the ~75% of B veins with straight, well-defined margins and little or no assemblage 1 Py_1, Sp, and Gl, have a wide range of quartz crystal sizes, and do not crosscut, nor are crosscut by, A-veins.

D Veins: D veins (Table 2) are the least common vein type in the hanging wall, and are found in ~27% of hanging wall granites and granodiorites. Like the D veins described by

Gustafson and Hunt (1975), they have straight margins, and are composed entirely of sulfides (Figure 16 E, H). D veins are typically 1-2.5 mm wide, are always found <0.5 cm from the margins of B veins, and are parallel to spatially associated B veins. D veins are composed entirely of assemblage 3 Py_2 (~90%) with its typical inclusions of assemblage 2 Cpy_1 (~8%) and Po (~2%), and are never crosscut by other vein types.

Alteration in Footwall and Hanging Wall Rocks

Potassic aAlteration: The most common alteration found in hanging wall granites and granodiorites and footwall quartz monzonites and granodiorites is potassic alteration (Figure 16 C, G). It is associated with all the vein types in the hanging wall and footwall, but is most well developed proximal to CL-bright quartz-rich A veins in the hanging wall, and CL-bright quartz-rich A_{NB} veins in the footwall. Potassic alteration typically forms a selvedge along quartz vein margins, is typically ~1-3x the width of its associated vein (typically ~2cm-2m), and is characterized by potassium feldspar replacement of plagioclase feldspar phenocrysts and fine-grained plagioclase in the ground mass of the granites, granodiorites, and quartz monzonites. While mostly affecting plagioclase phenocrysts and groundmass, this alteration does not affect primary biotite and quartz phenocrysts in host rocks. Rarely, orthoclase in potassic alteration selvedges along the outer margins of A_{NB} veins can be as large as 2mm wide.

Where potassic alteration is most well developed, original plagioclase textures including polysynthetic twining and original crystal textures are absent. The intensity of this alteration typically increases with proximity to vein margins, but where it is overprinted by green mica alteration, potassic alteration textures and minerals are absent. Also, this alteration commonly forms localized red-brown patches of fine-grained potassium feldspar on altered plagioclase

crystals that are partly or fully opaque in transmitted light. SEM-EDS analysis of these opaque areas showed only spectra for potassium feldspar, so the origin of these opaque patches is not known.

Green Mica Alteration: Green mica alteration is only found in hanging wall granites and granodiorites and occurs as B vein selvedges of intergrown dark green, subhedral to anhedral muscovite that ranges in size from ~20-100 µm, anhedral sericite that is typically < 50 µm, anhedral rutile that is typically 1-10 µm, and minor anhedral quartz and subhedral pyrite (Figure 16 E, G). This alteration is found in ~30-40% of the granite and granodiorite host rocks in the hanging wall and typically forms well-defined vein selvages with sharp outer boundaries that extend ~2.5-15 mm from B veins with straight margins, >40% CL-dark quartz, and a sulfide-filled center line.

Where green mica has altered host rock granites and granodiorites, phenocryst and groundmass textures have been destroyed. Furthermore, where a vein with a selvedge of this alteration type cross-cuts a vein with a potassic alteration selvedge, the potassic alteration minerals and textures have been completely destroyed.

Green muscovite in this alteration type occurs as masses of subhedral to anhedral crystals that range in size from ~50-300 µm and are most abundant proximal to vein margins. Grey sericite also occurs with this alteration type and forms masses of anhedral crystals that are typically <50 µm and intergrown with the green muscovite selvedges that characterize this alteration type.

Rutile is a common oxide mineral associated with green mica alteration. Rutile commonly occurs as masses of round, anhedral crystals that range in size from 1-25 µm, and form along cleavage planes or around the outer margins of individual green muscovite crystals in

the vein selvages. Where this alteration type is most intense, rutile is sufficiently abundant that masses of rutile crystals throughout the green muscovite cause the muscovite to appear opaque in transmitted light (Figure 17 G).

Where this alteration overprints primary euhedral biotite in host rock granites and granodiorites, the outer margins of the biotites are typically green. Many such altered biotites also contain elongate, euhedral rutile needles, which are disseminated throughout individual crystals of biotite, and differ from the aggregates of fine-grained rutile crystals that align along cleavage planes in green muscovite.

*Coarse Mica Alteration***:** Coarse mica alteration is only found in host rock granites and quartz monzonites in footwall rocks, is associated with all A_B veins and CL-dark A_{NB} veins, and over prints potassic alteration. This alteration is characterized by multiple, adjacent masses of clear euhedral muscovite that range in size from 50 µm-6 mm forming rims along the outer margins of banded quartz veins, individual CL-dark bands in banded quartz veins, and the outer margins of non-banded quartz veins (Figure 16 A, C, D). Minor grey, anhedral, 2-8 µm masses of sericite are also commonly intergrown with the coarse muscovite in selvedges along vein margins. In addition, both the sericite and muscovite in coarse muscovite alteration contain abundant masses of round, anhedral rutile, which are1-10 µm in diameter and commonly occur along cleavage planes or around the margins of the muscovite and sericite masses. This alteration is best developed proximal to footwall veins, and multiple, adjacent masses of clear euhedral muscovite and sericite commonly form vein selvages that extend into host rock granites and quartz monzonites ~0.5-3x the width of their associated vein, typically 5mm-<3.5m. Coarse muscovite from this alteration type also occurs in fractures that cut A_B and A_{NB} veins and host rock (Figure 15 I).

Chalcopyrite, pyrite, and molybdenite are also associated with coarse muscovite alteration. Chalcopyrite and pyrite commonly occur around the margins of or surrounded by masses of muscovite and sericite (Figure 15 B, J, K). Molybdenite occurs similarly to chalcopyrite and pyrite, but is only associated with muscovite and commonly occurs along cleavage planes (Figure 15 L).

The mineralogy and textures that characterize this alteration are consistent with greisen alteration (Stavast, 2006; Seedorff et al., 2008; Maher, 2008) that typically forms at significant depth in porphyry systems (Seedorff et al., 2008). Because of this similarity, this alteration type is interpreted to be analogous to greisen.

Vein and Alteration Interpretation: Footwall

A_{NB} veins in the footwall are analogous to individual bands within A_B veins and the formation of single CL-dark or CL-bright quartz-rich A_{NB} veins was concurrent with the formation of single CL-dark or CL-bright quartz-rich bands in A_B veins. Thus, the sequence of events presented below does not include a separate discussion of A_{NB} and A_B veins.

The paragenetic stages discussed in the following paragraphs are presented in order from oldest to youngest (Tables 2, 5) and are based on the crosscutting relationships between the vein minerals found in the footwall and their associated alteration types, as well as the inferred chemical evolution of this hydrothermal system. One important detail of this interpretation for the footwall is that both A_{NB} and A_B veins have undergone multiple periods of fracturing or reopening, and thus, contain two discrete quartz generations and multiple mineral phases that formed at multiple times intervals. These time intervals are represented by early CL-bright

quartz, which is associated with assemblage 1_F minerals, and later CL-dark quartz, which is associated with assemblage 2_F and 3_F minerals.

1) *Precipitation of CL-bright quartz and assemblage 1 (CPy_1, Po, Mo_1) and formation of potassic alteration.* CL-bright quartz and assemblage 1_F Cpy_1, Po, and Mo_1 precipitated concurrently and were the earliest minerals to form, as indicated by consistent intergrowths of these minerals with one another in the footwall. Potassic alteration formed concurrently with CL-bright quartz, Cpy_1, Po, and Mo_1 because of its common association with these minerals; all are commonly overprinted by later coarse muscovite alteration.

2) *Precipitation of CL-dark quartz, replacement of assemblage 1_F Cpy_1 and Po by assemblage 2_F Mt and Py_2, and formation of coarse muscovite alteration with assemblage 2_F rutile.* All assemblage 2_F minerals are intergrown with or surrounded by CL-dark quartz, which crosscuts and formed after CL-bright quartz. Also, Py_2, which is part of assemblage 2_F, encloses assemblage 1_F Cpy_1 and Po, and, thus, Py_2 formed after assemblage 1 minerals. Furthermore, assemblage 2_F Mt and Py_2 are intergrown with one another and Mt crystals intergrown with Py_2 commonly have a euhedral shape. These textures, as well as the fact that 1_F Po and 2_F Mt must have formed under different oxidation conditions, are consistent with Mt having formed after assemblage 1_F minerals.

Coarse muscovite, sericite, and Ru are always intergrown with CL-dark quartz, overprint potassic alteration, and are commonly adjacent to or intergrown with assemblage 2_F Mt and Py_2, indicating that these minerals formed under the same conditions and at approximately the same time. Because of its ubiquitous and consistent association with coarse muscovite, it is likely that rutile formed during this timeframe.

3) *Continued precipitation of CL-dark quartz and coarse mica alteration with assemblage 2_F rutile, and precipitation of assemblage 3_F CPy_2 and Mo_2.* Cpy_2 and Mo_2 are intergrown with coarse muscovite and rutile and fill fractures in assemblages 1_F and 2_F sulfide minerals; thus, assemblage 3_F Cpy_2 and Mo_2 formed after assemblages 1_F and 2_F. Also, coarse mica alteration formed concurrently with assemblage 3_F minerals because coarse muscovite crystals are commonly intergrown with or encompass assemblage 3_F minerals.

4) *Oxidation and precipitation of hematite (Hem).* Euhedral to anhedral hematite in the footwall occurs along the margins of Mt and Py_2. Hematite is not associated with quartz or hydrothermal alteration and formed by supergene oxidation processes after the system cooled.

Vein and Alteration Interpretation: Hanging wall

The petrographic steps discussed below for the hanging wall are presented in order from oldest to youngest (Table 6) and based on crosscutting relationships between vein mineral assemblages, vein types, and alteration types. Like the footwall, hanging wall A and B veins have undergone multiple periods of fracturing or reopening, and contain quartz and minerals that formed at two discrete times. These time intervals are represented by early CL-bright quartz, which is associated with assemblages 1 and 2 in the hanging wall, and later CL-dark quartz, which is associated with assemblages 3 and 4 in the hanging wall.

1) *Precipitation of CL-bright quartz and assemblage 1 Sp, Gl, Cc, and Py_1 in A and B veins, and the formation of potassic alteration.* CL-bright quartz is intergrown with, and therefore formed within the same timeframe as, assemblage 1 minerals. Also, because CL-bright quartz is crosscut by CL-dark quartz and mineral assemblages 2, 3, and 4, CL-bright quartz formed prior to CL-dark quartz. Furthermore, assemblage 1 minerals, which are associated with

CL-bright quartz, are commonly crosscut, replaced, or enclosed by minerals in assemblages 2, 3, and 4, indicating that assemblage 1 minerals formed prior to assemblages 2, 3, and 4. Similarly, potassic alteration is spatially associated with and formed concurrently with assemblage 1 minerals and CL-bright quartz.

2) *Continued precipitation of CL-bright quartz, precipitation of assemblage 2 Cpy_1 Po, and Mo_1, and continued formation of potassic alteration.* Cpy_1 and Po in assemblage 2 are always associated with one another and formed together, thus, they are likely to have formed within the same timeframe, and prior to Py_2, which now hosts them as inclusions. Mo_1 is part of assemblage 2 because, similar to Cpy_1 and Po, it is commonly partly surrounded by Py_2. CL-bright quartz continued to precipitate while assemblage 2 was precipitating because it is intergrown with assemblage 2 CPy_1 and Mo_1. Furthermore, assemblage 2 minerals formed after assemblage 1 minerals because Mo_1, Cpy_1, and CL-bright quartz fill fractures in assemblage 1 minerals.

3) *Reopening of B veins, fracturing of A veins, precipitation of CL-dark quartz and assemblage 3 Py_2, and Mt, formation of green mica alteration with assemblage 3 rutile, and formation of D veins.* Centerlines and fractures in CL-bright quartz in B veins and fractures that crosscut CL-bright quartz in A veins are filled with CL-dark quartz and assemblage 3 and 4 minerals. The formation of fractures and spatial relationships clearly indicate that CL-dark quartz and assemblage 3 and 4 minerals formed after CL-bright quartz and assemblages 1 and 2.

Given that green mica, sericite, and rutile are always associated with CL-dark quartz and commonly are adjacent to or intergrown with assemblage 3 Py2, Ru, and Mt, green mica alteration is likely to have formed concurrently with assemblage 3 minerals. Therefore, green mica alteration is interpreted to be part of assemblage 3.

4) *Continued reopening of B veins and fracturing of A veins, precipitation of CL-dark quartz and assemblage 4 Cpy2, Mo2, Bn, and further development of green mica alteration with assemblage 4 Ru.* Cpy_2 and Mo_2 from assemblage 4 are intergrown with green mica and/or CL-dark quartz, and partly enclose or fill fractures in all assemblage 1, 2, and 3 sulfide minerals. These textures indicate that Cpy_2 and Mo_2 formed after assemblages 1, 2, and 3. Also, Bn typically forms rims around either CPy_1 or CPy_2 and it is not clear which generation of chalcopyrite is associated with Bn. However, given that the majority of CPy_1 crystals occur as inclusions in Py_2, its likely that Bn is forming rims on CPy_2, and thus, it is included in assemblage 4 chalcopyrite mineralization.

Intergrown green micas, sericite, and Ru in CL-dark vein quartz and in alteration selvedges are most abundant in and commonly occur adjacent to samples with abundant assemblage 4 minerals. These textures indicate that green mica alteration continued to form during this timeframe and, therefore, green mic alteration is interpreted to also be part of assemblage 4.

5) *Oxidation and precipitation of hematite (Hem).* Assemblage 5 hematite occurs on the margins of Mt and Py_2 and is not associated with quartz veining or any observed hydrothermal alteration. These observations are consistent with formation of hematite by supergene processes after assemblages 1-4 formed and the system cooled.

CHAPTER 5

FLUID INCLUSION PETROGRAPHY AND ANALYSIS

Fluid Inclusions Assemblages (FIAs)

Most fluid inclusions studies of hydrothermal systems focus on spatially related assemblages of fluid inclusions that have consistent phase ratios indicating they synchronously trapped past hydrothermal fluids during a discrete time interval and have not been significantly altered following their formation, and therefore confidently record the pressure, temperature, and chemical (P-T-X) conditions of the hydrothermal fluid that were present during that time. These fluid inclusions assemblages, or FIAs (Goldstein and Reynolds, 1994), are commonly found within growth zones, healed fractures that terminate at the boundary of single crystals of translucent minerals, or along healed fractures the cut across multiple crystals of translucent minerals. FIAs are important because they record the evolution of P-T-X conditions within a hydrothermal system over time, and can be confidently linked to particular generations of hydrothermal minerals. However, recognition of FIAs in samples from porphyry environments is made difficult by the fact that the formation of a porphyry system involves many episodes of fracturing, input of hydrothermal fluids, and precipitation of mineral assemblages overprinting earlier assemblages. This process results in the overprinting of multiple generations of fluid inclusions, which makes it difficult to distinguish one generation from another and, because different generations of fluid inclusions can be hosted by the same mineral, the timing relationships between them can become obscured. To deal with this difficulty, past studies have used SEM-CL analysis to differentiate between multiple generations of quartz and the fluid inclusions they host (Rusk et al., 2004), and to place inclusions into discrete groups based on spatial association and consistent phase ratios.

In samples from the Kabba hanging wall and footwall, unambiguous FIAs were rare. Most inclusions found in hanging wall and footwall samples occur in scattered clusters and lack clear evidence for contemporaneous trapping, or occur within fractures in vein quartz, which crosscut crystal boundaries and inclusions are likely to be secondary. However, spatially related inclusions were found throughout these samples and were placed in groups based on their liquid to vapor ratios, CO_2 content, the consistent presence or absence of daughter crystals, and occurrence in either CL-bright or CL-dark quartz. All of these groups typically exhibited similar behavior during microthermometry and, based on this information, are inferred to have been trapped more or less synchronously and, thus, represent FIAs.

Fluid Inclusion Group Assignment and Notation

The system used herein to classify fluid inclusions places inclusions in groups based on liquid to vapor ratios, the number of phases present at room temperature, the presence or absence of CO_2 identified through either petrography or microthermometry, the presence of daughter crystals that homogenized during heating, and occurrence in either CL-bright or CL-dark quartz. This system is similar to and uses some of the same terminology as that used by Rusk et al. (2008) for distinguishing fluid inclusion types found in the Butte Cu-Mo porphyry system.

For the fluid inclusion groups outlined below, "B" stands for bubble, and the number denotes the average volume percent vapor, "D" is used to denote the presence of opaque or translucent daughter crystals, and "C" is used to denote the presence of CO_2 in an inclusion group. Using this system, six groups of fluid inclusions were identified in and described for the hanging wall (B15, B30D, B30H, B75, B20C, and B75C) and three groups were identified in and described for the footwall (B15C, B15D, and B30).

Fluid Inclusion Groups: Footwall

B15D: B15D inclusions represent 52% of all footwall inclusions, and occur as scattered clusters of individual inclusions in Cl-bright quartz in both A_B and A_{NB} veins (Figure 18 A, 19). These inclusions are similar to B15 inclusions found in the hanging wall in that B15D inclusions contain liquid, a vapor bubble that occupies ~5-15 vol% of the inclusions, and, rarely, a translucent or opaque daughter crystal. The inclusions range in size between 5-30 μm (~7.5 μm mode), and have outer walls that form triangular and rectangular shapes with rounded edges. However, unlike B15 inclusions, B15D inclusions, in some localities, have jagged or irregular boundaries and form large, elongate inclusions.

Approximately 19% of B15D inclusions contain an oval- or triangular-shaped opaque daughter crystal. The oval opaque daughter crystals are ~1-2 μm wide, did not homogenize during heating, and were not identified. The triangular daughter crystals typically occupied a volume slightly greater than or equal to the volume occupied by the vapor phase, approximately ~1.5-3 μm, and, based on their shape, are inferred to be chalcopyrite. These triangular daughter crystals did not homogenize during heating and only rarely occur in the same inclusions as the unidentified oval daughters.

Approximately 4% of B15D inclusions contain an elongate, rectangular, translucent daughter crystal. These daughter crystals never homogenized during heating and are up to ~1.5-4 μm wide. Similar daughter crystals in CO_2-rich inclusions in the footwall were identified by Raman analysis as calcite, and it is likely that these translucent daughter crystals in B15D inclusions are also calcite.

B30: B30 inclusions comprise 2% of all footwall inclusions and occur as scattered clusters in CL-bright quartz in A_B and A_{NB} veins (Figure 18 B, 19). These inclusions generally have a rectangle shape with a variably sinuous outer rim, contain liquid and a vapor phase that occupies ~10-30 vol% of the inclusion, and most contain an opaque daughter crystal. The inclusions contain no detectable CO_2 and range in size from 10-30 µm.

Eighty percent of B30 inclusions contain round or oval opaque daughter crystals that are ~1-2 µm wide and did not homogenize during heating. Like other inclusions with similar opaque daughters, this phase was not identified.

B15C: B15C inclusions comprise ~46% of all inclusions found in the footwall and occur as scattered clusters in bands of CL-dark quartz or in CL-dark quartz that fills fractures in CL-bright quartz (Figure 18 C, 19). These inclusions are two- or three-phase H_2O-CO_2 inclusions that normally have a rectangular or elongate shape and were typically ~10 µm in size, but range from 5-72 µm. B15C inclusions contain H_2O liquid and CO_2 vapor that typically occupies 5-15 vol% of the inclusion, but ranges between ~ 2-30 vol%. B15C inclusions also commonly contain a CO_2 liquid phase that is visible at room temperature, and occupies 2-5 vol% of the inclusion. The presence of liquid CO_2 is more common and consistently present in this inclusion group compared to other CO_2-bearing fluid inclusions groups; however, a distinct liquid CO_2 phase was difficult to observe in small inclusions.

Approximately 6% of B15C inclusions contain an elongate or round opaque daughter crystal. This opaque phase is typically ½ - ¼ the volume occupied by the inclusion's vapor bubble, approximately ~1-2µm, and did not homogenize during heating. As with other inclusions that contain a similar opaque phase, this daughter crystal was not identified. Also, ~3.5% of

B15C inclusions contain a rectangular, translucent daughter phase that is ~1.5-3μm wide, and did not homogenize during heating. Raman analysis of two of these crystals determined that they are calcite.

Fluid Inclusion Groups: Hanging Wall

B15: B15 inclusions comprise 6% of all hanging wall inclusions. These inclusions occur in randomly scattered clusters in CL-bright quartz in A and B veins, contain a vapor bubble that occupies 5-15 vol% of the inclusions, range in size from 5-17.5 μm (~7.5 μm mode), and have angular or sinuous outer walls (Figure 18 D, 19). B15 inclusions do not contain any opaque or translucent daughter crystals; however, their irregular shape made it difficult to inspect the interior of some inclusions for the presence of small elongate opaque daughters that might have been present in corners or alcoves against the inclusion's outer walls.

B30D: B30D inclusions comprise 31% of all fluid inclusions found in the hanging wall. These inclusions typically occur as scattered clusters spread throughout CL-bright quartz in A and B veins, contain liquid and a vapor bubble that occupies ~10-30 vol% of the inclusion, and some contain one or two translucent or one opaque daughter crystals. The inclusions range in size from 5-20 μm (~10 μm mode), and form rounded rectangular shapes (Figure 18 E, 19). In three locations in B veins, primary B30D inclusions are aligned within growth zones in CL-bright quartz; however, most B30D inclusions lack conclusive evidence for a primary origin.

At room temperature 44 % of B30D inclusions contain at least one, or in rare cases two, translucent daughter crystals. The most common translucent daughter is ~1.5-3 μm wide, rectangular or cubic with rounded edges, never melted during heating, and was not identified. The other common translucent daughter found in B30D inclusions is round or oval in shape,

always occurred with the rectangular translucent daughter, and is found in <10% of the B30D inclusions. This oval translucent daughter never melted during heating and was not identified.

Approximately 37% of B30D inclusions contain a single triangular or oval opaque daughter crystal. The oval opaque daughter crystal is ~1-2 µm wide, never homogenized, and represents ~80% of all of the opaque daughters observed in B30D inclusions. As with the oval opaque daughters identified in other inclusions groups, the opaque in B30D inclusions never homogenized and was not identified. The triangular opaque crystal comprises the other 20% of all the opaque phases observed in B30D inclusions, never homogenized, and is ~1-3µm wide. Based on its triangular shape it is likely that this opaque daughter is chalcopyrite. Both opaque crystals commonly occur with translucent daughter crystals, but never occur together in the same inclusion.

*B30H***:** B30H inclusions comprise ~9% of all hanging wall inclusions and occur as scattered clusters in CL-bright quartz near the outer boundary of individual quartz crystals in A and B veins (Figure 18 F, 19). B30H inclusions contain liquid, a vapor phase that occupies ~10-30 vol% of the inclusion, halite, and some contain one or two opaque daughter crystals. Within a cluster of B30H inclusions it is common for 3-5 of these inclusions to be within 15-30 µm of each other. The inclusions range in size from 5-20 µm (~10 µm mode) and have a sinuous or oval shape. All B30H inclusions contain a translucent halite daughter crystal at room temperature that has a rectangular or cubic shape, and is 1-3.5 µm in diameter. This halite daughter crystal was identified by its shape, similar index of refraction with quartz, and by melting during microthermometry.

Approximately 25% of B30H inclusions contain one to two opaque daughter crystals. Of these, 88% have an oval shape and range in size from 0.5-1.5 µm wide, never melted during

heating, and were not identified. The remaining 12% of opaque daughters are triangular in shape, range in size from 0.5-1 µm, never melted during heating and, based on the triangular shape, are likely to be chalcopyrite.

B75: B75 inclusions comprise 6% of all hanging wall inclusions, contain liquid, a vapor phase that occupies 70-85 vol% of the inclusion, and a few contain an opaque daughter crystal. The inclusions range in size from 5-17.5 µm (~10 µm mode), and have a rectangular shape with rounded edges (Figure 18 G, 19). These inclusions occur as scattered clusters of inclusions in CL-bright quartz in A and B veins and are absent from hanging wall samples that are dominated by CL-dark quartz. B75 inclusions are also commonly found interspersed with B30D inclusions in A and B veins.

Unlike the B75C inclusions that occur the hanging wall, these inclusions exhibited neither visible nor microthermometric behavior that would indicate the presence of CO_2. However, because of their similar shape, size, and vol% vapor to B75C inclusions, B75 inclusions are difficult to distinguish. Also, though B75 inclusions occur exclusively in CL-bright quartz and B75C inclusions occur exclusively in CL-dark quartz, distinguishing between the CL-dark and CL-bright quartz is not possible in transmitted light and these two quartz varieties and the fluid inclusions they contain are commonly adjacent. Thus, recognition of CO_2 or a lack thereof during microthermometry was key to differentiating between these two inclusion types.

Approximately 3% of B75 inclusions contain an oval opaque daughter crystal, which is similar to the oval opaque daughters described in B30D and B20C inclusions, but is slightly larger in size. This opaque crystal normally occupies an area within the small liquid portion of

B75 inclusions, did not homogenize during heating, is typically difficult to clearly view, and was not identified.

*B20C***:** B20C inclusions comprise 22% of the inclusions found in hanging wall samples and occur as scattered clusters of inclusions in CL-dark quartz in B veins or along randomly oriented CL-dark quartz-filled fractures that crosscut CL-bright quartz (Figure 18 H, 19). B20C inclusions contain liquid, a CO_2 vapor bubble that occupies 10-30 vol% (~15-25 vol% average) of the inclusion, and a few inclusions contain an opaque or translucent daughter crystal. Also, 50% of B20C inclusions contain visible liquid CO_2 that typically occupies ~2-5 vol% of the inclusions, but may reach 10 vol% in some inclusions. The inclusions typically have irregular shapes with sinuous or jagged boundaries and range in size from 5-32.5 µm (~10 µm mode).

Approximately 4% of B20C inclusions contain a rectangular translucent daughter, which occupies the same vol% as the vapor phase within the inclusion. Similar translucent daughters in CO_2-bearing inclusions analyzed with Raman were identified as calcite and it is concluded that these daughters are calcite as well.

Approximately 7% of B20C inclusions contain an elongate or oval opaque phase that is similar to that described in B30D inclusions. This phase also did not homogenize during heating and could not be identified optically. With the exception of 3 inclusions, B20C inclusions do not contain more than one daughter crystal.

*B75C***:** B75C inclusions comprise 26% of the inclusions found in hanging wall samples and contain liquid, a vapor bubble that occupies 70-85 vol% of the inclusion and contains CO_2, and many inclusions contain liquid CO_2 that occupies 2-3 vol% of the inclusion (Figure 18 F, 19). These inclusions commonly occur in scattered clusters in CL-dark quartz in B veins or in CL-dark quartz that filled fractures that cut CL-bright quartz in A veins, can range in size from

~5-25 μm (~7.5 μm mode), and have an oval or rectangular shape. No opaque or translucent daughter crystals were observed in B75C inclusions.

Fluid Inclusion Group Distribution

The A, A_B, A_{NB}, and B veins described in the previous sections host the fluid inclusion groups described above. These veins were collected from the hanging wall and the footwall areas that comprise the Kabba porphyry prospect and each vein type contains both CL-bright and CL-dark quartz.

B15D, B15C, and B30 inclusions are found only in the footwall (Figure 19) and occur in both A_B and A_{NB} veins. B15D and B30 inclusions were only identified in CL-bright quartz in A_B and A_{NB} veins associated with potassic alteration (Table 7) and comprise 54% of the inclusions in the footwall, with B15D inclusions representing 52% and B30 representing 2% of all footwall inclusions (Figure 19). In contrast, B15C inclusions were only identified in CL-dark quartz in A_B veins associated with coarse mica alteration and A_{NB} veins with well-defined coarse mica alteration selvedges, and comprise 46% of all footwall inclusions (Figure 19).

B15, B30D, B30H, B75, B20C, and B75C inclusions are all only found in the hanging wall and were trapped in CL-bright and CL-dark quartz in A and B veins (Table 7). The aqueous inclusion groups, B15, B30D, B30H, and B75, are found solely in CL-bright quartz and are most abundant in A veins with potassic alteration halos, and B veins which are composed of > 60% Cl-bright quartz and have no well-defined green mica alteration selvedge. In total, these inclusions comprise 52% of all hanging wall inclusions including 6% B15 inclusions, 31% B30D inclusions, 9% B30H inclusions, and 6% B75 inclusions (Figure 19).

The CO_2-bearing B20C and B75C inclusion groups are found solely in CL-dark quartz and are most abundant in B veins that are composed of >40% CL-dark quartz and have well-defined green mica alteration selvedges. B20C and B75C inclusions comprise 48% of the inclusions in the hanging wall, with B20C inclusions representing 22% and B75C representing 26% (Figure 19).

Microthermometric Evaluation of CO_2 Content

The CO_2 content of each inclusion group was evaluated and quantified during fluid inclusion petrography and microthermometry. The majority of fluid inclusions that contain CO_2 contain a visible liquid CO_2 phase at room temperature or exhibited one or more of the following criteria during microthermometry: condensation of liquid CO_2 during cooling below 10°C, discrete freezing of H_2O and CO_2 or "double freezing" while cooling, CO_2 ice melting at approximately -56.6 ± 0.1°C during heating, or clathrate melting between 0.2-10.0°C during heating.

B15C, B20C, and B75C inclusions all exhibited at least one of the above criteria and >75% of the inclusions in each group exhibited two or more of these criteria (Table 8). Recognition of the presence of CO_2 in B20C, B75C, and B15C inclusions is a key diagnostic characteristic for these inclusion groups, and differentiates them from fluid inclusions that have similar liquid to vapor ratios, but show no evidence for CO_2 during microthermometry. Inclusions in these three groups are referred to as "CO_2-bearing" here after.

Most commonly, the presence of CO_2 in each group was identified by clathrate melting between 0.2-10°C, which was observed in 94% of B20C inclusions, 86% of B75C inclusions, and 95% of B15C inclusions (Table 8). In other inclusions, CO_2 ice melting at approximately -

56.6 ± 0.1°C during heating indicated the presence of CO_2 (Appendix E). The presence of liquid CO_2 was highly variable for all three CO_2-bearing inclusion types, and observing liquid CO_2 was difficult because of the small size and vol% of the liquid CO_2 phase, the small size of the inclusions themselves, and the CO_2 homogenization temperature range for each group (23.1-28.8°C for B75C, 23.0-28.0°C for B20C and 20.6-30.5°C for B15C), which bridges typical room temperatures (~26°C) (Appendix E). However, where absent at room temperature, liquid CO_2 condensed in the majority of these inclusions during cooling to below ~10°C.

For B15C, B20C, and B75C inclusions, bulk CO_2 and mol% CO_2 were calculated using the MacFlincor program (Brown, 1989; Brown and Hagemann, 1994), based on the equation of state for H_2O-CO_2 (Bowers and Helgeson, 1983). This program calculates bulk CO_2 for CO_2-bearing inclusions from clathrate melting temperature, CO_2 homogenization temperature, and an estimated vol% CO_2 from petrography. With the exception of CO_2 homogenization temperature, all of these variables were observed in the vast majority of B20C, B75C, and B15C inclusions. For inclusions in which CO_2 homogenization was not observed, the average CO_2 homogenization temperature of an inclusion group was used for the calculations.

All B15, B15D, B30, B30D, B30H, and B75 inclusions lacked any evidence of the presence of CO_2 during petrographic analysis and microthermometry; thus, it was assumed that these inclusions either contain no CO_2 or contain a vanishingly small amount of CO_2. These inclusions are referred to hereafter as aqueous inclusions.

Raman Analyses

Raman analysis was used to measure CO_2 density in B15C, B20C, and B75C inclusions and to evaluate the possible CO_2 content of B15, B15D, B30, B30D, B30H, and B75 inclusion

groups (Table 9). This technique was also used to identify some of the translucent daughter crystals present in B15C inclusions. All calculations of CO_2 densities measured by Raman analysis were accomplished by measurement of the spacing and displacement of bands in the Fermi diad of CO_2 (Wang et al., 2011).

Raman analyses detected CO_2 in all analyzed B20C and B75C inclusions (Table 9). B20C inclusions have a CO_2 density between 0.01 – 0.76 g/cm^3, and an average density of 0.245 g/cm^3, with 70% inclusions being between 0.14-0.34 g/cm^3. B75C inclusions have a similar CO_2 density range of 0.001 – 0.76 g/cm^3 and an average density of 0.307 g/cm^3, and have a regular distribution of CO_2 densities throughout this range.

Though all seven B15C inclusions analyzed with Raman had exhibited evidence of CO_2 during microthermometry, Raman analysis only detected the presence of CO_2 in 4 of the 7 analyzed inclusions (Table 9). A probable explanation for the absence of a Raman signal for some B15C inclusions relates to the fact that the Raman laser must be focused on the vapor phase in an inclusion, and the small vapor fraction typically present in this inclusion group, movement of the vapor phase within the inclusions during analysis, and the typical small size of B15C inclusions made focusing on the vapor phase difficult. B15C inclusions that exhibited a Raman signal for CO_2 have a CO_2 density between 0.001-0.77 g/cm^3 and an average CO_2 density of 0.243 g/cm^3 (Table 9). The CO_2 densities measured for B15C inclusions have a regular distribution throughout this range, thus, the CO_2 density of B15C inclusions is highly variable. In addition to evaluating the CO_2 content of B15C inclusions, three translucent daughter crystals present in this inclusion group were analyzed with Raman microscopy. All three daughter crystals analyzed showed the same spectra, which are consistent with calcite.

None of the analyzed B15, B15D, B30D, B30H, and B75 inclusions exhibited microthermometric evidence of CO_2. However, fluid inclusions from porphyry environments that do not show evidence of CO_2 during microthermometry, such as the B35 or B60 fluid inclusions in the Butte porphyry (Rusk et al., 2008), exhibited evidence of CO_2 when analyzed using Raman spectroscopy. Thus inclusions from the B15, B15D, B30D, B30H, and B75 groups were analyzed with Raman to determine if CO_2 was present in any of these groups.

Raman analysis of the B15, B15D, B30D, B30H, and B75 groups showed that one of five analyzed B15, 15 of 24 of B30D, one of seven B30H, four of six B75, and eight Of 25 B15D inclusions contained detectable CO_2 (Table 9). CO_2-bearing inclusions in the B15D, B20D, and B75 groups had similar average CO_2 densities of 0.157 g/cm^3, 0.159 g/cm^3, and 0.11 g/cm^3, respectively. In the B15 and B30H groups, only one of the analyzed inclusions in each group contained detectable CO_2. The CO_2-bearing inclusions in the B15 group had a density of 0.77 g/cm^3 and the CO_2-bearing inclusion in the B30H group had a density of 0.14 g/cm^3. These CO_2-bearing inclusions were kept in their respective groups because they comprised only a small number of inclusions within their groups; however, they do provide evidence for at least a small component of CO_2 in these inclusion fluids. Also, as only small amounts of CO_2 were identified in inclusions within the aqueous inclusion groups, the presence of CO_2 is variable and generally minor. Therefore detection of CO_2 by Raman analysis was not used as a parameter for assigning fluid inclusions to particular groups.

No B30 inclusions were analyzed with Raman spectroscopy. However, given that many of the other inclusion groups that did not show microthermometric evidence of CO_2 contained detectable CO_2, it is likely that this inclusion group contains some CO_2-bearing inclusions as well.

Microthermometry: Application

All fluid inclusion groups described previously were initially evaluated using microthermometry to quantify P-T-X conditions related to fluids trapped in each inclusion group (Table 8). Detailed microthermometric data from the hanging wall and footwall are tabulated in Appendix E. Salinity, bulk density, bulk CO_2 fraction (where applicable), and isochors that are used to identify approximate trapping temperatures of fluid inclusions were determined using the MacFlincor program (Brown, 1989; Brown and Hagemann, 1994). Calculations for B15, B15D, B30, B30D, B30H, and B75 inclusions were based on phase equilibria for a fluid in the H_2O-NaCl-KCl system (Bodnar and Vityk, 1994). Other than the B30H inclusions, these inclusion groups did not contain halite at 25°C and did not exhibit microthermometic evidence for CO_2; thus, the final ice melting temperature was used to determine salinity, and final homogenization temperature was used to determine bulk density and construct isochors for each trapped fluid. B30H inclusions exhibited halite melting during heating; thus, the halite melting temperature was used to calculate salinity. B15, B15D, B30D, and B30 inclusions all homogenized to liquid and none exhibited critical behavior. B75 inclusions also did not exhibit critical behavior, but homogenized to vapor rather than liquid, and minimum homogenization temperatures were determined from the earliest apparent filling of the inclusion by vapor expansion.

B15C, B20C, and B75C inclusions all showed microthermometic and/or Raman evidence for the presence of CO_2 and were evaluated by the MacFlincor program (Brown, 1989; Brown and Hagemann, 1994) using phase equilibria for H_2O-CO_2 (Bowers and Helgeson, 1983). For these inclusions the variable used in the calculation of salinity was the final clathrate melting temperature; the variables used to determine bulk density and bulk CO_2 fraction include the

temperature of CO_2 liquid and CO_2 vapor homogenization and estimation of the CO_2 vapor fraction, respectively. For many B15C, B20C, and B75C inclusions, CO_2 homogenization temperatures were not observed because of the lack of visible liquid CO_2 and the small size of many of the inclusions, which made the liquid CO_2 phase difficult to see. Bulk density and mol% CO_2 calculations for such inclusions in the B15C, B20C, and B75C groups used the average observed CO_2 homogenization temperature for other inclusions within the same inclusion group.

Leaking or decrepitation occurred commonly while heating many inclusions within all fluid inclusion groups between 350-500°C. This problem was particularly common for B15C, B20C, B30D, B30H, B75C, and B75 inclusion groups when the rate of heating was > 10°C/min. Therefore, great care was taken during microthermometric heating to verify that inclusions did not leak, and a rate of 5°C/min was used to minimize decrepitation.

In the B15, B30D, B20C, B75C inclusion groups in the hanging wall and the B15D and B30 inclusion groups in the footwall, the temperature range of homogenization is typically wide, with the lowest and highest temperatures differing by as much as 100->200°C. Part of this large range is a result of each inclusion group containing with of at least 10 vol% vapor in the group. In addition, the range in homogenization temperatures might be linked to the variable CO_2 compositions of inclusions within these groups, but the true cause is not clear. However, within the overall range of homogenization temperatures for the B15, B30D, B20C, B15D, and B30 groups, many inclusions were part of smaller, spatially related inclusion groups with smaller homogenization temperature ranges. These smaller ranges are more representative of the homogenization behavior of an FIA and are presented in the following paragraphs.

Microthermometry: Footwall

*B15D***:** Approximately 32% of B15D inclusions contained minor CO_2 detectable during Raman analysis, but none showed behavior consistent with the presence of CO_2 during microthermometry. Therefore, ice melting temperatures were used to calculate salinities for these inclusions (Table 8). Ice melting temperatures in B15D inclusions ranged from -0.9 - -6.0°C, with an average of ~ -3.1°C. This melting point depression range corresponds to a salinity range of 2.0-9.0 wt% NaCl equivalent (5.0 wt% NaCl equivalent average), with 71% of inclusions having salinities between 2.5-5.9 wt% equivalent.

The majority of B15D inclusions homogenized to liquid between 115.0-271.0°C and had an average homogenization temperature of 203.0°C. Within this range of homogenization temperatures, 22% of B15C inclusions were between 120.0-137.0°C, and 25% were between 167.0-179.0°C (Figure 20). These homogenization temperatures correspond to a bulk density range of 0.85-1.00 g/cm^3 and an average bulk density of 0.94 g/cm^3. The fluid trapped by B15D inclusions is the second most dense fluid trapped in the hanging wall and the second most dense inclusion type overall. Daughter phases in B15D inclusions did not homogenize or shrink during heating.

B15C: Approximately 88% of B15C inclusions exhibited clathrate melting between 0.2 – 10°C and have an average clathrate melting temperature of 8.0°C (Table 8). These clathrate melting temperatures correspond to a salinity range of 0.0-15.0 wt% NaCl equiv. and an average salinity of 3.8 wt% NaCl equivalent. Within the 0.0-15.0wt% NaCl equiv range, 48 % of B15C inclusions have salinities between 0.0-1.8 wt% NaCl equivalent. Approximately 51.4% of B15C inclusions were successfully heated without leaking or decrepitation. All of these homogenized

to liquid between 115.0-271.0°C and have an average homogenization temperature 203.0°C (Figure 20).

Carbon dioxide homogenization was only observed in 36.5% of B15C inclusions and occurred between 20.6-30.5°C, with 87% of these homogenizing between 30-30.5°C (30.1°C on average). This CO_2 homogenization temperature range, as well as the average homogenization temperature of 30.1°C, yielded a range of CO_2 concentrations between 1-10.3 mol% CO_2, with ~79% of B15C inclusions containing between 3-5 mol% CO_2. Corresponding densities for these inclusions range from 0.89-1.10 g/cm^3 and an average CO_2 density of 0.98 g/cm^3. Based on these densities, B15C inclusions contain the densest fluid trapped in inclusions in the footwall and the second densest fluid trapped in all inclusion groups.

*B30***:** During microthermometry B30 inclusions exhibited similar behavior to B30D inclusions in the hanging wall, but had a narrower range in ice melting temperatures and salinities. Final ice melting in B30 inclusions occurred between -2.3 - -3.4°C and was -3.1°C on average (Table 8). These ice melting temperatures correspond to a salinity range of 4.0 - 6.0 wt% NaCl equivalent and an average salinity of 4.8 wt% NaCl equivalent.

B30 inclusions homogenized to liquid between 151.0-283.0°C and have an average homogenization temperature of 227.0°C. Within this range of homogenization temperatures, 80% of B30 inclusions homogenize between 242.0-282.0°C (Figure 20). The overall homogenization temperature range for B30 inclusions corresponds to a bulk density range of 0.80-0.92 g/cm^3 and an average bulk density of 0.84 g/cm^3. Also, none of the opaque phases in B30 inclusions homogenized during heating.

Microthermometry: Hanging Wall

*B15***:** B15 inclusions showed no behavior consistent with the presence of CO_2 during microthermometry and do not contain any opaque or translucent daughters. Ice melting temperatures are between -1.6 - -11°C (-4.5 °C average) (Table 8). This is a wide ice melting temperature range and B15 inclusions exhibit a regular distribution across this range; thus, there is no mode representing a majority of inclusions (Figure 20). However, this ice melting temperature range corresponds to a salinity range of ~3.0-15.0 wt% NaCl equivalent and an average salinity of 8.5 wt% NaCl equivalent.

Homogenization temperatures in B15 inclusions ranged from 167.0-342.0°C, and had an average temperature of ~257.0°C (Figure 20), with 37% of inclusions homogenizing between 239.0-265.5°C and 37% between 305.3-342.6°C. This homogenization temperature range corresponds to a bulk density range of 0.73-0.93 g/cm^3 and an average bulk density of 0.82 g/cm^3. Based on this density range, B15 inclusions have the second highest average bulk density of all fluids trapped in hanging wall inclusions.

*B30D***:** B30D inclusions do not show microthermometric evidence for CO_2 and none of the translucent or opaque daughter crystals in the inclusions melted during heating; thus, the variables that determine the salinities and bulk densities for these inclusions are final ice melting temperature and L-V homogenization, respectively. Ice melting temperatures for B30D inclusions ranged between -0.1 - -21.1°C and averaged -5.7°C, with 71% of B30D inclusions exhibiting ice melting between -2.5 - -4.6°C (Table 8). Inclusions in the total ice melting temperature range had corresponding salinities between 2.0 -16.0 wt% NaCl equivalent and an average salinity of 8.6 wt% NaCl equivalent, with 71% having salinities of 4.1-7.3 wt% NaCl equivalent.

Approximately 40% of the B30D inclusions homogenized to liquid between 106.0 – 430.0°C during heating (Figure 20). Within this homogenization temperature range, 36% homogenized between 220.0-234.0°C. The remaining 60% of B30D inclusions, which did not homogenize, either decrepitated before final homogenization or were not heated and were preserved for LA-ICP-MS analysis. The homogenization temperature range observed in B30D inclusions corresponds to a bulk density range of 0.55 – 0.97 g/cm^3 and an average bulk density of 0.75 g/cm^3, with 32% between 0.702-0.785 g/cm^3.

*B30H***:** None of the B30H inclusions showed microthermometric evidence for CO_2 and halite melting was used to calculate salinity. A total of 11 B30H inclusions were heated to homogenization without leaking or decrepitation. Of these 11 inclusions, 8 exhibited final homogenization to liquid via vapor bubble disappearance at a temperature above the halite melting temperature. The remaining three inclusions exhibited final homogenization via halite melting at temperatures above the liquid-vapor homogenization temperature.

For the 8 inclusions which exhibited final homogenization via vapor bubble disappearance, halite melting occurred along a wide temperature range between 176.6-312.1°C (~203.0 on average), which corresponds to a wide range in salinities between 31.0-39.0 wt% NaCl equivalent (Table 8). However, within the halite melting temperature range for these inclusions, ~88% exhibited halite melting along a narrower temperature range between 176.6-215.2°C, which corresponds to a salinity range between 31.0-33.0 wt% NaCl equivalent (Table 8). Following halite melting, these inclusions exhibited liquid-vapor homogenization along a wide temperature range between 210.5-437.6°C (~271.0°C on average), which corresponds to a bulk density range between 0.88-1.11 g/cm^3 (~1.06 g/cm^3 on average) (Table 8). Within the range in liquid-vapor homogenization temperatures for these inclusions, ~75% exhibited vapor

bubble disappearance within a narrower temperature range between 210.5-286.4°C, which corresponds to a narrower range in bulk density between 1.03-1.11 g/cm^3 (Table 8). Based on the overall bulk density range, B30H inclusions are the most dense inclusion group in the hanging wall and the most dense inclusion group over all.

For the three inclusions that exhibited final homogenization by halite melting, halite melting occurred between 312.1-365.0°C (~332.9°C on average) and vapor bubble disappearance occurred between 265.1-285.4°C (~277.4°C on average). These inclusions could have formed via three possibilities: 1) very high pressures during formation, 2) post entrapment modification, and 3) heterogeneous entrapment (Lecumberri-Sanchez, 2015). It is not clear which possibility is most likely and this uncertainty makes calculating salinities and bulk densities from these inclusions difficult. However, given the fact that only three inclusions in the B30H group exhibited this behavior, it is likely that they do not represent a pattern and are therefore excluded from the discussion and interpretation in the following chapters.

*B75***:** The large vapor fraction present in B75 inclusions made it difficult to observe the liquid fraction and collect ice melting temperatures for the majority of these inclusions. However, incremental heating and cooling during microthermomentry facilitated determination of accurate temperatures for many of these inclusions. Ice melting temperatures for B75 inclusions ranged between -1.0 - -5.5°C with an average of -2.9°C (Table 8). These temperatures correspond to a salinity range of 2.0-6.0 wt% NaCl equivalent and an average salinity of ~4.5 wt% NaCl equivalent, with 75% between 4.4-5.8 wt% NaCl equivalent.

As with all vapor-rich inclusions, final homogenization temperatures for B75 inclusions cannot be accurately determined because final homogenization to vapor cannot be accurately measured (Sterner and Bodnar, 1989; Sterner, 1992). Also, some inclusions from this group

decrepitated before homogenization. Thus, it was only possible to gather minimum homogenization temperatures for a limited number of B75 inclusions. Despite these limitations, 23% of analyzed inclusions yielded minimum homogenization temperatures between 357.0-405.0°C and averaged 378.0°C.

B75 inclusions contain the lowest density fluid trapped in the hanging wall and the second lowest density fluid over all. Bulk densities for these inclusions have a very narrow range between 0.53 - 0.58 g/cm^3 and an average bulk density of 0.55 g/cm^3.

B20C: Clathrate melting was observed in 91% of B20C inclusions between 5.3-10.0°C, and averaged 9.3°C (Table 8). This range corresponds to a salinity range of 0.0-8.0 wt% NaCl equivalent and an average salinity of 1.6 wt% NaCl equivalent. Within this salinity range 75% of B20C inclusions have salinities from 0.0-1.8 wt% NaCl equivalent.

Approximately, 49% of B20C inclusions were successfully heated without leaking or decrepitation. These inclusions all homogenized to liquid between 120.0-400.0°C and 294.0°C on average, with 40% homogenizing between 301.0-352.0°C.

CO_2 homogenization was observed in only 13.5% of B20C inclusions at temperatures between 23.0-28.0°C, with an average temperature of 27.3°C. These temperatures correspond to a range in CO_2 concentrations between 3.0-45.0 mol% and an average CO_2 content of ~15.0 mol%. Within this range, inclusions clustered between 3.0-15.0 mol% CO_2 and 21.0-45.0 mol% CO_2, with ~72% of inclusions being in the 3.0-15.0 mol% CO_2 group. Corresponding bulk densities for B20C inclusions are between 0.74-0.98 g/cm^3 and were approximately 0.88 g/cm^3 on average. Based on bulk density B20C inclusions are the second-most dense fluids trapped by inclusions in the hanging wall and the fourth most dense fluid inclusion group overall.

*B75C***:** Due to their large vapor fraction, clathrate melting temperatures for B75C inclusions were difficult to observe. However, 84% of B75C inclusions formed clathrate during cooling. Observed clathrate melting temperatures (Tm_{clath}) were between 3.5-10.0°C with an average temperature of 8.8°C (Table 8). This Tm_{clath} range corresponds to a salinity range of 0.0-9.0 wt% NaCl equivalent, with ~69% of B75 inclusion having salinities between 0.0–1.6 wt % NaCl equivalent.

All B75C inclusions homogenized to vapor, and recorded temperatures are minimum estimates owing to the difficulties of determining final homogenization temp (Sterner and Bodnar, 1989; Sterner, 1992). Minimum homogenization temperatures ranged between 101.0-533.0°C and were ~300.0°C on average, with 17% between 200.0-210.0°C and 46% between 300.0-393.0°C. As homogenization temperatures for B75C are minimum temperatures, the calculated bulk densities of these inclusions are also minimum values.

Mole % CO_2 for B75C was difficult to determine because liquid CO_2 was only observed in 3% of B75C inclusions at room temperature. It was hard to discern the CO_2 liquid-vapor homogenization temperature in inclusions that did have a clearly visible liquid CO_2 phase because there was usually <2-3% liquid CO_2 and the phase boundary was normally obscured by the wall of the inclusion. Of the 3% of B75C inclusions that contained visible liquid CO_2 at room temperature, CO_2 homogenization occurred between 23.0-29.0°C, with an average temperature of 25.0°C. For B75C inclusions in which CO_2 homogenization was not observed, the average temperature of 25.0°C was used to calculate mol% CO_2. Calculations using the observed and average CO_2 homogenization temperatures yielded a mol% CO_2 range for B75C inclusions between 3.0-27.0 mol% CO_2, with ~84% falling between 22.0-27.0 mol% CO_2. Corresponding bulk densities for B75C inclusions were between 0.47-0.90 g/cm^3, with an average value of 0.53

g/cm^3. Based on this bulk density and mol% CO_2, B75C inclusions trapped the lowest density CO_2-bearing fluid, and the lowest density fluid identified in this study.

CHAPTER 6

LA-ICP-MS

Following petrographic characterization of fluid inclusion groups and microthermometry, individual inclusions from the B15, B15C, B15D, B20C, B30D, B30H, B75, and B75C inclusion groups were analyzed by laser ablation, inductively coupled plasma, mass spectrometry (LA-ICP-MS) to quantify the abundance of a number of elements present in the fluids trapped within the inclusions. Single inclusion LA-ICP-MS signals and element ratios were quantified by integration of all measured elements, corrected for host rock contributions, compared to intensity ratios with a NIST glass standard, and referenced to the absolute concentration of Na determined by microthermometry. Because heating typically resulted in leakage or decrepitation of inclusions from most analyzed inclusion groups, and because inclusions that have leaked or decrepitated during heating are not acceptable for LA-ICP-MS analysis, inclusions from B15, B15D, B15C, B20C, B30D, B75, and B75C groups that were analyzed with LA-ICP-MS were frozen and incrementally thawed to determine their salinity, but were never heated above 30°C prior to LA-ICP-MS analysis. Because the analyzed inclusions have similar characteristics to, and are spatially related to, other inclusions within their respective fluid inclusions groups, it is reasonable to assume that the analyzed inclusions that were destroyed during LA-ICP-MS analysis had homogenization temperatures similar to analogous inclusions that were not analyzed with LA-ICP-MS and were heated during microthermometry. Also, the salinity of halite-bearing inclusions is typically determined by halite melting during heating, and it was not possible to determine salinities for B30H inclusions prior to analysis. To address this problem, salinities for B30H inclusions analyzed using LA-ICP-MS were derived from the average salinity of B30H inclusions that were heated to determine halite melting temperatures.

The elements chosen for analysis with LA-ICP-MS include Ag, Au, As, Ba, Ca, Cu, Cs, Fe, K, La, Li, Mn, Mo, Na, Pb, Rb, S, Si, Sn, Sr, Ti, V, W, Zn. These elements were chosen because they are major constituents of fluids found in other porphyry systems (Ulrich et al., 2001; Rusk et al., 2004). The LA-ICP-MS data presented herein are compared to LA-ICP-MS analysis of fluid inclusions from the Butte and Bajo de la Alumbrera deposits (Ulrich et al., 2001; Rusk et al., 2004), which analyzed a similar group of elements (Ag, Au, As, Ba, Ca, Cu, Cs, Fe, K, La, Li, Mn, Mo, Na, Pb, Rb, S, Si, Sn, Sr, Ti, W, Zn). The data presented below focus on Au, Ba, Ca, Cs, Cu, Fe, K, Mn, Mo, Na, Pb, Rb, Sr, and Zn, because these elements were commonly above the limit of detection (LOD) in samples from the Kabba prospect and in the Butte and Bajo de la Alumbrera porphyry deposits. Silver, As, La, S, Ti, V, and W were typically below the limit of detection in samples from Kabba and the Butte and Bajo de la Alumbrera porphyry deposits, and are excluded from the data presented below. However, concentrations for all analyzed elements are included in Appendices F and G.

LA-ICP-MS Results: Footwall

B15C and B15D inclusions were the only inclusion types analyzed from the footwall as they were the most abundant fluid inclusions found in footwall samples (Table 10 and Appendix F, G). B15C and B15D inclusions commonly contained detectable Ba, Ca, Cu, Cs, Fe, K, Mn, Mo, Na, Pb, Rb, Sn, Sr, and Zn, but the abundance of each element in individual inclusions is highly variable. Also, the concentrations of Ca, Cu, Fe, K, Mn, Na, Sn, and Zn in B15C and B15D inclusions typically had a wide range, and the difference between the maximum and minimum concentrations of each element within an inclusion group was as much as 98,400 ppm. This is due to the typically high concentrations (>10,000 ppm) of Ca, Cu, Fe, K, Mn, Na, Sn, and

Zn as well as the presence of at least one or two inclusions with in a group that contained low concentrations (<500 ppm) of each element. The consequence of this is that the standard deviation for many analyses of B15C and B15D inclusions is >25,000 ppm. However, for elements that have high standard deviations, there is commonly a mode within the total range, and a modal average that differs from the total average by <700 ppm. Where this mode and average are more representative of typical concentrations of elements within an inclusion group, they are reported in addition to the averages of the total range of elements quantified in the B15D and B15C inclusions. Furthermore, modes and modal averages typically have standard deviations < 500 ppm. Exceptions include Na, K, Fe, and Ca that typically have wide ranges in concentrations in individual inclusions that differ by as much as 1000 ppm per inclusion. In these cases the modes are commonly large and standard deviations are >1000 ppm.

B15D: Approximately 21% of B15D inclusions (20 inclusions) were analyzed by LA-ICP-MS. These inclusions are dominated by Na, K, and Ca; however, the abundance of each element varies between samples. Sodium is above the LOD in all analyzed B15D inclusions and ranges between 1,114-21,767 ppm (12,186 ppm average), with 50% of analyzed B15D inclusions having a mode between 15,206-17,955 ppm and a modal average of 16,342 ppm. Potassium is above the LOD in 40% of analyzed B15D inclusions and ranges from 1,121-75,681 ppm (20,679 ppm average), with 50% of K concentrations having a mode between 3,105-4,451 ppm and a modal average of 3,942 ppm. Calcium is above the LOD in 25% of B15D inclusions and has a total range of 4,736-25,372 ppm (13,732 ppm average). As only 25% of the inclusions contained detectable Ca, and Ca concentrations vary regularly across the total range, there is no mode for Ca in B15D inclusions. However, B15D inclusions also commonly contain translucent daughter crystals, which were identified using Raman analysis as calcite; thus, some of the

highest Ca values came from inclusions that contained translucent daughter crystals and this is consistent with the daughters being calcite.

Iron and Cu are also major constituents of B15D inclusions but their concentrations were below the LOD in many analyzed inclusions, and they are much lower than the concentrations determined for Na, K, or Ca. Iron exceeds the LOD in ~20% of analyzed B15D inclusions and had a range of concentrations between 2,800-6,283 ppm (4,560 ppm average) with no mode. In contrast, Cu exceeds the limit of detection in ~60% of analyzed B15D inclusions, and had a much wider range, but lower concentrations than Fe in some inclusions, with total Cu ranging between 227-9,280 ppm (3,587 ppm average). Also, Cu differed from Fe in that Cu exhibits a mode between 3,049-4,628 ppm and a modal average of 3,849 ppm in about a third of analyzed B15D inclusions. Though having a wide range of concentrations, B15D inclusions have the largest number of inclusions in the footwall with detectable Cu and Fe, and the inclusions that contain Fe and Cu typically have the largest Cu and Fe concentrations in the footwall.

Strontium and Rb were both above the LOD in many B15D inclusions but were typically in low concentrations relative to dominant cations such as Na, K, Ca, Fe, and Cu. Strontium was above the LOD in 60% of analyses and Rb in 35% of analyses, but both typically have low concentrations <150 ppm.

Other elements that were present but in low abundance in B15D inclusions include Ba, Pb, Mo, Cs, and Mn. All were above the LOD in <15% of B15D inclusions with the exception of Mn, which had concentrations of 589 ppm and 137 ppm in two inclusions. Gold was not found in any B15D inclusions.

Similar to Ba, Pb, Mo, Cs, and Mn, Zn is above the LOD in 15% of B15D inclusions but is present in higher concentrations relative to Ba, Pb, Mo, Cs, and Mn, with a range between

178-838 ppm (415 ppm average). Also, Sn exceeds the LOD in 25% of B15D samples and is slightly more enriched than Zn in that it had a wider total range of concentrations between 99-900 ppm, and a slightly higher total average of 484 ppm. Given the typically low concentrations and the low number of inclusions that host detectable concentrations of Zn and Sn, these elements are interpreted as being in low abundances in B15D inclusions.

B15C: Approximately 28% of B15C inclusions (23 inclusions) were analyzed with LA-ICP-MS. Sodium, K, and Ca were the dominant cations in B15C inclusions. Sodium is detected in all analyzed B15C inclusions and is regularly distributed between 27-35,544 ppm. Two modes occur within the total range of Na values. Approximately 35% of inclusions have a mode between 3,465-6,603 ppm Na and another 35% have a mode between 27-83 ppm with an average of 62 ppm. Potassium is above the LOD in 48% of B15C inclusions and has a total range of 10-86,392 ppm (16,714 ppm average). No mode was identified for K because of the regular distribution of values as indicated by a standard deviation of 25,501 ppm. Calcium is above the LOD in 35% of B15C inclusions and varies regularly between 95-98,488 ppm. Similar to K, no mode was identified because of the regular distribution of Ca concentrations and its large standard deviation of 32,996 ppm.

B15C inclusions contain only small amounts of Cu, Zn, Fe, and Sn. Copper is above the LOD in only 17% of the analyses and, with the exception of one inclusion, which had a concentration of 8927 ppm, has a narrow range between 1-79 ppm. This range in Cu concentrations is significantly lower than B15D inclusions and much lower than hanging wall inclusion groups. Similar to Cu, Zn was only present in small amount with only 22% of B15C inclusions having Zn concentrations above the LOD. Where above the LOD, Zn varies regularly

between 4-5,487 ppm. Within this range, 60% of the Zn-bearing B15C inclusions have a mode between 101-189 ppm and a modal average of 157 ppm. Iron exceeds the LOD in the same number of inclusions as Zn (22% of B15C inclusions) and had a wide range of concentrations between 121-1,431 ppm and an average concentration of 626 ppm. Because of its wide range in concentration no mode was identified for Fe. Tin is above the LOD in a slightly greater number of inclusions than Zn and Fe (26% of B15C inclusions) and varies regularly between 8-3397 ppm. Within this range, 60% of the analyses have a mode between 145-269 ppm and a modal average of 208 ppm.

Strontium is relatively abundant in B15C inclusions in that it is present in ~87% of B15C inclusions. Inclusions with Sr have a range in concentrations between 1-184 ppm and an average concentration of 39 ppm. Within this range ~61% of B15C inclusions have a mode between 1-25 ppm and a mode average of 6 ppm.

Other elements that typically have low concentrations in B15C inclusions include Au, Ba, Cs, Mo, Mn, Pb, and Rb. Barium, Mo, Cs, and Rb are above the LOD in <22% of B15C inclusions, with the exception of Rb, which is above the LOD in 40% of B15C inclusions, but at concentrations < 58 ppm. Gold, Pb, and Mn are above the LOD in <17% of B15C inclusions and typically have low concentrations, with the exception of one inclusion, which contains ~156 ppm Pb, and another that contains 942 ppm Mn. One inclusion was determined to contain 0.07 ppm Au; however, Au was not detected in any other B15C inclusions.

LA-ICP-MS Results: Hanging wall

Select fluid inclusions from B15, B30D, B30H, B75, B20C, and B75C inclusion groups in samples from the hanging were all analyzed with LA-ICP-MS (Table 10 and appendices F and

G). These inclusion groups typically contained detectable Ba, Ca, Cu, Cs, Fe, K, Li, Mn, Na, Pb, Rb, Sn, Sr, and Zn, but their abundance in each inclusion and the range of abundances within each inclusion group is highly variable. As in the footwall, the variation in abundance of an element within a particular inclusions group may be > 90,000 ppm. This range is related to concentrations for single elements that range from as low as <500 ppm to 97,000 ppm. Such elements have standard deviations in excess of 25,000 ppm. In such instances the average concentrations of these elements are not representative of the typical abundance of that element within an inclusion group. As with footwall inclusion groups, there is commonly a narrower mode of concentrations for some hanging wall inclusion groups, and a corresponding modal average that differs from the total average by >600 ppm. Where this mode and average are more representative than the total range and average concentration of an element within an inclusion group, the mode and average are reported in addition to the total range and average for the element. These modes and averages typically have standard deviations < 250 ppm but, as with B15C and B15D inclusions in the footwall, the total range of concentrations for cations such as Na, K, Fe, and Ca, which tend to dominate hanging wall inclusions, is still large as inclusions have concentrations that differ by as much as 1,000 ppm and standard deviations >1,000 ppm.

Many analyses of B15, B20C, B30D, B30C, B75, and B75C inclusion groups had very high LOD and, with the exception of Na, K, and Sr, analyses of many inclusions were either at or below the LOD. This is probably a result of the small size of the analyzed inclusions and the difficulty of distinguishing the LA-ICP-MS signal for small inclusions from the background signal from the quartz containing the ablated inclusions.

B15: Approximately 40% of B15 inclusions (7 inclusions) were analyzed by LA-ICP-MS. The dominant cations in B15 inclusions were Na, K, Fe, and Ca. All B15 inclusions have

Na above the LOD, but its concentrations vary regularly between 6,237-70,197 ppm (24,960 ppm average). The difference in Na concentrations between inclusions within B15 inclusions is commonly 3,000-4,000 ppm, as is indicated by its standard deviation of 22,423 ppm; thus, no mode was determined for Na. Potassium is present in 57% of inclusions and also varies regularly between 2,498-47,267 ppm (18,763 ppm average). As with Na, K has no mode because of its wide range of concentrations that vary from 3,000-20,000 ppm between inclusions. Calcium exceeds the LOD in only three B15 inclusions (43% of B15 inclusions) and is more abundant than any other element in the B15 group with concentrations ranging between 9,773-95,028 ppm. Because of the wide variation in Ca, no mode was determined for Ca within the B15 group. Therefore, the presence of Ca is highly variable but, where present, is abundant. Also, Ca and Fe are correlated with one another in that Fe is also only found in three of the seven analyzed B15 inclusions, all of which have high Ca. Iron is similar to Ca in that its concentrations have a wide range between 5,906-28,653 ppm (19,205 ppm average). An average value is not representative of the Fe content of this group and no mode was identified.

Copper, Zn, Pb, Mn, and Sn are also commonly above the LOD in B15 inclusions, and the B15 inclusion group is moderately enriched Cu, Zn, Pb, Mn, and Sn compared to the other hanging wall and footwall inclusions groups. Copper is detected in 71% of B15 inclusions and varies regularly between 132-7,933 ppm (3,754 ppm on average). Within the 71% of inclusions that contain Cu, 60% contained between 3,691-7,933 ppm with the remaining 40% between 132-516 ppm. Because of the wide range of Cu concentrations in B15 inclusions, no mode was identified. However, the high number of Cu-bearing inclusions in the B15 group makes this inclusion group the second most consistent Cu-bearing group. Pb is above the LOD in 86% of B15 inclusions and ranges between 36-1085 ppm, with 67% of B15 inclusions having a mode Pb

concentration between 36-77 ppm, and a mode average of 57 ppm, indicating that Pb is commonly present but in small concentrations. Lead is also commonly detected in B15 inclusions that contain high concentrations of Mn and Zn. Zinc is above the LOD in 43% of B15 inclusions and has a wide range between 542-5,473 ppm. Because of the wide range in Zn concentrations, no mode was identified for Zn. Manganese exceeds the LOD in 57% of B15 inclusions and has a regular range between 548-5804 ppm. Zinc and Mn in B15 inclusions have similar concentrations, were typically detected in the same inclusions, and correlate with one another. Similar to Mn, Sn exceeds the LOD in 57% of B15 inclusions, but has a narrow range between 123-539 ppm (268 ppm average). Tin also did not correlate with Zn, Pb, or Mn, but was commonly present in inclusions that had high Cu concentrations.

Strontium is above the LOD in 85% of B15 inclusions but at low concentrations, commonly between 11-185 ppm, with a single inclusion containing 9,416 ppm. The inclusion that contains 9416 ppm Sr, also contains high Ba (1028 ppm) and no Cu. Inclusions with low Sr typically contain the highest Cu concentrations and little or no Ba. Owing to high concentrations of Cu and low concentrations of Sr and Ba, B15 inclusions are referred to as Cu-enriched and Sr-Ba-depleted relative to other hanging wall and footwall inclusions groups. Rubidium and Sn were above the LOD in most inclusions but typically had low concentrations. Rubidium is above the LOD in 86% of B15 inclusions, but at low concentration with a mode between 10-31 ppm and a mode average of 21 ppm. Inclusions with the lowest Rb values also contain low Sr and Ba, and the highest Cu.

B30D: Thirty-six percent of B30D inclusions (25 inclusions) were analyzed with LA-ICP-MS. B30D inclusions were typically dominated by Na, K and Ca. Sodium exceeds the LOD in all B30D inclusions and had concentrations between 1351-89,537 ppm and an average of

24165 ppm. Approximately 48% of B30D inclusions have a mode of Na concentrations between 10,315-20,145 ppm and a mode average of 15,822 ppm. Potassium concentrations were above the LOD in 68% of B30D inclusions and vary regularly between 819-38,789 ppm. Within this range of K concentrations in B30D inclusions there are two modes, with 24% of analyzed inclusions between 15,204-17,675 ppm (16,522 average) and another 24% of B30D inclusions between 7,433-9,214 ppm (8,350 average). Calcium exceeds the LOD in 91% of B30D inclusions and has a regular range between 2,305-89,457 ppm (27,330 ppm average). The regular range and large standard deviation for Ca concentrations (45,865 ppm) made it difficult to identify a mode, and Ca is commonly present in B30D inclusions, but its concentration varies widely.

Relative to other hanging wall and footwall inclusion groups, Pb, Zn, and Mn were commonly moderately enriched in B30D inclusions. Lead exceeds the LOD in 72% of B30D inclusions and had a range of 16-3,645 ppm (677 ppm average), with 33% of analyzed B30D inclusions having a mode values between 16-85 ppm and a mode average of 51 ppm. Zinc exceeds the LOD in 44% of B30D inclusions and had a wider range of 181-11,101 ppm. Within the total range of Zn concentrations there are two modes with 33% of inclusions between 1215-1865 ppm (1485 ppm average) and 25% between 270-274 ppm (272 ppm average). Manganese is above the LOD in 60% of B30D inclusions and has a range of 149-17,513 ppm (3686 ppm average). As with Zn, Mn has two modes with 26% of inclusions containing between 2833-4621 ppm (3427 ppm average) and 22% of inclusions containing between 149-208 ppm (171 ppm average). Manganese concentrations are positively correlated with Pb and Zn concentrations in B30D inclusions in that Zn and Pb both have high concentrations in inclusions with high Mn concentrations.

Copper exceeds the LOD in 44% of B30D inclusions and had a wide range in concentrations between 145-12,224 ppm (2012 ppm average). Two modes were identified for Cu in B30D inclusions with 25% of inclusions containing 145-432 ppm (284 ppm average) and 25% of inclusions containing between 1254-1469 ppm (1397 ppm average). Despite being above the LOD in only 44% of B30D inclusions, Cu is moderately enriched in B30D inclusions in that it is commonly above 1000 ppm where present.

Iron exceeds the detection limit in only 24% of B30D inclusions but had a regular range of high concentrations between 4060-54,663 ppm (28,332 ppm average). Though having a wide range of concentrations, 50% of the Fe-bearing B30D inclusions had a narrower mode of high concentrations between 31,252-35,567 ppm (33,533 ppm average). However, though Fe is above the LOD in less than a quarter of B30D inclusions, it is in high abundance when present. Also, Cs, which exceeds the LOD in 44% of B30D inclusions and had a relatively narrow range of concentrations between 2-249 ppm (48 ppm average), has a positive correlation with Fe. Specifically, Fe and Cs are commonly above the LOD in the same inclusions, and the highest concentrations of Fe are found in inclusions with the highest Cs concentrations. Strontium exceeds the LOD in 84% of B30D inclusions and had a range between 15-2,252 ppm (186 ppm average) with 54% of B30D inclusions having a mode between 15-99 ppm and a modal average of 52 ppm. Relative to the B15 and B75 inclusion groups, B30D inclusions are moderately enriched in Sr. Also, Sr and Cu are negatively correlated with one another in that inclusions with high Cu concentrations have low Sr concentrations. Ba, which exceeds the LOD in 20% of B30D inclusions and varies between 17-529 ppm (280 ppm average), also correlates negatively with Cu, in that Ba was commonly absent in inclusions with high Cu values. Tin exceeds the LOD in only 24% of B30D inclusions and ranges between 100-10,112 ppm (3,232 ppm average), with

50% of B30D inclusions having a mode between 100-121 ppm (113 ppm modal average). Though much less abundant than Ca, Sn is correlated with Ca, in that Sn is most abundant in B20D inclusions, which had the highest Ca concentrations.

B30H: Approximately 34% of B30H inclusions (11 inclusions) were analyzed with LA-ICP-MS. The dominant cations in B30H inclusions include Na, K, Ca and Fe. Na exceeds the LOD in all B30H samples and had a wide range between 56,685-120,491 ppm (85,332 ppm average) with 90% of B30H inclusions having a mode between 56,685-9,9972 ppm (mode average of 81,816 ppm). Like Na, K exceeds the LOD in all B30H inclusions and had a similar total range of concentrations, with K concentrations being between 29,259-126,539 ppm (64,409 ppm average). Within this range, ~81% of B30H inclusions had a mode between 29,259-73,481 ppm and a modal average of 56,071 ppm. Calcium exceeds the LOD in 90% of B30H inclusions and ranged between 14,318-98,369 ppm (59,013 ppm average), with ~67% of B30H inclusions having a mode between 633-753 ppm and a modal average of 696 ppm. The particularly high concentrations of Na, K, and Ca in B30H inclusions are consistent with the presence of halite daughter crystals in B30H inclusions, and indicate high concentrations of other dissolved salts such as KCl and $CaCl_2$ in B30H fluids.

Despite having elevated concentrations of Fe, Pb, Zn, and Na, K and Ca, which are related to the presence of Cl, B30H inclusions contain less Cu than might be expected, and relative to other hanging wall inclusions groups, Cu is less abundant in B30H inclusions. Copper exceeds the LOD in 45% of B30H inclusions and ranged between 401-2,390 ppm (947 ppm average). Within this range, 80% of analyzed inclusions have a mode between 401-801 ppm and have a modal average of 586 ppm. The overall low range of Cu concentrations and low

abundance of inclusions with Cu in the B30H inclusions is unusual for highly saline, halite-bearing inclusions.

Iron exceeds the LOD in 91% of B30H inclusions and had a range of concentrations between 6,288-41,883 ppm (25,474 ppm average), with one elevated outlying concentration of 102,466 ppm. Within the range of Fe concentrations, ~70% of B30H inclusions had a mode between 21,604-41,883 ppm and a modal average of 30,427 ppm. Given its overall high concentrations, Fe is abundant in B30H inclusion compared to other inclusion groups. Iron shows a positive correlation with Na, K, and Ca, in that high Fe concentrations typically correspond to high Na, K, and Ca concentrations. Iron also shows a positive correlation with Cs in that Cs, which exceeds the LOD in 82% of B30H samples and had a range of concentrations between 20-113 ppm (51 ppm average), is commonly elevated in inclusions with elevated Fe. However, Cs concentrations are commonly lower than Na, K, or Ca concentrations and, thus, the correlation between Fe and Cs is more variable.

Relative to all other inclusions groups, B30H inclusions were enriched in Pb, Zn, and Mn. Lead exceeds the LOD in all B30H inclusions and had a range between 200-13,650 ppm (2,639 ppm average), with ~54% of B30H inclusions having a mode range of Pb concentrations between 1,388-1,901 ppm and a modal average of 1,561 ppm. Like Pb, Zn is also above the LOD in all B30H inclusions and has a range between 938-26,294 ppm (9,218 ppm average), with ~36% having a mode range between 5111-6485 ppm and a modal average of 5,807 ppm. Relative to Zn and Pb, Mn was one of the most enriched elements in B30H inclusions in that it exceeds the LOD in all B30H inclusions, and had a range between 2,529-60,222 ppm (20,516 ppm average). Also, Mn had a large modal range with ~36% of B30H inclusions between 13,382-23,777 ppm and a modal average of 18,188 ppm.

Strontium exceeds the LOD in all B30H inclusions and, relative to all inclusion groups, is highly enriched in B30H inclusions. This is illustrated in the wide and regular range of Sr concentrations in B30H inclusions between 249-10,713 ppm (2,160 ppm average) and the fact that ~55% of Sr-bearing B30H inclusions have a mode of Sr concentrations between 1,034-1,548 ppm and a modal average of 1,220 ppm. Like Sr, Rb is also above the LOD in all B30H inclusions and relative to all inclusion groups, Rb is highly enriched in B30H inclusions. This is illustrated by the fact that B30H inclusions have a consistent range of Rb concentrations between 235-877 ppm (414 ppm average), with 73% of B30H inclusions having a mode of Rb concentrations between 235-371 ppm and a modal average of 311 ppm. Similar to Sr and Rb, Ba is also enriched in B30H inclusions both in terms of its total and modal concentrations and the percentage of inclusions within this group that have Ba above the LOD. Barium exceeds the LOD in 73% of B30H inclusions and had a range of concentrations between 692-1,339 ppm (951 ppm average). Furthermore, ~50% of B30H inclusions have a mode of Ba concentrations between 993-1,162 ppm and a modal average of 1,043 ppm, and this indicates that most B30H inclusions have relatively high Ba concentrations.

Compared to other hanging wall inclusions groups, Sn is depleted in B30H inclusions. Tin concentrations exceed the LOD in 20% of B30H samples and had a low total range of concentrations between 1-269 ppm (69 ppm average). Within this range, Sn concentrations in 67% of B30H had a mode between 633-753 ppm and a mode average of 696 ppm.

B75: Approximately 43% of B75 inclusions (9 inclusions) were analyzed with LA-ICP-MS. B75 inclusions are dominated by Na, K, Ca, and Cu. Na exceeds the LOD in all B75 samples and had a range between 1,098-13,720 ppm (6,252 ppm average). Within this range there were two modes, with 44% of B75 inclusions containing between 1,098-4,463 ppm (2,396

ppm mode average) and 44% between 8,513-13,720 ppm (10,909 ppm modal average). Potassium exceeds the LOD in 55% of B75 inclusions and had a regular range of concentrations between 2,200-9,155 ppm (6,230 ppm average). Though having a wide range of concentrations, K has a regular distribution and does not exhibit a mode; the standard deviation is 2,950 ppm and concentrations did not cluster within the total concentration range. Calcium exceeds the LOD in 56% of B75 inclusions and had a regular range between 7,073-33,586 ppm (19,904 ppm average). Within this range, ~80% of B75 inclusions have a mode between 11,519-33,586 ppm and have a modal average of 23,111 ppm.

Copper is highly enriched in B75 inclusions and, as stated above, Cu is a dominant cation in the B75 inclusion group. Copper exceeds the LOD in 88% of B75 inclusions and has a wide range of concentrations between 24-17,724 ppm and an average concentration of 5,923 ppm, which is the highest average Cu concentration of any inclusion group. Approximately 63% of Cu-bearing B75 inclusions have a mode between 842-5,258 ppm, and a modal average of 2,720 ppm. Given the high number of inclusions with high average Cu concentrations, the B75 inclusion group is the most Cu-enriched inclusion group.

Relative to the B30H, B30D, and B15 inclusion groups, B75 inclusions are low in Pb, Mn, Zn, and Fe. Lead exceeds the LOD in 55% of B75 inclusions and ranged between 4-166 ppm (87 ppm average). Within the range of Pb concentrations there is a mode range between 111-166 ppm and a mode average of 136 ppm. Manganese exceeds the LOD in 56% of B75 inclusions and had a range of concentrations between 152-12,204 ppm with an average of 3099 ppm owing to two inclusions having high outlier concentrations (12,204 ppm and 2,026 ppm). Owing to a regular range of Mn concentrations, no Mn mode was identified for B75 inclusions. Zinc and Fe were only present in ~22% (2 inclusions each) of B75 inclusions. The inclusions

that contained detectable Zn, had concentrations of 779 ppm and 62 ppm, which are low relative to the B30H, B30D, and B15 inclusion groups. However, the two B75 inclusions that contained detectable Fe, had high Fe concentrations (2,7818 ppm and 13,852 ppm) comparable to the B30H, B30D, and B15 inclusion groups. These B75 inclusions are still generally low in Fe, however, because most (~78%) of B75 inclusions contain no detectable Fe.

Relative to the B30H, B30D, and B15 inclusions, Sr is low in B75 inclusions despite being consistently present in most B75 inclusions. Strontium exceeds the LOD in 89% of B75 inclusions and had a narrow range 3-112 ppm (44 ppm average).

Compared to other hanging wall samples Sn is somewhat enriched in B75 inclusions in that it has consistently elevated concentrations in many samples. Tin exceeds the LOD in 44% of hanging wall inclusions, and had a regular range between 21-1276 ppm (476 ppm average). B75 inclusions are low in Ba, Cs, and Rb in that they were detected in <22% of B75 inclusions and typically had concentrations <130 ppm. Neither Au nor Mo was detected in B75 inclusions.

B20C: Approximately 38% of B20C inclusions (23 inclusions) were analyzed with LA-ICP-MS analysis. Compared to aqueous inclusions in the hanging wall, B15, B30D, B30H, and B75 inclusions, B20C inclusions contain much lower concentrations of all elements. The ranges of concentrations of Na, K, Ca, Fe, Cu, Sr, Ba, Pb, Zn, and Mn vary, but these ranges are narrow compared to concentration ranges in aqueous inclusion groups.

The dominant cations in B20C inclusions are Na and Ca. Sodium exceeds the LOD in all samples and had a range between 33-32,211 ppm (4,774 ppm average). Within this range there are two modes, with 57% of B20C inclusions containing between 1,672-8,643 ppm (modal average of 4,753 ppm) and 35% of B20C inclusions containing between 33-83 ppm (modal average of 63 ppm). Calcium exceeds the LOD in 43% of B20C inclusions and had a wide range

between 54-26,100 ppm (7,550 ppm average). Within this range, Ca had two modes with 40% of B20C inclusions having a narrow mode between 54-97 ppm (modal average of 78 ppm) and 40% having a mode between 9,028-15,568 ppm (modal average of 11,401 ppm).

Unlike the Aqueous inclusion groups in the hanging wall, B20C inclusions are low in K, in that K is only above the LOD in 22% of B20C inclusions. This is the smallest number of inclusions with concentrations of K above the LOD of all hanging wall inclusion groups. However, K concentrations have a wide total range between 34-7,741 ppm and an average K concentration of 3,399 ppm.

Compared to all aqueous inclusions and B75C inclusions in the hanging wall, B20C inclusions are low in Cu. Copper exceeds the LOD in 48% of B20C inclusions and had a range between 3-4,052 ppm (454 ppm average). Within this range, 55% of B20C inclusions have a mode between 42-352 ppm and a modal average of 153 ppm. Though low relative to other hanging wall inclusion groups, B20C inclusions are enriched in Cu compared to B15C inclusions from the footwall.

B20C inclusions are also low in Pb, Zn, and Mn relative to aqueous inclusions in the hanging wall, in that Pb, Zn, and Mn are present in few B20C inclusions and have low concentrations. Lead exceeds the LOD in 57% of B20C inclusions and had a narrow range between 1-885 ppm (173 ppm average). Within this range, 77% of inclusions have a mode between 1-136 ppm and a modal average between 55 ppm. Manganese exceeds the LOD in 52% of B20C inclusions and had a range between 1-3,057 ppm (850 ppm average). Within this range there are two modes, with 42% of B20C inclusions having a range between 1-76 ppm (modal average of 22 ppm) and 33% having a range between 242-585 ppm (modal average of 476 ppm). Zinc exceeds the LOD in 39% of B20C inclusions and had a moderately wide range between 2-

1612 ppm (428 ppm average). However, Zn concentrations were consistently on the low end of this range with 56% of B20C inclusions having a mode between 2-93 ppm and a modal average of 24 ppm. Though low in Pb, Zn, and Mn, B20C inclusions are enriched in these elements relative to B75C inclusions in the hanging wall and B15C inclusions in the footwall.

Relative to the aqueous hanging wall inclusions, B20C inclusions are low in Fe, with Fe exceeding the LOD in only 26% of B20C inclusions. However Fe had a wide range between 31-16,557 ppm (4705 ppm average), and 50% of B20C inclusions have a mode between 1,321-5,768 ppm and a modal average of 3,864 ppm. Though low relative to the aqueous inclusions, B20C inclusions are enriched in Fe relative to B75C inclusions in the hanging wall and B15C inclusions in the footwall.

Relative to aqueous inclusions, B20C inclusions are depleted in Sr. Strontium exceeds the LOD in 57% of B20C inclusions and had a range between 1-755 ppm (104 ppm average). Within this range, Sr had a mode between 1-77 ppm and a modal average of 18 ppm. Though low relative to aqueous inclusions, B20C inclusions are enriched in Sr relative to B75C inclusions from the hanging wall and B15C inclusions in the footwall.

Ba is similar to Sr in B20C inclusions in that, relative to aqueous inclusion groups, Ba is low. However, relative to B75C inclusions from the hanging wall and B15C inclusions in the footwall, B20C inclusions are enriched in Ba. Barium exceeds the LOD in 39% of B20C inclusions and had a range between 1-629 ppm (113 ppm average), and within the range, Ba had a mode range in 78% of inclusions between 1-55 ppm and a mode average of 31 ppm.

Cs and Rb are low in B20C inclusion in that they were above the limit of detection in only 13% of B20C inclusions and both are present in concentrations < 20 ppm. No Au or Mo were detected in B20C inclusions.

B75C: Approximately 24% of B75C inclusions (20 inclusions) were analyzed with LA-ICP-MS. As with B20C inclusions, B75C inclusions contain much smaller concentrations of all elements analyzed with LA-ICP-MS relative to aqueous inclusions in the hanging wall, and though the ranges of high to low concentrations of some elements including Na, K, Ca, Fe, Cu, Sr, Ba, Pb, Zn, and Mn, are present in B75C inclusions, the range of concentrations is narrow compared to ranges for aqueous inclusions.

Sodium is the only element that is above the LOD in all B75C inclusions and is the dominant cation in B75C inclusions. Sodium has a range of concentrations between 41-18,375 ppm and an average concentration of 4,899 ppm. Within the range of Na concentrations there are two modes with 40% of B75C inclusions having a mode between 41-83 ppm (modal average of 65 ppm), and 25% having a mode of 6,194-11,641 ppm (modal average of 8,870 ppm).

Potassium exceeds the LOD in only 40% of B75C inclusions and had a range between 6-3268 ppm (628 ppm average). Within this range, 75% of B75C inclusions have a mode of 6-75 ppm and a mode average of 43 ppm. Despite having a regular range of concentrations, K in B75C inclusions is low relative to aqueous inclusions and B20C inclusions because of the small number of K-bearing inclusions and low K concentrations where present. Similarly, Ca is only above the LOD in 20% of B75C inclusion and, though it has a very wide range of concentrations between 23-31,198 ppm, it is considered low in B75C inclusions.

Relative to aqueous inclusion groups, B75C inclusions are depleted in Cu. However, relative to B20C inclusions and B15C inclusions, B75C inclusions are consistently enriched in Cu. Copper exceeds the LOD in 60% of B75C inclusions and had a range between 1-783 ppm (291 ppm average). Within this range, 58% of analyzed B75C inclusions have a mode of 283-783 ppm and a modal average of 463 ppm.

Relative to aqueous inclusions, B20C inclusions, and B15C inclusions, Pb, Zn, Mn, and Fe are all low in B75C inclusions. Lead exceeds the LOD in 55% of B75C inclusions and had a range of 1-241 ppm (57 ppm average). Within this range, 36% of B75C inclusions have a mode between 85-105 ppm and a modal average of 93 ppm. Mn exceeds the LOD in 50% of B75C inclusions and had a range between 1-1158 ppm (201 ppm average). Within the range, 70% of B75C inclusions have a mode between 1-49 ppm and a modal average of 23 ppm. Zinc exceeds the LOD in 40% of B75C inclusions and has a range between 2-836 ppm (201 ppm average). Within this range of Zn concentrations 63% of B75C inclusions have a mode of Zn concentrations between 2-18 ppm and a modal average of 9 ppm. Iron exceeds the LOD in 20% of B75C inclusions and has a range between 9-253 ppm (85 ppm average). Like Pb, Zn, and Mn, Fe concentrations within 75% of analyzed B75C inclusions have a mode between 9-61 ppm and a modal average of 30 ppm.

Relative to all other inclusions in the hanging wall B75C inclusions are low in Sr. Strontium exceeds the LOD in 70% of B75C inclusions and had a regular range between 1-193 ppm and an average value of 43 ppm. Within the range of Sr concentration 43% of B75C inclusions have a mode between 22-110 ppm and a modal average of 68 ppm.

Ba, Cs, Rb, and Sn were only above the LOD in <20% of B75C inclusions and were commonly in concentrations < 70 ppm. Also, Mo and Au were not detected in any B75C inclusions.

Patterns and Interpretation of LA-ICP-MS Data

The LA-ICP-MS data presented herein vary greatly between fluid inclusion groups, between aqueous and CO_2-rich inclusion groups, and between fluid inclusion groups in the

footwall and hanging wall. This variation between fluid inclusions groups and within fluid inclusions groups is likely owed to the fact that many of the inclusions analyzed were ~7.5µm or less in size. For small inclusions, the amount of background in the LA-ICP-MS signal from the quartz hosting the analyzed inclusions is much greater than it would be for larger inclusions. However broad patterns in concentrations of some elements are present and these patterns are outlined below.

1) Strontium, Rb, and Ba are typically high in inclusions that have relatively low Cu concentrations. This pattern is present in both the footwall and hanging wall, and in CO_2-bearing and aqueous inclusion groups, but is especially true for aqueous inclusion groups in the hanging wall and footwall. For example, 89% of B75 inclusions contain Sr and Cu, but the average Cu concentration in B75 inclusions is 5,923 ppm, whereas the average Sr concentration is 43 ppm. Furthermore, 22% of B75 inclusions contain Ba and Rb, but the average concentration of each is <70 ppm, far below the average concentration of Cu. For CO_2-bearing groups, this pattern is subtle, but is still present. For example, only 17% of B15C inclusions contain detectable Cu, whereas 87% contain detectable Sr, 22% contain Ba, and 39% contain Rb, and all are typically in greater concentrations than Cu. This inverse relationship between Rb, Ba, and Sr concentrations and Cu concentrations is commonly observed in other porphyry systems, such as Bajo de la Alumbrera (Ulrich et al., 2001), and is likely due to Cu behaving compatibly, and Rb, Ba, and Sr behaving incompatibly in sulfide mineral phases, with Sr being the most incompatible followed by Ba and Rb. Specifically, as sulfide minerals precipitate from hydrothermal fluid, Cu is readily incorporated into sulfide minerals; whereas Sr, Ba, and Rb behave incompatibly and remain in solution (Candela and Holland., 1986).

2) In both hanging wall and footwall inclusion groups with high to moderate Cu concentrations, Mn, Pb, and Zn are typically moderately elevated. The only groups that diverged from this pattern are vapor-rich B75 and B75C inclusions, which had regularly high Cu concentrations, but low Mn, Pb, and Zn concentrations. This pattern is likely due to differing compatibility of Cu and Mn, Pb, and Zn
3) The consistently high Cu concentrations found in B75C and B75 inclusions are consistent with partitioning of Cu into the vapor fraction of both CO_2-bearing and non CO_2-bearing fluids, and this has been observed in other Cu-bearing hydrothermal systems (Heinrich, et al., 1999). This is likely due to the fact that Cu can be portioned in to a low density fluid much easier than other metals ions (Candela and Holland., 1986).
4) B30H inclusions typically had very high Mn, Pb, and Zn concentrations, but low Cu concentrations. This is likely due to Cu precipitation from these fluids and/or partitioning of Cu into an immiscible vapor phase that may have formed at the same time as the brine fluid captured in B30H inclusions.
5) Inclusions that had round, opaque daughter crystals commonly had elevated Fe concentrations, and inclusions that had triangular, opaque daughter crystals commonly had elevated Cu concentrations. This indicates that the round opaque crystals may have been an Fe-bearing mineral, such as magnetite or hematite. Likewise, the elevated Cu concentrations in inclusions with triangular opaque daughter crystals strongly suggests that the triangular daughter crystals were chalcopyrite or another Cu-bearing mineral.
6) Inclusions that had translucent daughter crystals that did not melt during heating commonly had elevated Ca concentrations compared to the concentrations of other

cations in those inclusion. This indicates that the translucent daughter crystals may have been calcite or another Ca-bearing mineral

7) In the majority of analyzed inclusions, little or no Mo was detected, and this is consistent with observations made at other porphyries (Ulrich et al., 2001, Rusk et al., 2008). The lack of significant amounts of Mo in the fluid inclusions in the Kabba systems is likely related to the fact that Mo extraction from melts tends to be inefficient, compared to copper, resulting in the Mo:Cu ratio in early exsolved fluids being low (Candela and Holland, 1986). Also, because Mo is highly insoluble at temperatures below 400°C it is likely that Mo will precipitate early from hydrothermal fluids and, thus, is likely not to be present in high abundances in fluids trapped in fluid inclusions below 400°C (Candela and Holland, 1986).
8) Typical concentrations of most elements in B20C, B75C, and B15C inclusions were low relative to all other inclusion groups. This is likely due to the fact that these inclusions are CO_2-rich. As hydrothermal fluids exsolved from magmas at depth, CO_2 reduced the ability of the hydrothermal fluid to extract Cl-complexed Cu, as well as other metals, from the melt (Tattitch, et al., 2015). Therefore, the CO_2 in the B20C, B75C, and B15C inclusions likely reduced the ability of these fluids to transport dissolved ions and this would contribute to their over-all low metal concentrations.

CHAPTER 7

DISCUSSION AND INTERPRETATION

The focus of this project is to test the hypothesis that the footwall and hanging wall field areas of the Kabba prospect represent the deep roots and intermediate depths of a single porphyry-like hydrothermal system, respectively, which formed at the same time, but have since been separated by an extensional basin and range normal fault. This hypothesis was initially supported by several lines of evidence including: 1) the presence of pervasive veining and porphyry-style mineralization and alteration in footwall outcrops and hanging wall drill core, 2) the N-S trending Hualapai normal fault, which runs between the hanging wall and footwall areas, 3) seismic data, which show the presence of fault blocks that appear to have moved eastward along the Hualapai normal fault and are now buried under Quaternary gravels present in the hanging wall, 4) an aeromagnetic anomaly in the footwall that has historic Cu-Mo and Pb-Zn mines exposed at the surface around its flanks, and 5) a comparable aeromagnetic anomaly in the hanging wall with historic Cu, Pb-Zn, and Au mines exposed at the surface around its flanks. To further test the hypothesis, data from conventional vein and alteration petrography, fluid inclusion petrography and microthermometry, and single inclusion LA-ICP-MS analysis of samples from the hanging wall and footwall were integrated and compared to ore and alteration in the deep roots and intermediate depths of known porphyry deposits and to established fluid inclusion distribution models for porphyry systems. This comparison has led to the following interpretation of the evolution of the Kabba hydrothermal system, based on identified relationships between vein minerals and alteration in the hanging wall and footwall, and analyzed fluid inclusion populations from in each area.

The conventional petrography of veins and alteration from the hanging wall and footwall indicate that the A_{NB} and A_B veins in the footwall are broadly related to each other and to the A, B, and D veins in the hanging wall. This interpretation is based on similarities between vein minerals, alteration, and crosscutting relationships observed between vein types, and is supported by seven key observations.

1. All of the hanging wall and footwall veins are composed of the same two types of quartz: CL-bright and CL-dark. Both CL-bright and CL-dark quartz in the hanging wall and footwall have identical characteristics. Similarly, cross-cutting relationships between CL-dark quartz and CL-bright quartz in the hanging wall are identical to the crosscutting relationships between CL-bright and CL-dark quartz observed in the footwall.
2. The textures of the sulfide and oxide minerals found in hanging wall veins and the cross-cutting relationships these minerals have with one another are identical to textures and cross-cutting relationships observed in sulfide and oxide minerals found in the footwall.
3. The presence of abundant chalcopyrite and molybdenite and general lack of sphalerite and galena in the footwall is consistent with mineralization in the deep root zones of porphyry systems (Sillitoe, 2010). Likewise, the presences and relative abundances of chalcopyrite, molybdenite, sphalerite, and galena in the hanging wall are similar to what is observed in the intermediate depths of other porphyry systems (Sillitoe, 2010), with chalcopyrite and molybdenite dominating, and lesser sphalerite and galena.

4. The vein and alteration mineral assemblages observed in the A_{NB} and A_B veins in the footwall and the A, B, and D veins in the hanging wall are very similar in that footwall assemblages 1_F, 2_F, 3_F, and 4_F are nearly identical to hanging wall assemblages 2, 3, 4, and 5, and the precipitation of these assemblages aligns temporally with one another.
5. Coarse mica alteration observed in footwall samples always occurs with orthoclase feldspar that represents potassic alteration and is interpreted as greisen. This alteration type, found only in footwall rocks overprinting potassic alteration, is a hallmark of the root zone of porphyry systems, indicates that the footwall formed at a greater deeper depth than the hanging wall and in or near the central root zone of a porphyry-like hydrothermal system.
6. Green mica alteration at Kabba, which is found only in the hanging wall and commonly overprints potassic alteration, contains abundant sericite, quartz, and pyrite, analogous to phyllic alteration commonly found above or overlapping potassic alteration at intermediate depths in most porphyry systems. Thus, the green mica alteration and potassic alteration in the hanging wall indicate that hanging wall rocks formed at an intermediate depth in a porphyry-like hydrothermal system.
7. The A_{NB} and A_B veins in the footwall are wider than typical veins in the hanging wall and resemble large, feeder veins described in the root zones of many porphyry systems (Rusk et al., 2008; Sillitoe, 2010). In contrast, the narrow A, B, and D veins in the hanging wall are identical to A, B, and D veins in the central

and peripheral regions within typical porphyry systems (Gustafson and Hunt, 1975.

All of these observations support the hypothesis that the hanging wall and footwall areas formed at approximately the same time and represent two different levels within a single porphyry-like hydrothermal system, with the hanging wall representing an intermediate depth and the footwall representing a deep root zone.

A reasonable time-integrated model for the formation of the fossil hydrothermal system at Kabba is presented below and is based on a comparison between veins, alteration, and fluid inclusions found in the Kabba hanging wall and footwall, and the veins, alteration, and fluid inclusions found in the Butte porphyry deposit in Butte, Montana. The Kabba hydrothermal system is compared to Butte because the mineralization in both systems is associated with fluid inclusions that indicate less aqueous fluid immiscibility than is typical of most porphyry systems, and which contain significant CO_2. At Butte, the microthermometric behavior of fluid inclusions that contain CO_2 vapor in the deepest levels of the Butte porphyry system led to the interpretation that the base of the Butte porphyry formed under lithostatic pressures between ~2000-2500 bars and at a depth of ~10 Km (Rusk et al., 2008). Thus, a similarly high lithostatic pressure and depth of formation is suggested for the Kabba footwall, as it is interpreted to represent the deepest part of the Kabba hydrothermal system. This interpretation is further supported by the observation that the Kabba footwall contains no vapor-rich inclusions, which would indicate low to modereate pressures and depths of formation, and this is similar to what is observed in the deepest parts of the Butte porphyry, which contained rare vapor-rich inclusions. In addition, CO_2-bearing fluid inclusions at Kabba contain high CO_2, from 3->27 mol%, whereas Butte inclusions contain ~2-8 mol% CO_2. Furthermore, Kabba fluid inclusions commonly

contain both liquid and vapor CO_2, whereas, other than two inclusions, Butte fluid inclusions contain only CO_2 vapor. These observations indicate that the base of the Kabba system formed at greater pressure than the base of the Butte system and thus, lithostatic pressures of formation >2500 bars and a depth of formation >10 Km are estimated for the Kabba footwall. This interpretation is supported by the presence of greisen in the footwall, which was not recognized at Butte, but is found in the deepest levels of some porphyry systems (Seedorff et al., 2008). Correspondingly, the hanging wall of the Kabba system is interpreted to have formed under lower pressures than the footwall. This interpretation is supported by the fact that the hanging wall contains vapor-rich fluid inclusions that likely formed in response to fluid immiscibility at lower pressures than those interpreted for the footwall. Based on a comparison of fluid inclusion types and abundances in the hanging wall at Kabba with the depth and inferred pressure of the region that contains similar fluid inclusions at Butte, a lithostatic pressure of formation between ~1500-2000 bars is estimated for the Kabba hanging wall.

Subsequent to establishing reasonable lithostatic pressures for formation of the footwall and hanging wall at Kabba, trapping temperatures were interpreted for fluid inclusions analyzed using microthermometry based on isochors generated with MacFlincor (Brown, 1989; Brown and Hagemann, 1994). Using pressure, temperature and chemistry data available for all fluid inclusions groups, a time integrated model for the formation of the Kabba hydrothermal system was constructed. All time-integrated steps described in the following model are correlated with the paragenetic sequences observed for the mineral assemblages in the veins and alteration in the hanging wall and footwall, and are based on the interpretation that the footwall formed at greater depth than the hanging wall (Table 7).

Time 1: Precipitation of assemblage 1 minerals in the hanging wall from B30H fluids

B30H fluids are interpreted to have precipitated assemblage 1 Gl and Sp in the hanging wall because they contain the highest concentrations of Zn and Pb of any inclusion group and are commonly spatially related with Zn and Pb mineralization. Given that B30H inclusions contain a saline brine and are saturated in halite at 25°C, it is reasonable that B30H fluids formed as the result of aqueous fluid immiscibility and would, therefore, have formed with a coexisting immiscible vapor. Based on H_2O-NaCl phase equilibria (Bodnar et al., 1985), B30H fluids, which have a salinity of ~35 wt% NaCl equivalent, could have formed at 500-600°C along with a vapor with a salinity between <1-4 wt% NaCl equivalent. In a productive porphyry system, these immiscible fluids could have been derived from a parental aqueous fluid with ~5-8 wt% NaCl equivalent (Bodnar et al., 1985).

A reasonable scenario (Table 7) for the formation of B30H fluids begins with an ~5 wt% NaCl equivalent parental fluid moving buoyantly upwards through a fracture network into the hanging wall where pressure was reduced and immiscible B30H liquid and vapor formed at ~500-600°C. Depressurization could have occurred in response to a fracturing event which decreased pressure in the hanging wall from lithostatic pressure of ~1500-2000 bars, to hydrostatic pressure of ~550-750 bars. Following immiscibility, the dense B30H fluid may have ponded in the hanging wall (Henley and McNabb, 1978), cooled, precipitated assemblage 1 minerals, and been trapped as B30H fluid inclusions between <300-350°C and 550-750 bars. These estimated pressure-temperature conditions are based on isochors for B30H fluids (Figure 21, Table 11), derived from the microthermometric behavior of B30H inclusions (Table 8), and the interpreted hydrostatic pressure of the hanging wall. Furthermore, this temperature range is consistent with the precipitation of galena and sphalerite from B30H fluids. As isochors are not valid below 300°C due to the limitation of hydrothermal experiments from which the isochors

were derived (Bodnar et al., 1985), the lower limit of trapping temperatures is not precisely constrained. Also, though this model of formation for B30H fluids is plausible, the immiscible vapor and parental moderate salinity aqueous liquid were not captured by fluid inclusions in the hanging wall or footwall, and their presence and compositions are inferred.

Time 2) Precipitation of assemblage 1_F and trapping of B15D inclusions in the footwall, the onset of assemblage 2 mineral precipitation and trapping of B15 and B30D inclusions in the hanging wall, and transition to higher temperature hydrothermal fluids (Table 7)

B15D fluids are hypothesized to have exsolved from a magma at depth at temperatures >400°C, which allowed these fluids to transport Cu (Ulrich et al., 2001; Heinrich et al., 2004) as they ascended from an unknown depth into the footwall. As these fluids moved through the footwall, they cooled below 400°C and precipitated assemblage 1_F chalcopyrite and molybdenite. At ~2500-3000 bars lithostatic pressure, isochors indicate trapping of B15D fluids between ~225-370°C (Figure 21, Table 11). Because chalcopyrite precipitation begins as fluid temperatures decrease to about 400°C, the temperatures recorded by B15D inclusions are consistent with B15D fluids having been trapped as fluids cooled during or slightly after the initiation of chalcopyrite precipitation in the footwall. This interpretation is supported by LA-ICP-MS data from B15D inclusions which quantified high Cu concentrations in B15D fluids.

Concurrent with cooling and entrapment of some B15D fluids in the footwall, B15D fluids continued to rise into the hanging wall where they variably expanded in response to decreasing pressure and were trapped by B30D and B15 inclusions which, based on their spatial association with one another and relatively continuous range in salinity, are interpreted to have formed a continuum with one another (Figure 22, Table 11). Expansion to form B15/B30D fluids occurred in response to a drop in pressure from 2500-3000 bars in the footwall to 1500-2000 bars

in the hanging wall as fluids rose to shallower levels in the Kabba system. At these pressures, isochors for B15/B30D inclusions indicate temperatures at the time of entrapment were between <300-450°C (Figure 22, Table 11). This temperature range is consistent with B15/B30D fluids precipitating assemblage 2 chalcopyrite and molybendite in the hanging wall. Also, because the temperatures recorded by B15/B30D inclusions in the hanging wall are higher than those recorded by related B15D inclusions in the footwall, it is interpreted that the temperatures recorded by B15/B30D fluids represent a higher temperatures range for fluids in the hanging wall, and that the B15D fluids represent a lower end of the temperature range for fluids in the footwall. Between time 1 and time 2, system temperature appears to have increased as lower temperatures sulfides including galena and sphalerite gave way to precipitation of higher temperature minerals including chalcopyrite and molybdenite. Thus, it is interpreted that the minerals precipitated and the fluids trapped in the hanging wall and footwall during time 2 record increasing fluid temperatures and the transition from lower temperature fluids to higher temperature fluids throughout the Kabba system.

Time 3: Formation and trapping of B30 fluids in footwall fluid inclusions, and continued precipitation of assemblage 2 minerals and trapping of B75 inclusions in the hanging wall

B30 fluids are interpreted to have traveled upward through fractures into the footwall and were trapped under lithostatic pressure between 2500-3000 bars. At these pressures, B30 isochors indicate trapping at temperatures between 425-550°C (Figure 21, Table 11). This temperature range is above the 400°C threshold for chalcopyrite precipitation, suggesting that B30 fluids may have transported Cu through the footwall to the hanging wall with little loss of Cu to precipitation. However, as no LA-ICP-MS data were collected on B30 inclusions, the amount of Cu transported by B30 fluids is not known.

As B30 fluids ascended via fractures into the hanging wall, they may have become immiscible in response to a fracturing episode that produced vapor that was trapped in B75 inclusions under hydrostatic pressures. B30 fluids, which contain ~5 wt% NaCl equivalent, may have been the parental fluid for B75 fluids, which contain ~4.5 wt% NaCl equivalent. Water-NaCl phase equilibria predicts that unmixing of such a parent fluid under hydrostatic pressure of ~550-750 bars would occur between 500-575°C and would produce a brine containing ~20-35 wt% NaCl equivalent and a coexisting ~4.5wt% NaCl equivalent vapor.

The presence of B75 vapor-rich inclusions in the hanging wall supports the interpretation that a decrease in pressure and immiscibility occurred in the hanging wall during time 3. Isochors indicate that B75 fluids under hydrostatic pressures of ~550-750 bars, would have trapped B75 inclusions at temperatures between 425-525°C (Figure 22, Table 11). This temperature range is above the precipitation temperature of chalcopyrite and is consistent with the presence of abundant Cu in these inclusions as indicated by LA-ICP-MS analyses. Subsequent fluid cooling following immiscibility, likely led to the precipitation of assemblage 2 minerals at higher elevations in the hanging wall. However, as no coexisting brine inclusions were identified, the elevation of fluid immiscibility cannot be determined.

Time 4: Hiatus of hydrothermal activity.

A hiatus in hydrothermal fluid activity led to system cooling that was followed by incursion of a new hydrothermal fluid with a different trace element chemistry, responsible for precipitation of quartz with a different CL luminescence (Rusk et al,. 2006, Rusk et al ,.2001), into the system. Also, at some time during this hiatus, a tectonic event responsible for fracturing of existing minerals, especially CL-bright quartz, must have occurred. Incursion of the new hydrothermal fluid was likely related to this event.

Time 5: Incursion of CO_2-bearing hydrothermal fluids, precipitation of assemblage 2_F minerals and trapping of B15C inclusions in the footwall, and precipitation of assemblage 3 minerals and trapping of B20C inclusions in the hanging wall, and precipitation of CL-dark quartz.

Following the hiatus, hydrothermal activity was renewed and chemically distinct CO_2-bearing hydrothermal fluids ascended through fractures into the footwall, precipitated assemblage 2_F minerals Py_2, Mt, and CL-dark quartz in the footwall, cooled, and were trapped as B15C inclusions under lithostatic pressure between 2500-3000 bars and temperatures of <300-315°C (Table 7). Coincidently, some B15C fluids ascended into the hanging wall, where they expanded to form B20C fluids, and precipitated assemblage 3 Py_2, Mt, and CL-dark quartz. B20C fluids in the hanging wall formed from B15C footwall fluids that expanded with decreasing pressure to 1500-2000 bars in the hanging wall. Based on B20C isochors, these inclusions were trapped between <300-330°C (Figure 22, Table 11). The interpretation that B15C and B20C fluids are linked to the precipitation of assemblage 2_F minerals in the footwall and assemblage 3 minerals in the hanging wall is consistent with the moderate concentrations of Fe quantified by LA-ICP-MS analyses in B15C and B20C fluids (Table 11).

Time 6: Precipitation of assemblage 3_F in the footwall, and precipitation of assemblage 4 and trapping of B75C inclusions in the hanging wall.

During time 6, hydrothermal fluids in excess of ~400°C and capable of transporting Cu traveled upward through fractures into footwall rocks. As these fluids cooled they would have precipitated assemblage 3_F chalcopyrite and molybdenite in the footwall. Though, no fluid inclusions related to assemblage 3_F were identified, pressures of 2500-3000 bars and temperatures of <400°C, which would allow for chalcopyrite and molybdenite precipitation are inferred for assemblage 3_F mineral precipitation.

As hydrothermal fluids associated with assemblage 3_F mineralization ascended into the hanging wall, a drop in pressure from lithostatic to hydrostatic conditions, probably in response to a fracturing episode, caused the fluids to unmix, producing a CO_2-bearing vapor, captured in B75C inclusions. As the B75C fluid contains CO_2, which would decrease the fluid pressure, the hydrostatic pressure exerted by the fluid would be somewhat lower than the inferred hydrostatic pressure of 550-750 bars interpreted for the hanging wall during times 1 and 3. Therefore, hydrostatic pressure in the hanging wall during time 6 may have been reduced to ~500-650 bars, which would correspond to trapping temperatures between ~350-380°C for B75C fluids (Figure 22, Table 11). Though the B75C inclusions were trapped in the hanging wall, no corresponding saline inclusions, which would have formed in response to immiscibility and would further support this interpretation were found in the hanging wall.

Time 7: The hydrothermal system waned and over time Fe-bearing minerals were oxidized.

After the hydrothermal system terminated and the hanging and footwall regions were extended, faulted, uplifted and eroded, Fe-bearing minerals oxidized and were variably replaced by hematite. This process is confirmed by the presence of hematite rims on many oxide and sulfide minerals found in the hanging wall and footwall.

The paragenesis of fluids and minerals observed in the hanging wall and footwall, and observed patterns of fluid inclusion distribution from the footwall to the hanging wall broadly support the hypothesis that the footwall and the hanging wall represent a deep root zone and an intermediate depth zone in a single porphyry-like hydrothermal system, respectively. In particular, the presence of nearly identical quartz types and sulfide and oxide minerals in the footwall and hanging wall, as well as their similar parageneses, virtually confirms that the hydrothermal systems visible in both areas are genetically related. In addition, the temporal

evolution of fluids and minerals observed in the hanging wall and footwall is consistent with B15D, B30, and B15C fluids trapped in the footwall to have evolved to the somewhat or significantly lower density B15, B30H, B30D, B75, B75C, and B20C fluids trapped in the hanging wall. These patterns support a genetic link between the hanging wall and the footwall, as well as the faulted porphyry hypothesis. One aspect of the model of fluid evolution from the footwall to the hanging wall presented above that is somewhat different from most productive porphyries, is that the hanging wall, though having a broad similarity to the intermediate levels of other porphyry systems, contains only sparse brine inclusions, which typically dominate in the intermediate levels of most porphyry systems. An explanation for the low abundance of brine inclusions and mineralization in the hanging wall might be that the inferred depth of formation for the hanging wall, ~6-8 km, and the high lithostatic pressures between 1500-2000 bars interpreted for the hanging wall, might have greatly reduced the amount of fracturing in a system as deep as Kabba. Thus, the depth of the system may have reduced the amount of immiscibility associated with fracturing. A reduction in immiscibility would, in turn, reduce the potential for the formation of brine and coexisting vapor and would reduce the amount of mineralization that would occur in response to immiscibility. This explanation is plausible for the Kabba system; however, further exploration of the Kabba system is needed to better constrain the spatial relationship of hanging wall samples to the inferred Kabba porphyry hydrothermal system, and to identify the density of fracturing and fluid immiscibility present during the formation of alteration and mineralization in the Kabba hanging wall.

One significant aspect of the fluid inclusion analyses is that vapor-rich B75 fluids appear to have transported significant Cu, contributing to chalcopyrite mineralization in the hanging wall. This is indicated by LA-ICP-MS analyses that showed that B75 inclusions typically

contained the highest Cu concentrations of any analyzed inclusions. Zajacz et al. (2012) have shown experimentally that significant Cu can partition into vapor, and in the Bajo de la Alumbrera porphyry in Argentina, vapor transport of Cu is thought to have been an important factor in forming chalcopyrite mineralization in that system (Ulrich et al., 2001). Thus, it is feasible that vapor transport was important in forming chalcopyrite mineralization in the hanging wall; unfortunately, the partitioning of Cu between liquid and vapor phases cannot be determined for this study because of the lack of immiscible fluid pairs in examined samples.

In addition to the fluid inclusion petrography and microthermometry data and petrographic observations of the mineralization and alteration associated with veins in the footwall and hanging wall, the hypothesis that the Kabba systems is porphyry-like in nature is broadly supported by the patterns in Ba, Rb, and Sr concentration relative to Cu in inclusions in the hanging wall and footwall. LA-ICP-MS analysis showed that inclusions with the highest concentration of Ba, Rb, and Sr typically had the lowest Cu concentrations and vice versa. This pattern has been recognized in ore fluids from other porphyry deposits, including Butte and Bajo de la Alumbrera (Ulrich et al., 2001, Rusk et al., 2004), and indicates that the fluids in the Kabba system may have evolved in a similar way to fluids in other porphyry systems. This suggests that the Kabba is a porphyry-like hydrothermal system that may have economic mineralization. However, further exploration and drilling are needed to test this interpretation.

CHAPTER 8

CONCLUSIONS

The objective of this thesis project was to test the hypothesis that the structurally separated areas of mineralization and alteration in the Kabba footwall and hanging wall formed together within the same hydrothermal system, and represent the deep root and intermediate zones of a single porphyry-like hydrothermal system. Based on the results of this study, the following conclusions have been identified.

1. The alteration types observed in the hanging wall and footwall are consistent with alteration in intermediate zones and root zones of other porphyry systems and suggest, and this suggests that the Kabba system is similar to some other productive porphyry systems found around in the world.
2. The mineralization, alteration, and distribution of fluid inclusion types from the footwall and the hanging strongly suggest that the hanging wall and footwall formed as part of the same hydrothermal system, and that the hanging wall formed at a shallower depth than the footwall.
3. Based on the microthermometric behavior of the fluid inclusions found in the hanging wall and footwall it is possible for fluids found in the footwall to have evolved into the fluids found in the hanging wall, suggesting a genetic link between the two areas.
4. LA-ICP-MS data from the individual fluid inclusion groups found in the hanging wall and footwall indicate that the fluids trapped in the fluid inclusions associated with the mineralization and alteration in the hanging

wall and footwall were capable of forming the mineralization found throughout the Kabba system.

5. Patterns in the concentrations of Sr, Ba, and Rb relative to Cu in all inclusions groups in the hanging wall and foot wall are consistent with those found in other porphyry systems and this further suggests that the Kabba system is similar to other productive porphyry systems found around in the world.
6. Five distinct generations of hydrothermal fluid ascended from depth, traversed the footwall and the hanging wall, cooled, and precipitated the mineralization and alteration found in and adjacent to the veins in each area.
7. The fluids involved in forming the mineralization and alteration in the hanging wall and footwall changed from being H_2O to CO_2-bearing over time.
8. Chalcopyrite mineralization in the hanging wall was associated with a low-density vapor and the high Cu content of the vapor suggests that vapor transport may have been important in the Kabba system.
9. The lithostatic pressure recorded by fluid inclusions in the footwall was consistently at or between ~2500-3000 bars. The pressure conditions in the hanging wall fluctuated between lithostatic pressures of ~1500-2000 bars, and hydrostatic pressures of ~550-750 bars. These pressures correspond to depths between 6-8 Km for the hanging wall and 10-12 Km for the footwall, and indicate that the Kabba system formed at depths greater than those determined for the Butte porphyry deposit.

10. Temperatures in the Kabba system fluctuated from high to low over time with mineralization in the footwall forming between <300-545°C, and mineralization in the hanging wall forming between <300-525.
11. The exploration model used by Bell Copper Corp. to guide past and current drilling in the hanging wall, which is predicated on the assumption that the hanging wall and the footwall formed as part of the same hydrothermal system and have since been separated along a north-south trending normal fault, is broadly supported by the comparison between the vein minerals, alteration types, and fluid inclusion data from the hanging wall and footwall.
12. Additional drilling is needed to determine the economic potential of this system and to further delineate economic mineralization and alteration in the hanging wall that may have formed as part of the fossil hydrothermal system present at Kabba. Additional exploration drilling at Kabba should focus on the hanging wall area around the flanks of the Aeromagnetic anomaly, northeast and northwest of drill hole K-10, as these areas have potential to host economic mineralization. Conversely, further exploration and drilling in the footwall is not recommended as this area appears to represent the sparsely mineralized, root zone of the Kabba porphyry system and would have formed bellow the productive part of the system.

Table 1. Footwall Sulfide and Oxide Mineral Characteristics

	Mineral name	Characteristics and diagnostic features	Temporally associated sulfide/oxide phases	Associated vein and quartz type	Associated alteration type
Assemblage 1_F	Chalcopyrite 1 (Cpy_1)	Small - moderately large (5-50µm), round anhedral inclusions in Py_2, small (5-50µm) anhedral inclusions in Mt, or large (50-200µm) pitted crystals with sinuous boundaries that are intergrown with CL-bright quartz.	Mo_1 and Po	A_{NB} and A_B -veins; CL-bright	Potassic
	Molybdenite 1 (Mo_1)	Large (100-800µm) elongate clusters of euhedral crystals intergrown with individual CL-bright quartz crystals along the margins of CL-bright bands in A_B veins. Also occurs as small elongate clusters of euhedral crystals intergrown with individual CL-bright quartz along the inner vein margin in A_{NB} veins. In both A_B and A_{NB} veins Mo_1 is commonly surrounded by Mt, CPy_2, or Py_2 crystals.	CPY_1 and Po	A_{NB} and A_B -veins; CL-bright	Potassic
	Pyrrhotite (Po)	Small (5-50µm) round anhedral inclusions in CL-dark rimed Py_2 crystals, either as individual Po crystals or alongside CPy_1. Po is only found as an inclusions in pyrite .	CPy_1 and Mo_1	A_{NB} - and A_B -veins; CL-Bright	Potassic
Assemblage 2_F	Pyrite 2 (Py_2)	Large (100-1000µm) euhedral crystals that are rimmed by CL-dark quartz, and commonly contain round anhedral inclusions of CPy_1 and Po, small angular euhedral inclusions of Mt, and small subhedral-anhedral elongate inclusions of Ru. In A_B veins individual Py_2 crystals can align along the center of the veins long axis.	Mt and Ru	CL-dark bands in A_{NB} -veins and in CL-dark quartz-rich A_B -veins; CL-dark	Coarse Mica
	Magnetite (Mt)	Occurs as clusters of large (100-800µm), euhedral-subhedral crystals or as euhedral -subhedral inclusions in Py_2 crystals. Commonly contains inclusions of subhedral CPy_1 and Py_2, have patches of Hem on their surfaces and outer crystal margins, and is adjacent to clusters of Ru in CM. Found in both vein types but most abundant in A_{NB} veins.	Py_2 and Ru	Mostly A_{NB} - and in minor amounts in A_B -veins; CL-drak	Coarse Mica
	Rutile (Ru)	Occurs as clusters of small (10-200µm), anhedral crystals that coat individual muscovite crystals along their margins and cleavage planes. Ru is always associated with CL-dark quartz and forms along the margins or individual A_B veins and along the margins of individual bands in A_{NB} veins. Ru can also occur as an inclusions in Py_2	Py_2, Mt, CPy_2, and Mo_2	CL-dark bands in A_{NB}- viens and in CL-dark quartz-rich A_B- viens; CL-dark	Coarse Mica
	Coarse Muscovite (CM)	Occurs as clusters of large (10-500µm) euhedral crystals that host Ru and Mo_1 along their cleavage planes and outer crystal boundaries, and form along the margins of CL-dark bands in A_B veins and along the outer margins of CL-dark rich A_{NB} veins	Py_2, Ru, Mt, CPy_2, and Mo_2	Mostly CL-dark bands in A_{NB}- and in CL-dark quartz-rich A_B- viens; CL-dark	Coarse Mica
Assemblage 3_F	Chalcopyrite 2 (Cpy_2)	Clusters of crystals cryastals that range in size from 20-500µm , and occur adjacent to or fill fractures in Py_2. Only found in minor amounts and is surrounded by CL-Dark quartz and commonly adjacent to clusters of CM.	Mo_2 and Ru	CL-dark bands in A_{NB} -veins and in CL-dark quartz-rich A_B- viens; CL-dark	Coarse Mica
	Molybdenite 2 (Mo_2)	Occurs as large (50-100µm) elongate, subhedral-euhedral crystals that form along cleavage planes in CM crystals or at random orientations in elongate, "whispy", clusters of coarse, Ru-bearing muscovite in CL-Dark bands in A_B veins. In A_{NB} veins with abundant CL-dark quartz, Mo_2 typically occurs along the outer margins of the veins and can be with in or adjacent to accumulations of CM.	CPy_2 and Ru	CL-dark bands in A_{NB}- veins and in CL-dark quartz-rich A_B- viens; CL-dark	Coarse Mica
Assemblage 4_F	Hematite (Hem)	Always occurs as patchy rims of fine grained (<2µm) anhedral crystals that form along through going fractures and outer boundaries of Py_2 and Mt crystals.	No other associated minerals	A_{NB}- and A_B- viens	Coarse Mica

Table 2. Vein Types

	Vein Type	Characteristics	Width	Associated alteration type	Quartz type abundance	Sulfide/Oxide minerals present	Sulfide/Oxide occurrence	Location
Hanging Wall	A	Granular quartz vein with sinuous or jagged boundaries composed primarily of CL-bright quartz with cross-cutting CL-dark quartz-filled fractures. These veins never have sulfide centerlines, can be single veins or multiple branching vein, and are cross cut by B veins. Found in ~29% of hanging wall samples.	0.25 - 1 cm	Potassic	80-85% CL-bright 15-20% CL-dark	Py_1-Sp; Cpy_1-Mo 1-Po; Ru; Cpy_2-Bn; Hem	Along the vein margins or as disseminated clusters	Hanging wall (K-10 Drill Core)
	B	Granular quartz vein with straight, well defined margins. The edges of this vein type are typically composed of coarse, euhedral, highly fractures , CL-bright quartz, and the center of this vein type is typically composed of anhedral CL-dark quartz that surrounds the sulfide filled centerlines and fills in fractures in Cl-bright quartz. Sulfides in this vein type occur as disseminated clusters in the absence of a well defined centerline. Most common hanging wall vein type.	0.5 - 2 cm	Potassic and green mica	50-65% CL-bright 35-50% CL-dark	Py_1-Sphl-Gl; Cpy1-Mo1-Po; Py_2 -Ru-Mt; Cpy_2 -Mo_2 ; Hem	Along the vein margins, as disseminated clusters, or as a centerline along the veins long axis	Hanging wall (K-10 Drill Core)
	D	Straight, semi-continuous vein composed completely of sulfide minerals. Always found <0.5cm from the margins of B-type veins and are oriented parallel to the B-type vein's long axis. Found in ~27% of hanging wall samples and are never cross cut my any other vein type.	2-4 mm	Potassic and green Mica	n/a	Cpy_1-Po; Py_2	Through out this vein type	Hanging wall (K-10 Drill Core)
Foot Wall	A_{NB}	Moderately sinuous granular quartz veins that are identical to individual Cl-dark and Cl-bright bands in the A-$type_B$ veins in terms of their mineralogy and associated alteration selvedges. A-$type_{NB}$ differ form A-$type_B$ veins in that their sulfide and oxide phases only occur as disseminated clusters throughout the vein or along its margin, and are not aligned. These veins also host large masses of magnetite which are absent from A-$type_B$ veins.	0.5-5 cm	Potassic and coarse muscovite	50% CL-bright 50% CL-dark	Cpy_1-Mo_1-Po; Py-Mt-Ru; Cpy_2 -Mo_2; Hem	Along the vein margins or as disseminated clusters	Foot Wall (Outcrops)
	A_B	Vertically oriented vein with moderately sinuous or straight margins composed of multiple parallel bands of CL-bright and CL-dark quartz. Individual bands can have clusters of coarse sulfides that align parallel to the long axis and/or coarse muscovite along the band margins. This vein type also typically has an alteration selvedge which extends 10 cm-1.5m from the vein margins	0.05-2m	Potassic and coarse muscovite	50% CL-bright 50% CL-dark	Cpy 1-Mo 1-Po; Py-Mag- Ru; Cpy 2-Mo 2; Hem	Along the vein margins or as disseminated clusters that align parallel to vein's long axis	Foot Wall (Prospect Pits)

Table 3. Comparison Between A_B and A_{NB} Veins

	A_B	A_{NB}
CL-bright/dark Quartz	Both quartz types form multiple discrete bands within single veins	CL-bright quartz is most abundant in sinuous A_{NB} veins and little or no coarse mica. CL-dark quartz is most abundant in veins with straight margins and abundant coarse mica.
Ru and Mo2 - hosting coarse muscovite	Ru and Mo_2 hosting coarse muscovite typically occurs in between individual CL-dark and CL-bright bands or fills fractures in CL-bright bands.	Ru and Mo_2 hosting coarse muscovite occurs both within the A_{NB} veins and along its margins.
Mo1	Mo_1 is commonly intergrown with individual quartz crystals throughout a CL-bright quartz A_B band .	Mo_1 is intergrown with CL-bright quartz along the outer margin of A_{NB} veins
Cpy2	Cpy_2 is typically more abundant in A_B veins.	Cpy_2 is typically less abundant in A_{NB} veins.
Mo2	Mo_2 forms subhedral-euhedral, crystals along cleavage planes in coarse mica crystals, or at random orientations in "wispy", masses of coarse mica, which align parallel the outer margins of individual bands in A_B veins.	Mo_2 occurs mostly in moderately straight A_{NB} vein boundaries with abundant CL-dark quartz, and forms along the outer margins of the A_{NB} veins and can be adjacent to or surrounded by coarse muscovite
Py2	Py_2 is normally found in CL-Dark bands and forms subhedral-euhedral crystals which align parallel to the margins of individual bands.	Py_2 commonly occurs along the vein margins and individual crystals are only weakly aligned with one another.
Mt masses	Mt masses are commonly <1-2mm wide	Mt masses are commonly between 1-5mm wide. In A_{NB} veins with straight margins and abundant CL-dark quartz, Mt masses can be >5mm

Table 4. Hanging Wall Sulfide and Oxide Mineral Characteristics

	Mineral name	Characteristics and diagnostic features	Temporaly associated slufide/oxide phases	Associated vein and quartz type	Associated alteration type
Assemblage 1	Pyrite 1 (Py_1)	Euhedral pyrite crystals (50-200µm) with a rough or pitted appearance. Contain no inclusions of any other sulfide or oxide minerals. Can be partly or completely surrounded by other sulfides, particularly chalcopyrite.	Sp, Gl, cc	In B- veins and in minor amounts in A-veins; CL-bright	Potassic
	Sphalerite (Spl)	Large (50-500µm) anhedral crystals with smooth, undulating boundaries. Individual crystals can have abundant angular anhedral inclusions of chalcopyrite, minor round inclusions of galena, and can be trasparten yellow or fully opaque in transmitted light. Can occur as an inclusion in CPy_2, Py_2, or Mt.	Gl, cc, Py_1	B-vein that have <40% Cl-dark quatz, and in minor amount in A-veins; CL-bright	Potassic
	Galena (Gl)	Large (50-600µm) anhedral crystals with smooth, undulating boundaries. Always adjacent to Sp crystals which can surround or fill crack in individual Gl crystals. Also adjacent to Py_1 and calcite, and cross cut by CPy_2.	Sp, Py_1, CC	B-vein that have <40% Cl-dark quatz; CL-bright	Potassic
	Carbonate (cc)	Clumps of small (<2µm) anhedral, grey crystals that fill in around CL-bright quartz crystals, Sp, and Gl. Forms bands along the outer margins of B-type veins and is commonly intergrown with euhedral, CL-bright quartz crystals that can range in size from 5-8mm long.	Sp, Py_1, Gl	Only along the margins of B- veins; CL-bright	Potassic
Assemblage 2	Chalcopyrite 1 (Cpy_1)	Small (5-50µm) round anhedral inclusions in Py_2 crystals that are rimed by CL-Dark quartz. Can also occurs as small anhedral to subhedral crystals intergrown with CL-bright quartz or as small anhedral crystals disseminated in the host rock.	Mo_1 and Po	In B-veins as an inclusions in Py_2 andi n A-veins when occuring as induvidual crystals; CL-bright	Potassic
	Molybdenite 1 (MO_1)	Moderatly sized (100-500 µm) clumps of euhedral-subhedral, lath-shaped crystals that range in size from 50-100µm intergrown with CL-bright quartz crystals or as individual euhedarl crystals along the margins of CL-bright quartz domnianted veins. Individual euhedarl crystals rarely fill cracks in Py_1 or are surounded by Py_2.	CPy_1 and Po	In CL-bright dominated B-veins and in minor amounts in A-veins; CL-bright	Potassic
	Pyrrhotite (Po)	Small (5-50µm) round anhedral inclusions in Py_2. Commonly occurs with CPy_1 either within the same inclusion or as single inclusions adjacent to individual CPy_1 inclusions.	CPy_1 and Mo_1	In B- and D- veins, but also found in minor amounts in A-veins; CL-birght	Potassic
Assemblage 3	Pyrite 2 (Py_2)	Lar ge (100-1000 µm) euhedral-subhedral cystals that contain round anhedral inclusions of CPy_1 and Po, anhedral inclusions of Ru, and euhedral inclusions of Mt. Commonly forms centerlines in B-type veins, can have a shatered appearance, and are surrounded by CL-dark quartz.	Mt and Ru	In B-and D-veins, but also found in minor amounts in A-veins; CL-dark	Green phyllosilicate
	Magnetite (Mt)	Large (100-800µm) euhedral to subhedral crystals intergrown with CL-Dark quartz and GM, and in CL-dark filled fractures in CL-bright quartz. Can occur adjacent to or within inclusion Py_2 crystals. Mt inclusions in Py_2 are commonly euhedral . Normally rimmed by Hem.	Py_2 and Ru	Only in B-veins; CL-dark	Green phyllosilicate
Assemblage 4	Rutile (Ru)	Masses of small (10-200µm) round anhedral crystals adjacent to or within clusters of GM . Can also occur as oval or elongate subhedral- anhedral inclusion in Py_2.	Py_2 and Mt	In B-veins, and most abundant in B-veins with well developed green phyllosilicate alteration selvedges; CL-dark	Green phyllosilicate
	Greem muscovite (GM)	Clusters of dark green, crystals that range in size from 50-200µm, fill fractures in CL-bright quartz and are intergrown with CL-dark quartz. Most abundant in samples with well developed GM alteration selvedges.	Py_2, Mt, Ru, CPy_2, Mo_2, and Bn	Only found in B-veins; CL-dark	Green phyllosilicate
	Chalcopyrite 2 (Cpy_2)	Large (20-500µm) anhedral crystals that form adjeacent to inclusion bearing Py_2, and in CL dark filled fractures in Cl-bright quartz, Gl, Sp, and Py_1. Can have Gl inclusions or Bn rims.	Mo_2 and Bn	In B-veins but also in A-veins essecally when associated with Bn; CL-dark	Green phyllosilicate
	Molybednite 2 (Mo_2)	Clusters of (50-100µm) euhedral, lath-shaped cystals that occur within or adjacent to clusters green muscovite and Cl-dark quartz. Clusters of CL-dark quartz, GM, and Mo_2 cross-cut Cl-Bright quartz and filling fractures in shattered Py2 crystals.	CPy_2 and Bn	In B-veins with > 40% Cl-dark quartz; CL-dark	Green phyllosilicate
	Bornite (Bn)	Forms rims of small (10-50µm) anhedral crystals around CPy_2 crystals. Bn rimed CPy_2 are commonly surrounded by or adjecent to spalys of lath-shaped Hem.	Mo_2 and CPy_2	Only found in A-veins; CL-dark	Green phyllosilicate
Assemblage 5	Hematite (Hem)	Splays of large (5-150µm) elongate, euhedral, lath shaped crystals, or rims of small, anhedral crystals along the outer margins of Fe baring oxide and sulfide phases, and clusters of Ru.	No associated phases	In all vein types; Not associated with any quartz type	no associated alteration type

Table 5. Mineral Paragenisis For the Hanging Wall

Assemblage	Minerals	Time 1	Time 2	Time 3	Time 4	Time 5	Time 6	Time 7	
1	Pyrite 1								Hanging wall
	Sphalerite								
	Galena								
	Carbonate								
2	Chalcopyrite 1								
	Molybdenite 1								
	Pyrrhotite								
3	Pyrite 2								
	Magnetite								
4	Chalcopyrite 2								
	Molybednite 2								
	Bornite								
5	Hematite								
3 & 4	Greem muscovite + Rutile								
1 & 2	Cl-Bright Quartz								
3 & 4	CL-Dark Quartz								

Table 6. Mineral Paragenisis for the Footwall

Assemblage	Minerals	Time 1	Time2	Time3	Time 4	Time 5	Time 6	Time 7	
1_F	Chalcopyrite 1 Molybdenite 1 Pyrrhotite								Footwall
2_F	Pyrite 2 Magnetite								
3_F	Chalcopyrite 2 Molybdenite 2								
4_F	Hematite								
2_F & 3_F 1_F 2_F & 3_F	Coarse Muscovite + Rutile Cl-Bright Quartz CL-Dark Quartz								

Table 7. Interpretation of Fluid Evolution From the Footwall to the Hanging Wall and the Formation of Mineralization in Each Area

		Time 1	Time 2	Time 3	Time 4	Time 5	Time 6	Time 7
		Heating →			Cooling →	Heating →		Cooling →
Hanging Wall	Minerals Precipitated	Assemblage 1 (Gl, Sp, Py_1) CL-B, K-alt	Beginning Assemblage 2 CL-B, K-alt	Assemblage 2 (CPy_1, Mo_1, Po) CL-B, K-alt	Injection of hydrothermal fluids subsides and system cools. Fracturing of CL-B quartz.	Assemblage 3 (Py_2, Mt) CL-D, GM-Alt	Assemblage 4 (CPy_2, Mo_2, Bn) CL-D, GM-Alt	Injection of hydrothermal fluids subsides, system cools and Fe-bearing phases oxidize to Hematite (Assemblage 5)
	Entrapment Conditions	<300-350°C (Hydro) 550-750 Bars	325-450°C (Litho) 1500-2000 Bars	425-525°C (Hydro) 550-750 Bars		<300-330°C (Litho) 1500-2000 Bars	350-380°C (Hydro) 500-650 Bars	
	Inclusions	B30H brine (~35.4 wt% NaCl equiv) No Vapor Trapped (~1-4.5 wt% NaCl equiv)	B15 (~8 wt% NaCl equiv) B30D (~8 wt% NaCl equiv)	No brine trapped (~30-50 wt% NaCl equiv) B75 Vapor (~4.5 wt% NaCl equiv)		B20C (~2 wt% NaCl equiv)	No brine trapped B75C Vapor (~2 wt% NaCl equiv)	
	Immiscibility or Expansion ?	Immiscibility (Fracturing event and P decrease at 500-600°C)	Expansion	Immiscibility (Fracturing event and P decrease at 500-575°C)		Expansion	Immiscibility? (Fracturing event and P decrease)	
	Ascending hydrothermal fluids	↑	↑	↑		↑	↑	
Footwall	Minerals Precipitated	N/A	Assemblage 1_F (CPy1, Mo1, Po) CL-B, K-alt	CL-B, K-alt	Injection of hydrothermal fluids subsides and system cools. Fracturing of CL-B quartz.	Assemblage 2_F (Py_2, Mt) CL-D, CM-Alt	Assemblage 3_F (CPy2, Mo2) CL-D, CM-Alt	Injection of hydrothermal fluids subsides, system cools and Fe-bearing phases oxidize to Hematite (Assemblage 4_F)
	Entrapment Conditions	N/A	<300-370°C 2500-3000 Bars	425-545°C 2500-3000 Bars		<300-315°C 2500-3000 Bars	N/A	
	Inclusions	None trapped	B15D (~5 wt% NaCl equiv)	B30 (~5 wt% NaCl equiv)		B15C (~4 wt% NaCl equiv)	None trapped	
	Ascending hydrothermal fluids	↑	↑	↑		↑	↑	
	M^+-rich Fluids exsolved from H2O-saturated magma at depth							

*Predicated by H_2O-NaCl phase diagram

CL-B=CL-bright, CL-D=CL-dark, K-alt=Potassic alteration, GM-alt= green mica alteration, CM-alt=Coarse mica alteration

Table 8. Microthermometric Properties of Fluid Inclusions

Inclusion type	[3]Phases present	Tm_{Ice} Range (°C) Avg	Tm_{Cla} Range (°C) Avg	[4]Tm_H Range (°C) Avg	Th Range (°C) Avg	Th CO_2 (°C) Avg	[2]Salinity Range (Wt% NaCl equiv)	Mol% CO_2	[2]Bulk Density (g/cm^{3})
B15 n=20	H2O(L) + H2O(V)	-1.6 - -11.0 -4.5	n/a	n/a	167.0-342.0 (L) ~257.0 37% between 239.0-265.5 37% between 305.3-342.6	n/a	~3.0-15.0 avg = ~8.5	n/a	0.73 - 0.93 0.82
B30D n=98	H2O(L) + H2O(V) +/- TDC +/- T +/- O	-0.1 - -21.1 -5.7 71% between -2.5 - -4.6	n/a	n/a	106.0-430.0(L) ~325.0 36% between 220.0-234.0	n/a	~2.0 - 16.0 avg = 8.6 71% between 4.1 - 7.3	n/a	0.55 - 0.97 0.75
B30H n=42	H2O(L) + H2O(V) + H +/- T +/- O	n/a	n/a	176.6-312.1 203.0 88% between 176.6-215.2	210.5-437.6 (L) ~271.0	n/a	~31.0 - 39.0 avg = 32.0	n/a	0.88 - 1.11 1.06
B75 n=21	H2O(L) + H2O(V) +/- O	-1.0 - -5.5 -2.9	n/a	n/a	357.0-405.0 (V) ~378.0	n/a	~2.0 - 6.0 avg = 4.5 75% between 4.4 - 5.8	n/a	0.53 - 0.58 0.55
B20C n=77	H2O(L) +/- CO2(L) + CO2(V) +/- TDC +/- O	n/a	5.3 - 10.0 9.3	n/a	120.0 - 400.0 (L) ~294.0 40% between 301.0-352.0	23.0 - 28.0 27.3	~0.0 - 8.0 avg = 1.6 75% between 0.0 - 1.8	~3.0 - 45.0 72% between 3.0-15.0	0.74 - 0.98 0.88
B75C n=93	H2O(L) +/- CO2(L) + CO2(V)	n/a	3.5 - 10.0 8.8	n/a	101.0-533.0 (V) ~300.0 46% between 300.0-393.0	23.0 - 29.0 25.0	~0.0 - 9.0 avg = 2.1 69% between 0.0 - 1.6	~3.0-27.0 84% between 22.0-27.0	0.47 - 0.90 0.53
B15D n=120	H2O(L) + H2O(V) +/- TDC +/- T +/- O	-0.9 - -6.0 -3.1	n/a	n/a	115.0-271.0 (L) ~203.0 22% between 120.0-137.0 25% between 167.0-179.0	n/a	~2.0 - 9.0 avg = 5.0 71% between 2.5 - 5.9	n/a	0.85 - 1.00 0.94
B30 n=5	H2O(L) + H2O(V) +/- O	-2.3 - -3.4 -3.1	n/a	n/a	151.0-283.0 (L) ~227.0 80% between 242.0-282.0	n/a	~4 - 6 avg = 4.8	n/a	0.80 - 0.92 0.84
B15C n=107	H2O(L) +/- CO2(L) + CO2(V) +/- TDC +/- O	n/a	0.2 - 10.0 8.0	n/a	115.0-271.0 (L) ~203.0	20.6 - 30.5 30.1	0.0 - 15.0 avg = 3.8 48% between 0.0 - 1.8	~1.0-10.3 79% between 3.0-5.0	0.89 - 1.10 0.98

[1]Th= minimum temperature due to difficulty in observing final homogenization

[2]Calculated in MacFlincor. B15, B30D, B30H, B75, B30 and B15D: H_2O-NaCl-[KCl] system. B20C, B75C, and B15C: H_2O-CO_2-[NaCl] system.

[3] TDC= translucent daughter crystal, T= triangular opaque, O= Oval opaque

[4] Tm_H only for those inclusions which exhibited final homogenization by vapor bubble disapearance

Table 9. Raman Spectroscopy Data

Inclusion Type	Number of analyzed inclusions with detectable CO_2	CO_2 density range and average (g/cm^3)
B15 n=5	1	0 .77
B30D n=24	15	0.0 - 0.35 avg = 0.16
B30H n=7	1	[0.14]
B75 n=6	4	0.01 - 0.15 avg = 0.11
B15D n=25	8	0.0 - 0.77 avg = 0.16
B30 n=0	n/a	n/a
B20C n=10	10	0.01 - 0.76 avg = 0.25
B75C n=6	6	0.0 - 0.76 avg = 0.31
B15C n=7	4	0.00 - 0.77 avg = 0.24

Table 10. Summarry of Relative Abundnaces of Elements Within Inclusion Groups

		Cu	Zn, Pb, Mn	Sr, Rb, Ba	Fe	Cu	Zn, Pb, Mn	Sr, Rb, Ba	Fe
H2O-rich	B15	High	Moderate-Low	Moderate	Moderate-High	High	Moderate-Low	Moderate	Moderate-High
	B30D	Moderate-Low	Moderate-Low	Moderate	Low	Low	Moderate-Low	Moderate-Low	Moderate-Low
	B30H	Moderate-Low	Very high	High	High	Low	High	High	High
	B75	High	low-very low	Low-Very Low	Low-Very Low	High	Low	Low	Low
	B15D	High-moderate	Low	Low	Low	High-moderate	Moderate-Low	Moderate-Low	Moderate-Low
		Overall				Compared to other H2O inclusions			
CO2-rich	B20C	Low	Low	Low	Low	Low	Low	Moderate-High	Moderate-High
	B75C	Low	Low	Low	Low	moderate-high	Low	Low	Low
	B15C	Low	Low	Low	Low	Moderate	Moderate	Moderate	Moderate
		Overall				Compared to other CO2 inclusions			

Table 11.3 Summary of Hanging Wall and Footwall Isochors

		Aqueous						
	Inclusion groups	500-1000 Bars	1000-1500 Bars	1500-2000 Bars	2000-2500 Bars	2500-3000 Bars	3000-3500 Bars	3500-4000 Bars
HW	B15 High	275-315	315-350	350-385	385-415	415-455	455-490	n/a
	B15 Low	345-390	390-445	445-490	490-530	530-580	580-625	n/a
	B30D High 1	350-395	395-445	445-490	490-540	540-585	585-635	635-685
	B30D Low 1	425-515	515-590	590-675	675-750	n/a	n/a	n/a
	B30D High 2	270-290	290-325	325-355	355-385	385-420	420-450	450-480
	B30d Low 2	335-380	380-425	425-470	470-515	515-555	555-600	600-645
	B30H High	240-265	265-290	290-325	325-350	350-380	380-410	410-435
	B30H Low	320-350	350-385	385-420	420-455	455-490	490-525	525-560
	B75 High	425-510	510-600	600-680	680-770	n/a	n/a	n/a
	B75 Low	470-570	570-675	675-775	n/a	n/a	n/a	n/a
FW	B30 High	275-315	315-350	350-380	380-425	425-460	460-500	n/a
	B30 low	325-365	365-410	410-455	455-500	500-545	545-580	n/a
	B15D High 1	n/a	n/a	n/a	200-225	225-235	235-270	270-290
	B15D Low 1	n/a	n/a	220-245	245-260	260-290	290-320	320-345
	B15D High 2	n/a	220-245	245-275	275-305	305-335	335-365	365-380
	B15D Low 2	225-250	250-275	275-310	310-340	340-370	370-395	395-425
		CO2-Rich						
	Inclusion groups	500-1000 Bars	1000-1500 Bars	1500-2000 Bars	2000-2500 Bars	2500-3000 Bars	3000-3500 Bars	3500-4000 Bars
HW	B20C High	n/a	n/a	250-260	260-275	275-310	310-325	325-350
	B20C Low	n/a	265-290	290-330	330-365	365-390	390-435	435-470
	B75C High	350-475	475-600	n/a	n/a	n/a	n/a	n/a
	B75C Low	355-500	500-670	670-860	n/a	n/a	n/a	n/a
FW	B15C High	n/a	n/a	n/a	230-240	240-275	275-295	295-320
	B15C Low	n/a	n/a	240-265	265-280	280-315	315-330	330-360

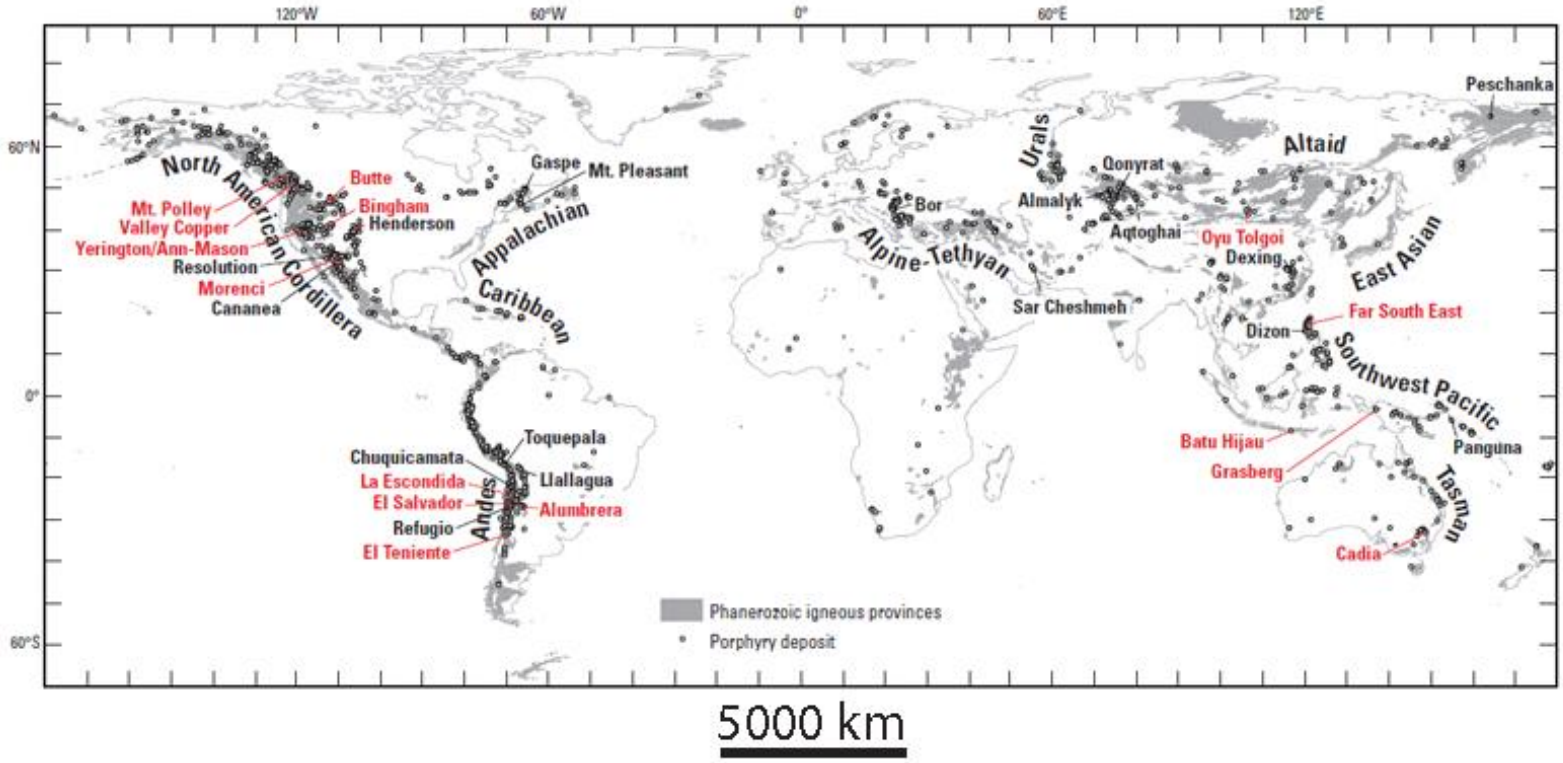

Figure 1. Global distribution of porphyry copper deposits. Major deposits are shown in red text. From John et al., 2010, modified from Seedorff et al., 2005.

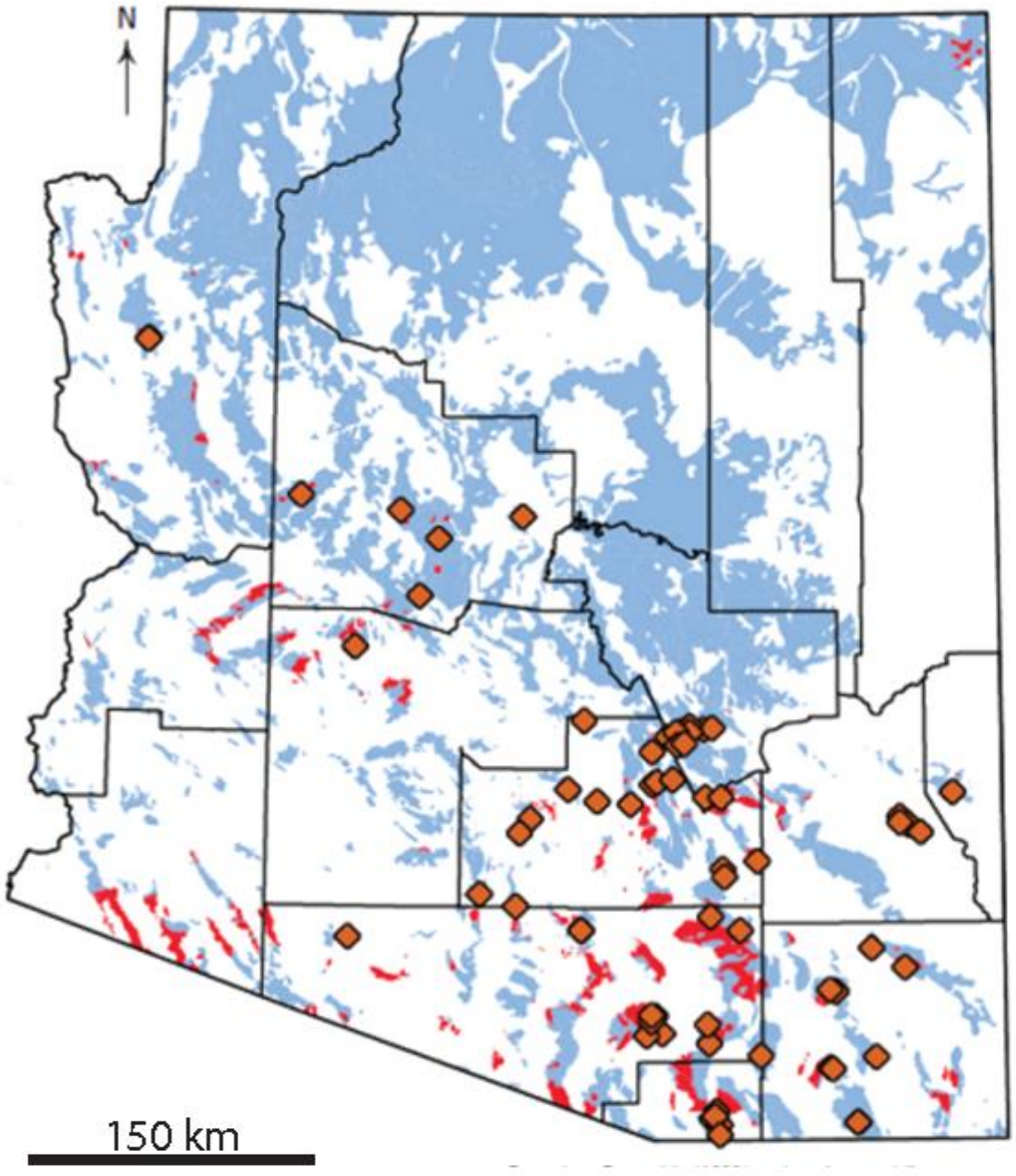

Figure 2. Distribution of porphyry copper deposits throughout Arizona. Porphyry copper deposits are denoted by orange diamonds, Laramide-aged igneous intrusive rocks are shown in red, older igneous intrusive rocks are shown in blue, and post-Laramide cover is shown in white. Modified from John et al., 2010.

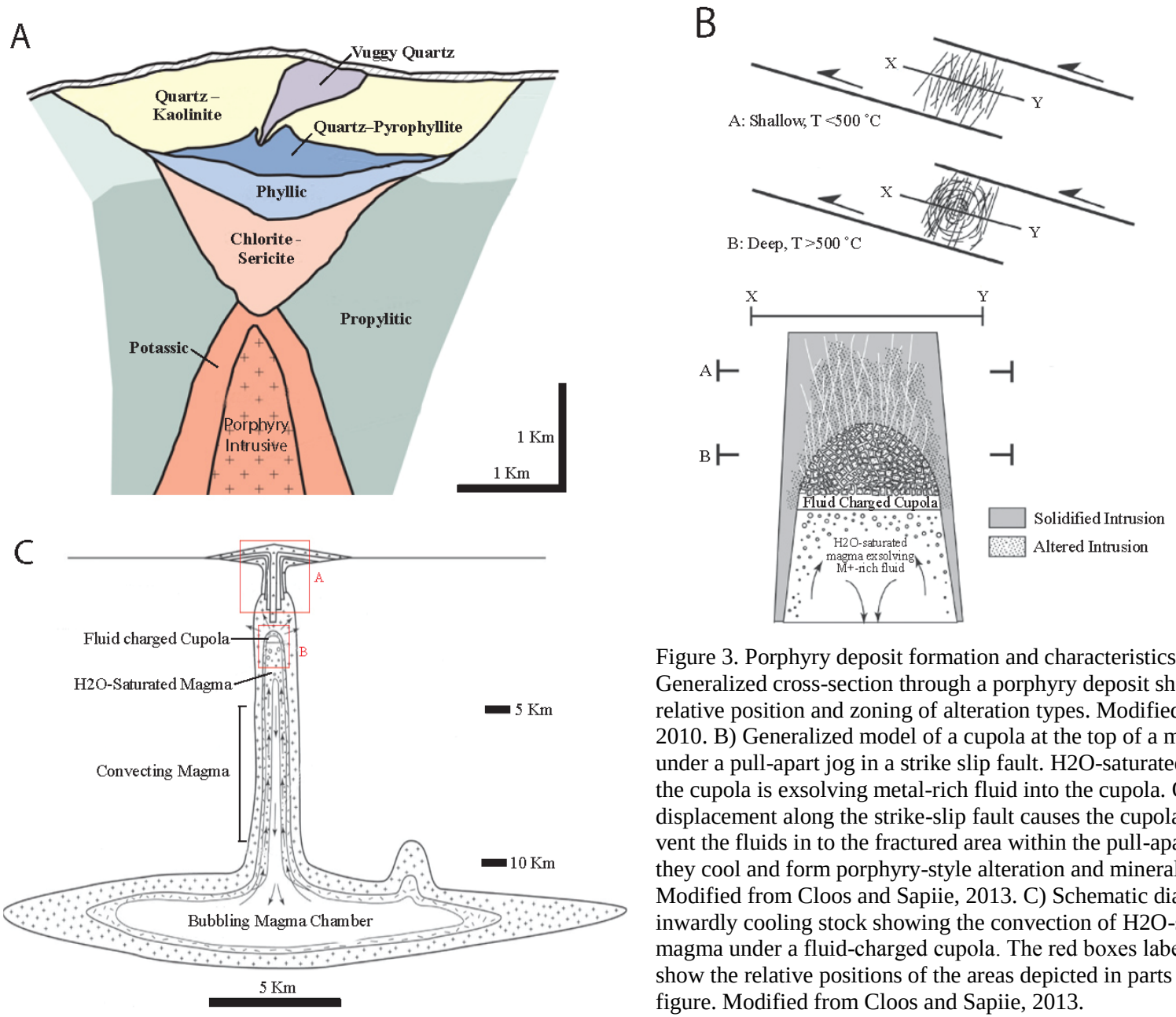

Figure 3. Porphyry deposit formation and characteristics. A) Generalized cross-section through a porphyry deposit showing the relative position and zoning of alteration types. Modified from Sillitoe, 2010. B) Generalized model of a cupola at the top of a magma chamber, under a pull-apart jog in a strike slip fault. H2O-saturated magma under the cupola is exsolving metal-rich fluid into the cupola. Over time, displacement along the strike-slip fault causes the cupola to rupture and vent the fluids in to the fractured area within the pull-apart jog where they cool and form porphyry-style alteration and mineralization. Modified from Cloos and Sapiie, 2013. C) Schematic diagram of an inwardly cooling stock showing the convection of H2O-saturated magma under a fluid-charged cupola. The red boxes labeled ‘A’ and ‘B’ show the relative positions of the areas depicted in parts A and B of this figure. Modified from Cloos and Sapiie, 2013.

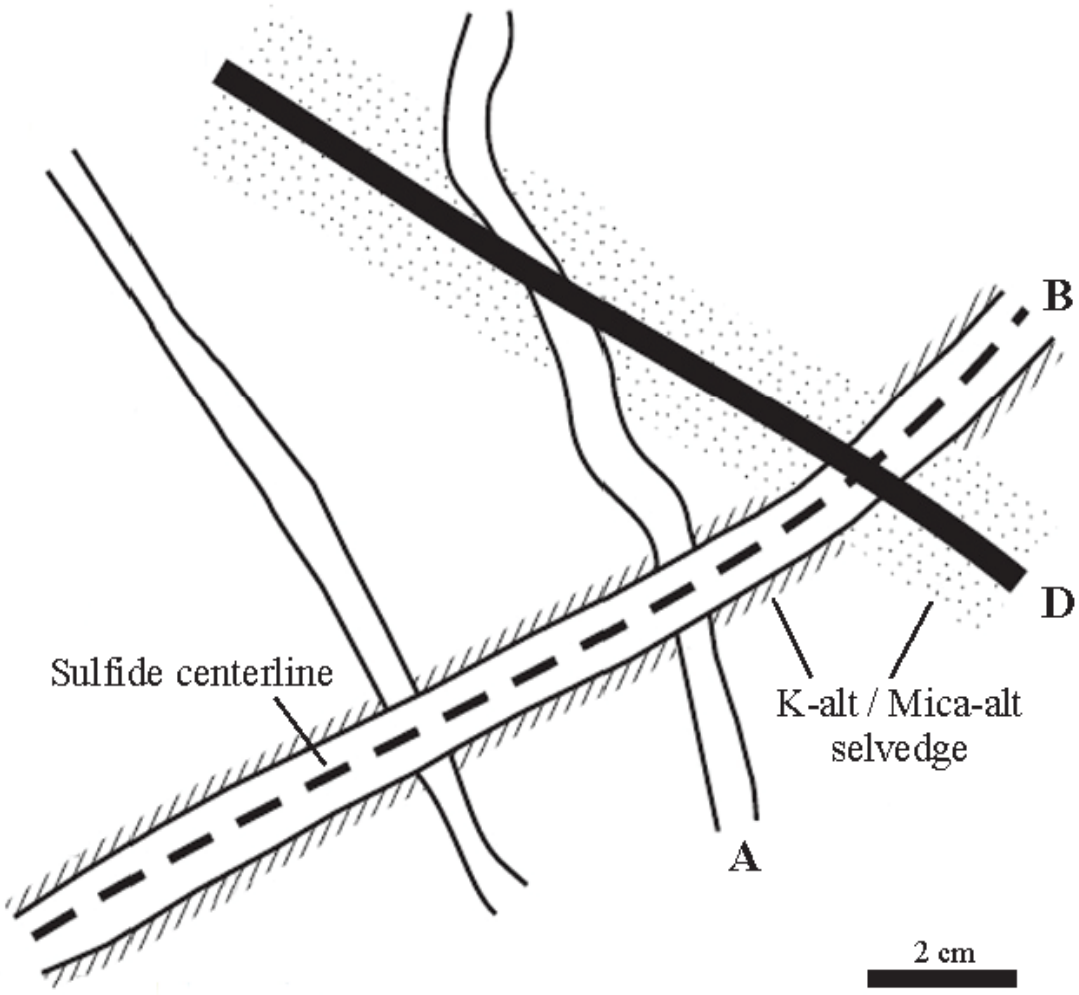

Figure 4. Schematic chronology of A, B and D veins in a typical Cu-Mo porphyry deposit. The dashed line in on the B veins signifies a centerline and the hashed and stippled areas around the veins represent potassic (K-alt) and mica (mica-alt) alteration selvedges. Modified from Sillitoe, 2010.

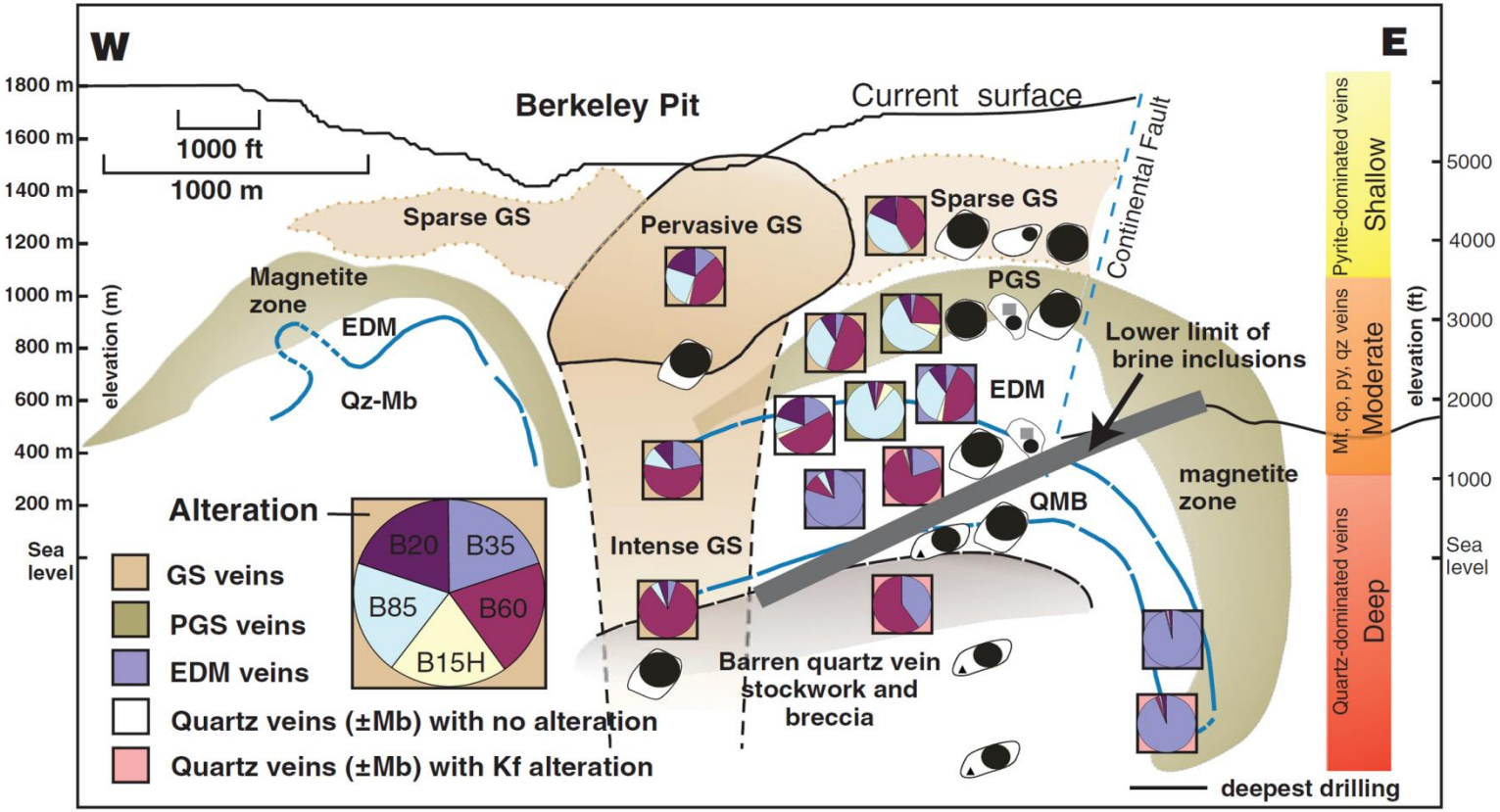

Figure 5. Fluid inclusion assemblage distribution model for the Butte porphyry deposit. The pie charts indicate the relative abundances of each identified FIA throughout the deposit. The notation B# indicates the vol% of vapor in a particular FIA (B20 = 20 vol% of this inclusion is occupied by a vapor bubble). The notation B15H indicates 15 vol% vapor and a halite daughter crystal. Note how the abundance of 85 vol% inclusions increases with decreasing depth. From Rusk et al., 2008.

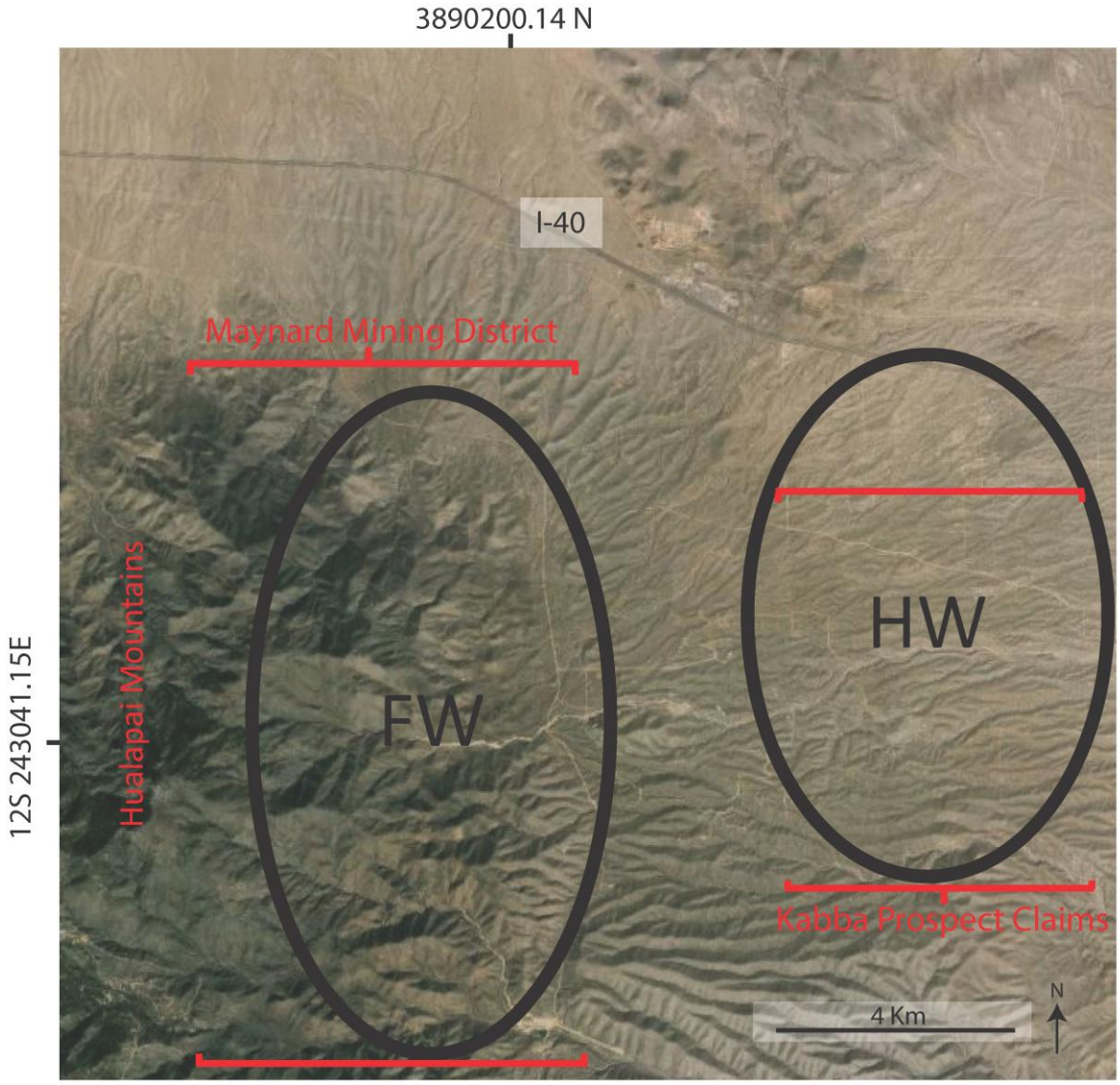

Figure 6. Satellite photo of the Maynard District and Kabba Prospect. Photo shows the approximate locations of the Maynard District, the Kabba Prospect claims, the Hualapai Mountains, and the footwall (FW) and the hanging wall (HW) areas. The red star on the inset map of Arizona denotes the approximate location of the area shown in the satellite photo.

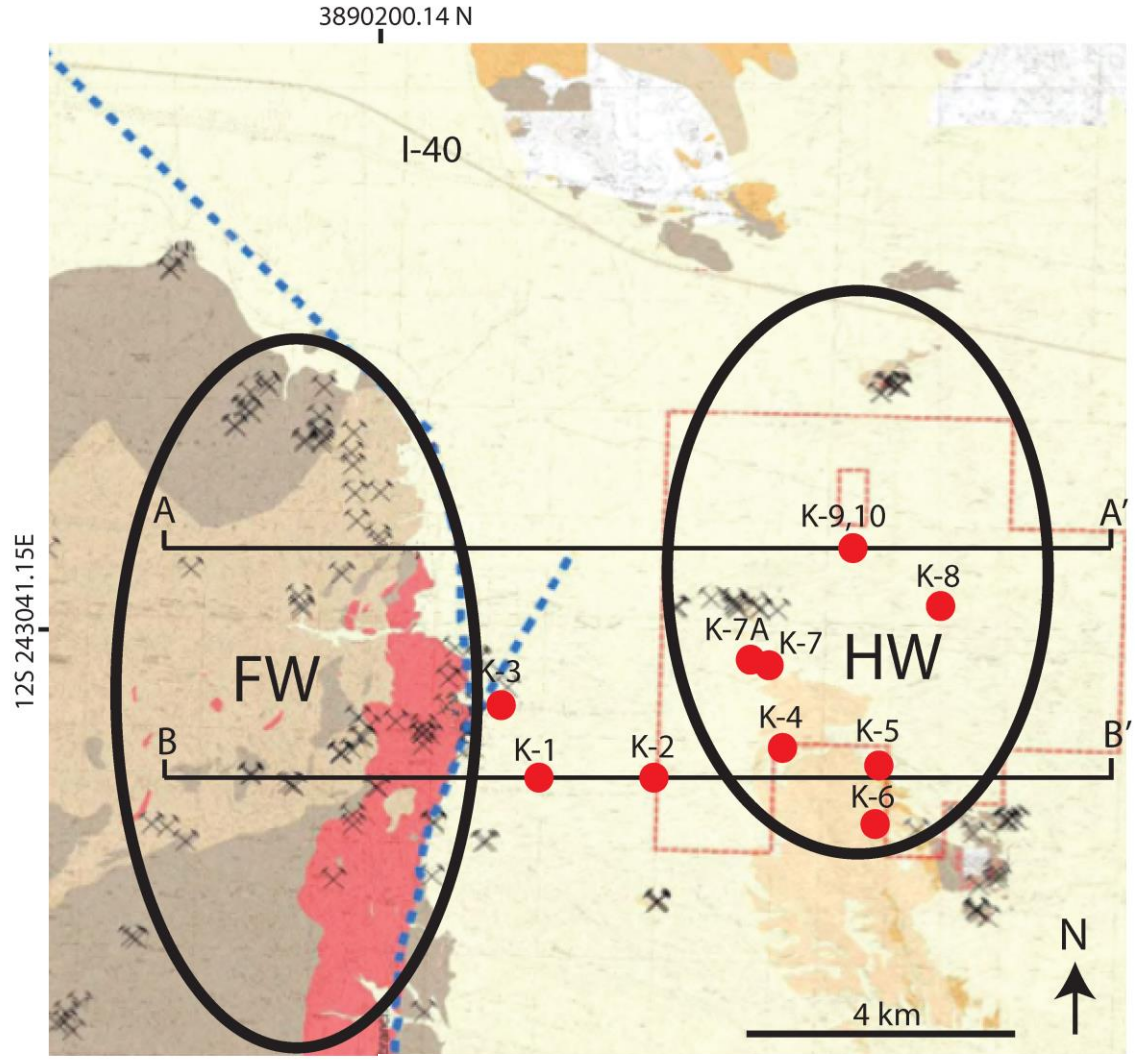

Figure 7. Geologic map of the hanging wall and footwall. The approximate locations of hanging wall (labeled HW) and footwall (labeled FW) areas are circled in black. The Hualapai fault is denoted by a dashed blue line, Bell Copper Co. drill holes are denoted by red dots, historic mines are denoted by crossed pick axes, and the locations of cross section shown in Figure 9 are denoted by lines A-A' and B-B'. In the footwall, surface outcrops of Laramide granites, granodiorites, monzonites, and quartz monzonites are west of the Hualapai fault and are shown in red, and Precambrian granites and gneisses are shown in tan and brown, respectively. In the hanging wall, Quaternary gravels are shown in light yellow and surface outcrops of granites and granodiorites are shown in light orange and yellow, respectively. Modified from Pastor, 2013. The red star on the inset map of Arizona denotes the approximate location of the area shown in the satellite photo.

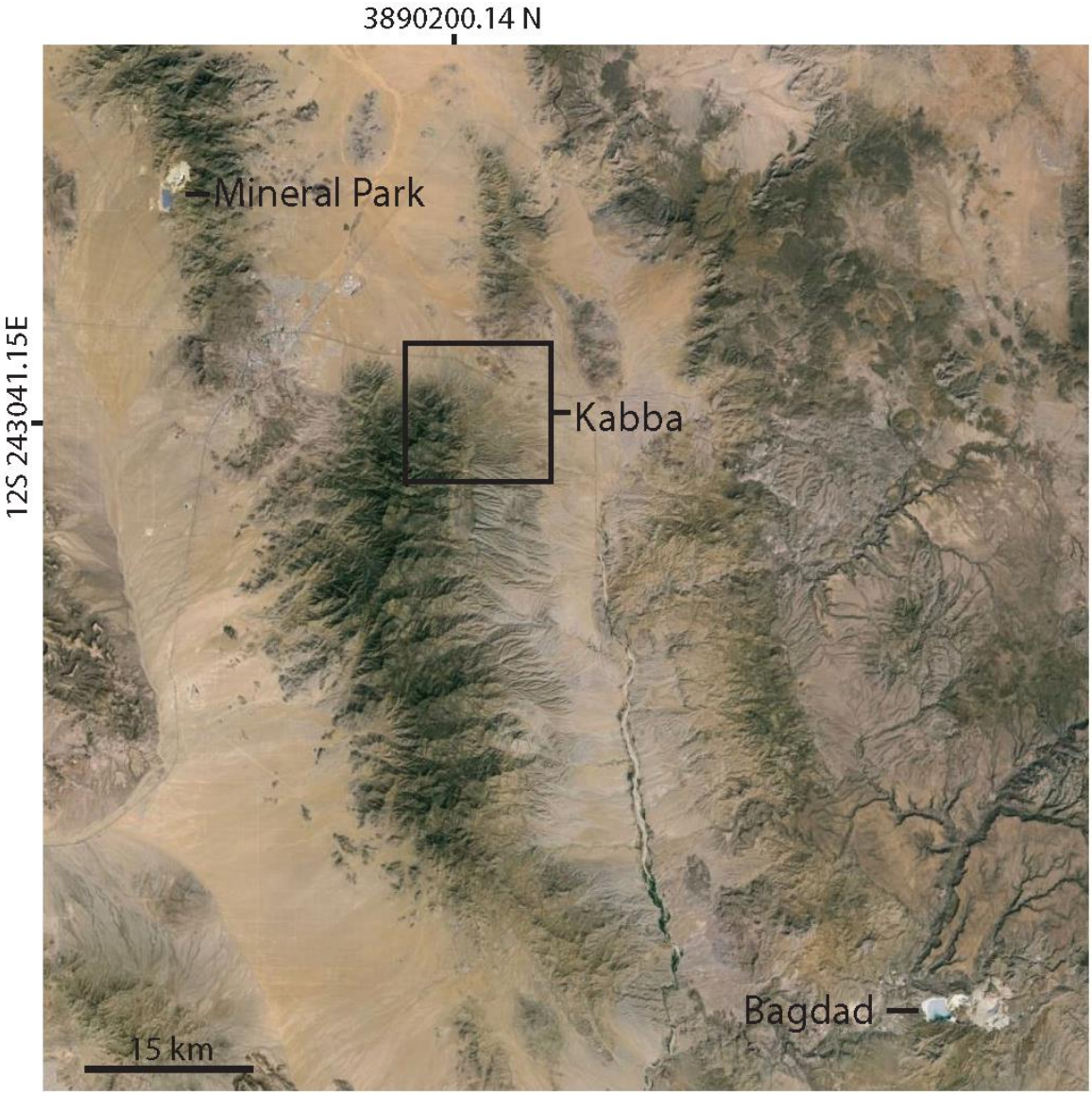

Figure 8. Satellite photo of Mineral Park and Bagdad porphyry copper deposits, and the Kabba hanging wall and footwall. The Kabba hanging wall and footwall locations are denoted by the black square.

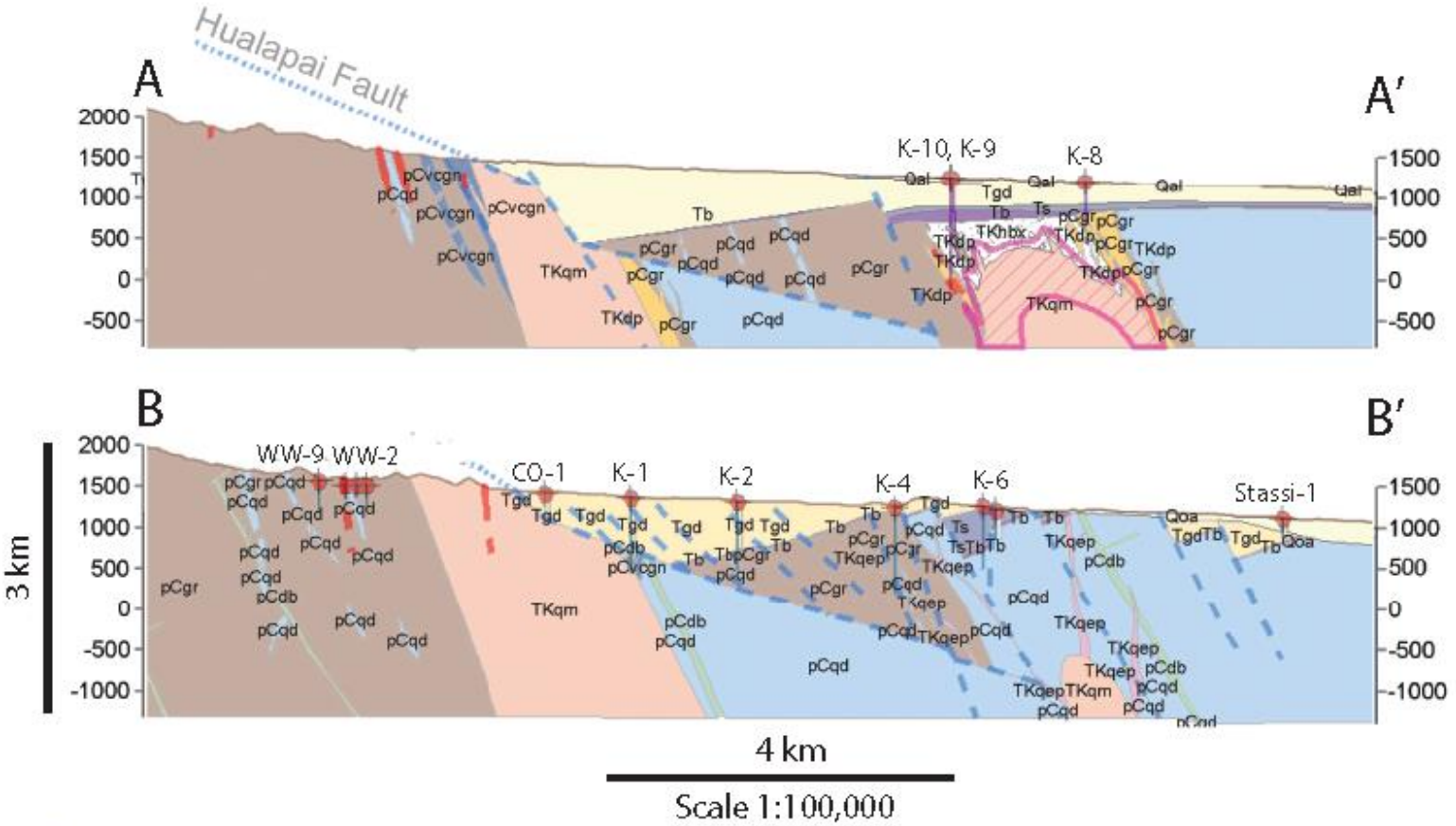

Figure 9. Interpreted east-west cross sections through the Kabba hanging wall and footwall. Cross-sections show the interpreted displacement along the Hualapai fault, the location of exploration holes drilled by Bell Copper Corp (K-1,2….) and others, and the potential location of a mineralized porphyry system (TKqm with purple cross hatching). Modified from Pastor, 2013.

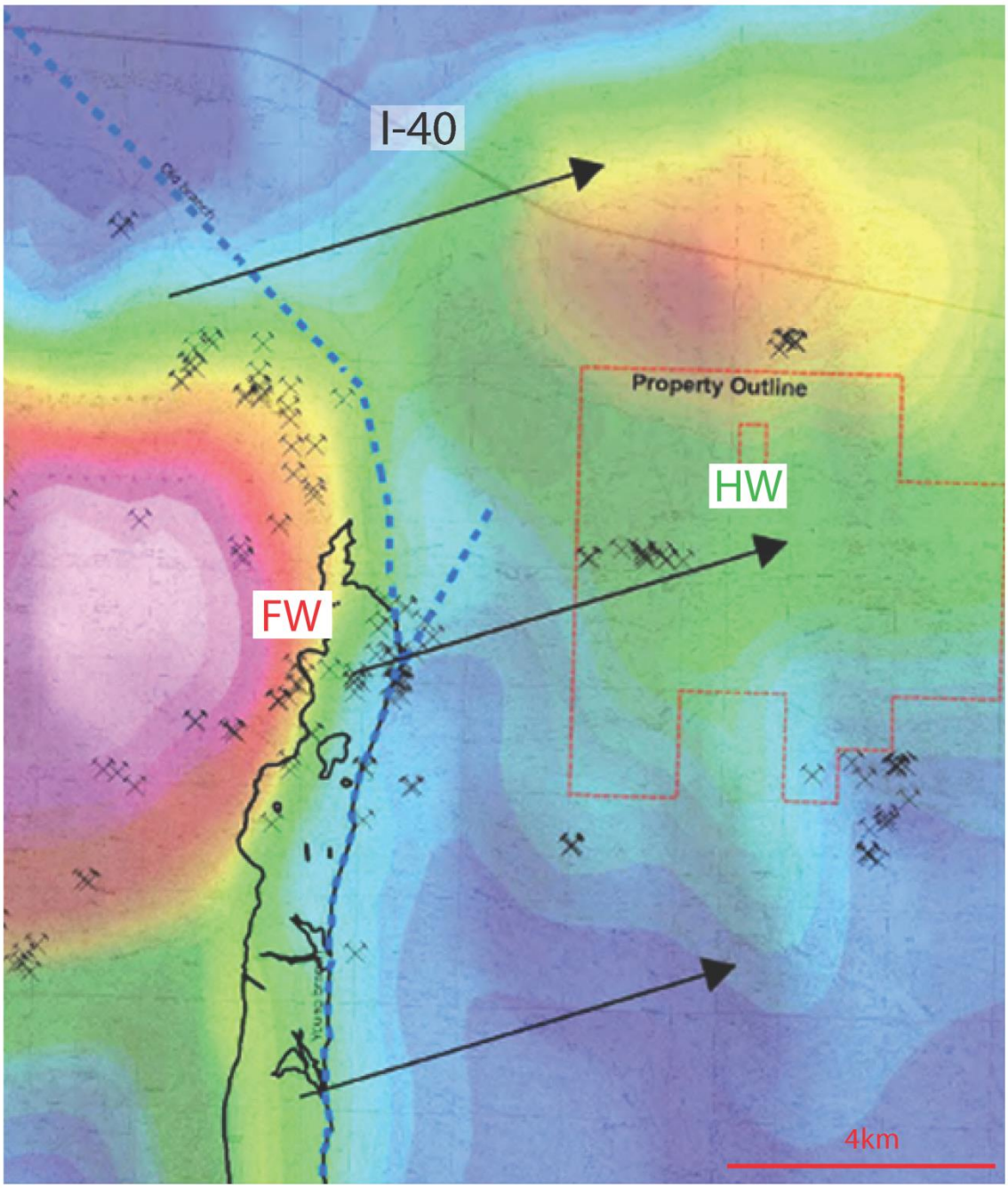

Figure 10. Aeromagnetic map of the Kabba hanging wall and footwall. The black arrows denote the approximate direction of displacement of interpreted faulted magnetic highs along the Hualapai normal fault (dashed blue line). The hot colors of the anomaly indicate a positive anomaly. Laramide granites, granodiorites, monzonites, and quartz monzonites in the footwall are outlined in black and the exploration claims owned by Bell Copper Co. are outlined with a red dashed line. Crossed pickaxes show the locations of the historic mining claims. USGS aeromagnetic data modified from Bell Copper Co. (2013), after Sweeney and Hill (2001).

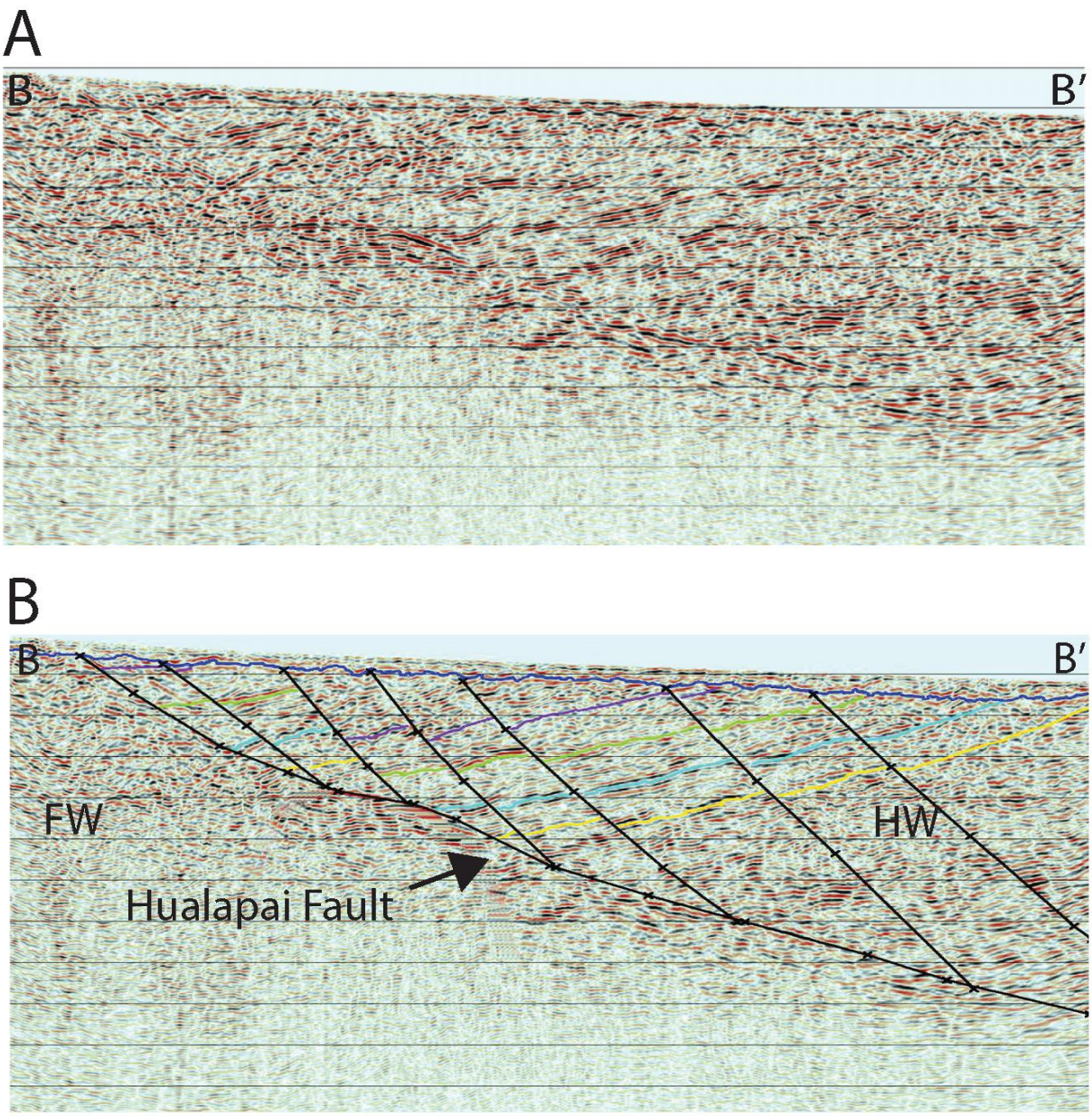

Figure 11. Seismic reflection data from the Kabba prospect. A) Seismic reflection data from the Kabba prospect. The survey line used to gather this seismic data is roughly parallel to the B-B' cross-section line shown in Figure 7 and this is denoted by the B and B' lettering on the top left and right-hand corners of this image. B) The same seismic reflection data shown in A, but with the Hualapai normal fault, as well as other smaller unnamed faults, traced in black. The purple, green, and yellow lines trace the contacts between layers of Quaternary sediments. Modified from Bell Copper Corp, 2013.

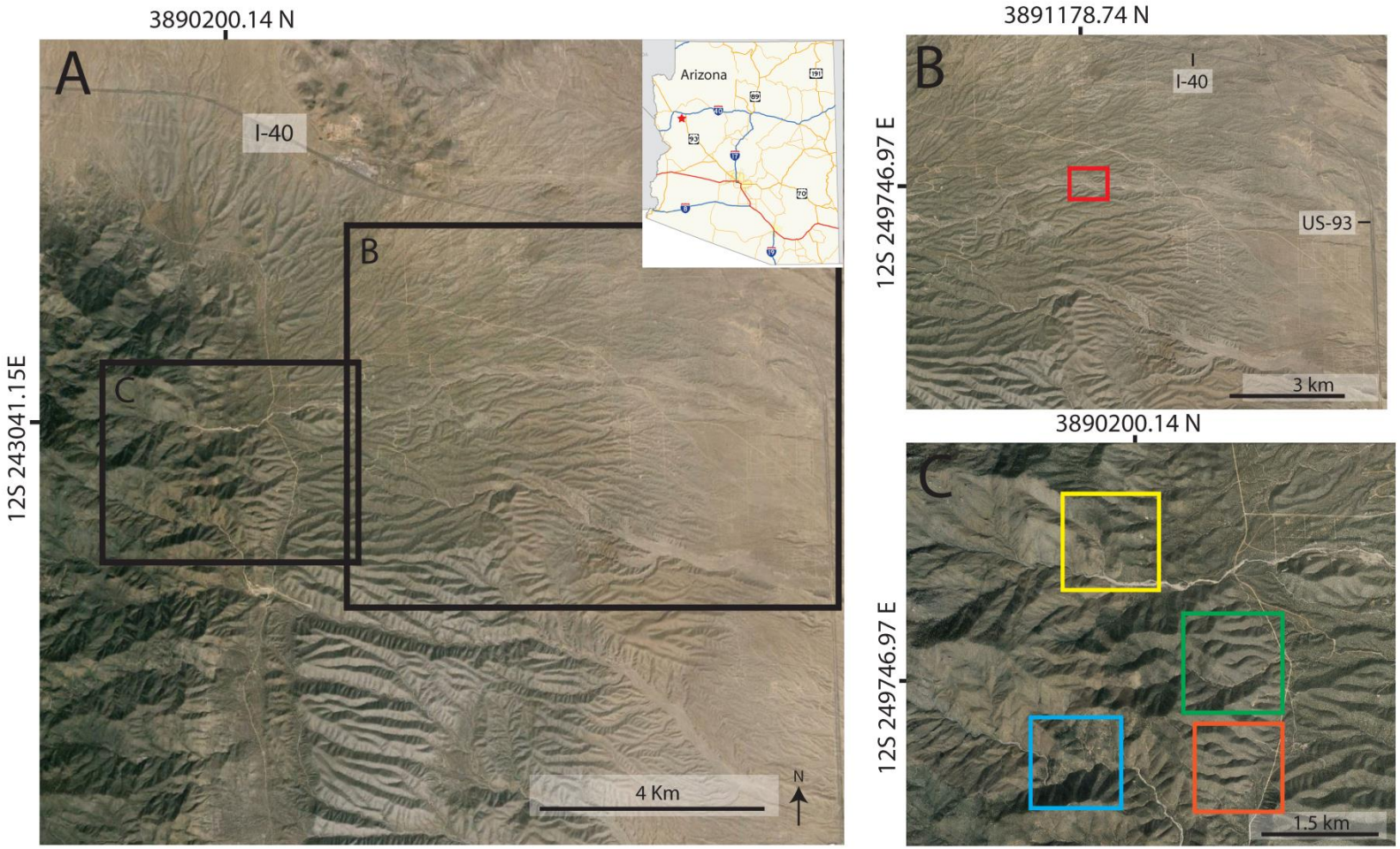

Figure 12. Satellite photos of the Kabba footwall and hanging wall area. A) Satellite photo of the Kabba hanging wall and footwall areas showing the approximate locations of images shown in B and C. The red star on the inset map of Arizona denotes the approximate location of the area shown in the satellite photos. B) Satellite photo of the Kabba hanging wall showing the approximate location of image A in Figure 13 (red box). C) Satellite photo of the Kabba footwall showing the approximate locations of images B (blue box), C (red box), D (green box), and E (yellow box) in Figure 13 (red box).

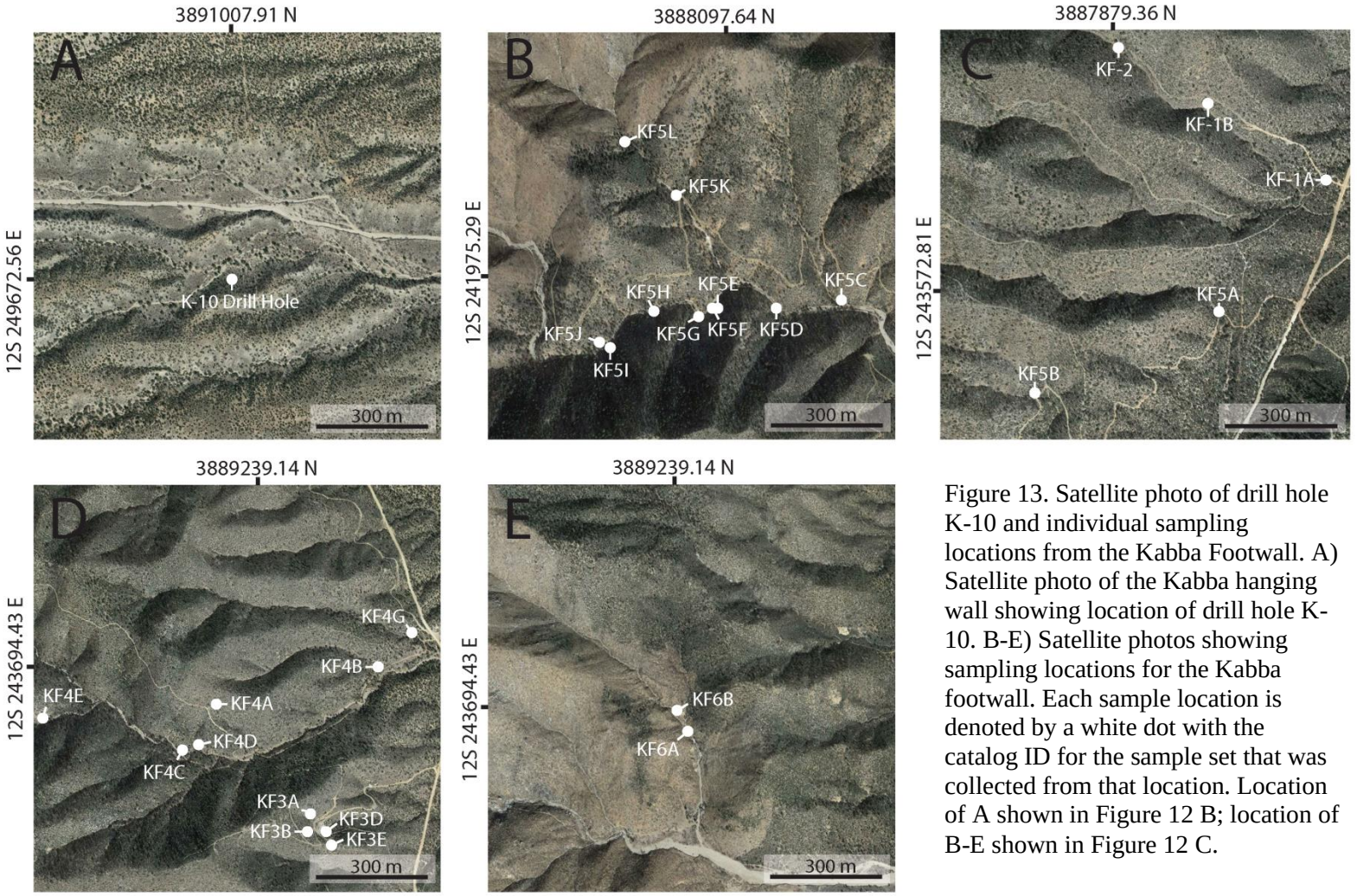

Figure 13. Satellite photo of drill hole K-10 and individual sampling locations from the Kabba Footwall. A) Satellite photo of the Kabba hanging wall showing location of drill hole K-10. B-E) Satellite photos showing sampling locations for the Kabba footwall. Each sample location is denoted by a white dot with the catalog ID for the sample set that was collected from that location. Location of A shown in Figure 12 B; location of B-E shown in Figure 12 C.

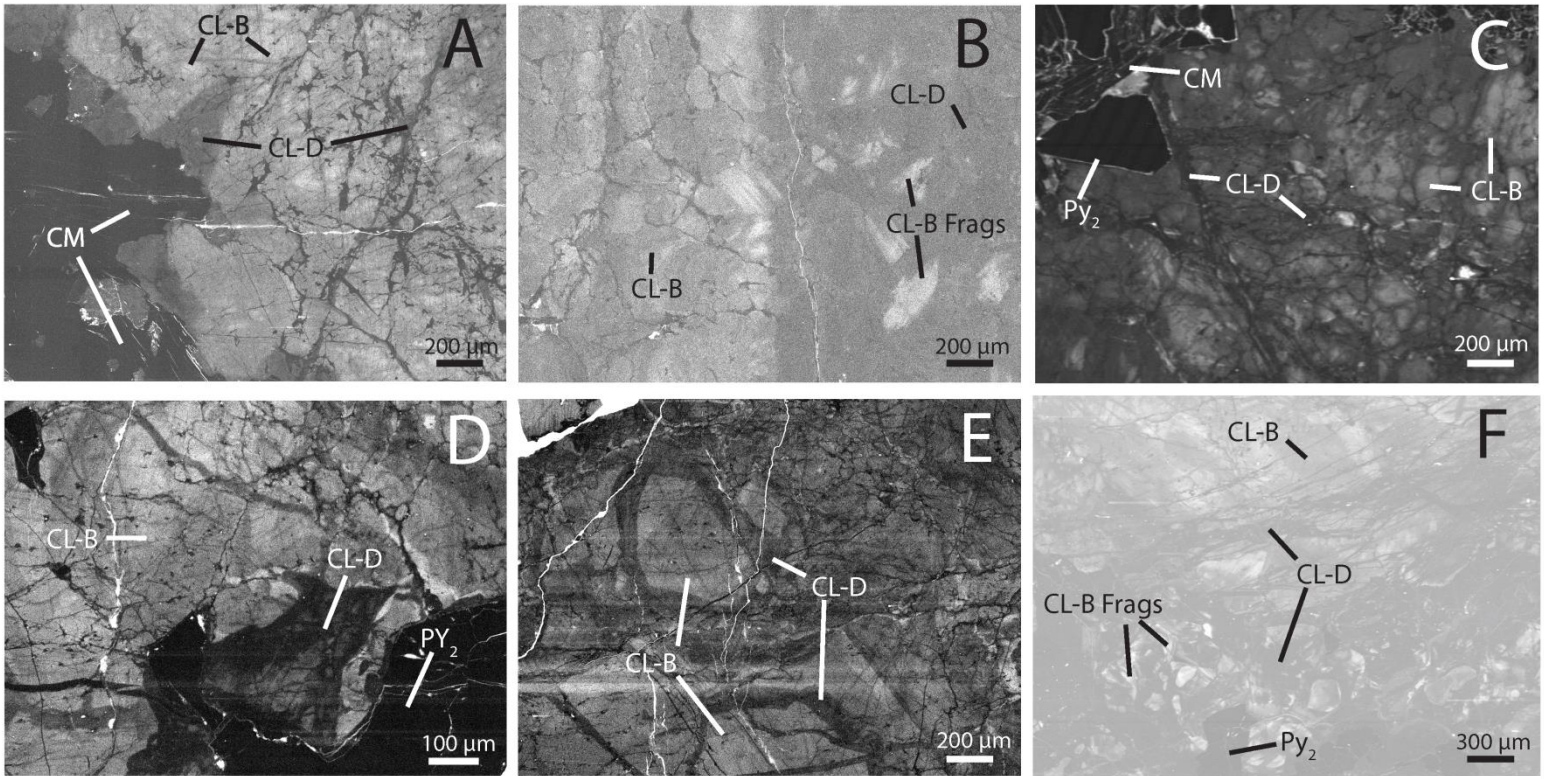

Figure 14. Scanning electron microscope cathodoluminescence (SEM-CL) images of hanging wall and footwall samples. Image abbreviations are as follows: CL-B=CL-bright, CL-D=CL-dark, CM=coarse mica, Py2=Pyrite 2, and CL-B frags= CL-bright quartz fragments. Variation in the image clarity and sharpness between CL images are due differences in brightness and contrast setting for each sample. A) CL image from footwall sample KF1-12 showing coarse mica rimed by CL-D quartz, and CL-D quartz cross-cutting CL-B quartz. B) CL image from footwall sample KF4D-2 showing the contact between a CL-B and CL-D band in an AB vein. On the left, fractures in the CL-B quartz band are filled with CL-D quartz and, on the right the CL-D band contains fragments CL-B quartz. C) CL image from footwall sample KF4F-2 showing coarse mica and Py2 rimmed by CL-D quartz, and CL-D quartz cross-cutting CL-B quartz. D) CL image from hanging wall sample 1193 showing Py2 rimmed by CL-D quartz, and CL-D quartz cross-cutting CL-B quartz. E) CL image from hanging wall sample 1193 showing CL-B quartz surrounded and cross-cut by CL-D quartz. F) CL image from hanging wall sample 1349.9 showing CL-D quartz filling highly fractured CL-B quartz. In the lower left-hand side of the image the CL- D quartz is rimming Py2 and contains CL-B fragments.

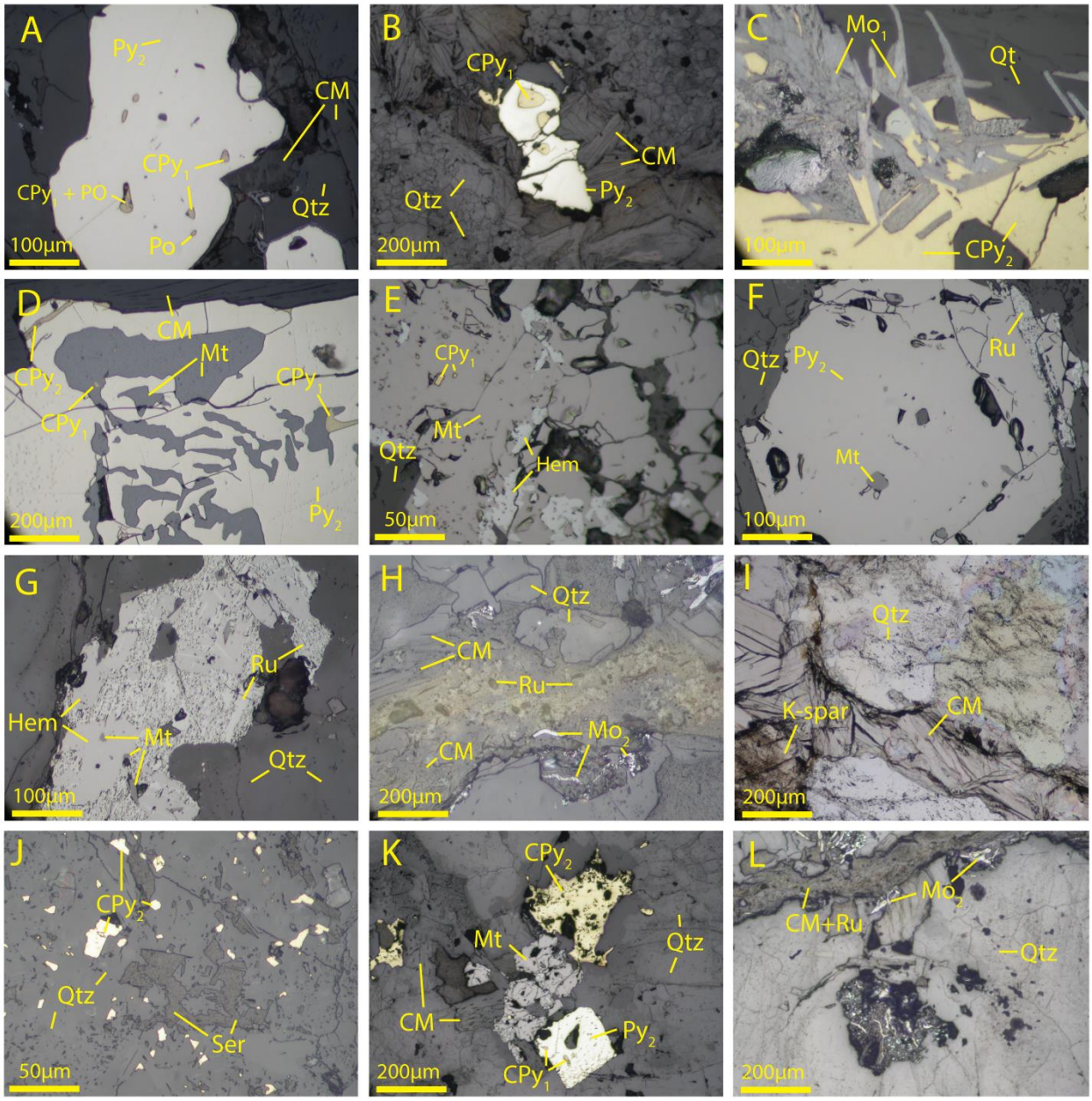

Figure 15. Photomicrograph of footwall sulfides, oxides, and silicate minerals. A) RL image of Py2 with inclusions of CPy1 and Po, partly surrounded by coarse muscovite (CM). From sample KF4B-5A. B) RL image of Py2 with inclusions of CPy1 in a coarse muscovite filled fracture. From sample KF4B-5B. C) RL image of Mo1, which is partly surrounded by CPy2. From sample KF4B-5B. D) RL image of intergrown Mt and Py2 with CPy1 inclusions. In the upper left of the image Cpy2 is filling a fracture in the Py2 crystal. From sample KF4B-5B. E) RL image of Mt with CPy1 inclusions. Some of the Mt in this image is rimmed by Hem. From sample KF3D-19. F) RL image of Py2 with inclusions of Mt. On the right side of the image the Py2 is intergrown with an elongate Ru crystal. From sample KF4B-5A. G) RL image of intergrown Ru and Mt that has largely oxidized to Hem. From sample KF1-11. H) RL image of a coarse mica and Ru filled fracture in quartz. In the top right and bottom center of the image, Mo2 crystals are present along the cleavage planes in the coarse mica. From sample KF2-4. I) RL image of coarse mica filled fracture in quartz. From sample KF4B-5B. J) RL image of CPy2 disseminated in quartz. Sericite in this image is filling in open space between individual quartz crystals. From sample KF4B-5A. K) RL image of Py2 with CPy1 inclusions adjacent to Mt, coarse mica, and CPy2. From sample KF3D-19. L) RL image of intergrown coarse mica and Mo2 crystals filling a fracture in quartz. From sample KF2-4. For figure abbreviations see Table 1. RL=Reflected light.

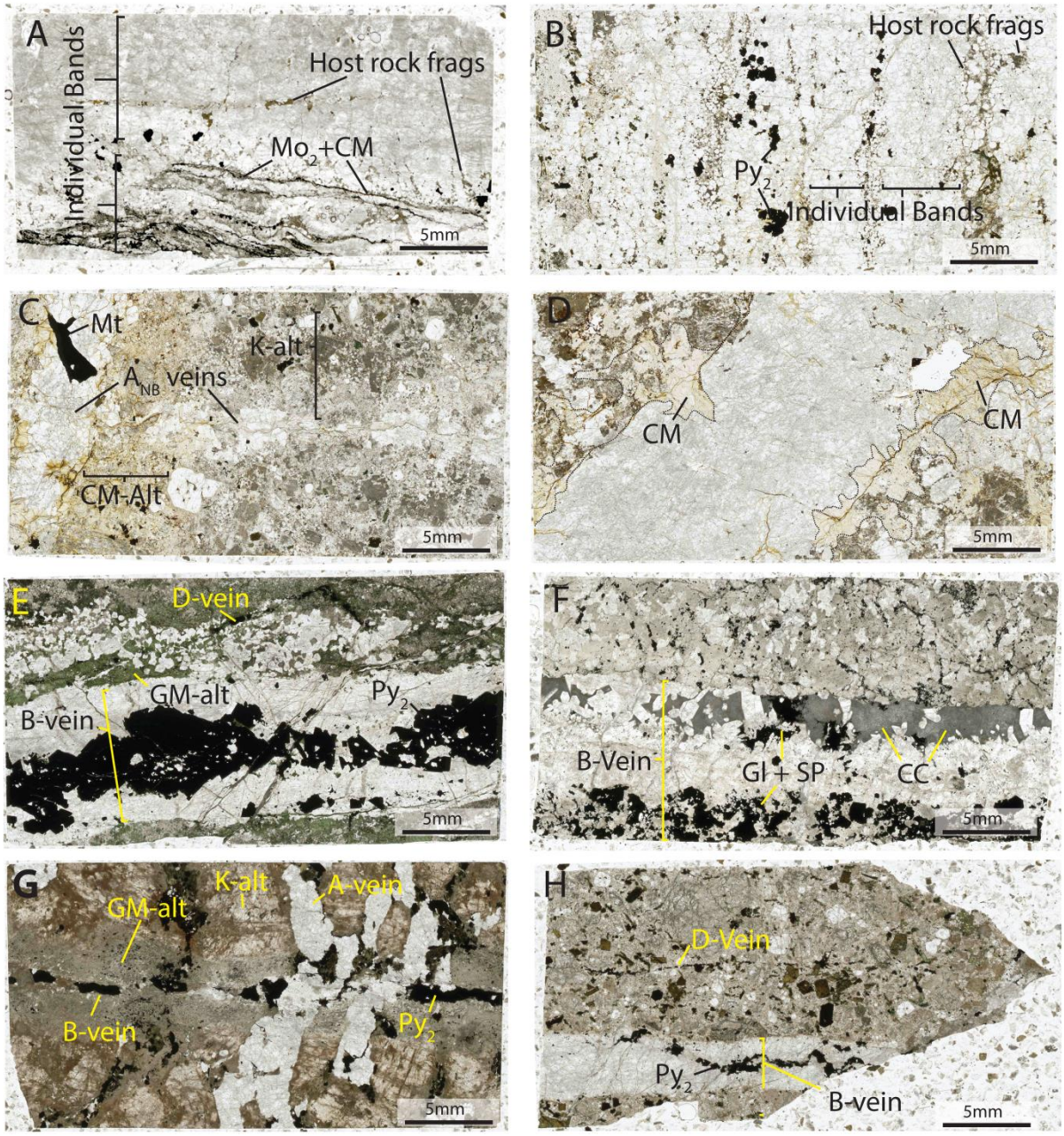

Figure 16. Scanned images of selected thick sections showing vein types from the footwall and hanging wall. A) A_B vein from footwall sample KF5E-2 showing host rock fragments and "wispy" bands of coarse mica (CM) + Molybdenite 2 (MO2). B) A_B vein from footwall sample KF3D-19 showing individual quartz bands separated by aligned host rock fragments. C) Two cross-cutting A_{NB} veins from footwall sample KF4B-5A showing potassic (K-alt) and coarse mica (CM) alteration selvedges and a mass of magnetite (Mt) crystals. D) A_{NB} veins from footwall sample KF1-13 showing well developed CM alteration selvedge along its outer margin (outlined with black dotted line). E) B and D veins from hanging wall sample 1343.9. The B vein in has a well-developed sulfide centerline and is rimed by a green mica (GM-alt) selvedge. F) Moderately sinuous B vein from sample 1279.9 showing calcite (CC) intergrown with CL-bright quartz along its margins. G) Hanging wall sample 1078.78 showing an A vein with potassic alteration selvedge being cross-cut by a B vein with a green mica alteration selvedge. H) B and D veins from sample 1201.1. A_{NB}=A "non-banded," A_B= A "banded."

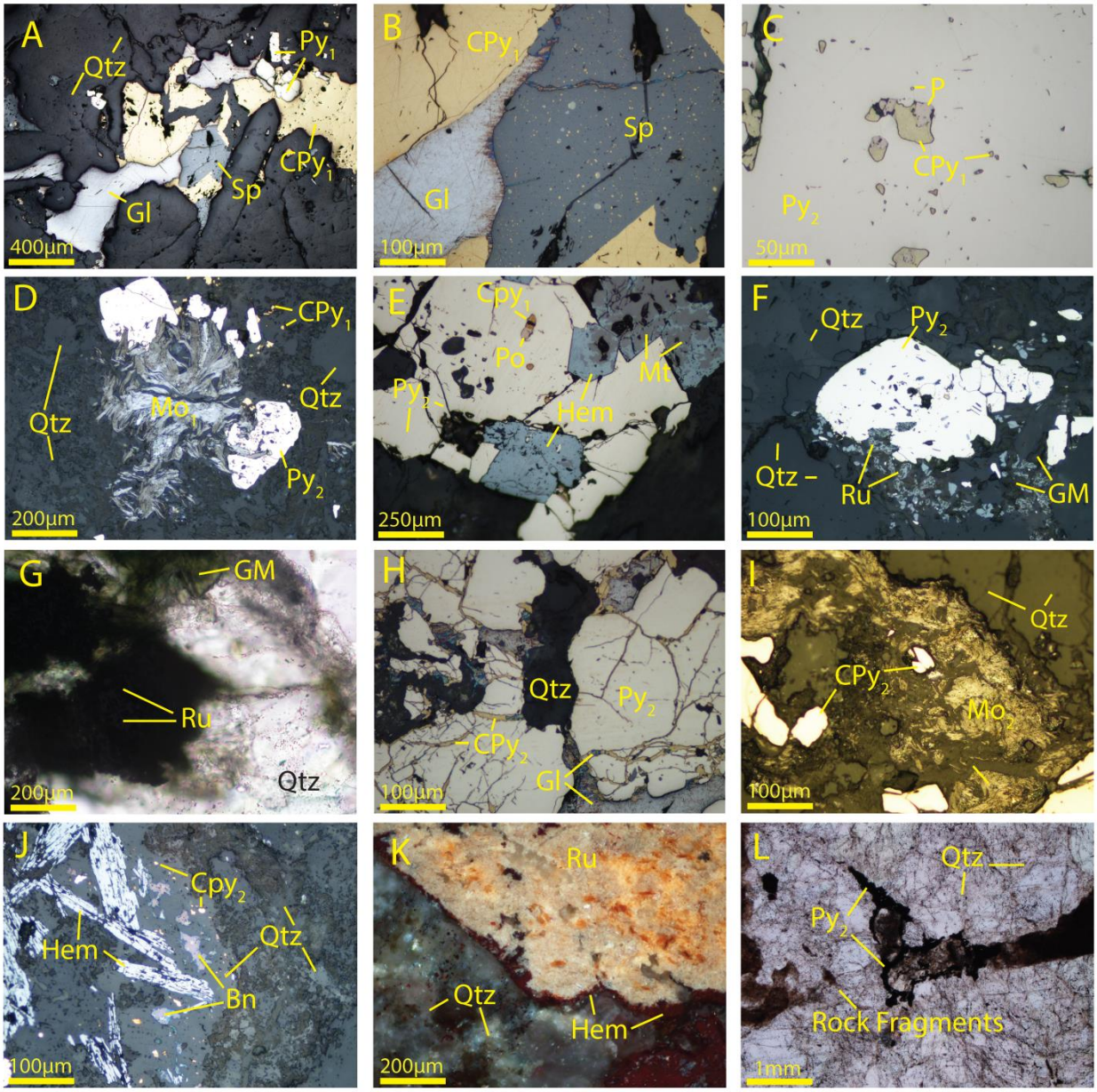

Figure 17. Photomicrograph of hanging wall sulfides, oxides, and silicate minerals. A) RL image of intergrown Sp, Gl, and Py1, which are partly encompassed by CPy1. From sample 1279.79. B) RL image of intergrown Sp and Gl, which are partly encompassed by CPy1. Sp contains inclusions of Cpy1. From sample 1279.9. C) RL image of Py2 showing inclusions of CPy1 and Po. From sample 1343.9. D) RL image of Mo1 partly encompassed by Py2 with CPy1 inclusions. From sample 1200.4. E) RL image of Py2, with inclusions of CPy1 and Po, intergrown with Mt. The Mt in this image is dark grey and has light grey rims of Hem (upper right), or has been completely replaced by Hem (lower left). From sample 1193. F) RL image of Py2 intergrown with Ru and partly surrounded by green mica (GM) crystals. From sample 1279.9. G) TL image of intergrown quartz (Qtz), green mica, and Ru. The green mica is opaque in parts of this image because of the presence of dense masses of Ru crystals. From sample 1343.9. H) RL image of CPy_2-filled fractures in Py2 crystals. The fracture-filling CPy2 contains abundant inclusions of Gl. From sample 1279.9. I) RL image of intergrown Mo2 and CPy2 filling a fracture in quartz. From sample1201.1. J) RL image of CPy2 with rims of Bn adjacent to Hem crystals and enclosed in. From sample 1086.6. K) RL image of a mass of fine-grained Ru rimed by Hem at extinction. From sample 1078.78. L) Host rock fragments in an A vein from sample 1078.78. For figure abbreviations see Table 4. RL=reflected light, TL=Transmitted light

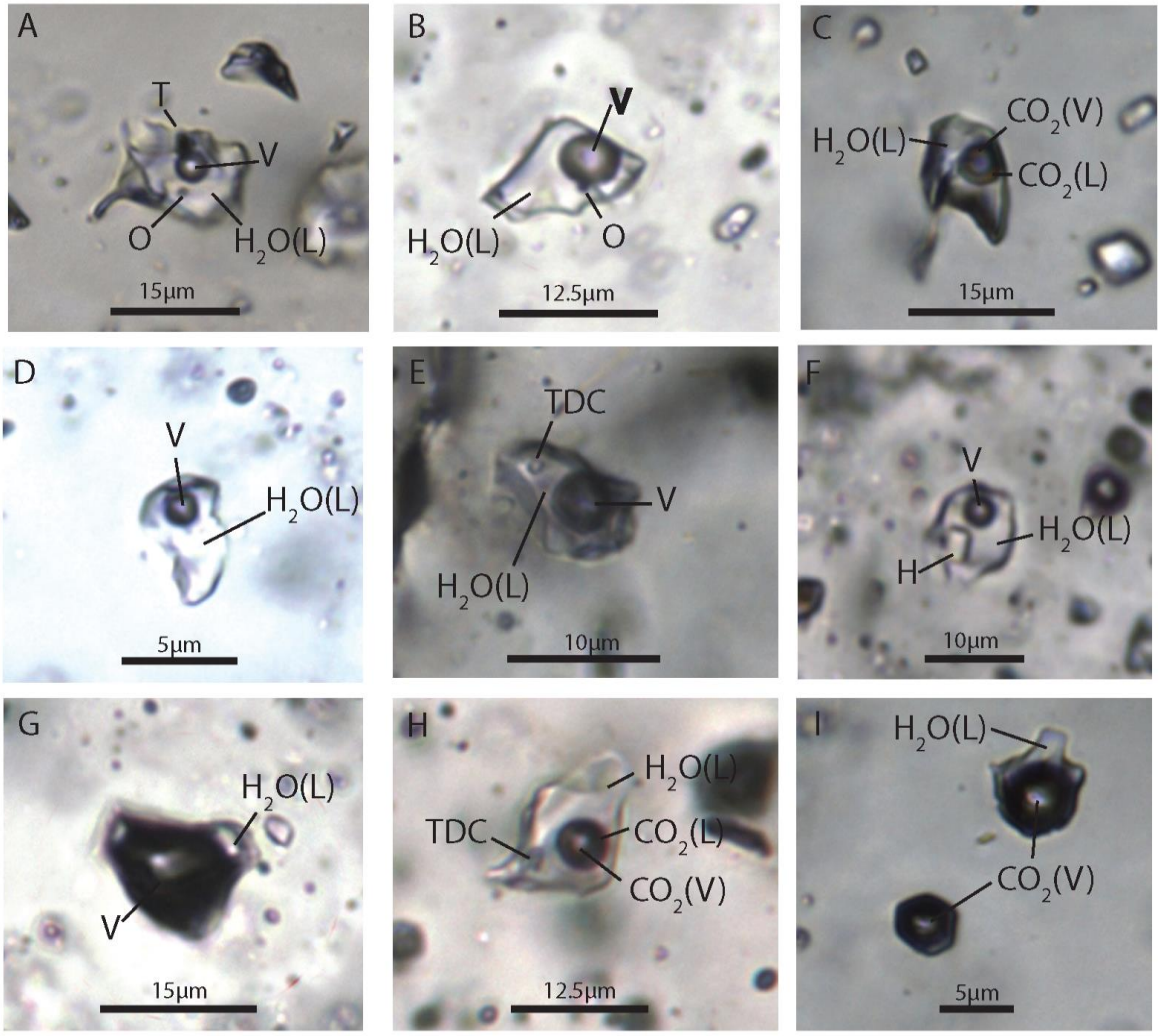

Figure 18. Photomicrographs of individual fluid inclusions from the nine inclusion groups found in the Kabba hanging wall and footwall. Abbreviations on micrograph labels are as follows: V=vapor, L=liquid, TDC=translucent daughter crystal, H=halite, T=triangular opaque daughter crystal, and O=oval opaque daughter crystal. Variation in the brightness and color between photomicrographs are due to the depth of the imaged inclusions from the surface of the thick sections that host them, and the level of magnification needed to resolve clear images. A) B15D inclusion in CL-bright quartz. B) B30 inclusion in CL-bright quartz. C) B15C inclusion in CL-dark quartz. D) B15 inclusion in CL-bright quartz. E) B30D inclusion in CL-bright quartz. F) B30H inclusion in CL-bright quartz. G) B75 inclusion in CL-bright quartz. H) B20C inclusion in CL-dark quartz. I) B75C inclusion in CL-dark quartz.

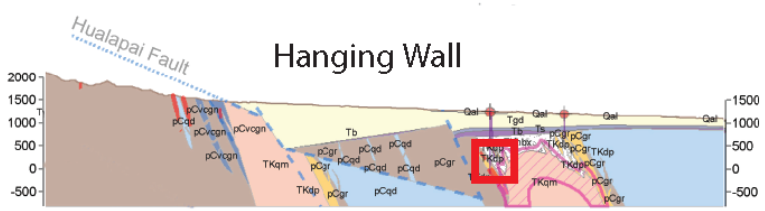

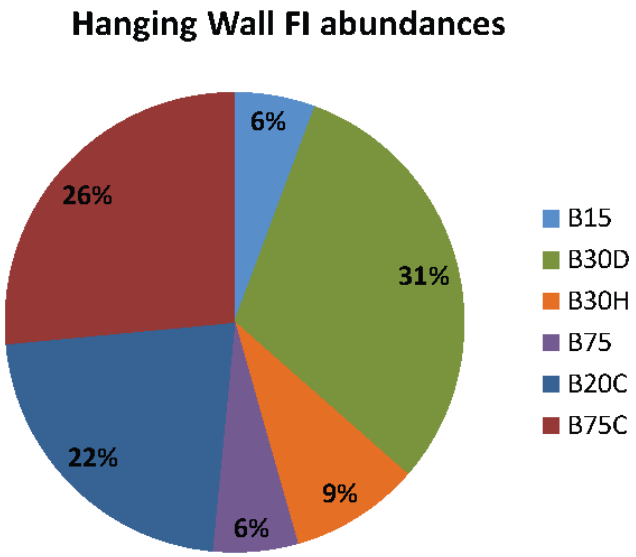

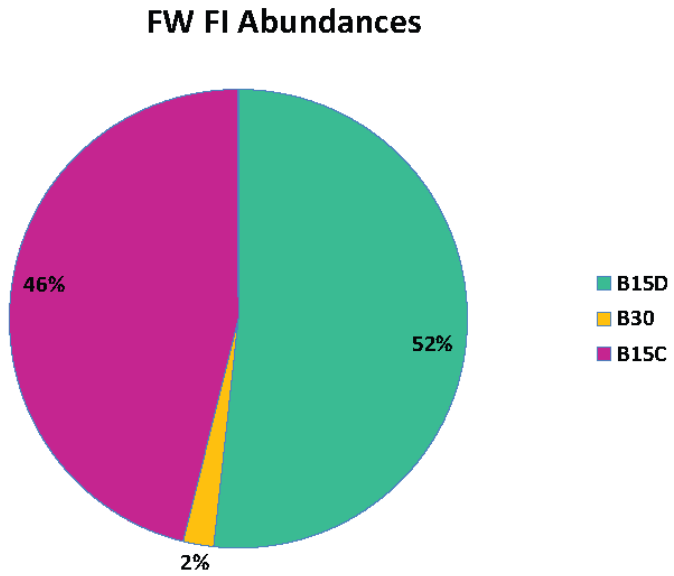

Figure 19. Abundance of fluid inclusion (FI) types in the hanging wall and footwall. The hanging wall fluid inclusion abundance pie chart corresponds to the cross-section in the upper left-hand corner and the footwall fluid inclusion abundance pie chart corresponds to the cross-section in the lower right hand corner. The red boxes on each cross-section denote the approximate areas sampled from the footwall and hanging wall and the pie charts represent the approximate abundance of fluid inclusion types in samples from those areas.

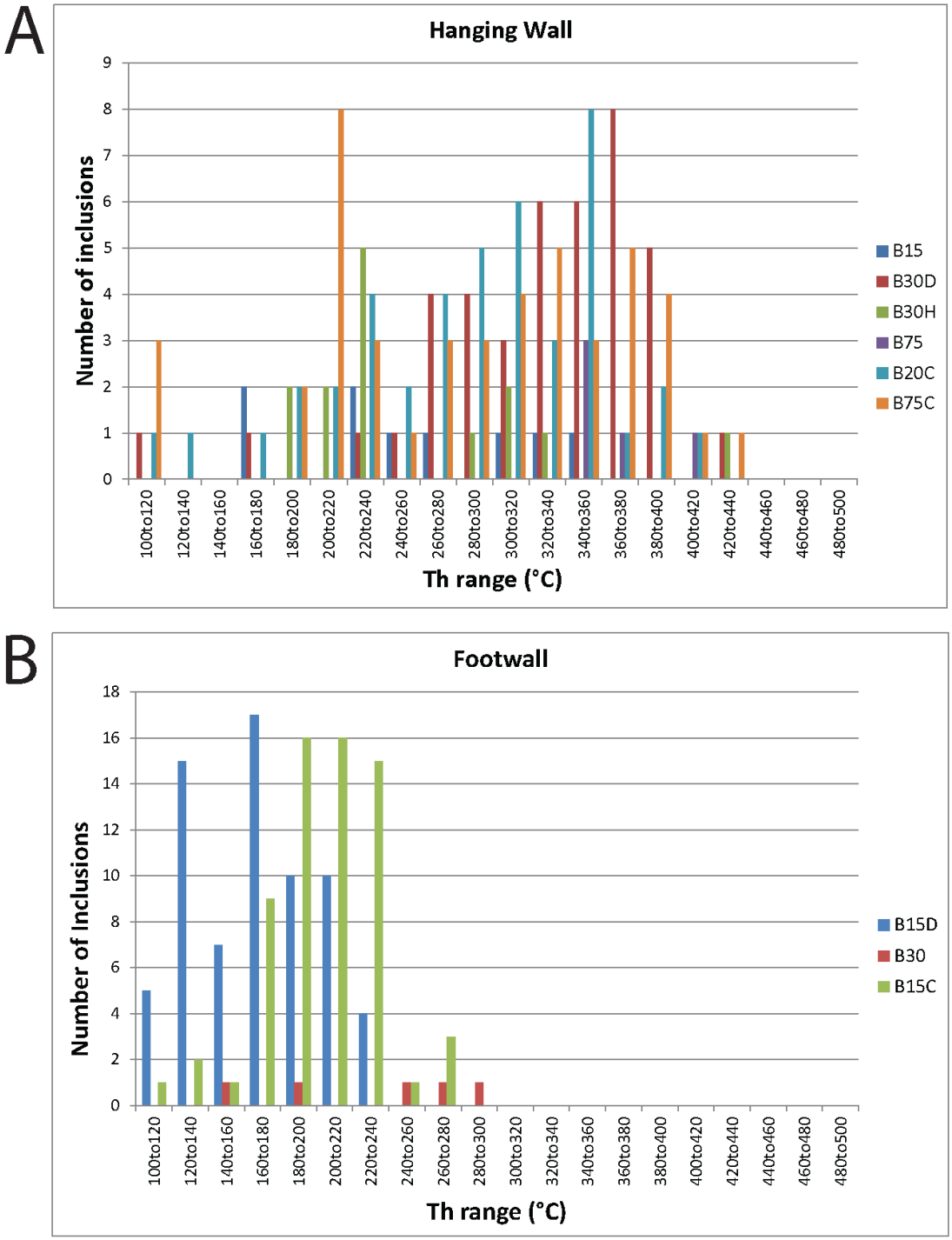

Figure 20. Bar charts showing range in homogenization temperatures for hanging wall and footwall groups. A) Range in final L-V homogenization temperatures for the inclusion groups in the hanging wall. B) Range in final L-V homogenization temperatures for the inclusion groups in the footwall. For inclusions that homogenized to vapor, B75 and B75C, the upper end of each range is a minimum homogenization temperature.

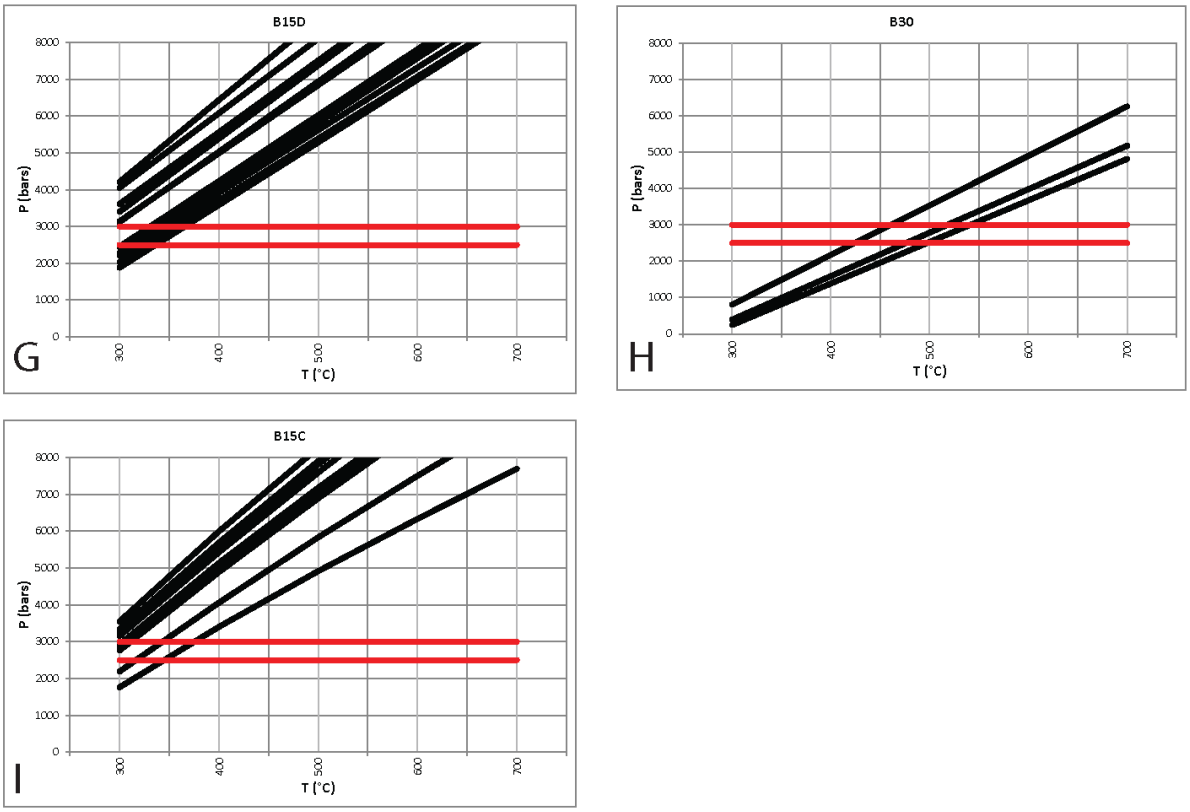

Figure 21. Isochors for B15D, B30, and B15C inclusions from the footwall. Isochors for B15D (G), B30 (H), and B15C (I) inclusions generated using the MacFlincor program (Brown, 1989; Brown and Hagemann, 1994). MacFlincor calculations for H_2O-, NaCl-, and KCl-bearing inclusions are based on data from Bodnar and Vityk (1994). Calculations for CO_2-bearing inclusions are based on thermodynamic data from Bowers and Helgeson (1983). Pressures in the footwall (red horizontal lines at 2500 and 3000 bars) were interpreted based on analogous pressure-depth conditions at the Butte porphyry copper deposit (Rusk et al., 2008). Intersections of pressure with inclusion isochors identify the upper and lower limits of trapping temperatures for each inclusion isochor. The equations of state used to generate isochors are only valid above 300°C, thus, isochors terminate at 300°C.

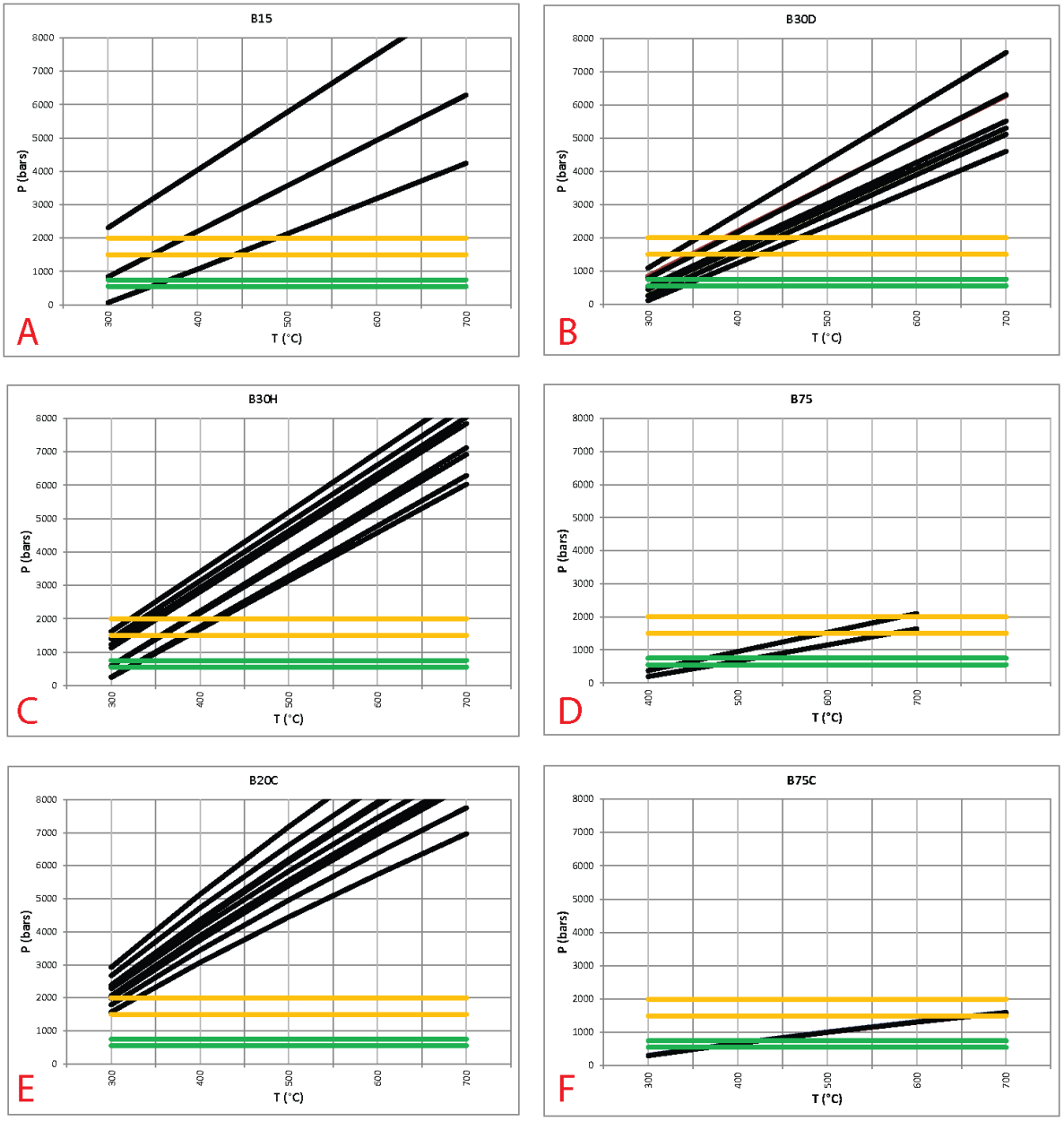

Figure 22. Isochors for B15, B30D, B30H, B75, B20C, and B75C inclusions from the hanging wall. Isochors for B15 (A), B30D (B), B30H (C), B75 (D), B20C (E), and B75C (F) inclusions were generated using the MacFlincor program (Brown, 1989; Brown and Hagemann, 1994). The yellow lines on each chart show the upper and lower limits for trapping temperatures along isochors at lithostatic pressures between 1500-2000 bars. The green lines on each chart show the upper and lower limits for trapping temperatures along isochors at hydrostatic pressures between 550-750 bars. The equations of state used to generate ischors are only valid above 300°C, thus, isochors terminate at 300°C.

APPENDIX A

HANGING WALL SAMPLES AND ANALYSIS

The following shows the samples collected from the K-10 drill hole and the analysis preformed on each sample. Sample IDs correspond to the depth in the K-10 drill hole which they were collected from (1201.1= collected at 1201.1 ft depth in the K-10 drill hole). Y= Yes, N= No.

Hanging wall Smaples	Thick Section	SEM-EDS	SEM-CL	Microthermometry	Raman	LA-ICP-MS	Northing	Easting	UTM Zone
1005.34	N	N	N	N	N	N	3890987.708	249594.823	12
1011.65	N	N	N	N	N	N	3890987.708	249594.823	12
1012.30	N	N	N	N	N	N	3890987.708	249594.823	12
1013.00	N	N	N	N	N	N	3890987.708	249594.823	12
1023.10	N	N	N	N	N	N	3890987.708	249594.823	12
1023.81	N	N	N	N	N	N	3890987.708	249594.823	12
1030.08	N	N	N	N	N	N	3890987.708	249594.823	12
1034.30	N	N	N	N	N	N	3890987.708	249594.823	12
1036.10	N	N	N	N	N	N	3890987.708	249594.823	12
1038.30	N	N	N	N	N	N	3890987.708	249594.823	12
1042.90	N	N	N	N	N	N	3890987.708	249594.823	12
1050.10	N	N	N	N	N	N	3890987.708	249594.823	12
1050.15	N	N	N	N	N	N	3890987.708	249594.823	12
1055.50	N	N	N	N	N	N	3890987.708	249594.823	12
1058.90	N	N	N	N	N	N	3890987.708	249594.823	12
1063.80	N	N	N	N	N	N	3890987.708	249594.823	12
1073.70	N	N	N	N	N	N	3890987.708	249594.823	12
1078.75	Y	Y	Y	N	N	N	3890987.708	249594.823	12
1081.10	N	N	N	N	N	N	3890987.708	249594.823	12
1086.20	N	N	N	N	N	N	3890987.708	249594.823	12
1086.60	Y	Y	Y	Y	Y	Y	3890987.708	249594.823	12
1095.40	Y	N	N	N	N	N	3890987.708	249594.823	12
1097.40	N	N	N	N	N	N	3890987.708	249594.823	12
1098.90	N	N	N	N	N	N	3890987.708	249594.823	12
1107.10	N	N	N	N	N	N	3890987.708	249594.823	12
1108.20	N	N	N	N	N	N	3890987.708	249594.823	12
1109.60	N	N	N	N	N	N	3890987.708	249594.823	12
1117.00	N	N	N	N	N	N	3890987.708	249594.823	12
1121.20	N	N	N	N	N	N	3890987.708	249594.823	12
1123.90	Y	N	N	N	N	N	3890987.708	249594.823	12
1125.60	N	N	N	N	N	N	3890987.708	249594.823	12
1132.30	N	N	N	N	N	N	3890987.708	249594.823	12
1148.80	Y	N	Y	N	N	N	3890987.708	249594.823	12
1152.10	N	N	N	N	N	N	3890987.708	249594.823	12
1176.80	N	N	N	N	N	N	3890987.708	249594.823	12
1181.00	N	N	N	N	N	N	3890987.708	249594.823	12
1181.50	N	N	N	N	N	N	3890987.708	249594.823	12
1181.60	N	N	N	N	N	N	3890987.708	249594.823	12
1185.50	N	N	N	N	N	N	3890987.708	249594.823	12
1189.00	N	N	N	N	N	N	3890987.708	249594.823	12
1189.60	N	N	N	N	N	N	3890987.708	249594.823	12
1193.00	Y	N	Y	Y	Y	Y	3890987.708	249594.823	12
1196.10	N	N	N	N	N	N	3890987.708	249594.823	12
1200.40	Y	N	Y	N	N	N	3890987.708	249594.823	12
1201.10	Y	Y	Y	Y	Y	Y	3890987.708	249594.823	12
1201.20	N	N	N	N	N	N	3890987.708	249594.823	12
1205.80	N	N	N	N	N	N	3890987.708	249594.823	12
1206.80	Y	N	N	N	N	N	3890987.708	249594.823	12
1219.10	N	N	N	N	N	N	3890987.708	249594.823	12
1227.40	N	N	N	N	N	N	3890987.708	249594.823	12
1228.10	N	N	N	N	N	N	3890987.708	249594.823	12
1234.10	Y	N	N	N	N	N	3890987.708	249594.823	12
1237.60	N	N	N	N	N	N	3890987.708	249594.823	12
1274.90	N	N	N	N	N	N	3890987.708	249594.823	12
1277.30	N	N	N	N	N	N	3890987.708	249594.823	12
1279.90	Y	Y	Y	N	N	N	3890987.708	249594.823	12
1286.00	N	N	N	N	N	N	3890987.708	249594.823	12
1297.00	N	N	N	N	N	N	3890987.708	249594.823	12
1298.10	N	N	N	N	N	N	3890987.708	249594.823	12
1314.20	N	N	N	N	N	N	3890987.708	249594.823	12
1322.50	N	N	N	N	N	N	3890987.708	249594.823	12
1327.70	N	N	N	N	N	N	3890987.708	249594.823	12
1329.50	Y	N	N	N	N	N	3890987.708	249594.823	12
1331.50	Y	N	N	N	N	N	3890987.708	249594.823	12
1340.20	Y	Y	Y	N	N	N	3890987.708	249594.823	12
1343.90	Y	Y	Y	Y	Y	Y	3890987.708	249594.823	12

APPENDIX B

FOOTWALL SAMPLES AND ANALYSIS

The following shows the samples collected from the Kabba footwall and the analysis preformed on each sample. Sample IDs correspond to the locations marked in Figure 12 B-E (KF3D-1=sample #1 from location KF3D). Y=Yes, N=No.

Footwall Samples	Thick Section	SEM-EDS	SEM-CL	Microthermometry	Raman	LA-ICP-MS	Northing	Easting	UTM Zone
KF4F-1	N	N	N	N	N	N	3889210.599	243844.815	12
KF4F-2	Y	N	Y	N	N	N	3889210.599	243844.815	12
KF4G-1	N	N	N	N	N	N	3889210.599	243844.815	12
KF5A-1	N	N	N	N	N	N	3887984.709	241784.827	12
KF5B-1	N	N	N	N	N	N	3887984.709	241784.827	12
KF5C-1	Y	N	Y	N	N	N	3887984.709	241784.827	12
KF5C-2	N	N	N	N	N	N	3887984.709	241784.827	12
KF5C-3	N	N	N	N	N	N	3887984.709	241784.827	12
KF5D-1	N	N	N	N	N	N	3887984.709	241784.827	12
KF5E-1	N	N	N	N	N	N	3887984.709	241784.827	12
KF5E-2	Y	N	N	N	N	N	3887984.709	241784.827	12
KF5F-1	N	N	N	N	N	N	3887984.709	241784.827	12
KF5F-2	N	N	N	N	N	N	3887984.709	241784.827	12
KF5F-3	N	N	N	N	N	N	3887984.709	241784.827	12
KF5F-4	N	N	N	N	N	N	3887984.709	241784.827	12
KF5G-1	N	N	N	N	N	N	3887984.709	241784.827	12
KF5G-2	N	N	N	N	N	N	3887984.709	241784.827	12
KF5H-1	N	N	N	N	N	N	3887984.709	241784.827	12
KF5I-1	Y	N	N	N	N	N	3888328.624	242396.492	12
KF5J-1	N	N	N	N	N	N	3888328.624	242396.492	12
KF5J	N	N	N	N	N	N	3888328.624	242396.492	12
KF5K	N	N	N	N	N	N	3888328.624	242396.492	12
KF5L	N	N	N	N	N	N	3891157.378	242582.800	12
KF6A	N	N	N	N	N	N	3891157.378	242582.800	12
KF6B	N	N	N	N	N	N	3891974.222	243508.156	12
KF6C-1	N	N	N	N	N	N	3889015.063	247283.645	12
KF6C-2	N	N	N	N	N	N	3889015.063	247283.645	12
KF6C-3	N	N	N	N	N	N	3889015.063	247283.645	12
KF6C-4	Y	N	N	N	N	N	3889015.063	247283.645	12

APPENDIX C

HANGING WALL HAND SAMPLE DESCRIPTIONS

General descriptions of drill core samples from drill hole K-10 from the Kabba hanging wall. All core samples from drill hole K-10 contain igneous host rocks and quartz +/- sulfide veins. Short descriptions of K-10 core samples were produced prior to thick section preparation in order to document ore and alteration mineralogy, textures, or crosscutting relationships related to the Kabba hydrothermal system prior to petrographic examination with transmitted and reflected light.

Sample ID	Description
1078.78	Host Rock: 70% subhedral pink potassium feldspar, 20% clear anhedral quartz, 10% black subhedral biotite. Individual potassium feldspar crystals have very clear exsolution lamellae. Individual quartz crystals have a weak alignment with one another. Masses of biotite crystals also show an alignment and yellow specs of leucoxene and green chlorite appears to form around the margins of the biotite masses. Veins: A variety of veins cut the host rock in this sample. Most veins in this sample are >1cm wide (1mm wide) and dominated by sulfides, mostly pyrite, and minor quartz. Veins have two dominant orientations that are roughly at a 60-120 angle to one another. The largest vein is composed of quartz and has a sulfide-filled (possibly pyrite and sphalerite) centerline, and an alteration selvedge composed of green mica.
1086.6	Host rock: 10-15%subhedral potassium feldspar; 40-45% sudhedral plagioclase; 20-30% subhdral-anhedral quartz; 2-5% subhedral-euhedral biotite. Much of the feldspar in this sample is altering from a white or pink color to tan-green color. This alteration increases in intensity with proximity to the quartz vein. Vein: Sinuous quartz veins with 2-5% disseminated soft, grey, euhedral sulfide metallic, crystals (Molybdenum or Galena?) and 2-5% euhedral pyrite.
1095.4	Host rock: Tan brown porphyry with 20%subhedral-anhedral, tan-white plagioclase; 2%sub-anhedral black bitotite; and 2-5% anhedral, clear quartz phenocrysts; with a brown-gray, very fine grained, quartz and feldspar rich groundmass. Veins: A large mass of quartz and multiple clear quartz veins. The veins are all parallel to one another, are mostly clear quartz. The largest vein in this sample has sinuous margins and a vugy centerline that contains a soft, pink, powdery mineral. The large quartz mass has a half football shape and is composed of alternating zones of clear quartz and plagioclase rich porphyry. The margins of the mass have an odd, coliform-like texture.
1123.9	Host Rock: Very altered tan-brown to dark brown porphyry with 20% subhedral-euhedral, tan-white to tan-pink plagioclase; 2%euhedral yellow-brown tabular amphiboles; 2% subhedral-anhedral black bitotite; and 2-5% anhedral quartz phenocrysts; with a dark green-brown, very fine grained, quartz-feldspar-phylosilicate rich

	groundmass. Veins and Alteration: Several 1-5mm quartz veins cut this sample and are parallel to one another. The largest vein (5 mm wide) is composed of clear quartz and has a pyrite filled centerline. All of the veins have selvedges of tan-green, soft, micas around their vein margins. This alteration is most intense closest to the outer margin to the veins and is characterized by abundant tan-green, soft, micas replacing parts of the host rock's ground mass and the phenocrysts.
1148.8	Host Rock: Pyrite rich porphyry with 30% subhedral, light greenish brown, plagioclase phenocrysts; and 5%anhedral, brown quartz phenocrysts; in a fine-grained, plagioclase and quartz rich ground mass. The porphyry host also rock contains ~5% disseminated, oxidized, fine grained pyrite. Veins and Alteration: Multiple sinuous quartz veins with moderated amounts of anhedral-euhedral grey and yellow sulfide crystals cut this sample. The veins all have alteration selvedges which are characterized by host rock plagioclase phenocrysts altering to soft, green-brown, powdery minerals.
1193	Host Rock: Greenish-white phaneritic granodiorite with 40-50% greenish-white, subhedral plagioclase; 30%gray, anhedral quartz; 5-10% black, euhedral amphibole; and 5-10% black, euhedral biotite. Veins and Alteration: This sample contains a single ~10mm wide quartz + sulfide vein. Sulfides hosted in the quartz vein occur at the vein margins and do not form a centerline. This vein also has an alteration selvedge composed of green mica which extends ~ 5mm from the vein's outer margins. Closest to the veins margin the igneous textures of the host rock are absent and most of the host rock plagioclase has been replaced by green mica.
1201.1	Host Rock: Greenish-white phaneritic granodiorite with 40-50% greenish-white, subhedral, coarse grained plagioclase; 30% gray, anhedral, coarse grained quartz; 5-10% black, euhedral, amphibole; and 5-10% black, euhedral biotite. The host rock also contains minor amounts of very fine disseminated pyrite and fine-grained accumulations of bright yellow-green, soft, powdery mineral. Veins and Alteration: Multiple quartz veins which range in size between 2-9 mm wide cut this sample. Most are only 1-2 mm across and are easily identified by the pink alteration seledvege around their margins and the very fine, darkly colored sulfides

	along their inner and outer margins. The largest quartz vein is 9 mm wide, has a pink alteration selvedge which extend ~1cm from the vein margin, contains euhedral-anhedral pyrite, and minor amounts of a soft grey metallic mineral (molybdenite / galena?) which forms euhedral crystals that range in size between 1-2mm. The typical width of the pink alteration selvedges around the veins in this sample is between 0.5-1cm and is interpreted to be potassic alteration. Potassic alteration appears to be attacking the margins of most plagioclase phenocrysts in this sample, and proximal to veins (0.1-1cm) potassic alteration becomes much more pervasive, forming a distinct pink selvedge where plagiocalse phenocrysts appear almost completely replaced by potassium-feldspar.
1206.8	Host Rock: Greenish-white phaneritic granodiorite with 40-50% greenish-white, subhedral, coarse grained plagioclase; 30% gray, anhedral, coarse grained quartz ; 5-10% black, euhedral amphibole; and 5-10% black, euhedral, medium grained biotite. Most of this sample is dominated by phenocryst and has very little fine grained ground mass. This sample also contains minor amounts of very fine disseminated pyrite. Veins and Alteration: Multiple quartz veins, which range in size from 0.5-2 cm wide, cut this sample. All of the veins are parallel to on another, have sinuous margins, and hosts minor amounts of euhedral-anhedral pyrite and a soft grey metallic mineral. The veins in this sample have pink alteration selvedges which range in thickness between 2-8mm. This alteration is interpreted to be potassic alteration and is characterized by host rock plagioclase phenocrysts alteration to potassium feldspar.
1200.4	Host Rock: Greenish-white phaneritic granodiorite with 40-50% greenish-white, subhedral, coarse grained plagioclase; 30% gray, anhedral, coarse grained quartz ; 5-10%, black, euhedral, amphibole; and 5-10%black, euhedral, medium grained biotite. Disseminate pyrite is very spars in this sample Veins and Alteration: Multiple quartz veins, which range in thickness between .5-1 cm, cut this sample. All of the veins have roughly about the same orientation to one another and have straight edges. The biggest vein (~1cm wide) hosts large masses (>0.7cm wide) of euhedral-anhedral pyrite and a soft grey metallic mineral (molybdenum/galena?). These masses occur on the inner margins of the quartz vein at the vein-host rock interface. The veins in this sample have tan-pink alteration selvedges which range in thickness between 2-8mm. This alteration is characterized by host rock plagioclase phenocrysts alteration to potassium feldspar or a soft, tan mineral.
1279.9	Host Rocks:

	Intensely altered dark green-gray phaneritic granodirote/quartz monzonite with ~20% green-black, anhedral-subhedral, coarse grained biotites; ~50% green-gray, subhedral, coarse grained plagioclase; ~5% green-black, anhedral-subhedral, amphiboles; and ~20% gray-green, coarse grained, anhedral quartz. Very fine disseminated pyrite occurs throughout and increases in abundance closer to the quartz vein that cross-cuts this sample. Veins and Alteration: A single quartz vein, which is ~1 cm wide, cuts this sample and hosts accumulations of white, amorphous carbonate, coarse euhedral pyrite, coarse subhedral-euhedral chalcopyrite, and minor amounts of very fine-grained molybdenum. Carbonate only occurs along the inner margins of the quartz veins but the sulfides occur on both sides of the vein-host rock interface. Sulfide abundances are highest right at the vein host-rock interface. Green mica and soft brown-tan alteration minerals pervade this sample and form a selvedge around the margins of the vein. This alteration is most intense proximal to the veins margins and where it is most well developed the original textures of the igneous host is obscured.
1343.9	Host rock: Altered dark green-gray phaneritic granodirote/quartz monzonite with ~30% green-black, anhedral-subhedral, coarse grained biotites; ~40-50% green-gray, subhedral, coarse grained plagioclase; ~5% green-black, anhedral-subhedral, amphiboles; and ~20% gray-green, coarse grained, anhedral quartz. Very fine, disseminated pyrite throughout. Veins and Alteration: Multiple veins cut this sample and range in size from 5-10 mm. The biggest vein (~1cm wide) has a center line filled with block anhedral-euhedral pyrite, and minor amounts of very fine-grained carbonate. Alteration in this sample is characterized by plagioclase phenocrysts and groundmass being replaced by green micas. The intensity of this alteration increases abruptly proximally to quartz veins and tends to form a distinct, green, selvedge that extends <1cm out from the vein-host rock interface and obscures the igneous textures of the host.
1234.1	Host rock: Intensely altered porphyry with 50% tan-white, coarse grained, anhedral plagioclase; and 20-25% gray, anhedral quartz phenocrysts; and a quartz and plagioclase-rich, fine-grained groundmass. The host rock's original texture and mineralogy has been destroyed by alteration and much of the plagioclase in this rock has been replaced by tan clay minerals (koalinite, sericite, illite, and swelling clays/). Veins and Alteration: A single banded quartz vein cuts this sample. The outer most band is 1.2 cm think, is composed of quartz, and has minor amounts of very fine grained pyrite

	and a very fine-grained gray, soft, metallic mineral (molybdenite/galena ?) on its upper and lower inner margins. The inner band is ~4 cm wide and composed mostly of quartz with abundant white carbonate along its inner margins. The inner band also has a distinct center line composed of multiple anhedral-euhedral, coarse grained sulfides.
1329.5	Host Rock: Altered dark green-gray phaneritic granodirote/quartz monzonite with ~30% green-black, anhedral-subhedral, biotites; ~40-50% green-gray, subhedral, plagioclase; ~5% green-black, anhedral-subhedral, amphiboles; and ~20% gray-green, anhedral quartz. Very fine-medium grained, pyrite disseminated throughout. Veins and Alteration: The vein in this sample as composed of granular quartz and multiple euhedral-anhedral , fine-coarse grained sulfides (~5-10%). The outer boundary of this veins is sinuous, and appears to be "eating away" the host rock. Minor amounts of alteration are associated with the vein and are characterized by plagioclase phenocrysts in the host rock altering to fine clay-like minerals.
1331.5	Host Rock: Altered dark green-gray phaneritic granodirote/quartz monzonite with ~30% green-black, anhedral-subhedral, biotites; ~40-50% green-gray, subhedral, plagioclase; ~5%green-black, anhedral-subhedral, amphiboles; and ~20% gray-green, coarse grained, anhedral quartz. Host rock also contains ~2-3% disseminated pyrite throughout. Veins and Alteration: A single ~1.5cm wide quartz vein with poorly defined sinuous boundaries cuts this sample. This vein hosts multiple euhedral-anhedral , fine-coarse grained yellow and grey sulfides (Pyrite ~4% > molybdenum/galena? ~3-2%) and minor amounts of bright white carbonate. Sulfides mostly occur within the vein but do also occur disseminated in the host rock. In addition, multiple veinlets can be seen cross-cutting one another in this sample and are identified by the presence of coarse sulfides and the faint green alteration halo that surrounds them. Alteration in this sample does not form a selvedge and is characterized by host rock plagioclase altering to a soft, clay-like mineral.
1340.2	Host Rock: Altered dark green-gray phaneritic granodirote/quartz monzonite with ~30% green-black, anhedral-subhedral, coarse grained biotites; ~40-50% green-gray, subhedral, plagioclase; ~0-2% green-black, anhedral-subhedral, amphiboles; and ~20% gray-green, anhedral quartz. The host rock also includes ~2-3% pyrite disseminated throughout. Veins and Alteration:

	A ~5cm wide vein cuts this sample and is composed quartz and ~1-2% euhedral-anhedral pyrite and a soft, gray, metallic mineral (molybdenum/galena?) which occurs along its inner margins. Small (<2mm wide) veinlets also occur throughout this sample, and can contain a variety of minerals including sulfides and a very fine grained, soft, powdery mineral. Around the veins margins there is a 2-4mm wide alteration selvedge composed of green mica. This alteration selvedge is most well developed proximal to the vein and obscures the original texture of the host rock. A bright yellow-green, soft, fine grained mineral (jerosite?) also occurs within the mica selvedge and appears to form a irregular halo in the host rock surrounding the vein. This mineral also fills a ~1mm wide veinlet that comes off the large quartz vein.

APPENDIX D

FOOTWALL HAND SAMPLE DESCRIPTIONS

General descriptions of drill core samples from surface outcrops in the Kabba footwall. All surface samples from the footwall contain igneous host rocks and quartz +/- sulfide veins. Short descriptions of surface sample from the footwall that follow were produced prior to petrographic examination with transmitted and reflected light in order to document ore and alteration mineralogy, textures, or crosscutting relationships related to the Kabba hydrothermal system prior.

Sample #	Description
KF1-11	Sample from a fresh looking pile near a prospect pit. In area with abundant veining, neoticite, and chrisicola coming out of water seeps. Host Rock: ~45% white to greenish white, euhedral to subhedral, <15 mm wide plagioclase phenocrysts; ~45% clear, subhedral to anhedral, <6 mm wide quartz phenocrysts; ~8%, black to greenish black, subhedral, <2 mm phyllosilicate phenocrysts. Many of the plagioclase pheonocrysts are turning green and have a powdery look to them. Near the two largest veins in the sample the plagioclase crystals are turning pink and possibly altering to potassium feldspar. The host rock seems to have small amounts (1-2%) of magnetite and coarse tan phyllosilicates disseminated throughout, especially between grain boundaries. These minerals are most abundant where small, subtly apparent veins cut through the sample, and are not present where the plagioclase are altered to potassium feldspar. Veins and Alteration: This sample contains 2 quartz veins with significant amounts (~ 5% of the entire vein) of molybdenum. The older of the two veins is in the bottom corner of the sample, composed mostly of quartz, has a sinuous and poorly defined outer boundary, and is cross-cut by the younger quartz. The older vein also has molybdenum along its outer margins and has a pink alteration selvedge which host rock plagioclase are altering to potassium feldspar. The younger vein cuts across the front of this sample and is composed mostly of quartz with minor molybdenite, has sinuous boundaries outer boundaries, and crosscuts the older vein. Like the older vein, the younger vein has molybdenum along the inside of its outer boundary and a bright pink alteration selvedge. This sample has at least two veins which contain quartz, magnetite, and coarse mica. Though they occur at a similar angle to the quartz + molybdenite veins they are not as visually apparent and are defined by dark accumulations of coarse tan phyllosilicates (muscovite) +/- magnetite that occur along/within a vein of quartz. Most of the magnetite that is associated with these veins occurs in the host rock near the veins so the veins themselves are only weakly magnetic. These magnetite-bearing veins do not have well developed halos but host masses of coarse mica similar to the coarse phyllosilicates that occur along crystal boundaries between phenocrysts in the host rock. The phyllosilicate masses in the host rock seem to be most abundant adjacent to veins of either type.
KF2-6	Sample from prospect pit up the wash from the KF1-11 Host Rock: The original textures of this rock have been completely obliterated by alteration and the rock is now composed mostly of fine to coarse, anhedral quartz crystals (~60-70%), fine grained, subhedral to anhedral, red-brown to gray-green, weathered phyllosilicates (~20-30%), and minor amounts of disseminated

	sulfides and oxides (mostly pyrite and magnetite). In spots primary plagioclase can be seen altering from white to a red-brown color and turning into a powdery mineral. On cut surfaces one can see that some of the quartz in the host rock was once anhedral phenocrysts. The abundance of this secondary quartz increases sharply close to the outer margin of the veins which cut the host rock. Veins and Alteration: The largest in the sample has sinuous boundaries, is ~4cm wide and is composed mostly of white, granular looking quartz with small masses of dark fine grained magnetite and euhedral pyrite disseminated throughout. This vein also contains trace amounts of a soft grey mineral that is commonly associated with coarse phyllosilicates. Around the veins margins, fine to medium grained phyllosilicates are very abundant and the amount of disseminated pyrite in the host rock increases with proximity to the vein. Other veins in this sample are typically composed of ~50% anhedral quartz, ~25% euhedral to subhedral pyrite, and ~25% anhedral magnetite. Where quartz dominates in these samples pyrite and magnetite are almost absent, and vice versa. Where the sulfides and oxides dominate, magnetite lines the outside of the vein and pyrite forms a blocky centerline. All the veins in this sample typically have an alteration selvedge which is characterized by coarse phyllosilicates replacing host rock phenocrysts and groundmass. This selvedge commonly obscures the host rock textures and the host fine grained disseminated pyrite.
KF3A-6	Sample from the standard mine Host Rock: The original texture of this host rock has been completely obliterated by alteration, especially with in 2cm of the vein's outer margin where the alteration selvedge is most intense. Where some original textures are still visible, the host rock is composed of ~50-70% anhedral, fine to coarse grained feldspars that are turning green or pink, and ~20-30% anhedral, coarse grained quartz crystals. The remaining 10-20% of the rock is composed of disseminated coarse, gray phyllosilicates (muscovite), the amount of which increases with proximity to the alteration selvedge. Veins and Alteration: This sample contains two white, parallel quartz veins that have sinuous, poorly defined boundaries. Both of these veins are associated with a 2cm wide, well developed green-brown alteration selvedge that destroys the original rock texture. These alteration selvedges are composed mostly of coarse, euhedral, grey-brown phyllosilicates (muscovite); gray, anhedral, quartz; and fine grained, disseminated masses of dark brown-black, magnetic magnetite;, and the intensity of the alteration increases with proximity to their associated veins.
KF3A-5	Sample of Standard Mine host rock from nearby the northern shaft.

	Host Rock: The host rock is composed of anhedral, bright pink potassium feldspar (~80%), and anhedral quartz (~15%)phenocrysts in a fine-grained feldspathic ground mass. Veins and Alteration: This sample is cut by multiple generations of quartz veins. Most of the veins are composed entirely of quartz, have sinuous, poorly defined boundaries, and clearly crosscut a second generation of thin quartz + mica veins. The quartz + mica veins are dominated by soft, gray, coarse, mica (muscovite), and are generally thin (<3mm) with sinuous boundaries. Alteration is most well developed around the quartz + mica veins and is characterized by a yellow-brown alteration selvedge that extends <3mm from the outer boundary of the quartz + mica veins. These selvedges are composed mostly of brown to yellow brown, fuzzy looking muscovite.
KF3D-19	Sample from the south mine shaft of the Standard Mine Host Rock: This rock is composed of ~50%, white to greenish-white, subhedral to euhedral, <5mm plagioclase phenocrysts; ~40%, gray, anhedral to euhedral, <6mm quartz crystals; and ~10% black to greenish black subhedral to euhedral biotites. There are also minor amounts of subhedral to anhedral pyrite and magnetite disseminated throughout the host rock and the abundance of these minerals increases with proximity to the vein. Veins and Alteration: Half of this sample contains a large quartz vein with a sinuous, poorly defined boundary. The vein contains abundant bands or elongate masses of fine-grained, anhedral, black to reddish black, magnetite; and blocky, coarse grained pyrite. These bands of magnetite and pyrite are parallel to the veins outer boundary. No well-defined selvedge exists around the vein . However, many of the plagioclase phenocrysts in the sample are altering to a soft powdery mineral.
KF4B-6	Host rock from pile next to prospect pit. Host Rock: The host rock is composed of ~ 40-45% anhedral, white to white-gray, quartz phenocrysts; ~40-45%, subhedral to anhedral white to greenish white, plagioclase phenocrysts; ~5-10%, euhedral to subhedral, black to greenish black, soft, mica (biotite?) phenocrysts; ~2-3%, euhedral to subhedral, disseminated pyrite. Many of the plagioclase phenocrysts in this sample are green around their margins, and the greener phenocrysts tend to be softer. Host rock textures ~1-2cm from the veins have been completely obliterated by alteration.

	Veins and Alteration: This sample is cut by a grey quartz-pyrite veins that has a 1-3cm thick alteration selvedge. The vein itself is mostly grey quartz with small intervals of pyrite along its long axis and many parts of this vein are magnetic . Also in some parts of the vein there are ~1-2mm wide vugs with some euhedral open space filling crystals in them. The alteration selvedge around this vein completely destroys the textures of the host rock and is characterized by the replacement of host rock ground mass and phenocrysts with fine grained, gray to brownish gray phyllosilicates (muscovite?). The selvedge is also rich in disseminated sulfides and has a faint outer margin that is defined by plagioclase phenocrysts going from white to green.
KF4B-5	Ore rock from pile next to prospect pit where AK found the javelina skull Host Rock: The host rock contains ~45%, euhedra to subhedral, white to greenish white, plagioclase phenocrysts; ~45%, anhedral, white to grayish white, quartz phenocrysts; ~5-10%, euhedral to subhedral, black to greenish black, biotite phenocrysts; and ~1-2% disseminated sulfides. ~ 50% of the plagioclase in this sample is greenish white and has a soft, powdery texture. Veins and Alteration: This sample contains a sinuous quartz vein composed mostly of clear quartz and has a soft grey mineral (molybdenite) and a green oxidized mineral that was not identified along its margins. This vein has a faint alteration selvedge that extends out from the vein margin ~1-1.5cm and is composed of silica and muscovite that has replaces the host rock groundmass and phenocrysts. This sample also contains sinuous veins composed mostly of quartz with small intervals of blocky, euhedral pyrite. Where pyrite dominates, the vein is weakly magnetic. The vein also contains intervals of coarse, brown to red brown phyllosilicates and has a selvedge of course phyllosilicates.
KF3A-8	Sample from the north pit at the standard mine. Host Rock: The original texture of the host rock has been completely destroyed by alteration but based on residual crystal shape of replaced and nonreplaced minerals, the rock may have been originally composed mostly of plagioclase and quartz. The replaced plagioclase is only visible 2-3cm from the outer margin of the large vein that cuts this sample. Two minerals are replacing the plagioclase. One is fine-grained, medium hardeness, and pink. The other is green, very soft, and maintains the original shape and size of the plagioclase phenocrysts. Vein and Alteration: A 5cm wide quartz vein cuts this sample and contains large (~1cm wide), fine grained clumps of magnetite. The vein also contains clumps of soft, flakey,

	phyllosilicates. Along the top of the vein, immediately outside the vein's margin there is a band of very coarse, flakey phyllosilicates. Outside of this band, on both sides of the vein there is a 2-3cm think, green gray selvedge of silica and green phyllosilicates that have totally replaced the host rock. This selvedge also contains black, fine-grained accumulations of magnetite and some reddish, nonmagnetic clumps fe-oxide (hematite?). Further out from the vein the green gray halo fades into the zone of green and pink, altered plagioclase.
KF2-4	Massive, Vugy quartz vein from quarry west of the traverse parking lot No host rock is present in this sample. Vein and Alteration: This sample is from a ~1-2 m wide quartz vein and is much like the samples KF4F-2, KF4D-2, and KF4E-2. Other than fine-grained quartz, this sample is contains ~5-10% sulfides (molybdenum>pyrite>>chalcopyrite?), ~1-2% hematite and magnetite, and ~ 1-2% coarse grained mica. The accumulations of sulfides commonly line vugs in the quartz but can also occur within the quartz. On non-cut surfaces, HCl turns the staining on the outside of the rock bright yellow.
KF4F-2	Massive quartz vein from quarry west of KF4B No host rock is present in this sample. Vein: This sample is from a ~1-1.5 m wide quartz vein and is much like the samples KF2-4, KF4D-2/1, and KF4E-1. Other than fine-grained quartz, this sample contains ~10-15% blocky, euhedral pyrite. This pyrite occurs in masses of euhedral-anhedral crystals that have a random orientation or are sometimes elongate, and can be 2-3cm wide. Also, throughout the sample there are faint metallic gray "wisps" that are particularly abundant proximal to the accumulations of pyrite. This metallic gray mineral might be molybdenite. The vein quartz also has abundant small (<5mm) vugs that are commonly filled with euhedral pyrite and quartz. These vugs occur in the quartz and along the outer boundary of some of the pyrite crystals.
KF4E-1	Massive quartz with sulfides vein from a molybdenite prospect pit west of KF4D No host rock is present in this sample. Vein: This vein sample was collected from a molybdenite prospect pit that exposes a 1-2.5 m wide, vertical quartz vein that occurs between two different igneous rock types. This vein is very similar to the veins that samples KF2-4, KF4D-2/1, and KF4F-1 came from and is composed mostly of fine grained quartz (~75-80%) with ~10% coarse, euhedral-subhedral pyrite, and ~3-5% of a metallic blue-gray,

	wispy mineral that may be molybdenite. The pyrites and the blue-gray wisps occur together in clearly defined trails that are parallel to the outer boundary of the vein itself. Like sample KF4F-1, this sample has small (<5mm) vugs throughout that can host open space filling crystals. These vugs occur in quartz or along the outer boundary of the individual pyrite crystals. Some of the vugs that are associated with the pyrites may not be primary and were created by weathering.
KF4D-2	Massive quartz with sulfide vein from unmapped prospect pit east of KF4E and KF4C. No host rock is present in this sample. Veins: This vein was collected from a prospect pit that was not mapped by Vuich 1975. The pit hosted many, 5-6cm wide, closely spaced veins which had a texture and orientation similar to the veins samples in KF2-4, KF4E-1, and KF4F-1. However, the veins also had elongate vugs that were lined with open space filling quartz crystals which were coated with a red-brown, powdery mineral, or rarely a bright yellow powder that appeared to host small (<1mm) pyrite crystals. Many of the individual veins also had 5-6cm wide, coarse to fine grained, brown gray, mica salvages around them. The veins in the pit are composed of ~95-99%, fine grained quartz with 1-2% subhedral to anhedral pyrite, and 1-3% powder coated vugs. The pyrites do not seem to have any preferred orientation accept for the fact that they mostly occur in the solid quartz rather than in vugs. The vugs are commonly elongate, 2-6mm wide, are stacked parallel to one another, and are coated with open space filling crystals and a red-brown or bright yellow, powdery material. These vugs do not host any noticeable accumulations of sulfides, but the yellow powder mineral may have some small sulfide crystals.
KF3C-16	Standard mine ore sample: massive quartz with wispy molybdenite . No host rock is present in this sample. Vein and Alteration: This sample was taken from a rock dump by the water tanks at the standard mine. The pile contained abundant rocks with molybdenite and copper oxides so it was interpreted to be an ore pile. The vein in this sample is composed mostly of fine-grained quartz (~95%), with scattered masses of coarse euhdral quartz crystals surrounded my fine grained, granular quartz. Throughout the sample there are small wispy masses, of a metallic blue-gray mineral that may be molybdenite (~2-5%). Also, small bits of a dark red-brown, magnetic, fine-grained mineral appear throughout the sample. Along fractures in the quartz, and on the un-cut surface of the sample there is a lot of red-orange oxidation. This

	gives the sample an orange appearance. Two parallel, uncut surfaces of the sample are coated by brown-gray to silvery gray, flaky mica crystals. These surfaces are interpreted to be the top and bottom outer margins of the vein and suggest that the vein had a micaceous vein selvedge.
KF1-13	Quartz vein sample from outcrops east of the KF2 pit. Host Rock: The host rock is composed of ~75% white to greenish-pink, subhedral to anhedral plagioclase, ~20-25% anherdal to subhedral quartz, and 1-5% coarse, greenish-gray, flaky muscovite. Much of the original texture of the host rock is obscured by alteration which increases with proximity to the vein margins. Veins and Alteration: Two parallel, sinuous veins cut this sample and are composed entirely of fine-grained quartz and they have very distinct coarse green-gray, flaky phillosilicate alteration selvedge that completely destroy the original texture of the host rock. Compared to other samples (such as KF3A-6 and KF3A-8) the phillosilicate alteration halos here are much more discrete and extend out from the vein ~0.5X the width of the vein itself.
KF1-12	Multiple quartz veins with pyrite, molybdenite, and magnetite Host Rock: The host rock is composed ~70%, white to greenish-white to pinkish-orange, coarse subhedral to euhedral plagioclase feldspar, ~25% gray-clear, subhedral to anhedral quartz, and ~2-5% coarse grained mica. Much of the host rock's original texture is intact but becomes more obscured by alteration with proximity to the veins. Veins and Alteration: Two thin (<3mm) quartz veins cut this sample parallel to one another. These veins are composed entirely of quartz, do not have clearly defined alteration halos, and have sinuous boundaries. These veins are cut by sinuous veins which are composed of ~95-85% fine-grained quartz, ~5% fine-grained, molybdenite, and ~2-5% fine-grained, magnetite. The molybdenum and magnetite in these crosscutting veins occur along the inside of the margins of this vein and are parallel to the vein boundary. The sample also contains veins which are composed of ~75% coarse, anhedral sulfides and ~25% anhedral quartz. The relationship between these sulfide-dominated veins and the quartz-dominated veins is not clear. All vein-types in this sample seem to be associated with green-gray phyllosilicate-rich alteration selvedges that extends out from the vein margin ~0.5-1X the width of their associated vein. The host-rock feldspars in the phyllosilicte-rich selvedge appear to be alternating to a pinkish-green soft mineral

	and in between the feldspar grains there is abundant, coarse, flaky phyllosilicates.
KF1-3	A veins with potassic and mica alteration halos. Host Rock: The host rock is composed of ~75% pinkish-white subhedral feldspar, ~25-23% gray, anhedral to subhedral quartz, and ~1-2% medium grained, flaky phyllosilicates. A lot of the plagioclase feldspars in the host rock are pink around their margins and might be altering to potassium feldspar. Veins and Alteration: There are two types of veins in this sample. The oldest vein is composed entirely of quartz, has sinuous boundaries, and has a distinct selvedge of potassicaly altered feldspars around its margins. This vein and its textures are cut by the younger vein which has straight margins, a phyllosilicate alteration selvedge, and is composed entirely of quartz. Both the mica and potassic alteration increase in abundance with increasing proximity to the veins.
KF5E-2	Quartz vein sample from a prospect pit west of the river fork in the southern part of the footwall. No host rock is present in this sample. Vein: This sample is from one of the "big vein" prospect pits. It is composed of 85% fine grained quartz, ~5% fine-grained molybdenite , ~5% coarse anhedral phyllosilicates, and ~5% coarse (~5-10mm), subhedral to euhedral pyrite crystals. This vein is very similar to the veins in samples KF2-4, KF4D-2/1, and KF4F-1.
KF6C-4	Quartz vein sample from pile on near a shaft on the ridge above Century mine. No host rock is present in this sample. Vein: The exact origin of this sample is not clear but given its location in a pile of ore rocks next to a mine shaft for the century mine, it is likely that this is an ore sample from the century mine. The Vein is composed of ~97% fine-grained quartz and ~3% sulfide and oxide minerals. The oxides occurs as a red powdery mineral in cracks in the quartz and the sulfides occur as large (>3 mm) blocky euhedral pyrite crystals in the quartz mass. In spots the vein quartz has rectangular voids that are coated with a soft, fine grained mineral that might have replace feldspars crystals.
KF5I-1	Quartz + feldspar "vein" sample of pinching and swelling veins from prospect pits at the south west end of the footwall

	No host rock is present in this sample. Vein and Alteration: This sample is composed of 50% coarse, subhedral feldspars, ~25% soft, fine-grained phyllosilicates and sulfides, and ~25% anhedral quartz. The quartz seems to "flow" around the individual feldspar crystals and is mixed with the sulfide/phyllosilicate mixture. It is not clear if the feldspars in this sample are from the host rock or are part of the vein. The phyllosilicates associated with this vein are green or grey and occur as soft anhedral crystals mixed with fine-grained sulfides (mostly pyrite). It is not clear whether the mixture of phyllosilicates is part of the vein or part of an alteration selvedge in the host rock.
KF5C-1	Quartz vein sample from a prospect pit at the turn in the river in the southwest sampling area. No host rock is present in this sample. Vein: The vein is composed of ~90% fine to medium sized, anhedral- subhedral quartz crystals. Quartz crystals in this vein typically form alternating bands of fine and medium crystals. Bands of coarse (<4mm) subhedral pyrite (~6%) and fine grained, anhedral molybdenite (~4%) commonly form parallel to the alternating quartz bands. Along cracks and on the surface of the sample there is a lot of secondary oxidation.

APPENDIX E

MICROTHERMOMETRIC OBSERVATIONS AND DATA

Observed microthermometic behavior and calculated mole percent NaCl (Mol% NaCl), weight percent NaCl (wt% NaCl), bulk density (Bulk Den), bulk CO_2 (Bulk xCO_2), and mole percent CO_2 (Mol% CO_2) of fluid inclusion groups from the hanging wall and the footwall are presented in the following tables. Fluid inclusions without Mol% NaCl, wt% NaCl, Bulk Den, Bulk xCO_2, and Mol% CO_2 values had either insufficient data for calculations or were destroyed or modified during analysis. Abbreviations for microthermometric behavior are as follows: T_F-H_2O = H_2O freezing temperature, T_M-H_2O = H_2O melting temperature, T_F-clath = clathrate freezing temperature, T_M-clath = clathrate melting temperature, T_F-CO_2 = CO_2 freezing temperature, T_M-CO_2 = CO_2 melting temperature, T_H-CO_2 = CO_2 liquid-vapor homogenization temperature, T_H-H_2O = H_2O liquid-vapor homogenization temperature, and T_M-halite = halite melting temperature. Note that approximate "freezing" temperatures, collected while samples were frozen, provide non-diagnostic information that can be helpful in distinguishing FIAs; however, these data were not used to interpret phase changes or phase equilibria.

B15D									
Sample	T_f-H_2O	T_m-H_2O	T_h-H_2O	Size (µm)	Shape	Photo ID	Molal NaCl	Wt% NaCl	Bulk Den
KF3C-16	-36.4	-3.4	162.5	~10	Negative crystal	KF3C-16-FI-18	0.99	5.47	0.945
KF3C-16	-36.4	-3.4	150	~10	Undulating	KF3C-16-FI-18	0.99	5.47	0.955
KF3C-16	-35.3	-1.5	137	~7.5	Negative crystal	KF3C-16-FI-21	0.43	2.47	0.948
KF3C-16	-35	-3.2	233.3	~7.5	Negative crystal	KF3C-16-FI-13	0.93	5.17	0.869
KF3C-16	-35	-3.2	151	~7.5	Negative crystal	KF3C-16-FI-13	0.93	5.17	0.953
KF3C-16	-35	-3.2	151	~5	Negative crystal	KF3C-16-FI-13	0.93	5.17	0.953
KF3C-16	-35	-3.2	169.7	~5	Negative crystal	KF3C-16-FI-13	0.93	5.17	0.937
KF3C-16	-34.5	-4	137	~5	Undulating	KF3C-16-FI-8	1.16	6.37	0.97
KF3C-16	-34.5	-4	114.5	~7.5	Undulating	KF3C-16-FI-8	1.16	6.37	0.984
KF3C-16	-34.5	-4	137	~7.5	Undulating	KF3C-16-FI-8	1.16	6.37	0.97
KF3C-16	-32.3	-1.2	137	~7.5	Undulating	KF3C-16-FI-16	0.35	1.98	0.945
KF3C-16	-37	-3.7	162.4	~5	Undulating	KF3C-16-FI-22	1.08	5.93	0.948
KF3C-16	-37	-3.7	162.4	~5	Undulating	KF3C-16-FI-22	1.08	5.93	0.948
KF3C-16	-37	-3.7	179	~5	Undulating	KF3C-16-FI-22	1.08	5.93	0.934
KF3C-16	-37	-3.7	204.3	~5	Undulating	KF3C-16-FI-22	1.08	5.93	0.91
KF3C-16	-37	-3.7	204.3	~5	Undulating	KF3C-16-FI-22	1.08	5.93	0.91
KF3C-16	-37	-2.7	204.3	~7.5	Undulating	KF3C-16-FI-22	0.79	4.39	0.898
KF3C-16	-37	-2.7	204.3	~7.5	Undulating	KF3C-16-FI-22	0.79	4.39	0.898
KF3C-16	-35	-3.2	151.9	~12.5	Undulating	KF3C-16-FI-13	0.93	5.17	0.952
KF3C-16	-36	-2.5	n/a	~10	Negative crystal	KF3C-16-FI-28	0.73	4.07	
KF3C-16	-40	-3.6	n/a	~12.5	Undulating	KF3C-16-FI-28	1.05	5.78	
KF3C-16	-38	-3.5	n/a	~12.4	Undulating	KF3C-16-FI-29	1.02	5.62	
KF3C-16	-38	-3.5	n/a	~7.5	Negative crystal	KF3C-16-FI-29			
KF3C-16	-39.4	-2.8	n/a	~7.5	Negative crystal	KF3C-16-FI-29	0.81	4.55	
KF3C-16	-39.4	-2.8	n/a	~10	Negative crystal	KF3C-16-FI-29			
KF3C-16	-37	-2.8	n/a	~12.5	Negative crystal	KF3C-16-FI-32	0.81	4.55	
KF3C-16	-34	-2.8	n/a	~10	Negative crystal	KF3C-16-FI-32	0.81	4.55	
KF3C-16	-41.3	-2.5	n/a	~10	Negative crystal	KF3C-16-FI-40	0.73	4.07	
KF3C-16	-37.7	-2.8	n/a	~7.5	Negative crystal	KF3C-16-FI-44	0.81	4.55	
KF3C-16	-38.7	-2.8	n/a	~7.5	Negative crystal	KF3C-16-FI-44			
KF3C-16	-37.5	-2.7	n/a	~10	Negative crystal	KF3C-16-FI-45	0.79	4.39	
KF3C-16	-40	-3.2	n/a	~12.5	Undulating	KF3C-16-FI-46	0.93	5.17	
KF3C-16	-37.1	-3	n/a	~12.5	Negative crystal	KF3C-16-FI-48	0.87	4.86	
KF3C-16	-39.5	-2.8	n/a	~10	Negative crystal	KF3C-16-FI-55	0.81	4.55	
KF3C-16	-37.7	-3	n/a	~7.5	Negative crystal	KF3C-16-FI-52	0.87	4.86	
KF3C-16	-38.1	-3	n/a	~10	Negative crystal	KF3C-16-FI-52			
KF3C-16	-37.5	-2.8	n/a	~12.5	Undulating	KF3C-16-FI-51	0.81	4.55	
KF3C-16	-37	-3	n/a	~20	Negative crystal	KF3C-16-FI-53	0.87	4.86	
KF3C-16	-34	-2.8	117	~15	Undulating	KF3C-16-FI-15	0.81	4.55	0.973
KF3C-16	-34	-3.4	137	~15	Undulating	KF3C-16-FI-7	0.99	5.47	0.965
KF3C-16	-35.8	-3	179.4	~15	Undulating	KF3C-16-FI-7			
KF3C-16	-32	-3	179.5	~12.5	Undulating	KF3C-16-FI-6	0.87	4.86	0.926

B15D									
Sample	T_f-H_2O	T_m-H_2O	T_h-H_2O	Size (µm)	Shape	Photo ID	Molal NaCl	Wt% NaCl	Bulk Den
KF3C-16	-35	-3	n/a	~15	Undulating	KF3C-16-FI-26	0.87	4.86	
KF3C-16	-35	-2.8	n/a	~15	Undulating	KF3C-16-FI-27	0.81	4.55	
KF3C-16	-37.6	-3	n/a	~10	Negative crystal	KF3C-16-FI-30			
KF3C-16	-38.6	-2.4	n/a	~10	Negative crystal	KF3C-16-FI-31	0.7	3.92	
KF3C-16	-36	-2.6	n/a	~15	Negative crystal	KF3C-16-FI-33			
KF3C-16	-35	-2.4	n/a	~30	Undulating	KF3C-16-FI-37	0.7	3.92	
KF3C-16	-36.6	-2.8	n/a	~10	Negative crystal	KF3C-16-FI-38			
KF3C-16	-35.6	-2.6	n/a	~7.5	Negative crystal	KF3C-16-FI-39			
KF3C-16	-37.5	-2.9	n/a	~25	Negative crystal	KF3C-16-FI-41	0.84	4.7	
KF3C-16	-39.9	-3	n/a	~25	Negative crystal	KF3C-16-FI-42	0.87	4.86	
KF3C-16	-37.2	-2.5	n/a	~15	Undulating	KF3C-16-FI-43	0.73	4.07	
KF3D-19	-38.6	-5.4	191.1	~15	Undulating	KF3D-19-FI-5	1.19	6.52	0.981
KF3D-19	-34.5	-4.2	120.4	~10	Undulating	KF3D-19-FI-4			
KF3D-19	-34.5	-4.2	205.6	~7.5	Undulating	KF3D-19-FI-4			
KF3D-19	-38.5	-4.2	205.6	~5	Undulating	KF3D-19-FI-4			
KF3D-19	-34.5	-4.4	182.6	~10	Undulating	KF3D-19-FI-3			
KF3D-19	-38	-4.4	191.1	~10	Undulating	KF3D-19-FI-3			
KF3D-19	-37	-3.7	200.4	~15	Undulating	KF3D-19-FI-2			
KF3D-19	-37	-4.2	210.4	~15	Undulating	KF3D-19-FI-2			
KF3D-19	-42.2	-5.5	190	~5	Negative crystal	KF3D-19-FI-6	1.59	8.51	0.942
KF3D-19	-38	-4.9	161.6	~7.5	Negative crystal	KF3D-19-FI-8			
KF3D-19	-38	-2.2	161.6	~7.5	Negative crystal	KF3D-19-FI-8			
KF3D-19	-38	-2.2	161.6	~7.5	Negative crystal	KF3D-19-FI-8			
KF3D-19	-36	-3	130.4	~10	Undulating	KF3D-19-FI-14			
KF3D-19	-39	-3	235.2	~7.5	Undulating	KF3D-19-FI-14	0.87	4.86	0.864
KF3D-19	-35	-3.9	141.6	~10	Negative crystal	KF3D-19-FI-15			
KF3D-19	-39	-3.9	164	~7.5	Negative crystal	KF3D-19-FI-15	1.14	6.23	0.949
KF3D-19	-37.4	-3.9	130.4	~7.5	Undulating	KF3D-19-FI-17			
KF3D-19	-36.5	-1.6	149.6	~7.5	Undulating	KF3D-19-FI-18			
KF3D-19	-36.5	-1.6	130.4	~7.5	Undulating	KF3D-19-FI-18	0.46	2.63	0.953
KF3D-19	-35.1	-3.4	120.4	~7.5	Undulating	KF3D-19-FI-18	0.99	5.47	0.976
KF3D-19	n/a	-2.4	130.4	~10	Negative crystal	KF3D-19-FI-19			
KF3D-19	-38.5	-3	161.6	~10	Undulating	KF3D-19-FI-20	0.87	4.86	0.942
KF3D-19	-38.5	-3	161.6	~7.5	Undulating	KF3D-19-FI-20			
KF3D-19	-37.5	-2.9	156.4	~5	Negative crystal	KF3D-19-FI-20			
KF3D-19	-37.5	-2.9	135.4	~5	Negative crystal	KF3D-19-FI-20			
KF3D-19	-37.2	-2.5	100	~10	Undulating	KF3D-19-FI-1	0.73	4.07	0.981
KF3D-19	-41.1	-4	169.9	~10	Undulating	KF3D-19-FI-17	1.16	6.37	0.945
KF3D-19	-41	-6	110.9	~5	Undulating	KF3D-19-FI-3	1.73	9.19	1.002
KF4D-2	-27	-2.8	n/a	~12.5	Undulating	KF4D-2-FI-3			
KF4D-2	-33	-3	n/a	~10	Negative crystal	KF4D-2-FI-3			
KF4D-2	-34	-6	n/a	~10	Negative crystal	KF4D-2-FI-7	1.73	9.19	

B15D									
Sample	T_f-H_2O	T_m-H_2O	T_h-H_2O	Size (µm)	Shape	Photo ID	Molal NaCl	Wt% NaCl	Bulk Den
KF4D-2	-37	-3	n/a	~12.5	Undulating	KF4D-2-FI-7	0.87	4.86	
KF4D-2	-34	-3	n/a	~10	Negative crystal	KF4D-2-FI-4			
KF4D-2	-34	-1.8	n/a	~7.5	Negative crystal	KF4D-2-FI-4			
KF4D-2	-34	-1.8	n/a	~7.5	Negative crystal	KF4D-2-FI-4			
KF4D-2	-34	-1.6	n/a	~7.5	Negative crystal	KF4D-2-FI-4			
KF4D-2	-34	-0.9	n/a	~7.5	Negative crystal	KF4D-2-FI-4	0.26	1.49	
KF4D-2	-32	-2.5	n/a	~12.5	Undulating	KF4D-2-FI-9	0.73	4.07	
KF4D-2	-32	-2.5	n/a	~15	Undulating	KF4D-2-FI-9	0.73	4.07	
KF4D-2	-34	-2.8	n/a	~10	Negative crystal	KF4D-2-FI-8			
KF4D-2	-36	-4.1	129.5	~5	Negative crystal	KF4D-2-FI-16			
KF4D-2	-36	-4.1	203.4	~5	Negative crystal	KF4D-2-FI-16	1.19	6.52	0.915
KF4D-2	-36	-4.1	170.7	~5	Negative crystal	KF4D-2-FI-16	1.19	6.52	0.945
KF4D-2	-36	-4.1	129.5	~7.5	Negative crystal	KF4D-2-FI-16	1.19	6.52	0.975
KF4D-2	-36	-4.1	136.2	~7.5	Negative crystal	KF4D-2-FI-16			
KF4D-2	-36	-4.1	185.5	~7.5	Negative crystal	KF4D-2-FI-16			
KF4D-2	-37	-2.3	114.8	~5	Negative crystal	KF4D-2-FI-19	0.67	3.76	0.97
KF4D-2	-37	-2.3	239.4	~5	Negative crystal	KF4D-2-FI-19	0.67	3.76	0.847
KF4D-2	-37	-2.3	221.9	~5	Negative crystal	KF4D-2-FI-19			
KF4D-2	-37	-2.3	170.7	~7.5	Negative crystal	KF4D-2-FI-19	0.67	3.76	0.927
KF4D-2	-30	-2	200	~7.5	Negative crystal	KF4D-2-FI-20			
KF4D-2	-40	-3.7	n/a	~7.5	Negative crystal	KF4D-2-FI-30			
KF4D-2	-38.5	-3.7	n/a	~7.5	Negative crystal	KF4D-2-FI-30			
KF4D-2	-38.5	-3.7	n/a	~7.5	Negative crystal	KF4D-2-FI-30_1	1.08	5.93	
KF4D-2	-38.5	-3.7	n/a	~5	Negative crystal	KF4D-2-FI-30			
KF4D-2	-39	-3	n/a	~7.5	Negative crystal	KF4D-2-FI-31			
KF4D-2	-39	-2.3	n/a	~7.5	Negative crystal	KF4D-2-FI-31	0.67	3.76	
KF4D-2	-39	-2	n/a	~5	Negative crystal	KF4D-2-FI-31			
KF4D-2	-40	-2.6	n/a	~17.5	Negative crystal	KF4D-2-FI-1			
KF4D-2	-36	-2	179.1	~7.5	Negative crystal	KF4D-2-FI-18	0.58	3.28	0.916
KF4D-2	-37	-3	n/a	~10	Negative crystal	KF4D-2-FI-27	0.87	4.86	
KF4D-2	-40	-3.4	n/a	~10	Negative crystal	KF4D-2-FI-25	0.99	5.47	
KF4D-2	-35	-3	n/a	~10	Negative crystal	KF4D-2-FI-24	0.87	4.86	
KF4D-2	n/a	-2.6	n/a	~7.5	Negative crystal	KF4D-2-FI-28			
KF4D-2	n/a	-2.6	n/a	~7.5	Negative crystal	KF4D-2-FI-28	0.76	4.23	
KF4D-2	-33	-2.8	n/a	~20	Undulating	KF4D-2-FI-10	0.81	4.55	
KF4D-2	-33	-2.2	n/a	~10	Negative crystal	KF4D-2-FI-10			

B30									
Sample	T_e-H_2O	T_m-H_2O	T_h-H_2O	Size (µm)	Shape	Photo ID	Molal NaCl	Wt% NaCl	Bulk Den
KF3C-16	-30.7	-3.2	282.6	~30	Negative crystal	KF3C-16-FI-17	0.93	5.17	0.797
KF3C-16	-35.3	-3	189.4	~10	Negative crystal	KF3C-16-FI-21	0.87	4.86	0.917
KF3C-16	-29.8	-3.4	270.2	~12.5	Negative crystal	KF3C-16-FI-11			
KF3C-16	-30	-2.3	150.9	~15	Undulating	KF3C-16-FI-5	0.67	3.76	0.8
KF3C-16	-34.6	-3.4	242.2	~10	Negative crystal	KF3C-16-FI-10	0.99	5.47	0.861

B15C																
Sample	T_F-clath	T_F-H_2O	T_F-CO_2	T_m-CO_2	T_m-H_2O	T_m-clath	T_H-CO_2	T_H-H_2O	Size (μm)	Shape	Photo ID	Molal NaCl	Wt% NaCl	Bulk XCO2	Bulk Den	Mol % CO2
KF3C-16	n/a	-37	n/a	n/a	-2.7	9.3	30	204.3	~7.5	Undulating	KF3C-16-FI-22	0.246	1.419	0.027	0.96	2.7
KF3C-16	n/a	-37	-96	n/a	-2.7	9.3	30	204.3	~7.5	Undulating	KF3C-16-FI-22	0.246	1.419	0.027	0.96	2.7
KF3C-16	n/a	-37	-96	n/a	-2.7	9.3	30	221.9	~10	Undulating	KF3C-16-FI-22	0.246	1.419	0.027	0.96	2.7
KF3C-16	n/a	-37	-96	-95	-2.7	9.3	30	n/a	~12.5	Undulating	KF3C-16-FI-22	0.246	1.419	0.027	0.96	
KF3C-16	n/a	-36	n/a	n/a	-3.5	9	29.8	179.5	~12.5	Undulating	KF3C-16-FI-16	0.35	2.003	0.027	0.965	2.7
KF3C-16	n/a	-32.3	n/a	n/a	-2.9	9	29.8	179.5	~10	Undulating	KF3C-16-FI-16	0.35	2.003	0.027	0.965	2.7
KF3C-16	n/a	34.5	-94	-55.8	-6	8.4	29.9	221.9	~17.5	Undulating	KF3C-16-FI-24	0.556	3.147	0.027	0.972	2.7
KF3C-16	~-20.4	-39.1	-94	-55.2	-5	8.4	29.9	233.3	~5	Negative crystal	KF3C-16-FI-8	0.556	3.147	0.027	0.972	2.7
KF3C-16	n/a	-34	n/a	n/a	-2.7	9.4	20.6	220	~72	Undulating	KF3C-16-FI-15	0.212	1.222	0.034	0.977	3.4
KF3C-16	n/a	-36.4	n/a	n/a	-2.6	8.4	30.5	221.9	~10	Negative crystal	KF3C-16-FI-18	0.556	3.147	0.025	0.969	2.5
KF3C-16	n/a	-37	n/a	n/a	-2.5	8.5	30.5	221.9	~7.5	Negative crystal	KF3C-16-FI-23	0.522	2.959	0.025	0.968	2.5
KF3C-16	n/a	-37	n/a	n/a	-2.5	8.5	30.5	233.2	~5	Negative crystal	KF3C-16-FI-23	0.522	2.959	0.025	0.968	2.5
KF3C-16	n/a	-37	n/a	n/a	-2.5	8.5	30.5	233.2	~5	Negative crystal	KF3C-16-FI-23	0.522	2.959	0.025	0.968	2.5
KF3C-16	n/a	-37	n/a	n/a	-2.5	8.5	30.5	221.9	~5	Negative crystal	KF3C-16-FI-23	0.522	2.959	0.025	0.968	2.5
KF3C-16	n/a	-37	n/a	n/a	-2.5	8.5	30.5	221.9	~5	Negative crystal	KF3C-16-FI-23	0.522	2.959	0.025	0.968	2.5
KF3C-16	n/a	-37	n/a	n/a	-2.5	8.5	30.5	221.9	~5	Negative crystal	KF3C-16-FI-23	0.522	2.959	0.025	0.968	2.5
KF3C-16	n/a	-37	n/a	n/a	-2.5	8.5	30.5	179.5	~5	Negative crystal	KF3C-16-FI-23	0.522	2.959	0.025	0.968	2.5
KF3C-16	n/a	-37	n/a	n/a	-2.5	8.5	30.5	137	~5	Negative crystal	KF3C-16-FI-23	0.522	2.959	0.025	0.968	2.5
KF3C-16	n/a	-30	n/a	n/a	-2.5	8.5	30.5	221.9	~10	Negative crystal	KF3C-16-FI-23	0.522	2.959	0.025	0.968	2.5
KF3C-16	-25	-39.7	-102.2	-56.6	-3	7.9	n/a	n/a	~7.5	Undulating	KF3C-16-FI-25	0.727	4.074	0.026	0.978	2.6
KF3C-16	n/a	-39.7	n/a	n/a	-3	7.9	n/a	n/a	~7.5	Undulating	KF3C-16-FI-25	0.727	4.074	0.026	0.978	2.6
KF3C-16	n/a	-39.7	n/a	n/a	-3	7.9	n/a	n/a	~7.5	Undulating	KF3C-16-FI-25	0.727	4.074	0.026	0.978	2.6
KF3C-16	-25	-39.7	-102.2	-56.6	-3	7.9	n/a	n/a	~7.5	Undulating	KF3C-16-FI-25	0.727	4.074	0.026	0.978	2.6
KF3C-16	n/a	-41.1	n/a	n/a	-3.4	10.1	n/a	n/a	~10	Undulating	KF3C-16-FI-25	0.004	0.021			
KF3C-16	n/a	-41.7	n/a	n/a	-3.3	10.1	n/a	n/a	~5	Undulating	KF3C-16-FI-25					
KF3C-16	n/a	-41.7	n/a	n/a	-3.3	10	n/a	n/a	~7.5	Undulating	KF3C-16-FI-25					
KF3C-16	-34	-40.7	n/a	n/a	-4.2	9.4	n/a	n/a	~10	Undulating	KF3C-16-FI-35					
KF3C-16	-32	n/a	n/a	n/a	-3.2	9.4	n/a	n/a	~7.5	Undulating	KF3C-16-FI-36	0.212	1.222	0.103	0.894	10.3
KF3C-16	-32	n/a	n/a	n/a	-3.2	8.2	n/a	n/a	~7.5	Undulating	KF3C-16-FI-36					
KF3C-16	-33	-40	n/a	n/a	-2.8	9.5	n/a	n/a	~10	Undulating	KF3C-16-FI-47					
KF3C-16	-32	-40	n/a	n/a	-3.7	10	n/a	n/a	15	Undulating	KF3C-16-FI-34_1	0.004	0.021	0.029	0.956	2.9
KF3C-16	-32.8	-40.9	n/a	n/a	-3.2	10	n/a	n/a	~10	Undulating	KF3C-16-FI-49					
KF3C-16	-33	-40.5	-101	-56.4	-3	8.7	n/a	n/a	~20	Undulating	KF3C-16-FI-54	0.453	2.58	0.045	0.956	4.5
KF3C-16	-34.5	-41.5	-101	-56.4	-2.5	8.3	n/a	n/a	~12.5	Undulating	KF3C-16-FI-50	0.59	3.334	0.045	0.961	4.5
KF3C-16	-34.2	n/a	<-20	8.7	-54.5	2.9	30.5	204.3	~10	Negative crystal	KF3C-16-FI-19	2.338	12.02	0.025	1.031	2.5
KF3C-16	-34.2	n/a	n/a	9.3	n/a	3.5	30.5	189.4	~15	Negative crystal	KF3C-16-FI-20	2.157	11.193	0.025	1.025	2.5
KF3C-16	34.2	n/a	n/a	9.3	n/a	3.5	30.5	221.9	~10	Negative crystal	KF3C-16-FI-20	2.157	11.193	0.025	1.025	2.5
KF3C-16	-29.1	n/a	<-25	9.3	n/a	3.5	30.5	189.4	~12.5	Negative crystal	KF3C-16-FI-20	0.246	1.419	0.045	0.948	4.5
KF3C-16	-32.3	-96	-31.2	8.7	-55.3	3.2	30	270.5	~12.5	Negative crystal	KF3C-16-FI-16	2.248	11.611	0.027	1.031	2.7
KF3C-16	-27	n/a	-15	8.6	n/a	3.8	30	204.3	~12.5	Negative crystal	KF3C-16-FI-1	2.157	11.193	0.027	1.028	2.7
KF3C-16	-38.8	-100	-30	9.3	-56.5	3.7	n/a	n/a	27.5	Undulating	KF3C-16-FI-34_2	2.095	10.91	0.026	1.026	2.6
KF3D-19	-39	n/a	n/a	-5	n/a	6.4	30.5	242.4	~5	Undulating	KF3D-19-FI-6	1.231	6.71	0.025	0.994	2.5

B15C																
Sample	T_f-clath	T_f-H_2O	T_f-CO_2	T_m-CO_2	T_m-H_2O	T_m-clath	T_H-CO_2	T_H-H_2O	Size (µm)	Shape	Photo ID	Molal NaCl	Wt% NaCl	Bulk XCO2	Bulk Den	Mol % CO2
KF3D-19	-37	n/a	n/a	-4.5	n/a	7.9	30.5	196.1	~12.5	Undulating	KF3D-19-FI-13	0.727	4.074	0.025	0.975	2.5
KF3D-19	-37	n/a	n/a	-4.5	n/a	7.9	30.5	191.1	~10	Undulating	KF3D-19-FI-13	0.727	4.074	0.025	0.975	2.5
KF3D-19	-41.2	n/a	-30	-4.5	n/a	8	30.5	191.1	~15	Undulating	KF3D-19-FI-12	0.693	3.89	0.025	0.974	2.5
KF3D-19	-41	n/a	n/a	-4.6	n/a	7.6	30.5	210.4	~10	Negative crystal	KF3D-19-FI-11	0.828	4.618	0.025	0.979	2.5
KF3D-19	-40.2	n/a	n/a	-4.5	n/a	7.5	30.5	200.4	~12.5	Negative crystal	KF3D-19-FI-10	0.862	4.798	0.025	0.98	2.5
KF3D-19	-42.5	n/a	n/a	-4.5	n/a	7.5	30.5	200.4	~10	Undulating	KF3D-19-FI-10	0.862	4.798	0.025	0.98	2.5
KF3D-19	-31.5	n/a	n/a	-4.7	n/a	7	30.5	196.1	~10	Negative crystal	KF3D-19-FI-9	1.031	5.681	0.025	0.987	2.5
KF3D-19	-38.5	n/a	n/a	-6	-55.8	5	30.5	264.1	~15	Undulating	KF3D-19-FI-8	1.687	8.975	0.025	1.01	2.5
KF3D-19	-38.5	n/a	n/a	-5.4	-56.6	5.5	30.5	231.4	~10	Undulating	KF3D-19-FI-7	1.526	8.188	0.025	1.004	2.5
KF3D-19	-40	n/a	-32	-3	n/a	10	n/a	n/a	~12.5	Undulating	KF3D-19-FI-21	0.004	0.021	0.029	0.956	2.9
KF3D-19	-38	n/a	-32	-3	n/a	8	n/a	n/a	~7.5	Undulating	KF3D-19-FI-23					
KF3D-19	-32	-95	-40	-3	-55.4	10	n/a	n/a	~15	Undulating	KF3D-19-FI-24	0.004	0.021	0.045	0.939	4.5
KF3D-19	-32	-95	-40	-3	-55.4	10	n/a	n/a	~12.5	Undulating	KF3D-19-FI-24	0.004	0.021	0.045	0.939	4.5
KF3D-19	-41	n/a	-32	-5	n/a	10	n/a	n/a	~10	Undulating	KF3D-19-FI-26					
KF3D-19	-41	n/a	-32	-5	n/a	10	n/a	n/a	~7.5	Undulating	KF3D-19-FI-26					
KF3D-19	-40	n/a	-32	-3	n/a	7.7	n/a	n/a	~12.5	Undulating	KF3D-19-FI-25	0.795	4.438	0.029	0.986	2.9
KF3D-19	-40	n/a	-32	-3	n/a	7.7	n/a	n/a	~7.5	Undulating	KF3D-19-FI-25					
KF3D-19	-40	n/a	-34	-3	n/a	7.6	n/a	n/a	~7.5	Undulating	KF3D-19-FI-25					
KF3D-19	-40	n/a	-34	-3	n/a	7.6	n/a	n/a	~12.5	Undulating	KF3D-19-FI-25	0.828	4.618	0.029	0.988	2.9
KF3D-19	-38	n/a	-32	-5	n/a	10	n/a	n/a	~10	Undulating	KF3D-19-FI-25					
KF3D-19	-43.1	n/a	n/a	-3	n/a	7.5	n/a	n/a	~10	Undulating	KF3D-19-FI-27	0.862	4.798	0.045	0.97	4.5
KF3D-19	-43.1	n/a	n/a	-2.3	n/a	7.5	n/a	n/a	~7.5	Undulating	KF3D-19-FI-27	0.862	4.798	0.029	0.989	2.9
KF4D-2	-33	n/a	n/a	n/a	-1	2.6	n/a	n/a	~15	Undulating	KF4D-2-FI-3	2.427	12.421	0.005	1.078	0.5
KF4D-2	-32	n/a	n/a	n/a	-2.2	0.2	n/a	n/a	~15	Undulating	KF4D-2-FI-3	3.094	15.314	0.006	1.099	0.6
KF4D-2	-32	n/a	n/a	n/a	-2.2	0.2	n/a	n/a	~17.5	Undulating	KF4D-2-FI-3	3.094	15.314	0.006	1.099	0.6
KF4D-2	-36	n/a	n/a	n/a	-3.4	10	n/a	136.2	~12.5	Undulating	KF4D-2-FI-15					
KF4D-2	-36	n/a	n/a	n/a	-3.4	10	n/a	179.1	~12.5	Undulating	KF4D-2-FI-15					
KF4D-2	-36	n/a	n/a	n/a	-3.2	11	n/a	179.1	~10	Negative crystal	KF4D-2-FI-14	0.004	0.021	0.029	0.956	2.9
KF4D-2	-36	n/a	n/a	n/a	-3.2	11	n/a	195.5	~10	Negative crystal	KF4D-2-FI-14					
KF4D-2	N/a	n/a	n/a	-55.5	-4.2	9	30.5	203.3	~7.5	Negative crystal	KF4D-2-FI-13	0.35	2.003	0.025	0.961	2.5
KF4D-2	N/a	n/a	n/a	-55.5	-4.2	9	30.5	185.5	~7.5	Negative crystal	KF4D-2-FI-13	0.35	2.003	0.025	0.961	2.5
KF4D-2	-34	n/a	-13	-55.6	-5.3	9.1	30.5	213.9	~12.5	Negative crystal	KF4D-2-FI-12	0.315	1.81	0.025	0.96	2.5
KF4D-2	-35	n/a	<-30	-55.3	-3.5	9.5	30.5	221.9	~7.5	Negative crystal	KF4D-2-FI-12	0.177	1.024	0.025	0.954	2.5
KF4D-2	-35	n/a	n/a	n/a	-3.5	9.2	n/a	213.9	~5	Negative crystal	KF4D-2-FI-12					
KF4D-2	-35	n/a	n/a	n/a	-3.5	9.2	n/a	213.9	~5	Negative crystal	KF4D-2-FI-12					
KF4D-2	-36	n/a	n/a	n/a	-2.3	8.9	n/a	115	~7.5	Negative crystal	KF4D-2-FI-22	0.384	2.197	0.029	0.971	2.9
KF4D-2	-36	n/a	n/a	n/a	-2.3	8.9	n/a	203.3	~7.5	Negative crystal	KF4D-2-FI-22					
KF4D-2	-36	n/a	n/a	n/a	-2.3	8.9	n/a	203.3	~7.5	Negative crystal	KF4D-2-FI-22					
KF4D-2	-35	n/a	n/a	n/a	-3	9	n/a	203.3	~12.5	Undulating	KF4D-2-FI-21	0.35	2.003	0.029	0.97	2.9
KF4D-2	-37	-96	n/a	-56.3	-3	9	n/a	270	~10	Negative crystal	KF4D-2-FI-23	0.35	2.003	0.103	0.898	10.3
KF4D-2	-33.7	-100	-18	n/a	-3.8	9	n/a	n/a	~12.5	Negative crystal	KF4D-2-FI-29	0.35	2.003	0.045	0.952	4.5
KF4D-2	-37	n/a	n/a	-55.8	-2.3	9.3	n/a	n/a	~12.5	Undulating	KF4D-2-FI-31					

B15C															
Sample	T_f-clath	T_f-H_2O	T_f-CO_2	T_m-CO_2	T_m-H_2O	T_m-clath	T_H-CO_2	T_H-H_2O	Size (µm)	Shape	Photo ID	Molal NaCl	Wt% NaCl	Bulk XCO2	Bulk Den	Mol % CO2
KF4D-2	-33.5	n/a	n/a	-55.8	-2.3	9.3	n/a	n/a	~15	Undulating	KF4D-2-FI-31_1	0.246	1.419	0.029	0.966	2.9
KF4D-2	-37	n/a	n/a	n/a	-0.9	n/a	n/a	n/a	~12.5	Negative crystal	KF4D-2-FI-32					
KF4D-2	-37	n/a	n/a	n/a	-0.9	n/a	n/a	n/a	~10	Negative crystal	KF4D-2-FI-32					
KF4D-2	-34.6	n/a	n/a	n/a	-0.9	n/a	n/a	n/a	~15	Undulating	KF4D-2-FI-33					
KF4D-2	-37.5	n/a	n/a	n/a	-3.3	9.5	n/a	n/a	~10	Undulating	KF4D-2-FI-35	0.177	1.024	0.029	0.963	2.9
KF4D-2	-37.5	n/a	n/a	n/a	-3.3	9.5	n/a	n/a	~10	Undulating	KF4D-2-FI-35					
KF4D-2	-37	n/a	-18	-57.6	-3.6	10.5	n/a	n/a	~10	Undulating	KF4D-2-FI-34					
KF4D-2	-37	n/a	n/a	n/a	-3.6	10.5	n/a	n/a	~7.5	Negative crystal	KF4D-2-FI-34					
KF4D-2	-37	n/a	n/a	n/a	-3.6	10.5	n/a	n/a	~7.5	Negative crystal	KF4D-2-FI-34					
KF4D-2	-34		n/a	n/a	-0.4	2.8	n/a	n/a	~10	Negative crystal	KF4D-2-FI-2					
KF4D-2	-36.2	n/a	n/a	n/a	-3.4	9.4	n/a	203.3	~10	Negative crystal	KF4D-2-FI-17					
KF4D-2	-36.2	n/a	n/a	n/a	-3.4	9.4	n/a	146	~7.5	Negative crystal	KF4D-2-FI-17					
KF4D-2	-36.2	n/a	n/a	n/a	-3.4	9.4	n/a	179.1	~7.5	Negative crystal	KF4D-2-FI-17					
KF4D-2	-36.2	n/a	n/a	n/a	-3.4	9.4	n/a	179.1	~5	Negative crystal	KF4D-2-FI-17					
KF4D-2	-36.2	n/a	n/a	n/a	-3.4	9.4	n/a	167.5	~5	Negative crystal	KF4D-2-FI-17					
KF4D-2	n/a	n/a	n/a	-56.1	-7	n/a	n/a	n/a	~7.5	Negative crystal	KF4D-2-FI-29					
KF4D-2	n/a	n/a	n/a	-56.1	-10	n/a	n/a	n/a	~10	Negative crystal	KF4D-2-FI-29					
KF4D-2	-39	n/a	n/a	na/	-2.3	9	n/a	n/a	~7.5	Negative crystal	KF4D-2-FI-31					
KF4D-2	-32	n/a	n/a	1.2	n/a	7	n/a	n/a	~17.5	Undulating	KF4D-2-FI-6	2.826	14.175	0.005	1.091	0.5
KF4D-2	-33.3	n/a	n/a	n/a	n/a	5	n/a	n/a	~12.5	Undulating	KF4D-2-FI-7_1					
KF4D-2	-32	n/a	n/a	n/a	n/a	0.9	n/a	n/a	~10	Undulating	KF4D-2-FI-33					
KF4D-2	-30	n/a	n/a	2.8	n/a	6	n/a	n/a	~10	Negative crystal	KF4D-2-FI-2	2.368	12.155	0.005	1.076	0.5
KF4D-2	-35	n/a	n/a	9	n/a	4	n/a	167.5	~10	Negative crystal	KF4D-2-FI-20	0.35	2.003	0.045	0.952	4.5

B15

Sample	T_f-H_2O	T_m-H_2O	T_H-H2O	Size (µm)	Shape	Photo ID	Molal NaCl	Wt% NaCl	Bulk Den
1086	n/a	-1.6	265.5	~7,5	Negative crystal	1086.6-FI-27	0.46	2.63	0.794
1086	n/a	-5.3	342.6	~7.5	Negative crystal	1086.6-FI-15	1.54	8.24	0.733
1086	-32.1	-4.6	n/a	~12.5	Undulating	10866-FI-55			
1086	-32.2	-4.5	n/a	~12.5	Undulating	1086.6-FI-54			
1086	n/a	-20	n/a	~10	Negative crystal	1086.6-FI-48	4.93	22.35	
1086	n/a	-8.5	n/a	~10	Negative crystal	1086.6-FI-44	2.4	12.29	
1086	-34.1	-2.2	n/a	~17.5	Undulating	1086.6-FI-42	0.64	3.6	
1086	N/a	-6.1	n/a	~7.5	Negative crystal	1086.6-FI-41	1.76	9.32	
1193	-42.1	-2.1	239.6	~7.5	Negative crystal	1193-FI-6	0.61	3.44	0.844
1193	-44.9	-2.5	166.7	~7.5	Negative crystal	1193-FI-17	0.73	4.07	0.933
1193	-44.9	-2.5	166.7	~5	Negative crystal	1193-FI-18			
1193	-52	-4.8	305.3	~10	Negative crystal	1193-FI-29	1.39	7.54	0.79
1193	-47	-5.5	327.1	~10	Negative crystal	1193-FI-30	1.59	8.51	0.766
1193	-45.7	-5.6	n/a	~10	Negative crystal	1193-FI-38			
1193	n/a	-2.8	n/a	~7.5	Negative crystal	1193-FI-41			
1193	-35	-2.8	n/a	~10	Negative crystal	1193-FI-41			
1193	-46.6	-11	n/a	~12.5	Negative crystal	1193-FI-56	3.01	14.98	
1201	-35.5	-7.1	240	~7.5	Negative crystal	1201.1-FI-14	2.03	10.61	0.91
1201	-36.5	-3	n/a	~7.5	Undulating	1201-FI-47			
1201	-35	-2	n/a	~10	Undulating	1201-FI-48	0.58	3.28	

B30D Sample	T_f-H_2O	T_m-H_2O	T_H-H2O	Size (µm)	Shape	Photo ID	Molal NaCl	Wt% NaCl	Bulk Den
1086	-30	-2	337.2	~10	Negative crystal	1086.6-FI-29	0.58	3.28	0.657
1086	-31	-3.2	321.8	~7.5	Negative crystal	1086.6-FI-33	0.93	5.17	0.724
1086	-38.5	-3.7	n/a	~7.5	Negative crystal	1086.6-FI-57			
1086	n/a	-4.2	n/a	~10	Negative crystal	1086.6-FI-49	1.22	6.67	
1086	-38.5	-2.5	n/a	~12.5	Negative crystal	1086.6-FI-65			
1086	-35	-3	n/a	~10	Negative crystal	1086.6-FI-68			
1086	-34.3	-2	n/a	~7.5	Negative crystal	1086.6-FI-70	0.58	3.28	
1086	-38.5	-4.4	n/a	22.5	Negative crystal	1086.6-FI-71	1.28	6.96	
1086	-35.4	-3	n/a	~10	Negative crystal	1086.6-FI-72	0.87	4.86	
1086	-32.5	-3	373.6	~7.5	Negative crystal	1086.6-FI-8	0.87	4.86	0.598
1193	-16	-2.3	n/a	~12.5	Negative crystal	n/a			
1193	-43.9	-2.1	266.2	~10	Negative crystal	1193-FI-5	0.61	3.44	0.803
1193	-43.1	-1	263.6	~7.5	Negative crystal	1193-FI-6	0.29	1.65	0.785
1193	n/a	-3	n/a	~10	Negative crystal	1193-FI-63			
1193	-41.9	-5.9	n/a	~15	Negative crystal	1193-FI-36	1.7	9.05	
1193	n/a	-2.7	n/a	~10	Negative crystal	1193-FI-40	0.79	4.39	
1193	-32	-3.2	n/a	~10	Negative crystal	1193-FI-35			
1193	-32	-3.3	n/a	~10	Undulating	1193-FI-45	0.96	5.32	
1193	-41.6	-3.7	n/a	~10	Negative crystal	1193-FI-46			
1193	-41.6	-4.9	n/a	~10	Negative crystal	1193-FI-46			
1193	-55.6	-15	n/a	~10	Negative crystal	1193-FI-55			
1193	n/a	-4.4	n/a	~7.5	Negative crystal	1193-FI-62			
1193	-33.5	-4.4	n/a	~10	Negative crystal	1193-FI-62	1.28	6.96	
1193	-48.6	-10.4	347.9	~12.5	Negative crystal	1193-FI-11			
1193	-35.6	-1	362.9	~10	Negative crystal	1193-FI-20	0.29	1.65	0.558
1193	-44	-6.7	282.2	~10	Negative crystal	1193-Fi-22	1.92	10.1	0.856
1193	-40.5	-6.7	279	~10	Negative crystal	1193-FI-26			
1193	-58.4	-12	n/a	~15	Negative crystal	1193-FI-40_2	3.25	15.96	
1193	-35	-4	n/a	~7.5	Negative crystal	1193-FI-42	1.16	6.37	
1193	-35	-10	n/a	~7.5	Negative crystal	1193-FI-54	2.77	13.95	
1193	-28	-4.4	n/a	~10	Negative crystal	1193-FI-52	1.28	6.96	
1193	-28	-4.4	n/a	~10	Negative crystal	1193-FI-52	1.28	6.96	
1193	-40.2	-12	n/a	~10	Negative crystal	1193-FI-50			
1193	-50.9	-11		~10	Negative crystal	1193-FI-57			
1193	-47.8	-7.1	390	~7.5	Negative crystal	1193-FI-13	2.03	10.61	0.679
1201	-36	-5.5	295.3	~5	Negative crystal	1201.1-FI-16	1.59	8.51	0.819
1201	-36	-6	338	~7.5	Undulating	1201.1-FI-20	1.73	9.19	0.757
1201	-30.8	-5.3	358	~7.5	Negative crystal	1201.1-Fi-30	1.54	8.24	0.702
1201	n/a	-2.5	n/a	~7.5	Negative crystal	1201-FI-43	0.73	4.07	
1201	n/a	n/a	n/a	~7.5	Negative crystal	1201-Fi-55			
1201	-34.8	-5.3	245.5	~7.5	Undulating	1201.1-FI-17	1.54	8.24	0.884
1201	-34.5	-5.5	330.2	~7.5	Undulating	1201.1-FI-15			

B30D Sample	T_e-H_2O	T_m-H_2O	T_H-H2O	Size (µm)	Shape	Photo ID	Molal NaCl	Wt% NaCl	Bulk Den
1201	-34.8	-7	389.8	~7.5	Negative crystal	1201.1-FI-22	2	10.48	0.676
1201	-35	-4.6	353.7	~20	Undulating	1201.1-Fi-25	1.34	7.25	0.693
1201	-28.4	-4.9	367.1	~12.5	Negative crystal	1201.1-Fi-26			
1201	n/a	-4.5	370	~15	Undulating	1201.1-Fi-27			
1201	-34.5	-3	302.3	~7.5	Negative Crysta;	1201.1-Fi-28	0.87	4.86	0.757
1201	-40.1	-2.7	n/a	~12.5	undulating	1201-FI-45	0.79	4.39	
1201	-37.6	-3	n/a	~17.5	undulating	1201-FI-46	0.87	4.86	
1201	-37.5	-3.3	n/a	~10	Negative crystal	1201-FI-46	0.96	5.32	
1201	-38.2	-3	n/a	~10	Negative crystal	1201-FI-47	0.87	4.86	
1201	-38	-2.5	n/a	~10	undluating	1201-FI-47	0.73	4.07	
1201	-39.5	-2.5	n/a	~12.5	Negative crystal	1201-FI-49	0.73	4.07	
1201	n/a	-2.8	n/a	~7.5	Negative crystal	1201-Fi-56			
1201	n/a	-7.1	396.2	~5	Negative crystal	1201.1-FI-12			
1201	-35.5	-5.5	336.4	~10	undulating	1201.1-FI-21			
1201	-33.6	-4.4	361.7	~7.5	Negative crystal	1201.1-FI-23	1.28	6.96	0.67
1201	-29.4	-3.9	361.7	~12.5	Undulating	1201.1-FI-29			
1201	n/a	-4.6	365.4	~5	Negative crystal	1201.1-FI-29	1.34	7.25	0.667
1201	n/a	-4.6	282.9	~5	Negative crystal	1201.1-FI-29	1.34	7.25	0.822
1201	-34.8	-7	283	~10	Negative crystal	1201.1-FI-22	2	10.48	0.859
1201	-34.8	-5.5	358	~7.5	Negative crystal	1201.1-FI-24			
1201	n/a	-3.9	n/a	~7.5	Negative crystal	1201.1-FI-37			
1201	n/a	n/a	n/a	~7.5	Negative crystal	1201.1-FI-37			
1201	n/a	-3	n/a	~10	Undulating	1201.1-FI-37	0.87	4.86	
1201	-47.5	-6.6	n/a	~10	Undulating	1201-FI-51	1.9	9.97	
1201	n/a	n/a	n/a	~7.5	Undulating	1201-FI-51	1.9	9.97	
1201	-38.7	-3.9	n/a	~10	Negative crystal	1201-FI-52	1.02	5.62	
1201	n/a	-3.5	n/a	~15	Negative crystal	1201-FI-52	1.02	5.62	
1201	-38	-3.6	n/a	~17.5	Undulating	1201-FI-41			
1201	-35	-4.4	n/a	~12.5	Undulating	1201-Fi-53	1.28	6.96	
1201	-34.4	-2.8	n/a	~7.5	Negative crystal	1201-Fi-54	0.81	4.55	
1201	-34.4	-2.8	n/a	~7.5	Negative crystal	1201-Fi-54			
1201	-38.6	-3.2	n/a	~10	Negative crystal	1201.1-FI-33			
1343	-38.2	-4.4	n/a	~10	Undulating	1343-FI-14	1.28	6.96	
1343	-35	-3	331.1	~10	Negative crystal	1343-FI-16	0.87	4.86	0.699
1343	-35	-2	260.2	~7.5	Negative crystal	1343-FI-19	0.58	3.28	0.81
1343	-36	-3	n/a	~12.5	Undulating	1343-FI-15	0.87	4.86	
1343	-33.8	-0.5	n/a	~7.5	Negative crystal	1343-FI-3			
1343	-31.3	-3	n/a	~10	Negative crystal	1343-FI-5	0.87	4.86	
1343	-31.3	-4	n/a	~10	Negative crystal	1343-FI-10			
1343	n/a	-3	n/a	~7.5	Negative crystal	1343-FI-68			
1343	n/a	-3	n/a	~12.5	Undulating	1343-FI-69	0.87	4.86	
1343	-40	-3.7	n/a	~20	Undulating	1343-FI-69	1.08	5.93	

B30D									
Sample	T_E-H_2O	T_m-H_2O	T_H-H2O	Size (µm)	Shape	Photo ID	Molal NaCl	Wt% NaCl	Bulk Den
1343	-40	-3	n/a	~10	Negative crystal	1343-FI-70	0.87	4.86	
1343	-30.5	-2.7	n/a	~10	Negative crystal	1343-FI-84			
1343	-37	-3	319.3	~12.5	Negative crystal	1343-FI-91	0.87	4.86	0.724
1343	-35.5	n/a	n/a	~15	Negative crystal	1343-FI-63			
1343	-42.7	-3	106.3	~12.5	Negative crystal	1343-FI-29	0.87	4.86	
1343	n/a	n/a	170.4	~10	Negative crystal	1343-FI-39			
1343	-32	-4.2	319.4	~12.5	Negative crystal	1343-FI-44	1.22	6.67	0.752
1201	-35.5	-2.7	342	~7.5	Negative crystal	1201.1-FI-8			
1201	n/a	-0.1	393.1	~7.5	Negative crystal	1201.1-Fi-11			
1201	-33.4	-2.1	393.1	~7.5	Negative crystal	1201.1-FI-19			
1201	-38.6	-3.2	n/a	~7.5	Negative crystal	1201.1-FI-33			
1193	-30.4	-7.3	362.2	~7.5	Negative crystal	1193-FI-19			
1193	-42.3	-3.8	359.4	~5	Negative crystal	1193-FI-24			
1193	-35	-5	n/a	~7.5	Negative crystal	1193-FI-35			
1201	-72.1	-21.1	n/a	~7.5	Negative crystal	1201-FI-58	5.14	23.08	
1201	-61.4	-20.9	n/a	~7.5	Negative crystal	1201-FI-57	5.1	22.95	
1201	-69.8	-20.5	n/a	~10	Undulating	1201-FI-42	5.02	22.69	
1343	-42.1	-20.6	n/a	~7.5	Negative crystal	1343-FI-52	5.04	22.76	
1343	-50	-20.6	n/a	~5	Negative crystal	1343-FI-52	5.04	22.76	
1086	-46.7	-15	n/a	~17.5	Undulating	1086.6-FI-75	3.91	18.62	
1086	n/a	-15.5	430.4	~7.5	Negative crystal	1086.6-Fi-10	4.02	19.03	0.754
1193	-50	-14.5	233.9	~7.5	Negative crystal	1193-FI-23	3.81	18.2	0.971
1086	-61.6	-20.4	n/a	~10	Negative crystal	1086.6-FI-45	5	22.62	
1086	-52.5	-16	n/a	~17.5	Undulating	1086.6-FI-50	4.13	19.43	

B30H

Sample	T_f-H_2O	T_m-H_2O	T_M-Halite	T_H-H2O	Size (microns)	Shape	Photo ID	Molal NaCl	Wt% NaCl	Bulk Den
1086	-70	-40.2	365	n/a	~12.5	Negative crystal	1086.6-FI-1	13.35	43.83	
1086	-64	-25.4	180	286.4	~10	Negative crystal	1086.6-FI-7	7.66	30.92	1.034
1086	-66.5	-25.6	365	265.6	~10	Negative crystal	1086.6-FI-3	13.35	43.83	1.182
1086	-66.5	-40.2	180	229.1	~7.5	Negative crystal	1086.6-FI-3	7.66	30.92	1.089
1086	-73.3	-34	180	437.6	~10	Negative crystal	1086.6-FI-4	7.66	30.92	0.876
1086	n/a	-30	312.1	329.7	~12.5	Undulating	1086.6-FI-35	10.99	39.12	1.07
1086	-70	-41.9	n/a	n/a	~10	Negative crystal	1086.6-FI-52			
1086	n/a	-40	n/a	n/a	~10	Negative crystal	1086.6-FI-61			
1086	-85	-39.7	n/a	n/a	~10	Negative crystal	1086.6-FI-67			
1086	-55.4	-23.8	n/a	n/a	~15	Negative crystal	1086.6-FI-26			
1086	-74.4	-40.2	n/a	211	~12.5	Negative crystal	1086.6-FI-2			
1086	-80	-40.6	n/a	n/a	~5	Negative crystal	1086.6-FI-58			
1086	-76	-40	312.1	286.4	~15	Undulating	1086.6-FI-23	10.99	39.12	1.113
1086	-74.2	-45.1	321.7	265.1	~17.5	Undulating	1086.6-FI-23	11.36	39.91	1.142
1086	-56	-27.2	n/a	n/a	~20	Undulating	1086.6-FI-53			
1086	n/a	-25	n/a	n/a	~7.5	Negative crystal	1086.6-FI-47			
1086	-68	-27.2	n/a	n/a	~5	Negative crystal	1086.6-FI-43			
1086	~70	-45.5	n/a	n/a	~5	Negative crystal	1086.-FI-59			
1086	-72	-24.2	n/a	n/a	~10	Negative crystal	1086.6-FI-64			
1086	n/a	-45.7	n/a	n/a	~10	Undulating	1086.6-FI-73			
1086	n/a	-51.1	n/a	n/a	~10	Negative crystal	1086.6-FI-76			
1086	n/a	-41.3	n/a	n/a	~10	Negative crystal	1086.6-FI-78			
1086	-71.8	-23	n/a	n/a	~7.5	Negative crystal	1086.6-FI-63			
1193	-69.8	-28	176.6	220.2	~15	Undulating	1193-FI-9	7.6	30.77	1.096
1193	-74.8	-25	215.2	220.2	~12.5	Undulating	1193-FI-10	8.3	32.66	1.113
1193	-61.5	-24	190.2	210.5	~10	Undulating	1193-FI-10	7.83	31.4	1.11
1193	-66.1	-25.6	190.2	233.9	~10	Negative crystal	1193-FI-12	7.83	31.4	1.089
1193	-58.1	-17.7	n/a	n/a	~15	Undulating	1193-FI-33			
1343	-33	-40	n/a	319.4	~7.5	Negative crystal	1343-FI-40			
1343	-42.1	-20	n/a	n/a	~5	Negative crystal	1343-FI-52			
1343	-80	-22.5	n/a	227.1	~10	Negative crystal	1343-FI-90			
1343	n/a	-39.9	n/a	315.5	~12.5	Negative crystal	1343-FI-36			

B75									
Sample	T_f-H_2O	T_m-H_2O	T_H-H_2O	Size (microns)	Shape	Photo ID	Molal NaCl	Wt% NaCl	Bulk Den
1086	n/a	-3	373.6	~5	Negative crystal	1086.6-FI-6			
1086	n/a	-3.6	405	~5	Negative crystal	1086.6-FI-5	1.05	5.78	0.533
1086	n/a	n/a	356.7	~13	Negative crystal	1086.6-FI-12			
1086	-33.5	-1	356.7	~10	Undulating	1086.6-Fi-14	0.29	1.65	0.575
1086	n/a	n/a	356.7	~5	Undulating	1086.6-Fi-14			
1086	n/a	-1	n/a	~7.5	Negative crystal	1086.6-FI-60			
1086	-34.2	-2	n/a	~5	Negative crystal	1086.6-FI-56	0.58	3.28	
1086	n/a	-3.4	n/a	~10	Negative crystal	1086.6FI-39	0.99	5.47	
1086	n/a	-3.3	n/a	~10	Negative crystal	1086.6-Fi-38	0.96	5.32	
1086	n/a	-3.3	n/a	~10	Negative crystal	1086.6-Fi-38			
1086	-33.4	-3.2	n/a	~17.5	Undulating	1086.6-FI-42	0.93	5.17	
1086	n/a	-3	n/a	~10	Negative crystal	1086.6-FI-62			
1086	-42	n/a	n/a	~10	Negative crystal	1086.6-FI-66			
1086	-42	-2.5	n/a	~10	Negative crystal	1086.6-FI-66			
1086	n/a	-2.8	n/a	~10	Negative crystal	1086.6-FI-69			
1086	n/a	-2.8	n/a	~12.5	Undulating	1086.6-FI-74	0.81	4.55	
1086	n/a	-2.7	n/a	~15	Undulating	1086.6-FI-77	0.79	4.39	
1193	-25.5	-5.5	n/a	~7.5	Negative crystal	n/a			
1201	n/a	n/a	n/a	~10	Negative crystal	1201.1-FI-32			
1201	n/a	n/a	n/a	~7.5	Negative crystal	1201.1-FI-32			
1201	n/a	n/a	n/a	~7.5	Negative crystal	1201-FI-48_1			

B20C

Sample	T_f-clath	T_f-H_2O	T_f-CO_2	T_m-CO_2	T_m-H_2O	T_m-clath	T_H-CO_2	T_H-H_2O	Size (μm)	Shape	Photo ID	Molal NaCl	Wt% NaCl	Bulk XCO2	Bulk Den	Mol% CO2
1193	`-30.1	-95.8	n/a	-53	n/a	9.1	n/a	310.4	~12.5	Negative crystal	1193-FI-1					
1193	-32.9	n/a	n/a	-51.5	n/a	8	n/a	173.3	~12.5	Undulating	1193-FI-2					
1193	-32.9	n/a	n/a	n/a	n/a	n/a	n/a	n/a	~20	Undulating	n/a					
1193	-31.3	-95.8	n/a	-54	n/a	8.5	n/a	278.1	~10	Negative crystal	1193-FI-3					
1193	-30.5	-93.8	n/a	-55.5	n/a	8.6	n/a	287.8	~12.5	Negative crystal	1193-FI-4					
1193	-42.6	-99.5	-31.1	-56.1	-3.1	9.2	n/a	n/a	~7.5	Negative crystal	1193-FI-37	0.281	1.615			
1193	-45.5	-100	-32	-55.6	-5.8	10.4	n/a	n/a	20	Undulating	1193-FI-32	0.004	0.021	0.212	0.82	21.2
1193	-45.5	-100	-32	-55.6	-5.8	10.4	n/a	n/a	~25	Undulating	1193-FI-32	0.004	0.021			
1193	n/a	-96	n/a	-56	-5.5	10.4	n/a	n/a	~30	Undulating	1193-FI-34	0.004	0.021			
1193	-45	-98	-32	-56	-3	9	n/a	n/a	~10	Undulating	1193-FI-47	0.35	2.003	0.082	0.916	8.2
1193	-45	-98	-32	-56	-3	9	n/a	n/a	~12.5	Undulating	1193-FI-47	0.35	2.003	0.082	0.916	8.2
1193	-36.7	-97.1	-30	-55.5	-3.3	10	n/a	n/a	~32.5	Undulating	1193-FI-48	0.004	0.021	0.103	0.888	10.3
1193	-45	-98.3	-37.2	-56	-4	8	n/a	n/a	~20	Undulating	1193-FI-49	0.693	3.89	0.063	0.946	6.3
1193	-45	-98.3	-37.2	-56	-4	9.2	n/a	n/a	~7.5	Negative crystal	1193-FI-49	0.315	1.81	0.029	0.968	2.9
1193	n/a	-98.5	n/a	-56	-3.2	9.1	n/a	n/a	~15	Undulating	1193-FI-58	0.315	1.81	0.029	0.968	2.9
1193	-32.1	-99.8	-32.1	-55.8	-2.5	8.9	n/a	n/a	~10	Negative crystal	1193-FI-38	0.384	2.197	0.063	0.935	6.3
1193	n/a	-98.9	n/a	-56.1	-3.3	8.8	n/a	n/a	~12.5	Negative crystal	1193-FI-40_1					
1201	-33.8	93	-12.3	-55.5	n/a	8.4	25.4	236.3	~7.5	Undulating	1201.1-FI-6					
1201	-32.9	93	-12.3	n/a	n/a	8.4	26.6	260.5	~7.5	Undulating	1201.1-FI-9	0.556	3.147	0.03	0.981	3
1201	-32.9	93	-12.3	-55.5	n/a	8.4	25.4	236.3	~5	Negative crystal	1201.1-FI-3	0.556	3.147	0.088	0.937	8.8
1201	-33.4	n/a	-33.4	n/a	n/a	4.6	n/a	120	~7.5	Negative crystal	1201.1-FI-5					
1201	-33.5	n/a	n/a	n/a	-3.3	10	n/a	n/a	~10	Negative crystal	1201.1-FI-34	0.004	0.021	0.067	0.931	6.7
1201	-42.1	n/a	n/a	n/a	-3.1	10.4	n/a	n/a	~10	Undulating	1201-FI-44	0.004	0.021	0.045	0.939	4.5
1343	-52	-99.5	-35	-56.2	-3	8.5	n/a	306.9	~10	Negative crystal	1343-FI-21	0.522	2.959	0.126	0.885	12.6
1343	-33.2	-97.8	-47.7	-55.8	-2.5	8.3	30.1	230	~12.5	Undulating	1343-FI-22	0.59	3.334	0.103	0.906	10.3
1343	-35	-92.1	n/a	-55.6	n/a	7	n/a	260	~30	Undulating	1343-FI-45					
1343	n/a	-97	n/a	-55.6	n/a	9.7	n/a	230	~10	Negative crystal	1343-FI-47					
1343	-46	-101.8	-32	-56	-3	9.7	n/a	n/a	~10	Undulating	1343-FI-53	0.108	0.626	0.103	0.891	10.3
1343	-46	-101.8	-32	-56	-3	9.7	n/a	n/a	~10	Undulating	1343-FI-53					
1343	-46	-101.8	-32	-56	-3	9.7	n/a	n/a	~20	Undulating	1343-FI-53	0.108	0.626	0.082	0.908	8.2
1343	n/a	-101.7	-33	-56.6	-2.3	7.8	n/a	n/a	~10	Negative crystal	1343-FI-58	0.761	4.256	0.082	0.929	8.2
1343	-32	-101.3	-42	-55.8	-3	9	n/a	n/a	~7.5	Negative crystal	1343-FI-59					
1343	-37	-98	-32	-56.6	n/a	n/a	n/a	n/a	~25	Undulating	1343-FI-62	0.073	0.425	0.082	0.907	8.2
1343	-45	-98	-32	-56.6	n/a	9.8	n/a	n/a	~12.5	Negative crystal	1343-FI-62	0.073	0.425	0.063	0.924	6.3
1343	-43	n/a	-33	n/a	-5	8.9	n/a	n/a	~15	Undulating	1343-FI-65	0.384	2.197	0.029	0.971	2.9
1343	-47.5	-100	-35	-56	-3	8	n/a	n/a	~10	Negative crystal	1343-FI-66	0.693	3.89	0.332	0.779	33.2
1343	-35.9	-99.7	-28.4	-56	-3	12	n/a	317.3	~10	Negative crystal	1343-FI-82	0.004	0.021	0.446	0.735	44.6
1343	-51	-101	-32	-56	-3	9.6	n/a	n/a	~7.5	Negative crystal	1343-FI-71	0.142	0.825	0.333	0.771	33.3
1343	n/a	-101	n/a	-55.8	-2.8	11	n/a	n/a	~10	Undulating	1343-FI-72	0.004	0.021	0.152	0.854	15.2
1343	-45	-100	-32.2	-55	-3.2	9.2	30.8	250	~12.5	Undulating	1343-FI-75					
1343	-40.9	-100.3	-33	-56.3	-3	10	31.1	320.3	~10	Negative crystal	1343-FI-92					
1343	n/a	-98.5	-31	-56.1	-2.9	11	n/a	345.8	~10	Negative crystal	1343-FI-85					

B20C																
Sample	T_f-clath	T_f-H_2O	T_f-CO_2	T_m-CO_2	T_m-H_2O	T_m-clath	T_H-CO_2	T_H-H_2O	Size (µm)	Shape	Photo ID	Molal NaCl	Wt% NaCl	Bulk XCO2	Bulk Den	Mol% CO2
1343	-43	-100	-31.5	-56	-3	9.5	30.8	345.8	~10	Negative crystal	1343-FI-86					
1343	-43	-100	-31.5	-56	-3	9.5	30.8	202.8	~7.5	Negative crystal	1343-FI-86					
1343	-42	-101	n/a	-56	-3.6	8.5	n/a	364.5	~10	Negative crystal	1343-FI-88	0.522	2.959	0.211	0.831	21.1
1343	-44	-101	n/a	n/a	-3.6	8.5	n/a	200	~5	Negative crystal	1343-FI-88	0.522	2.959	0.385	0.758	38.5
1343	-41.6	-100.7	-32	-56	-2.6	9.6	n/a	348.9	~15	Negative crystal	1343-FI-89					
1343	n/a	-95.3	n/a	-56	n/a	10.1	n/a	348.9	~12.5	Negative crystal	1343-FI-94					
1343	-58.2	-101	-38.3	-55.9	-3	5.5	n/a	n/a	~10	Negative crystal	1343-FI-48	1.526	8.188	0.103	0.932	10.3
1343	-42.1	-101	n/a	-55.5	n/a	9	n/a	n/a	~7.5	Negative crystal	1343-FI-52					
1343	-46	-101.3	-35	-55.8	-3	9	n/a	n/a	~7.5	Negative crystal	1343-FI-59					
1343	-45.5	-101.3	-33	-55.8	-2	7	n/a	n/a	~12.5	Undulating	1343-FI-64					
1343	n/a	-101.3	n/a	-55.8	n/a	9.6	n/a	n/a	~5	Negative crystal	1343-FI-3					
1343	-32.2	-97.7	-32.2	-56	-2	9.6	n/a	n/a	~12.5	Undulating	1343-FI-8	0.142	0.825	0.385	0.753	38.5
1343	-45.2	-98.4	-32.2	-55.7	-2	11.3	n/a	n/a	~15	Undulating	1343-FI-12	0.004	0.021	0.103	0.888	10.3
1343	-32	-101	-32	-56.1	-2.5	10	n/a	n/a	~7.5	Negative crystal	1343-FI-15	0.004	0.021	0.103	0.888	10.3
1343	n/a	n/a	-29	-56.4	-3	10	n/a	331.5	~10	Undulating	1343-FI-18					
1343	-49.7	-99.3	-32.3	-56	-2.7	10.3	n/a	301.4	~7.5	Negative crystal	1343-FI-23					
1343	-50	-100	-32	-55.6	-2.5	9.7	n/a	n/a	~10	Undulating	1343-FI-24	0.108	0.626	0.103	0.891	10.3
1343	-35	-98.5	-35	-56	-2.7	10	n/a	n/a	~10	Negative crystal	1343-FI-25	0.004	0.021	0.126	0.871	12.6
1343	-32.5	-94	-25.5	-56	-2.5	10.6	n/a	285.2	~25	Undulating	1343-FI-30					
1343	-35.3	-97.1	-29.8	-55.6	n/a	8.8	n/a	310	~15	Negative crystal	1343-FI-31					
1343	-35	n/a	n/a	-55.7	-3.2	11	n/a	290.3	~7.5	Negative crystal	1343-FI-32	0.004	0.021	0.103	0.888	10.3
1343	-35	n/a	n/a	-55.7	-3.2	11	n/a	285.2	~7.5	Negative crystal	1343-FI-33					
1343	n/a	-98.2	n/a	-55.7	n/a	n/a	n/a	380.5	~7.5	Negative crystal	1343-FI-34					
1343	n/a	-98.2	n/a	-55.6	-3.3	5.3	n/a	n/a	~10	Negative crystal	1343-FI-35					
1343	-40.1	-100	-31	-55.6	-3.3	8.3	n/a	329.4	~12.5	Negative crystal	1343-FI-36					
1343	-37	n/a	n/a	-55.6	-3	7.5	n/a	299.7	~10	Undulating	1343-FI-37					
1343	n/a	-97	n/a	-55.7	n/a	9.7	n/a	351.6	~7.5	Negative crystal	1343-FI-46					
1343	n/a	-97	n/a	-55.7	n/a	9.7	n/a	351.6	~7.5	Negative crystal	1343-FI-46					
1343	n/a	-98.2	n/a	-55.6	-4	10	n/a	342.1	~12.5	Undulating	1343-FI-10	0.004	0.021	0.446	0.735	44.6
1343	-31	-99.5	-31	-55.7	n/a	9.2	n/a	351.7	~10	Negative crystal	1343-FI-11					
1343	-35	-98.8	-35	-56.1	-2.4	9.5	n/a	319.9	~10	Negative crystal	1343-FI-16	0.177	1.024	0.287	0.789	28.7
1343	n/a	-100	-29	-56.4	n/a	10	n/a	279.9	-12.5	Undulating	1343-FI-18					
1343	-38.5	-98.1	n/a	-56.1	-4.4	n/a	n/a	n/a	~15	Negative crystal	1343-FI-1					
1343	-50.2	-96	n/a	-56	-3.5	n/a	n/a	400	~7.5	Undulating	1343-FI-2					
1343	-32	-99.6	-32	-56	-3	8.4	n/a	n/a	~10	Negative crystal	1343-FI-4	0.556	3.147	0.152	0.868	15.2

B75C															
Sample	T_F-clath	T_F-H_2O	T_F-CO_2	T_m-CO_2	T_m-H_2O	T_m-clath	T_H-CO_2	T_H-H_2O	Size (µm)	Shape	Photo ID	Molal NaCl	Wt% NaCl	Bulk XCO2	Bulk Den	Mol% CO2
1086	n/a	-96	n/a	-56.4	n/a	n/a	n/a	n/a	~12.5	Undulating	1086.6-FI-25					
1086	-33.7	n/a	n/a	-56.4	-11.5	n/a	n/a	n/a	~10	Undulating	1086.6-FI-17					
1086	n/a	-100	n/a	-54	-8	n/a	n/a	365	~10	Undulating	1086.6-FI-18					
1086	-26.7	-100	n/a	-55.4	-19	12.3	n/a	365	~10	Undulating	1086.6-FI-22					
1086	-41.5	-96.2	n/a	-55.2	-22.2	n/a	n/a	n/a	~7.5	Negative crystal	1086.6-FI-21					
1086	-30.1	-95.4	n/a	-55	-7.7	7.4	n/a	430.4	~25	Negative crystal	1086.6-FI-32	0.896	4.976			
1086	-30	-96	n/a	n/a	-5	7.2	n/a	373.6	~10	Negative crystal	1086.6-FI-31					
1086	n/a	n/a	n/a	n/a	-12	7.8	n/a	373.6	~7.5	Negative crystal	1086.6-FI-30					
1086	n/a	n/a	n/a	n/a	-12	7.8	n/a	410	~7.5	Negative crystal	1086.6-FI-30	0.761	4.256	0.267	0.477	26.7
1086	n/a	n/a	n/a	-56.4	-15	7.1	n/a	n/a	~7.5	Negative crystal	1086.6-FI-46					
1086	n/a	-96	n/a	-56.4	n/a	10	n/a	n/a	~5	Negative crystal	1086.6-FI-56	0.004	0.021	0.268	0.469	26.8
1193	n/a	-100	n/a	-56	-3	9.4	n/a	n/a	~10	Negative crystal	1193-FI-59	0.212	1.222	0.221	0.506	22.1
1193	n/a	-100	n/a	-55.9	n/a	8.8	n/a	n/a	~7.5	Negative crystal	1193-FI-61					
1193	-35	-100	-35	-56.1	-3.2	8.8	n/a	n/a	~7.5	Negative crystal	1193-FI-35					
1193	n/a	-107.1	n/a	-56	n/a	8.2	n/a	n/a	~10	Negative crystal	1193-FI-36_1					
1193	n/a	-99.7	n/a	-55.1	-3.4	10	n/a	n/a	~7.5	Negative crystal	1193-FI-39					
1193	-31.9	n/a	n/a	n/a	n/a	6.5	n/a	n/a	~7.5	Negative crystal	1193-FI-14					
1193	-8	n/a	n/a	n/a	n/a	11.2	n/a	n/a	~7.2	Negative crystal	1193-FI-15	0.004	0.021	0.268	0.469	26.8
1193	-32.7	n/a	n/a	n/a	n/a	9.2	n/a	287.8	~5	Negative crystal	1193-FI-16	0.281	1.615	0.268	0.472	26.8
1193	-9.5	n/a	n/a	n/a	n/a	8.2	n/a	n/a	~7.5	Negative crystal	1193-FI-21.4					
1193	-41.2	n/a	n/a	n/a	n/a	5.2	n/a	n/a	~7.6	Negative crystal	1193-FI-25	1.623	8.663	0.184	0.562	18.4
1193	n/a	n/a	n/a	n/a	n/a	3.5	n/a	n/a	~5	Negative crystal	1193-FI-27					
1193	-41	n/a	n/a	n/a	n/a	6.1	n/a	n/a	~5	Negative crystal	1193-FI-28					
1193	n/a	n/a	n/a	n/a	n/a	7.4	n/a	n/a	~7.5	Negative crystal	1193-FI-30					
1193	-28.5	n/a	-101	-55.3	1	6	n/a	502.3	~15	Negative crystal	1193-FI-7, DB	1.363	7.376	0.029	0.897	2.9
1193	-46.6	-94.1	-27.7	-55.6	-4	8.4	n/a	533	~12.5	Negative crystal	1193-FI-21.4					
1193	-28.4	-94	n/a	-56.4	-4	8.8	n/a	300	~12.5	Negative crystal	1193-FI-21.4	0.419	2.389	0.221	0.509	22.1
1193	n/a	-94.1	n/a	-55.8	-4	8.2	n/a	300	~7.5	Negative crystal	1193-FI-21.4					
1201	n/a	-100	n/a	-56.4	-2	10.1	n/a	n/a	~10	Negative crystal	1201.1-FI-36	0.004	0.021	0.222	0.504	22.2
1201	-48.2	-101	-35	n/a	-3	10.1	n/a	n/a	~10	Negative crystal	1201.1-FI-35	0.004	0.021	0.268	0.469	26.8
1201	n/a	-100	n/a	-56.4	-2	9.6	n/a	n/a	~12.5	Undulating	1201.1-FI-39	0.142	0.825	0.268	0.47	26.8
1201	n/a	-100	n/a	-56.4	-2	n/a	n/a	n/a	~10	Undulating	1201.1-FI-39	0.004	0.021	0.268	0.469	26.8
1201	n/a	-100	n/a	-56.4	-2	10.1	n/a	n/a	~15	Negative crystal	1201.1-FI-39	0.004	0.021	0.268	0.469	26.8
1201	n/a	-101	n/a	-56	n/a	8.6	n/a	n/a	~10	Negative crystal	1201.1-FI-40					
1201	n/a	-101	n/a	-56	n/a	8.6	n/a	n/a	~12.5	Negative crystal	1201.1-FI-40	0.487	2.77	0.268	0.474	26.8
1201	n/a	-101	n/a	-56	n/a	8.6	n/a	n/a	~7.5	Negative crystal	1201.1-FI-40					
1201	n/a	-101	n/a	-56	n/a	8.6	n/a	n/a	~7.5	Negative crystal	1201.1-FI-40					
1201	n/a	-99.5	n/a	-56	n/a	n/a	n/a	n/a	~12.5	Undulating	1201-FI-52					
1201	n/a	-99.5	n/a	-56	n/a	n/a	n/a	n/a	~15	Negative crystal	1201-FI-52_1					
1201	-35	-101	n/a	-56	n/a	8.6	n/a	n/a	~12.5	Undulating	1201-Fi-53	0.487	2.77	0.184	0.546	18.4
1201	n/a	96	n/a	-55.8	n/a	8	n/a	338	~7.5	Negative crystal	1201.1-FI-1.1					
1201	n/a	96	n/a	-55.8	n/a	8	n/a	338	~7.5	Negative crystal	1201.1-FI-1.2					

B75C															
Sample	T_F-clath	T_F-H_2O	T_F-CO_2	T_m-CO_2	T_m-H_2O	T_m-clath	T_H-CO_2	T_H-H_2O	Size (µm)	Shape	Photo ID	Molal NaCl	Wt% NaCl	Bulk XCO2	Bulk Den	Mol% CO2
1201	n/a	96	n/a	-55.8	n/a	8	n/a	358	~7.5	Negative crystal	1201.1-FI-1.2	0.693	3.89	0.267	0.476	26.7
1201	n/a	96	n/a	-55.8	n/a	8	n/a	358	~10	Negative crystal	1201.1-FI-1.3					
1201	n/a	96	n/a	-55.8	n/a	8	n/a	358	~7.5	Negative crystal	1201.1-FI-1.3					
1201	-33.6	-94.1	n/a	-55.3	-3.5	8.8	n/a	385	~12.5	Undulating	1201.1-Fi-13	0.419	2.389	0.348	0.805	34.8
1201	-32.4	-95	n/a	-55.3	-1.8	6.8	n/a	393.1	~7.5	Undulating	1201.1-FI-18					
1201	n/a	-94	-11	-56.6	-4.6	7.1	23.1	393.1	n/a	Undulating	1201.1-FI-31	0.997	5.507	0.057	0.709	5.7
1201	-29.1	n/a	-13.8	n/a	-0.6	8.1	23.5	393.1	~12.5	Negative crystal	1201.1-FI-11					
1343	n/a	-97	n/a	-56.3	n/a	9	n/a	260.2	~15	Negative crystal	1343-FI-75					
1343	n/a	-97	n/a	-56.3	n/a	9	n/a	202.7	~12.5	Undulating	1343-FI-75					
1343	n/a	-100	n/a	-56	n/a	9.5	n/a	223	~7.5	Negative crystal	1343-FI-76					
1343	n/a	-100	n/a	-56	n/a	n/a	n/a	223.1	~7.5	Negative crystal	1343-FI-76	0.35	2.003			
1343	n/a	-100	n/a	-56	n/a	9.5	n/a	223.2	~10	Negative crystal	1343-FI-76					
1343	n/a	-98	n/a	-55.5	n/a	n/a	n/a	202.7	~10	Negative crystal	1343-FI-77					
1343	n/a	-100	-32	-55.9	-3	9.2	n/a	210.7	~10	Negative crystal	1343-FI-78					
1343	n/a	-99.8	-32	-56	n/a	8	n/a	300.2	~7.5	Negative crystal	1343-FI-80	0.693	3.89	0.267	0.476	26.7
1343	n/a	n/a	-32	-55.8	-3	10	n/a	300.3	~10	Negative crystal	1343-FI-81					
1343	n/a	-96	n/a	-56	-2.6	6	n/a	260.2	~10	Negative crystal	1343-FI-83					
1343	n/a	-100	n/a	-56	n/a	6	n/a	260.3	~10	Negative crystal	1343-FI-83					
1343	n/a	-99.9	n/a	-56	n/a	9.1	n/a	202.7	~7.5	Negative crystal	1343-FI-87					
1343	n/a	-99.9	n/a	-56	n/a	9.1	n/a	202.8	~7.5	Negative crystal	1343-FI-87					
1343	-39.1	-101	-32	-55.5	n/a	9.3	n/a	N/a	~12.5	Negative crystal	1343-FI-93					
1343	-39.1	-101	-32	-55.5	n/a	9.3	n/a	330.3	~12.5	Negative crystal	1343-FI-93					
1343	n/a	-101.4	n/a	-56	n/a	9	n/a	n/a	~10	Negative crystal	1343-FI-49	0.35	2.003	0.268	0.473	26.8
1343	-46	-100.9	-32	-55.3	-2.5	8.5	n/a	n/a	~12.5	Undulating	1343-FI-50	0.522	2.959	0.268	0.474	26.8
1343	-35	-101.6	n/a	-55.7	-3.1	8.8	n/a	n/a	~7.5	Undulating	1343-FI-51	0.419	2.389	0.268	0.473	26.8
1343	-35	-101.6	n/a	-55.7	-3.1	8.8	n/a	n/a	~7.5	Undulating	1343-FI-51	0.419	2.389	0.268	0.473	26.8
1343	n/a	-101.3	n/a	-56.2	n/a	11.4	n/a	n/a	~10	Negative crystal	1343-FI-54	0.004	0.021	0.268	0.469	26.8
1343	n/a	-102.1	-32.4	-56	-3	9.3	n/a	n/a	~7.5	Negative crystal	1343-FI-56					
1343	n/a	-101.3	n/a	-56.6	n/a	9.8	n/a	n/a	~10	Undulating	1343-FI-57	0.073	0.425	0.222	0.504	22.2
1343	n/a	-101.5	-32	-56.3	n/a	9.4	n/a	n/a	~10	Negative crystal	1343-FI-60	0.212	1.222	0.268	0.471	26.8
1343	-39.2	-100.5	-30	-56.6	-3	10	n/a	n/a	~12.5	Negative crystal	1343-FI-61	0.004	0.021	0.222	0.504	22.2
1343	n/a	-98	n/a	-56.6	n/a	9.8	n/a	n/a	~7.5	Negative crystal	1343-FI-62					
1343	n/a	-100.2	n/a	-56.2	-3	10.1	n/a	n/a	~10	Negative crystal	1343-FI-73	0.004	0.021	0.268	0.469	26.8
1343	n/a	-101	n/a	-55.8	n/a	10	n/a	n/a	~7.5	Negative crystal	1343-FI-74					
1343	n/a	-101	n/a	-55.8	n/a	10	n/a	n/a	~7.5	Negative crystal	1343-FI-74					
1343	n/a	-101	n/a	-55.8	n/a	10	n/a	n/a	~7.5	Negative crystal	1343-FI-74					
1343	-31.6	-101	-31.6	-55.8	-2.2	10	n/a	n/a	~12.5	Negative crystal	1343-FI-9					
1343	-31.6	-101	-31.6	-55.8	-2.2	10	n/a	n/a	~7.5	Negative crystal	1343-FI-9					
1343	-31.6	-101	-31.6	-55.8	-2.2	10	n/a	n/a	~7.5	Negative crystal	1343-FI-9					
1343	n/a	-100	n/a	-55.6	n/a	n/a	n/a	n/a	~10	Negative crystal	1343-FI-13					
1343	n/a	-97.6	n/a	-55.8	n/a	10.3	n/a	112.7	~7.5	Negative crystal	1343-FI-22					
1343	n/a	-99.3	n/a	-56	n/a	10.2	n/a	112.7	~5	Negative crystal	1343-FI-23					

B75C															
Sample	T_F-clath	T_F-H_2O	T_F-CO_2	T_m-CO_2	T_m-H_2O	T_m-clath	T_H-CO_2	T_H-H_2O	Size (µm)	Shape	Photo ID	Molal NaCl	Wt% NaCl	Bulk XCO2	Bulk Den	Mol% CO2
1343	n/a	-98.5	n/a	-56	-2.7	11.2	n/a	n/a	~5	Negative crystal	1343-FI-25	0.004	0.021	0.222	0.504	22.2
1343	n/a	-100	n/a	-55.6	n/a	n/a	n/a	101.1	~7.5	Negative crystal	1343-FI-38					
1343	n/a	-100	n/a	-55.7	n/a	n/a	n/a	200	~7.5	Negative crystal	1343-FI-42					
1343	n/a	-100	n/a	-55.7	-4.4	8	n/a	200	~7.5	Negative crystal	1343-FI-42					
1343	n/a	-98.5	n/a	-55.6	n/a	n/a	n/a	209.8	~7.5	Undulating	1343-FI-43					
1343	-46	-98	-32	-55	-3	10	28.8	250	~10	Negative crystal	1343-FI-79					
1343	-56.5	-100	-37.6	-55.6	-4	6.4	n/a	371.4	~12.5	Negative crystal	1343-FI-26					
1343	-53.6	-96.2	-33	-55.6	-3.3	10	n/a	336.9	~12.5	Negative crystal	1343-FI-27	0.004	0.021	0.062	0.747	6.2
1343	-49.1	-97.4	n/a	-55.8	-2.8	10	n/a	336.9	~10	Negative crystal	1343-FI-28					

APPENDIX F

UNPROCESSED LA-ICP-MS DATA

Unprocessed LA-ICP-MS data from selected fluid inclusions for the footwall and hanging wall fluid inclusion groups. Numbers in red are detection limits for particular elements in individual inclusions and indicate that the element was either at or below the limit of detection. Numbers in black represent absolute concentrations for an element in an inclusion.

B15D		Li7	Na23	Si28	S34	K39	Ca44	V51	Mn55	Fe57	Cu65	Zn66	As75
Location	Photo ID	µg/g	µg/g	µg/g	µg/g	µg/g	µg/g	µg/g	µg/g	µg/g	µg/g	µg/g	µg/g
KF4D-2	KF4D-2-FI-7	7.47	7,770.09	2,670.72	3,389.35	75,681.06	1,338.42	5.59	588.71	583.58	28.88	58.82	37.34
KF3C-16	KF3C-16-FI-29	96.59	21,767.47	30,573.47	36,423.19	9,131.99	13,889.11	66.48	377.88	6,520.49	347.13	599.66	411.94
KF3C-16	KF3C-16-FI-53	1,408.02	16,024.12	151,625.62	184,494.01	46,749.73	92,845.26	411.58	2,050.87	36,998.52	2,032.48	4,310.63	2,316.47
KF3C-16	KF3C-16-FI-32	74.68	16,103.13	27,522.01	32,900.90	8,204.11	12,568.95	57.24	339.36	5,865.10	301.70	524.73	369.71
KF3C-16	KF3C-16-FI-32	74.68	16,103.13	27,522.01	32,900.90	8,204.11	12,568.95	57.24	339.36	5,865.10	301.70	524.73	369.71
KF3C-16	KF3C-16-FI-51	211.79	15,205.79	37,800.67	46,164.93	11,664.81	21,993.98	90.60	499.90	8,835.92	484.00	945.08	577.58
KF3C-16	KF3C-16-FI-28	192.17	15,849.86	32,604.82	39,116.74	9,759.06	15,044.29	74.32	402.83	7,053.20	3,689.25	652.66	451.00
KF3C-16	KF3C-16-FI-40	37.50	3,464.62	10,664.37	13,261.43	3,339.99	11,995.82	24.08	149.51	2,870.74	152.54	311.35	175.88
KF4D-2	KF4D-2-FI-9	13.74	2,192.61	19,493,282.92	20,811.16	673.10	25,371.55	5.75	28.92	513.68	81.18	49.93	31.29
KF4D-2	KF4D-2-FI-9	34.05	1,114.38	5,910.32	7,450.12	39,721.27	2,932.07	13.55	78.01	1,322.11	616.76	837.57	85.21
KF3C-16	KF3C-16-FI-26	82.96	16,958.31	6,555.15	7,741.36	4,396.61	2,984.69	12.51	80.00	2,799.86	3,049.41	178.48	88.80
KF3C-16	KF3C-16-FI-42	36.59	17,954.64	6,241.64	7,650.34	3,104.68	3,869.13	12.67	82.76	2,876.01	6,227.14	227.58	94.71
KF4D-2	KF4D-2-FI-27	34.92	16,539.66	3,204,091.18	50,330.54	1,120.53	4,735.78	11.82	49.72	909.66	226.13	95.90	53.93
KF3C-16	KF3C-16-FI-27	45.01	14,771.87	7,922.29	9,345.80	4,450.76	3,690.31	19.54	98.60	1,611.08	948.43	169.55	108.65
KF4D-2	KF4D-2-FI-10	39.26	5,469.56	5,736.56	7,281.56	33,143.48	2,973.47	15.14	136.65	1,423.11	622.91	139.08	84.25
KF4D-2	KF4D-2-FI-24	125.76	8,263.20	21,664,104.36	230,990.77	9,593.05	16,410.85	73.30	414.03	7,639.79	4,028.07	718.97	448.61
KF3C-16	KF3C-16-FI-43	138.35	11,751.03	17,901.73	23,217.43	5,528.04	10,881.96	37.59	235.96	4,225.83	4,628.12	475.05	266.98
KF3C-16	KF3C-16-FI-30	138.09	13,973.52	28,885.54	34,409.36	8,639.88	13,367.56	64.49	355.60	6,282.93	9,279.66	566.29	396.67
KF3C-16	KF3C-16-FI-31	138.09	13,973.52	28,885.54	34,409.36	8,639.88	13,367.56	64.49	355.60	6,282.93	9,279.66	566.29	396.67
KF3C-16	KF3C-16-FI-37	79.30	8,464.18	9,286.80	11,646.67	3,815.21	10,146.14	24.73	129.09	2,438.08	141.51	285.54	153.60

B15D		Rb85	Sr88	Mo95	Ag107	Sn118	Cs133	Ba137	La139	W182	Au197	Tl205	Pb208
Location	Photo ID	µg/g	µg/g	µg/g	µg/g	µg/g	µg/g	µg/g	µg/g	µg/g	µg/g	µg/g	µg/g
KF4D-2	KF4D-2-FI-7	18.83	1.58	11.36	3.73	37.69	14.27	21.27	4.33	17.56	2.32	1.41	39.48
KF3C-16	KF3C-16-FI-29	42.86	18.79	152.09	47.99	392.94	19.31	143.00	8.44	78.69	25.80	14.78	77.92
KF3C-16	KF3C-16-FI-53	224.07	139.25	719.48	259.80	2,190.33	88.53	737.14	58.55	442.42	174.69	113.09	419.11
KF3C-16	KF3C-16-FI-32	30.88	21.84	114.34	39.22	371.56	13.46	129.98	6.54	74.06	23.71	13.59	77.53
KF3C-16	KF3C-16-FI-32	30.88	21.84	114.34	39.22	371.56	13.46	129.98	6.54	74.06	23.71	13.59	77.53
KF3C-16	KF3C-16-FI-51	42.06	21.07	178.46	68.10	544.14	15.79	166.04	16.53	107.40	35.45	21.85	97.31
KF3C-16	KF3C-16-FI-28	49.40	20.59	163.19	57.57	453.30	17.61	184.29	16.69	116.15	34.00	20.29	92.55
KF3C-16	KF3C-16-FI-40	12.61	142.21	40.60	18.96	175.33	4.79	44.52	3.82	24.86	10.79	5.85	26.87
KF4D-2	KF4D-2-FI-9	12.22	2.16	11.08	4.32	899.69	1.27	12.86	1.28	6.89	2.31	1.70	6.14
KF4D-2	KF4D-2-FI-9	7.56	3.99	65.85	8.67	82.19	3.46	29.77	2.74	48.27	5.76	3.17	15.30
KF3C-16	KF3C-16-FI-26	10.72	50.19	26.28	9.12	82.16	3.59	19.29	1.13	12.02	4.75	3.07	16.72
KF3C-16	KF3C-16-FI-42	23.69	13.53	26.04	10.23	99.22	4.18	30.89	2.80	15.77	5.84	2.30	56.94
KF4D-2	KF4D-2-FI-27	6.29	3.85	27.58	12.10	146.25	3.16	44.15	2.33	15.10	5.79	3.72	12.31
KF3C-16	KF3C-16-FI-27	16.26	6.12	45.69	14.77	108.26	4.31	35.80	3.50	27.19	8.06	4.25	21.40
KF4D-2	KF4D-2-FI-10	8.67	5.11	34.35	11.00	87.55	4.28	31.31	3.35	18.96	7.29	3.24	31.45
KF4D-2	KF4D-2-FI-24	86.52	27.95	170.36	68.73	814.12	21.69	130.19	15.26	93.05	37.90	22.61	88.94
KF3C-16	KF3C-16-FI-43	20.76	42.12	76.61	27.41	460.30	8.91	68.01	8.58	46.39	18.67	12.87	45.25
KF3C-16	KF3C-16-FI-30	34.44	40.71	122.14	43.51	378.67	13.75	111.77	13.14	75.62	25.68	12.87	82.23
KF3C-16	KF3C-16-FI-31	34.44	40.71	122.14	43.51	378.67	13.75	111.77	13.14	75.62	25.68	12.87	82.23
KF3C-16	KF3C-16-FI-37	14.45	18.72	45.70	19.21	153.49	5.59	48.11	4.73	29.27	11.71	6.96	27.41

B15C		Li7	Na23	Si28	S34	K39	Ca44	V51	Mn55	Fe57	Cu65	Zn66	As75
Location	Photo ID	µg/g	µg/g	µg/g	µg/g	µg/g	µg/g	µg/g	µg/g	µg/g	µg/g	µg/g	µg/g
KF4D-2	KF4D-2-FI-3	217.03	6,602.99	78,323,146.07	95,923.30	11,250.10	98,488.42	84.55	477.27	8,583.73	424.61	861.49	511.19
KF4D-2	KF4D-2-FI-3	101.48	27,844.49	23,053.17	29,953.27	86,392.40	12,243.92	58.33	942.21	20,404.15	319.53	572.80	341.25
KF4D-2	KF4D-2-FI-2	111.74	35,544.30	13,444.39	17,313.16	25,499.97	7,408.08	36.75	183.62	3,199.77	8,927.42	5,487.18	200.23
KF3D-19	KF3D-19-FI-27	472.61	18,875.09	84,488.73	107,909.49	28,483.98	44,667.08	208.52	1,166.22	20,209.99	1,021.66	1,959.05	1,256.59
KF3D-19	KF3D-19-FI-25	87.20	18,166.98	16,171.15	20,418.00	5,200.47	8,340.42	34.04	223.84	3,786.13	172.66	355.22	234.37
KF3C-16	KF3C-16-FI-50	37.50	3,464.62	10,664.37	13,261.43	3,339.99	11,995.82	24.08	149.51	2,870.74	152.54	311.35	175.88
KF3C-16	KF3C-16-FI-54	37.50	3,464.62	10,664.37	13,261.43	3,339.99	11,995.82	24.08	149.51	2,870.74	152.54	311.35	175.88
KF4D-2	KF4D-2-FI-29	27.31	5,107.86	3,454,584.05	4,001.39	991.65	5,089.23	10.04	43.52	818.04	51.30	100.70	47.68
KF4D-2	KF4D-2-FI-32	31.88	2,063.72	6,758.52	8,401.87	15,476.43	3,330.48	14.63	90.64	1,574.82	78.31	161.09	97.93
KF4D-2	KF4D-2-FI-32	15.75	572.43	3,193.42	3,971.54	19,452.86	1,529.19	7.05	95.78	1,431.17	37.40	182.43	45.22
KF4D-2	KF4D-2-FI-33	67.28	5,909.72	13,493.80	17,040.58	5,221.34	6,534.70	42.94	184.39	3,121.02	161.36	322.11	196.05
KF4D-2	KF4D-2-FI-7_1	19.88	2,676.40	2,162,033.37	6,850.79	1,734.44	8,396.10	10.58	72.54	1,197.21	56.03	122.05	75.97
KF4D-2	KF4D-2-FI-31	4.48	593.21	6,354,339.32	5,399.43	188.23	9,160.17	1.66	8.14	149.34	36.86	14.77	18.75
KF3C-16	KF3C-16-FI-34_2	5.40	4,941.51	998.87	1,185.02	473.12	850.69	2.28	12.32	203.35	10.54	18.38	13.66
KF4D-2	KF4D-2-FI-35	3.13	794.12	4,327,751.80	5,397.46	718.58	5,443.43	1.56	8.77	255.91	78.49	188.89	9.61
KF3C-16	KF3C-16-FI-25	0.43	52.52	136.79	165.11	41.23	68.25	0.25	1.71	30.58	1.89	2.91	1.91
KF3C-16	KF3C-16-FI-25	0.43	52.52	136.79	165.11	41.23	68.25	0.25	1.71	30.58	1.89	2.91	1.91
KF3C-16	KF3C-16-FI-25	0.43	52.52	136.79	165.11	41.23	68.25	0.25	1.71	30.58	1.89	2.91	1.91
KF3C-16	KF3C-16-FI-25	0.37	71.79	147.20	176.77	44.33	73.26	0.29	1.87	32.09	2.02	3.10	2.11
KF3C-16	KF3C-16-FI-34_1	0.16	71.27	33.39	39.68	18.17	15.61	0.06	0.41	7.18	0.37	0.64	0.45
KF3D-19	KF3D-19-FI-21	0.23	27.38	26.56	33.75	9.90	94.59	1.05	0.38	120.64	0.46	4.40	0.41
KF3D-19	KF3D-19-FI-24	2.49	82.61	287.19	362.24	2,103.83	156.28	3.73	7.12	695.97	3.29	6.71	4.31
KF3D-19	KF3D-19-FI-24	0.76	82.61	117.40	149.55	37.37	61.62	0.28	1.63	28.22	1.44	2.64	1.74

B15C		Rb85	Sr88	Mo95	Ag107	Sn118	Cs133	Ba137	La139	W182	Au197	Tl205	Pb208
Location	Photo ID	µg/g	µg/g	µg/g	µg/g	µg/g	µg/g	µg/g	µg/g	µg/g	µg/g	µg/g	µg/g
KF4D-2	KF4D-2-FI-3	40.90	82.55	178.78	63.49	3,397.68	19.88	193.67	18.94	101.23	36.88	23.78	156.17
KF4D-2	KF4D-2-FI-3	31.32	183.73	126.41	48.71	337.52	11.37	110.80	12.02	82.91	22.13	15.12	65.02
KF4D-2	KF4D-2-FI-2	43.64	82.07	79.96	27.86	213.21	8.96	87.39	7.31	46.90	14.56	10.82	40.19
KF3D-19	KF3D-19-FI-27	120.54	72.84	434.94	158.25	1,267.61	47.80	435.70	47.07	215.87	82.37	69.25	227.16
KF3D-19	KF3D-19-FI-25	22.24	24.45	73.46	24.60	241.28	10.91	72.61	7.78	35.02	15.52	8.38	41.59
KF3C-16	KF3C-16-FI-50	12.61	142.21	40.60	18.96	175.33	4.79	44.52	3.82	24.86	10.79	5.85	26.87
KF3C-16	KF3C-16-FI-54	12.61	142.21	40.60	18.96	175.33	4.79	44.52	3.82	24.86	10.79	5.85	26.87
KF4D-2	KF4D-2-FI-29	5.81	3.42	25.32	8.20	145.43	2.94	58.39	2.07	14.19	4.83	3.31	11.22
KF4D-2	KF4D-2-FI-32	10.09	18.31	45.23	12.09	98.62	3.98	31.42	3.69	27.99	6.79	4.89	20.04
KF4D-2	KF4D-2-FI-32	18.67	13.14	17.28	5.50	47.16	1.68	42.10	1.44	9.59	3.16	2.17	9.13
KF4D-2	KF4D-2-FI-33	17.78	9.71	71.03	25.40	202.91	9.94	73.51	7.18	42.58	13.61	7.96	38.79
KF4D-2	KF4D-2-FI-7_1	7.22	72.44	23.68	7.92	74.31	2.64	21.14	2.12	14.88	3.98	2.01	13.78
KF4D-2	KF4D-2-FI-31	1.81	0.64	3.76	1.33	268.81	0.49	3.94	0.42	2.15	0.84	0.51	1.93
KF3C-16	KF3C-16-FI-34_2	2.17	18.82	4.41	1.79	13.42	1.14	4.06	0.51	2.87	0.93	0.47	2.69
KF4D-2	KF4D-2-FI-35	7.20	1.79	3.29	0.99	208.42	0.45	8.87	0.38	1.96	0.57	0.50	1.87
KF3C-16	KF3C-16-FI-25	0.18	0.17	0.67	0.25	2.06	0.06	0.31	0.05	0.37	0.12	0.04	0.38
KF3C-16	KF3C-16-FI-25	0.18	0.17	0.67	0.25	2.06	0.06	0.31	0.05	0.37	0.12	0.04	0.38
KF3C-16	KF3C-16-FI-25	0.18	0.17	0.67	0.25	2.06	0.06	0.31	0.05	0.37	0.12	0.04	0.38
KF3C-16	KF3C-16-FI-25	0.15	0.16	0.62	0.24	2.22	0.08	0.54	0.05	0.39	0.14	0.07	0.40
KF3C-16	KF3C-16-FI-34_1	0.09	0.09	0.16	0.06	0.44	0.03	0.17	0.02	0.10	0.03	0.02	0.18
KF3D-19	KF3D-19-FI-21	0.06	0.06	0.49	0.12	0.41	0.02	0.82	14.29	0.10	0.07	0.02	0.09
KF3D-19	KF3D-19-FI-24	10.68	0.71	1.56	0.83	7.49	0.19	21.73	0.17	0.84	0.35	0.15	0.74
KF3D-19	KF3D-19-FI-24	0.16	0.92	0.55	0.19	1.75	0.08	0.53	0.06	0.29	0.14	0.08	0.36

B15		Li7	Na23	Si28	S34	K39	Ca44	V51	Mn55	Fe57	Cu65	Zn66	As75
Location	Sample ID	µg/g	µg/g	µg/g	µg/g	µg/g	µg/g	µg/g	µg/g	µg/g	µg/g	µg/g	µg/g
1086	1086.6-FI-48	705.64	70,197.10	128,954.25	173,981.10	47,266.94	63,640.12	214.78	2,437.46	21,911.24	1,443.33	3,456.37	2,244.88
1193	1193-FI-56	43.42	6,237.02	6,445.23	9,716.01	2,498.32	95,027.61	70.12	5,094.56	28,652.94	131.78	541.57	106.09
1086	1086.6-FI-44	7,972.25	35,461.67	7,595.09	10,203.16	20,167.53	9,773.43	26.35	5,804.37	23,055.21	516.10	5,473.26	131.72
1086	10866-FI-55	23.45	26,390.25	9,376.06	12,885.35	2,372.50	5,013.78	16.01	112.92	1,654.90	7,933.10	270.20	165.74
1086	1086.6-FI-54	147.56	13,207.01	33,758.39	46,006.42	8,709.98	23,080.70	55.15	408.27	5,905.97	6,498.97	926.09	594.72
1086	1086.6-FI-42	59.18	14,162.22	14,047.32	18,932.00	3,740.10	6,783.84	29.16	547.85	2,520.21	3,690.88	646.23	239.65
1201	1201-FI-48	51.88	9,061.98	8,458.04	9,812.82	5,119.04	4,238.44	18.72	109.84	1,589.07	107.08	204.15	130.48

B15		Rb85	Sr88	Mo95	Ag107	Sn118	Cs133	Ba137	La139	W182	Au197	Tl205	Pb208
Location	Sample ID	µg/g	µg/g	µg/g	µg/g	µg/g	µg/g	µg/g	µg/g	µg/g	µg/g	µg/g	µg/g
1086	1086.6-FI-48	463.55	9,416.29	452.91	207.32	1,663.89	111.57	1,028.21	40.84	269.69	91.25	68.39	366.65
1193	1193-FI-56	9.64	165.49	28.06	12.49	79.73	2.79	22.65	12.61	19.43	6.25	2.59	76.92
1086	1086.6-FI-44	93.56	184.60	27.56	13.35	276.88	15.03	35.96	5.08	15.27	7.39	4.84	1,084.49
1086	10866-FI-55	27.29	30.09	31.13	12.35	122.49	3.02	15.24	1.79	13.68	6.81	4.59	46.88
1086	1086.6-FI-54	31.79	21.22	133.17	53.34	438.51	16.39	120.07	11.79	65.43	21.75	17.26	89.83
1086	1086.6-FI-42	30.97	8.31	51.47	24.13	538.51	6.99	60.40	5.25	30.47	11.32	4.41	69.53
1201	1201-FI-48	16.37	10.57	40.66	13.34	134.71	4.64	43.06	3.49	27.44	8.56	5.59	35.46

B30D		Li7	Na23	Si28	S34	K39	Ca44	V51	Mn55	Fe57	Cu65	Zn66	As75
Location	Sample ID	µg/g	µg/g	µg/g	µg/g	µg/g	µg/g	µg/g	µg/g	µg/g	µg/g	µg/g	µg/g
1343	1343-FI-52	1,202.44	76,763.88	55,505.25	72,432.55	15,203.78	43,878.83	348.34	5,108.82	54,662.55	894.18	4,161.16	911.06
1086	1086.6-FI-45	495.94	37,379.75	59,667.65	81,329.60	29,658.55	74,329.21	687.30	1,952.60	10,727.61	671.21	1,540.47	1,045.08
1086	1086.6-FI-50	12.56	1,359.89	2,936.38	12,229.31	819.29	137,280.42	5.31	13,799.45	35,566.55	29.19	1,865.31	50.55
1086	1086.6-FI-75	96.89	49,691.00	16,730.72	22,111.75	38,788.70	16,546.64	39.86	3,422.41	10,669.16	3,277.17	3,489.96	288.05
1193	1193-FI-40_2	110.98	47,104.15	12,323.40	21,748.18	15,534.89	18,095.32	31.45	4,620.76	4,059.47	416.63	1,645.74	240.21
1201	1201-FI-51	146.67	30,683.93	23,493.96	26,451.42	17,675.24	11,429.59	49.37	2,832.72	4,665.07	1,468.72	1,214.79	354.80
1201	1201-FI-51	146.67	30,683.93	23,493.96	26,451.42	17,675.24	11,429.59	49.37	2,832.72	4,665.07	1,468.72	1,214.79	354.80
1193	1193-FI-36	134.37	26,695.44	10,520.46	12,518.86	12,476.75	7,762.09	29.15	176.04	2,314.45	156.27	301.38	179.55
1343	1343-FI-14	19.96	2,947.48	3,854.69	4,576.55	1,226.00	2,304.54	8.55	150.50	804.18	431.85	274.22	56.17
1086	1086.6-FI-71	189.60	17,972.40	7,212.08	9,463.49	8,475.83	11,437.06	136.05	148.80	33,780.29	2,313.94	269.65	125.75
1201	1201-Fi-53	1,786.08	20,144.53	319,688.63	338,768.84	93,769.49	154,854.81	813.50	4,118.67	67,258.00	3,970.94	7,329.52	4,833.70
1086	1086.6-FI-49	203.78	17,680.19	43,013.68	57,484.35	11,370.51	21,379.77	92.02	523.61	7,913.53	12,224.13	1,234.42	755.54
1193	1193-FI-42	442.46	9,661.41	45,659.40	74,638.32	12,243.64	28,197.44	124.95	578.65	9,795.47	656.82	1,296.31	839.35
1201	1201-FI-52	46.91	15,744.91	4,098.37	4,555.67	5,943.22	7,592.03	8.39	51.36	787.42	48.77	95.18	61.06
1201	1201-FI-52	124.21	18,374.74	20,571.23	23,005.04	6,073.34	9,766.69	46.07	258.89	3,971.29	283.33	467.11	304.28
1343	1343-FI-52	403.15	89,536.69	80,857.00	101,510.36	33,295.30	70,213.02	152.37	17,513.24	31,252.25	854.44	11,100.47	1,261.21
1343	1343-FI-15	703.58	19,118.99	91,315.64	110,214.93	28,942.21	86,456.59	263.43	1,200.22	22,229.30	1,319.85	2,196.24	1,340.36
1201	1201-FI-46	95.84	16,461.33	5,031.20	5,793.15	1,698.48	3,710.06	10.99	449.96	972.70	65.58	125.32	77.49
1201	1201-FI-47	26.50	13,519.66	6,794.15	7,995.80	8,278.01	4,580.59	15.27	1,100.05	1,353.55	145.37	273.46	106.38
1086	1086.6-FI-72	51.03	4,607.22	6,973.34	9,167.97	2,481.55	24,935.57	14.36	207.76	1,344.58	276.21	180.62	121.02
1201	1201.1-FI-37	199.36	10,315.44	55,844.56	61,260.35	16,312.24	26,963.43	122.34	711.71	11,044.91	720.51	1,371.62	845.51
1193	1193-FI-40	105.42	7,136.87	17,885.70	29,646.43	9,214.38	12,370.29	44.49	230.17	3,668.45	265.99	490.14	327.03
1201	1201-FI-45	51.64	15,416.59	11,836.14	13,042.06	4,942.10	5,540.31	23.68	146.18	2,293.01	124.98	279.15	175.26
1201	1201-FI-49	166.67	13,223.54	22,786.12	26,202.87	7,433.03	11,546.21	70.41	977.91	4,846.20	1,254.08	831.99	359.10
1193	1193-FI-45	481.58	11,892.88	74,486.60	125,270.68	19,823.92	48,422.22	172.43	960.07	15,600.50	1,113.55	2,123.84	1,391.86

B30D		Rb85	Sr88	Mo95	Ag107	Sn118	Cs133	Ba137	La139	W182	Au197	Tl205	Pb208
Location	Sample ID	µg/g	µg/g	µg/g	µg/g	µg/g	µg/g	µg/g	µg/g	µg/g	µg/g	µg/g	µg/g
1343	1343-FI-52	67.56	182.73	225.92	100.92	778.48	41.81	358.29	22.53	160.09	63.73	40.21	1,399.07
1086	1086.6-FI-45	66.23	2,252.26	211.58	108.04	8,644.64	56.22	208.88	21.33	104.82	48.21	35.32	803.38
1086	1086.6-FI-50	12.52	126.81	9.74	3.79	117.90	2.35	17.54	15.63	4.91	1.86	1.29	744.87
1086	1086.6-FI-75	228.38	179.54	90.46	33.48	296.56	30.03	152.24	291.99	275.43	17.23	10.61	990.19
1193	1193-FI-40_2	58.16	205.58	53.98	24.01	181.75	8.84	340.59	5.11	36.61	13.04	9.39	424.66
1201	1201-FI-51	80.04	67.79	117.74	41.44	302.99	11.41	95.29	7.07	74.57	21.27	15.85	332.26
1201	1201-FI-51	80.04	67.79	117.74	41.44	302.99	11.41	95.29	7.07	74.57	21.27	15.85	332.26
1193	1193-FI-36	40.65	67.64	63.01	23.55	157.16	8.54	68.48	7.24	36.41	15.30	8.52	104.88
1343	1343-FI-14	7.19	18.47	20.14	7.11	99.99	3.60	18.40	2.01	12.81	3.88	2.41	64.82
1086	1086.6-FI-71	60.60	34.00	37.27	15.44	120.52	248.98	24.65	4.22	23.01	15.46	3.68	22.55
1201	1201-Fi-53	471.34	176.37	2,052.76	648.70	4,320.00	174.03	1,772.02	196.46	1,103.94	380.62	258.22	1,096.07
1086	1086.6-FI-49	43.84	99.05	193.31	78.62	595.60	20.08	168.56	21.42	107.73	40.34	32.67	123.67
1193	1193-FI-42	63.62	49.33	263.11	91.75	642.32	26.84	274.95	8,742.43	183.91	62.75	39.60	2,800.53
1201	1201-FI-52	50.43	76.50	237.76	5.37	55.49	5.16	18.27	0.85	11.91	3.00	1.04	55.24
1201	1201-FI-52	21.20	96.26	76.25	23.85	269.08	11.99	68.48	4.26	52.43	15.43	5.21	85.39
1343	1343-FI-52	85.97	240.88	225.43	109.03	1,008.70	107.63	529.23	11.22	268.87	53.11	37.64	3,645.38
1343	1343-FI-15	174.22	66.56	574.52	209.97	10,112.80	66.51	561.43	69.90	358.88	126.56	73.96	325.54
1201	1201-FI-46	25.13	17.38	20.54	7.87	71.02	9.26	16.56	1.95	14.41	4.20	2.38	15.76
1201	1201-FI-47	21.77	21.70	32.33	13.32	101.50	12.72	23.73	3.74	18.60	6.81	3.41	132.30
1086	1086.6-FI-72	12.80	34.39	24.82	11.49	93.07	4.06	31.99	3.32	16.64	6.01	4.51	53.22
1201	1201.1-FI-37	70.97	26.78	329.33	109.44	740.12	35.09	295.65	32.98	172.24	63.98	37.49	171.98
1193	1193-FI-40	27.47	12.33	82.66	34.19	251.30	10.27	88.10	8.71	263.27	19.60	13.20	54.88
1201	1201-FI-45	11.78	14.95	51.77	18.29	155.29	3.98	42.31	5.40	34.71	8.45	2.90	32.97
1201	1201-FI-49	688.80	36.36	149.30	51.52	316.84	15.28	160.03	12.24	92.22	30.03	20.07	169.88
1193	1193-FI-45	110.75	82.95	373.66	151.95	1,023.07	48.20	458.95	39.22	248.59	90.49	58.99	232.51

B30H		Li7	Na23	Si28	S34	K39	Ca44	V51	Mn55	Fe57	Cu65	Zn66	As75
Location	Sample ID	µg/g	µg/g	µg/g	µg/g	µg/g	µg/g	µg/g	µg/g	µg/g	µg/g	µg/g	µg/g
1086	1086.-FI-59	203.34	86,377.82	46,361.57	63,135.73	54,183.16	59,788.19	72.48	37,307.30	41,882.94	800.72	16,667.05	804.46
1086	1086.6-FI-58	527.08	71,527.77	46,397.31	64,131.05	57,399.81	84,838.69	85.99	22,211.67	28,241.97	506.81	10,941.48	817.16
1086	1086.6-FI-53	931.90	85,696.68	255,478.14	345,454.68	126,538.95	122,128.11	453.61	60,221.51	102,465.84	2,808.86	26,293.68	4,494.83
1086	1086.6-FI-43	545.22	56,684.48	104,277.97	139,125.21	77,329.54	98,368.48	5,284.97	8,957.08	19,582.88	1,257.81	6,484.56	1,825.40
1086	1086.6-FI-52	635.30	94,456.44	31,638.14	41,873.35	57,136.71	42,921.70	68.16	23,776.90	21,603.86	433.55	12,381.57	543.22
1086	1086.6-FI-76	55.29	93,225.40	23,944.77	31,503.99	73,481.04	33,927.58	44.03	26,320.82	37,506.21	706.40	8,478.66	412.07
1086	1086.6-FI-73	121.17	120,490.51	25,743.82	33,005.34	29,258.70	14,318.08	46.05	8,435.62	24,892.19	2,390.41	5,111.09	430.35
1086	1086.6-FI-61	196.69	74,132.59	48,190.05	61,239.60	69,655.43	71,617.14	97.57	13,381.76	29,429.36	556.75	5,816.24	814.22
1086	1086.6-FI-78	196.69	74,132.59	48,190.05	61,239.60	69,655.43	71,617.14	97.57	13,381.76	29,429.36	556.75	5,816.24	814.22
1086	1086.6-FI-64	159.15	99,971.52	23,057.35	29,301.41	45,145.57	41,052.58	51.87	9,154.13	9,993.78	278.53	2,473.37	393.04
1086	1086.6-FI-47	146.40	81,951.90	36,059.62	48,784.12	48,719.51	71,676.56	67.96	2,529.44	6,288.37	401.29	937.86	618.38

B30H		Rb85	Sr88	Mo95	Ag107	Sn118	Cs133	Ba137	La139	W182	Au197	Tl205	Pb208
Location	Sample ID	µg/g	µg/g	µg/g	µg/g	µg/g	µg/g	µg/g	µg/g	µg/g	µg/g	µg/g	µg/g
1086	1086.-FI-59	286.75	1,258.71	154.95	75.41	632.50	55.68	1,002.76	21.67	85.63	36.14	21.22	2,582.50
1086	1086.6-FI-58	335.58	856.35	171.67	73.68	661.81	37.64	992.64	41.89	92.52	40.89	27.47	1,572.82
1086	1086.6-FI-53	727.32	718.84	954.19	406.09	7,381.42	99.26	396.72	97.91	489.54	170.93	129.04	2,680.83
1086	1086.6-FI-43	877.33	1,548.21	425.50	189.67	1,382.26	57.66	510.92	49.38	188.85	91.03	75.84	13,650.00
1086	1086.6-FI-52	272.15	1,264.39	120.27	50.99	406.31	38.81	1,015.26	13.25	73.70	29.45	15.04	1,901.44
1086	1086.6-FI-76	371.13	1,034.21	95.23	31.68	326.49	23.98	1,338.54	9.52	58.56	19.02	10.58	1,507.53
1086	1086.6-FI-73	235.22	249.43	83.76	34.62	737.43	19.65	71.71	8.44	63.15	17.94	10.74	1,606.41
1086	1086.6-FI-61	354.15	1,108.49	237.30	484.85	614.86	63.28	692.28	20.59	152.38	39.51	25.76	1,387.78
1086	1086.6-FI-78	354.15	1,108.49	237.30	484.85	614.86	63.28	692.28	20.59	152.38	39.51	25.76	1,387.78
1086	1086.6-FI-64	276.47	3,899.61	100.20	36.82	462.06	45.05	713.80	11.96	58.88	21.65	12.29	555.33
1086	1086.6-FI-47	461.11	10,712.93	127.98	53.17	753.43	112.68	1,161.67	15.52	68.89	29.25	16.16	200.23

B75		Li7	Na23	Si28	S34	K39	Ca44	V51	Mn55	Fe57	Cu65	Zn66	As75
Location	Photo ID	µg/g	µg/g	µg/g	µg/g	µg/g	µg/g	µg/g	µg/g	µg/g	µg/g	µg/g	µg/g
1086	1086.6FI-39	1,355.09	3,052.20	11,296.93	14,981.18	3,099.85	33,586.08	30.42	332.92	2,405.31	4,655.87	309.37	197.93
1086	1086.6-Fi-38	129.02	8,513.00	23,241.69	30,376.01	9,155.21	16,491.59	40.33	778.35	4,130.48	16,037.42	602.43	394.10
1086	1086.6-FI-42	113.06	12,350.15	23,771.86	30,841.50	6,550.11	11,519.28	49.56	297.63	4,205.19	17,723.99	635.10	404.04
1086	1086.6-FI-74	12.41	1,097.95	4,547.44	22,172.64	1,234.67	30,848.41	8.83	55.56	878.24	1,090.49	116.68	78.23
1086	1086.6-FI-77	101.81	13,720.24	12,195.51	16,249.51	6,693.64	6,006.91	22.59	2,026.04	27,818.19	841.76	779.21	208.64
1086	1086.6-FI-56	45.02	9,051.10	7,170.78	9,783.48	1,857.37	7,072.93	14.87	151.94	1,332.24	1,753.36	210.02	127.80
1086	1086.6-FI-60	1,282.34	4,462.58	7,006.27	9,718.31	8,742.48	3,733.24	12.01	12,204.14	13,852.19	5,258.41	209.04	152.33
1201	1201.1-FI-32	3.07	2,035.56	1,067.74	1,158.25	4,360.20	502.44	2.70	13.41	212.08	24.40	61.96	15.98
1201	1201-FI-48_1	25.91	1,987.86	7,056.75	8,177.21	2,200.13	3,476.22	17.08	90.21	1,357.68	96.64	177.17	110.63

B75		Rb85	Sr88	Mo95	Ag107	Sn118	Cs133	Ba137	La139	W182	Au197	Tl205	Pb208
Location	Photo ID	µg/g	µg/g	µg/g	µg/g	µg/g	µg/g	µg/g	µg/g	µg/g	µg/g	µg/g	µg/g
1086	1086.6FI-39	16.73	74.95	73.40	22.58	156.83	8.62	69.33	5.67	36.35	14.94	9.74	165.58
1086	1086.6-Fi-38	24.42	23.37	97.80	41.05	1,275.52	11.68	100.09	8.63	61.09	19.38	10.91	131.05
1086	1086.6-FI-42	28.94	26.13	125.74	44.32	507.83	12.92	97.44	11.47	71.31	26.38	14.46	74.24
1086	1086.6-FI-74	4.71	111.96	18.28	7.15	59.23	1.96	23.38	5.09	11.50	3.87	1.53	13.75
1086	1086.6-FI-77	42.76	83.87	59.84	70.69	162.06	6.76	59.82	6.76	30.83	12.16	7.25	111.08
1086	1086.6-FI-56	7.57	5.55	33.26	132.43	96.82	4.10	19.26	3.24	17.47	7.47	2.98	21.49
1086	1086.6-FI-60	69.86	10.36	25.56	13.10	98.60	3.66	130.26	1,505.15	15.38	6.21	3.41	18.11
1201	1201.1-FI-32	1.38	3.26	5.48	1.38	21.26	0.41	4.41	0.52	3.41	1.04	0.39	3.63
1201	1201-FI-48_1	9.84	15.33	37.11	14.03	98.29	3.13	19.50	4.08	25.18	7.37	4.34	22.51

B20C		Li7	Na23	Si28	S34	K39	Ca44	V51	Mn55	Fe57	Cu65	Zn66	As75
Location	Photo ID	µg/g	µg/g	µg/g	µg/g	µg/g	µg/g	µg/g	µg/g	µg/g	µg/g	µg/g	µg/g
1343	1343-FI-48	189.05	32,211.18	33,633.64	40,684.57	8,565.43	26,099.52	64.73	3,056.73	6,307.10	379.96	1,611.55	501.94
1193	1193-FI-49	71.90	8,058.73	11,260.15	15,341.81	4,061.37	10,504.38	21.16	537.76	1,985.88	116.70	267.71	167.24
1343	1343-FI-66	77.62	15,303.06	16,402.35	56,062.15	4,718.20	7,439.48	30.27	2,330.00	4,503.52	159.83	659.68	217.96
1193	1193-FI-38	46.90	7,454.38	8,677.59	10,456.12	2,501.26	4,416.84	1,212.68	114.77	1,805.53	4,052.18	242.04	149.90
1193	1193-FI-40_1	45.06	6,785.81	10,006.29	16,857.69	3,352.53	6,923.92	22.01	130.80	2,052.87	142.07	276.70	184.16
1343	1343-FI-65	104.59	8,642.89	6,240.70	7,259.22	6,651.26	15,568.41	9.88	2,801.12	5,767.74	54.48	1,266.44	81.91
1193	1193-FI-49	71.90	8,058.73	11,260.15	15,341.81	4,061.37	10,504.38	21.16	537.76	1,985.88	116.70	267.71	167.24
1193	1193-FI-37	37.96	5,560.52	3,389.13	3,985.31	975.72	1,699.08	9.59	44.09	689.02	50.15	93.04	57.14
1343	1343-FI-71	73.47	3,245.51	4,898.46	19,428.05	1,441.74	2,258.72	9.29	58.37	16,556.95	261.08	101.64	93.97
1343	1343-FI-8	103.79	3,245.51	18,354.62	22,124.97	7,740.81	9,066.56	51.23	245.45	4,291.08	351.93	454.69	267.00
1343	1343-FI-53	28.87	2,462.65	4,948.06	6,042.35	1,267.24	3,488.19	10.36	584.74	1,321.04	52.32	194.21	73.09
1343	1343-FI-53	51.81	2,462.65	7,378.91	8,990.65	1,887.06	4,257.06	15.39	242.13	1,430.71	76.24	178.97	109.37
1343	1343-FI-24	22.24	2,462.65	4,848.78	5,699.53	1,545.27	2,307.07	10.33	62.58	1,064.68	56.89	101.94	68.20
1343	1343-FI-62	35.61	1,671.93	5,565.53	6,637.80	2,317.90	9,027.91	11.70	76.11	1,015.33	158.81	124.18	76.90
1343	1343-FI-62	3.47	1,671.93	584.10	689.54	252.86	298.49	1.29	16.07	110.78	54.15	12.76	8.01
1193	1193-FI-32	0.19	70.02	65.20	75.91	18.74	31.93	0.14	0.84	12.98	3.14	1.66	1.62
1193	1193-FI-32	0.79	51.80	147.90	172.92	42.58	72.35	0.32	1.90	27.23	7.57	3.92	3.33
1193	1193-FI-34	1.42	47.59	263.06	305.08	75.95	124.65	0.53	3.39	50.88	11.44	6.82	4.32
1201	1201.1-FI-34	0.52	53.24	112.12	121.93	32.88	53.94	0.26	1.42	21.82	1.28	2.53	1.70
1201	1201-FI-44	0.47	32.82	142.30	157.92	41.92	68.86	0.32	1.79	27.63	1.75	3.33	2.14
1343	1343-FI-72	0.23	82.61	36.53	42.93	34.35	97.04	0.07	1.37	49.69	3.28	1.59	0.51
1343	1343-FI-12	0.67	82.61	95.61	113.02	30.03	90.40	0.22	1.22	30.59	41.67	5.44	1.37
1343	1343-FI-25	0.47	82.61	105.62	123.43	33.94	70.08	0.23	16.10	22.82	1.18	6.64	1.46

B20C		Rb85	Sr88	Mo95	Ag107	Sn118	Cs133	Ba137	La139	W182	Au197	Tl205	Pb208
Location	Photo ID	µg/g	µg/g	µg/g	µg/g	µg/g	µg/g	µg/g	µg/g	µg/g	µg/g	µg/g	µg/g
1343	1343-FI-48	31.00	754.82	92.76	41.13	387.78	12.79	168.95	7.81	94.61	20.02	13.82	885.13
1193	1193-FI-49	12.66	76.62	41.60	17.29	139.67	3.69	47.37	5.14	29.24	9.93	5.57	136.19
1343	1343-FI-66	19.24	713.57	77.75	21.74	198.86	5.33	629.23	6.05	47.14	10.18	7.96	342.06
1193	1193-FI-38	14.43	10.11	54.99	20.52	133.73	5.84	46.61	6.60	31.72	12.74	8.44	29.76
1193	1193-FI-40_1	11.48	16.79	43.27	17.91	138.73	6.05	38.75	4.85	42.84	8.78	5.54	29.89
1343	1343-FI-65	19.58	136.69	21.45	8.05	73.92	10.47	55.20	0.90	14.99	3.53	2.56	472.08
1193	1193-FI-49	12.66	76.62	41.60	17.29	139.67	3.69	47.37	5.14	29.24	9.93	5.57	136.19
1193	1193-FI-37	3.76	3.26	18.95	7.79	50.05	2.29	47.99	1.81	10.27	4.21	2.53	10.56
1343	1343-FI-71	4.43	33.00	18.69	30.76	61.15	2.30	16.11	1.64	14.56	3.33	1.35	65.48
1343	1343-FI-8	27.67	16.21	118.66	42.41	278.12	10.68	117.71	13.12	63.68	26.61	17.00	92.84
1343	1343-FI-53	5.54	10.99	17.43	6.43	56.37	3.08	18.23	1.82	16.65	4.00	3.07	102.41
1343	1343-FI-53	11.21	13.88	27.67	10.55	88.63	4.34	24.63	2.61	21.45	5.82	2.34	21.49
1343	1343-FI-24	6.56	5.14	27.85	9.04	64.98	2.84	23.53	2.58	15.10	4.58	3.05	14.08
1343	1343-FI-62	6.09	3.70	21.05	7.77	62.53	2.23	17.64	1.81	16.47	4.42	2.61	15.41
1343	1343-FI-62	0.83	1.46	2.21	0.74	6.56	0.24	1.49	0.20	1.51	0.44	0.16	9.11
1193	1193-FI-32	0.08	0.05	0.29	0.12	1.17	0.03	0.28	0.02	0.20	0.06	0.04	0.20
1193	1193-FI-32	0.19	0.09	0.80	0.29	2.30	0.10	0.74	0.07	0.45	0.15	0.09	0.42
1193	1193-FI-34	0.34	0.12	1.21	0.50	3.68	0.16	1.44	0.13	0.75	0.29	0.11	0.80
1201	1201.1-FI-34	0.15	0.09	0.54	0.19	1.50	0.05	0.49	0.05	0.38	0.10	0.06	0.47
1201	1201-FI-44	0.18	0.10	0.74	0.26	1.95	0.08	0.73	0.05	0.43	0.14	0.09	0.46
1343	1343-FI-72	0.04	0.38	0.16	0.06	0.95	0.02	0.41	0.01	0.11	0.03	0.01	0.33
1343	1343-FI-12	0.13	0.42	0.47	0.17	1.38	0.05	0.45	0.03	0.29	0.09	0.05	0.97
1343	1343-FI-25	0.12	0.89	0.45	0.15	3.59	0.06	0.42	0.05	0.27	0.07	0.03	3.82

B75C		Li7	Na23	Si28	S34	K39	Ca44	V51	Mn55	Fe57	Cu65	Zn66	As75
Location	Photo ID	µg/g	µg/g	µg/g	µg/g	µg/g	µg/g	µg/g	µg/g	µg/g	µg/g	µg/g	µg/g
1343	1343-FI-50	21.93	11,640.56	3,391.75	4,094.17	1,501.24	2,070.88	7.41	48.68	640.64	157.33	82.65	50.46
1201	1201.1-FI-40	144.74	6,193.47	30,438.85	33,326.94	8,953.24	14,461.58	63.94	390.07	6,161.03	391.57	700.43	447.28
1201	1201-Fi-53	59.63	9,238.89	16,350.00	17,138.70	4,775.57	7,607.14	32.29	414.93	2,944.97	156.80	361.52	236.54
1343	1343-FI-51	165.41	9,398.20	36,950.92	44,989.43	9,456.16	31,197.60	66.65	428.19	7,421.73	782.66	867.52	554.75
1343	1343-FI-13	80.66	4,028.36	17,956.14	21,377.19	5,654.17	8,740.15	45.62	232.28	4,110.73	453.52	396.38	264.23
1343	1343-FI-49	93.41	7,879.70	16,405.60	20,360.08	4,177.22	11,062.69	30.68	1,157.64	3,302.73	449.53	835.86	253.29
1201	1201-FI-52	124.21	18,374.74	20,571.23	23,005.04	6,073.34	9,766.69	46.07	258.89	3,971.29	283.33	467.11	304.28
1201	1201-FI-52_1	124.21	18,374.74	20,571.23	23,005.04	6,073.34	9,766.69	46.07	258.89	3,971.29	283.33	467.11	304.28
1193	1193-FI-59	129.46	3,222.50	17,381.99	29,164.84	4,630.07	10,975.94	41.16	221.16	3,593.06	596.05	477.73	324.01
1343	1343-FI-60	19.58	4,807.29	2,702.68	3,249.27	3,267.73	1,419.31	5.87	49.32	4,472.36	93.25	100.20	37.50
1201	1201.1-FI-39	35.89	2,629.34	7,548.94	8,310.64	2,216.43	3,503.33	19.08	95.48	1,489.21	87.93	177.54	116.33
1343	1343-FI-57	52.90	1,671.93	8,223.00	9,758.65	2,139.09	4,494.98	16.77	276.16	1,682.05	86.04	576.86	114.95
1086	1086.6-FI-56	0.55	50.84	151.55	204.93	75.07	72.45	0.27	35.72	60.78	1.67	15.60	2.67
1201	1201.1-FI-36	0.23	51.57	59.26	80.78	47.44	28.08	0.13	0.74	252.55	0.66	1.94	0.89
1201	1201.1-FI-35	0.21	56.93	37.02	40.29	35.39	22.79	0.08	1.35	8.77	0.42	0.87	0.55
1201	1201.1-FI-39	4.56	71.83	551.41	608.48	162.80	260.65	1.44	7.01	110.19	7.05	12.86	8.36
1201	1201.1-FI-39	0.48	40.70	107.95	118.29	31.66	62.65	0.27	1.35	20.75	1.37	2.51	1.60
1343	1343-FI-54	0.57	82.61	80.81	98.59	24.33	46.71	0.14	2.81	15.79	2.19	3.36	1.21
1343	1343-FI-61	1.01	82.61	247.54	291.99	66.88	125.65	0.44	22.59	46.01	3.21	17.70	3.31
1343	1343-FI-73	0.09	82.61	19.41	22.60	6.35	9.21	0.04	0.95	3.84	0.71	3.94	0.26

B75C		Rb85	Sr88	Mo95	Ag107	Sn118	Cs133	Ba137	La139	W182	Au197	Tl205	Pb208
Location	Photo ID	µg/g	µg/g	µg/g	µg/g	µg/g	µg/g	µg/g	µg/g	µg/g	µg/g	µg/g	µg/g
1343	1343-FI-50	4.17	192.56	12.59	5.02	40.47	1.52	14.29	1.09	8.92	2.88	1.84	9.67
1201	1201.1-FI-40	41.20	22.36	149.19	55.08	409.19	15.37	136.27	10.23	103.41	28.33	12.52	94.75
1201	1201-Fi-53	19.36	4.49	72.84	24.64	269.27	7.34	47.35	3.45	48.88	11.02	6.90	50.78
1343	1343-FI-51	40.16	19.96	126.59	49.10	442.95	17.53	134.16	14.51	110.30	29.32	17.74	106.72
1343	1343-FI-13	28.16	15.83	112.71	40.89	265.66	14.06	105.09	7.85	69.79	20.46	14.30	97.03
1343	1343-FI-49	16.07	43.73	57.15	23.40	203.66	5.85	64.91	2.83	36.71	12.97	8.56	240.73
1201	1201-FI-52	21.20	96.26	76.25	23.85	269.08	11.99	68.48	4.26	52.43	15.43	5.21	85.39
1201	1201-FI-52_1	21.20	96.26	76.25	23.85	269.08	11.99	68.48	4.26	52.43	15.43	5.21	85.39
1193	1193-FI-59	20.56	13.39	73.97	32.05	244.30	9.43	77.28	7.54	73.22	17.58	11.50	55.26
1343	1343-FI-60	3.17	110.11	10.51	4.29	31.79	1.67	10.10	1.01	8.43	2.09	1.59	8.01
1201	1201.1-FI-39	10.55	5.32	38.33	13.04	103.58	4.60	33.57	3.55	23.25	7.26	4.34	22.58
1343	1343-FI-57	9.95	40.93	30.82	11.20	92.85	3.92	32.23	3.24	19.64	7.42	4.74	105.41
1086	1086.6-FI-56	0.43	0.43	0.57	0.24	4.38	0.06	0.24	0.06	0.29	0.10	0.08	1.59
1201	1201.1-FI-36	0.07	0.16	0.30	0.09	0.81	0.02	0.25	0.03	0.17	0.05	0.02	0.47
1201	1201.1-FI-35	0.11	0.07	0.20	0.06	0.48	0.02	0.19	0.02	0.12	0.04	0.02	0.39
1201	1201.1-FI-39	0.68	0.48	3.25	1.02	7.79	0.33	3.00	0.18	1.76	0.53	0.32	1.75
1201	1201.1-FI-39	0.13	0.21	0.58	0.20	1.41	0.05	0.49	0.05	0.34	0.10	0.06	0.33
1343	1343-FI-54	0.08	0.17	0.26	0.12	0.95	0.03	0.31	0.02	0.21	0.06	0.04	0.26
1343	1343-FI-61	0.24	0.57	0.85	0.27	2.85	0.08	0.72	0.08	0.56	0.14	0.05	7.76
1343	1343-FI-73	0.04	0.08	0.09	0.03	0.29	0.01	0.07	0.01	0.06	0.02	0.01	1.46

APPENDIX G

SUMMARY OF LA-ICP-MS DATA

Summary of all absolute values from unprocessed LA-ICP-MS data for all analyzed inclusion groups from the hanging wall and footwall. The concentration of each element within an inclusion group is summarized and includes the percent of inclusions within a group that were above the limit of detection, the minimum and maximum concentrations of that element, the range between that elements maximum and minimum concentration, the average overall concentration of that element, and the overall standard deviation for that element. If elements had smaller mode ranges within an inclusion group, their mode ranges are summarized in the rows underneath the summary of the overall concentrations of that element.

Hanging wall

Inclusions type { # of analyzed inclusions } [% of inclusions analyzed within a group]			Na	K	Fe	Cu	Sr	Ba	Au	Pb	Mo	Cs	Rb	Zn	Mn	Ca	Sn
B15 {7} [40%]	All Analyses	% of inclusions >LOD	**100%**	**43%**	**43%**	**71%**	**86%**	**29%**	**0%**	**86%**	**0%**	**29%**	**86%**	**43%**	**57%**	**52%**	**24%**
		Min (ppm)	6237.02	2498.32	5905.97	131.78	10.57	35.96	n/a	35.46	n/a	15.03	9.64	541.57	547.85	2304.54	99.99
		Max (ppm)	70197.10	47266.94	28652.94	7933.10	9416.29	1028.21	n/a	1084.49	n/a	111.57	463.55	5473.26	5804.37	137280.42	10112.80
		Range(ppm)	63960.07	44768.62	22746.97	7801.32	9405.72	992.24	n/a	1049.04	n/a	96.54	453.91	4931.68	5256.52	134975.88	10012.81
		Average (ppm)	24959.61	18762.96	19204.70	3754.17	1638.04	n/a	n/a	279.99	n/a	n/a	106.90	2220.35	3471.06	35787.93	3232.07
		Standard dev (ppm)	22423.01	20535.70	11852.26	3485.98	3811.31	na/	n/a	413.38	n/a	n/a	177.28	2817.58	2428.55	42462.76	4784.29
	Mode 1	% of inclusions >LOD	n/a	n/a	n/a	n/a	n/a	n/a	n/a	67%	n/a	n/a	67%	n/a	n/a	n/a	n/a
		Min (ppm)	n/a	n/a	n/a	n/a	n/a	n/a	n/a	35.46	n/a	n/a	9.64	n/a	n/a	n/a	n/a
		Max (ppm)	n/a	n/a	n/a	n/a	n/a	n/a	n/a	76.92	n/a	n/a	30.97	n/a	n/a	n/a	n/a
		Range(ppm)	n/a	n/a	n/a	n/a	n/a	n/a	n/a	41.46	n/a	n/a	21.33	n/a	n/a	n/a	n/a
		Average (ppm)	n/a	n/a	n/a	n/a	n/a	n/a	n/a	57.20	n/a	n/a	21.07	n/a	n/a	n/a	n/a
		Standard dev (ppm)	n/a	n/a	n/a	n/a	n/a	n/a	n/a	19.32	n/a	n/a	9.82	n/a	n/a	n/a	n/a
B30D {25} [36%]	All Analyses	% of inclusions >LOD	**100%**	**68%**	**24%**	**44%**	**84%**	**20%**	**4%**	**72%**	**0%**	**44%**	**60%**	**44%**	**60%**	**91%**	**24%**
		Min (ppm)	1359.89	819.29	4059.47	145.37	14.95	17.54	15.46	15.76	n/a	2.35	7.19	180.62	148.80	14318.08	99.99
		Max (ppm)	89536.69	38788.70	54662.55	12224.13	2252.26	529.23	15.46	3645.38	n/a	248.98	688.80	11100.47	17513.24	98368.48	10112.80
		Range(ppm)	88176.79	37969.41	50603.08	12078.76	2237.31	511.69	0.00	3629.62	n/a	246.63	681.61	10919.85	17364.44	84050.40	10012.81
		Average (ppm)	24164.67	13505.55	28331.71	2012.76	189.16	279.58	15.46	677.06	n/a	47.87	98.66	2210.18	3686.25	59012.61	3232.07
		Standard dev (ppm)	21674.46	11166.18	18357.45	3504.71	477.30	198.20	n/a	1014.48	n/a	73.86	172.02	3077.54	5174.29	25610.19	4784.29
	Mode 1	% of inclusions >LOD	48%	24%	50%	25%	55%	n/a	n/a	33%	n/a	70%	87%	33%	27%	n/a	n/a
		Min (ppm)	10315.44	15203.78	31252.25	145.37	14.95	n/a	n/a	15.76	n/a	2.35	7.19	1214.79	2832.72	n/a	n/a
		Max (ppm)	20144.53	17675.24	35566.55	431.85	99.05	n/a	n/a	85.39	n/a	41.81	85.97	1865.31	4620.76	n/a	n/a
		Range(ppm)	9829.09	2471.46	4314.30	286.48	84.10	n/a	n/a	69.62	n/a	39.46	78.78	650.52	1788.04	n/a	n/a
		Average (ppm)	15822.10	16522.29	33533.03	284.19	52.30	n/a	n/a	51.23	n/a	14.44	43.29	1485.16	3427.15	n/a	n/a
		Standard dev (ppm)	3053.16	1338.16	2167.75	117.10	29.24	n/a	n/a	24.34	n/a	15.28	27.87	324.81	842.90	n/a	n/a
	Mode 2	% of inclusions >LOD	n/a	24%	n/a	25%	n/a	n/a	n/a	n/a	n/a	n/a	n/a	25%	22%	n/a	n/a
		Min (ppm)	n/a	7433.03	n/a	1254.08	n/a	n/a	n/a	n/a	n/a	n/a	n/a	269.65	148.80	n/a	n/a
		Max (ppm)	n/a	9214.38	n/a	1468.72	n/a	n/a	n/a	n/a	n/a	n/a	n/a	274.22	207.76	n/a	n/a
		Range(ppm)	n/a	1781.35	n/a	214.64	n/a	n/a	n/a	n/a	n/a	n/a	n/a	4.57	58.96	n/a	n/a
		Average (ppm)	n/a	8350.31	n/a	1397.18	n/a	n/a	n/a	n/a	n/a	n/a	n/a	272.44	170.78	n/a	n/a
		Standard dev (ppm)	n/a	732.35	n/a	123.92	n/a	n/a	n/a	n/a	n/a	n/a	n/a	2.45	27.62	n/a	n/a
B30H {11} [34.4%]	All Analyses	% of inclusions >LOD	**100%**	**100%**	**91%**	**45%**	**100%**	**73%**	**n/a**	**100%**	**n/a**	**82%**	**100%**	**100%**	**100%**	**20%**	**20%**
		Min (ppm)	56684.48	29258.70	6288.37	401.29	249.43	692.28	n/a	200.23	n/a	19.65	235.22	937.86	2529.44	22.79	0.29
		Max (ppm)	120490.51	126538.95	102465.84	2390.41	10712.93	1338.54	n/a	13650.00	n/a	112.68	877.33	26293.68	60221.51	31197.60	269.27
		Range(ppm)	63806.03	97280.25	96177.47	1989.12	10463.50	646.27	n/a	13449.77	n/a	93.03	642.11	25355.82	57692.07	31174.81	268.98
		Average (ppm)	85331.61	64409.44	33173.39	946.48	2159.97	951.15	n/a	2639.33	n/a	51.12	413.76	9218.34	20516.18	8944.50	68.68
		Standard dev (ppm)	16943.26	24947.52	26689.49	825.25	2984.51	237.02	n/a	3724.17	n/a	27.85	204.31	7225.83	16551.82	14983.13	133.73
	Mode 1	% of inclusions >LOD	91%	82%	70%	80%	55%	50%	n/a	55%	n/a	n/a	73%	36%	36%	50%	67%
		Min (ppm)	56684.48	29258.70	21603.86	401.29	1034.21	992.64	n/a	1387.78	n/a	n/a	235.22	5111.09	13381.76	33927.58	632.50
		Max (ppm)	99971.52	73481.04	41882.94	800.72	1548.21	1161.67	n/a	1901.44	n/a	n/a	371.13	6484.56	23776.90	71676.56	753.43
		Range(ppm)	43287.04	44222.34	20279.09	399.43	514.00	169.03	n/a	513.66	n/a	n/a	135.91	1373.47	10395.15	37748.97	120.94
		Average (ppm)	81815.72	56070.60	30426.56	585.49	1220.42	1043.08	n/a	1560.63	n/a	n/a	310.70	5807.03	18188.02	49873.32	696.29
		Standard dev (ppm)	12957.09	14013.20	7030.89	198.29	184.70	79.60	n/a	190.25	n/a	n/a	49.24	560.82	5586.46	15444.11	58.35
B75 {9} [43%]	All Analyses	% of inclusions >LOD	**100%**	**56%**	**22%**	**89%**	**89%**	**22%**	**n/a**	**56%**	**n/a**	**11%**	**22%**	**22%**	**56%**	**56%**	**44%**
		Min (ppm)	1097.95	2200.13	13852.19	24.40	3.26	59.82	n/a	3.63	n/a	6.76	42.76	61.96	151.94	7072.93	21.26
		Max (ppm)	13720.24	9155.21	27818.19	17723.99	111.96	130.26	n/a	165.58	n/a	6.76	69.86	779.21	12204.14	33586.08	1275.52
		Range(ppm)	12622.29	6955.08	13966.00	17699.59	108.70	70.44	n/a	161.95	n/a	0.00	27.10	717.25	12052.21	26513.14	1254.27
		Average (ppm)	6252.29	6230.33	n/a	5923.21	43.65	n/a	n/a	86.77	n/a	n/a	n/a	n/a	3098.68	19903.66	475.80
		Standard dev (ppm)	4768.06	2950.44	n/a	7020.01	40.57	n/a	n/a	70.36	n/a	n/a	n/a	n/a	5142.39	11763.97	574.30
	Mode 1	% of inclusions >LOD	44%	n/a	n/a	63%	n/a	n/a	n/a	60%	n/a	n/a	n/a	n/a	n/a	80%	n/a
		Min (ppm)	1097.95	n/a	n/a	841.76	n/a	n/a	n/a	111.08	n/a	n/a	n/a	n/a	n/a	11519.28	n/a
		Max (ppm)	4462.58	n/a	n/a	5258.41	n/a	n/a	n/a	165.58	n/a	n/a	n/a	n/a	n/a	33586.08	n/a
		Range(ppm)	3364.63	n/a	n/a	4416.65	n/a	n/a	n/a	54.50	n/a	n/a	n/a	n/a	n/a	22066.79	n/a
		Average (ppm)	2395.99	n/a	n/a	2719.98	n/a	n/a	n/a	135.90	n/a	n/a	n/a	n/a	n/a	23111.34	n/a
		Standard dev (ppm)	1443.63	n/a	n/a	2080.18	n/a	n/a	n/a	27.57	n/a	n/a	n/a	n/a	n/a	10766.91	n/a
	Mode 2	% of inclusions >LOD	44%	n/a	n/a	n/a	n/a	n/a	n/a	n/a	n/a	n/a	n/a	n/a	n/a	n/a	n/a
		Min (ppm)	8513.00	n/a	n/a	n/a	n/a	n/a	n/a	n/a	n/a	n/a	n/a	n/a	n/a	n/a	n/a
		Max (ppm)	13720.24	n/a	n/a	n/a	n/a	n/a	n/a	n/a	n/a	n/a	n/a	n/a	n/a	n/a	n/a
		Range(ppm)	5207.24	n/a	n/a	n/a	n/a	n/a	n/a	n/a	n/a	n/a	n/a	n/a	n/a	n/a	n/a
		Average (ppm)	10908.62	n/a	n/a	n/a	n/a	n/a	n/a	n/a	n/a	n/a	n/a	n/a	n/a	n/a	n/a
		Standard dev (ppm)	2528.02	n/a	n/a	n/a	n/a	n/a	n/a	n/a	n/a	n/a	n/a	n/a	n/a	n/a	n/a

Hanging wall

Inclusions type { # of analyzed inclusions } [% of inclusions analyzed within a group]			Na	K	Fe	Cu	Sr	Ba	Au	Pb	Mo	Cs	Rb	Zn	Mn	Ca	Sn
B20C {23} [38%]	All Analyses	% of inclusions >LOD	**100%**	**22%**	**26%**	**48%**	**57%**	**39%**	n/a	**57%**	n/a	**13%**	**13%**	**39%**	**52%**	**43%**	**17%**
		Min (ppm)	32.82	34.35	30.59	3.14	0.09	0.41	n/a	0.33	n/a	3.08	0.83	1.59	1.37	53.94	0.95
		Max (ppm)	32211.18	7740.81	16556.95	4052.18	754.82	629.23	n/a	885.13	n/a	10.47	19.58	1611.55	3056.73	26099.52	3.59
		Range(ppm)	32178.35	7706.47	16526.36	4049.04	754.73	628.83	n/a	884.80	n/a	7.39	18.75	1609.96	3055.37	26045.58	2.64
		Average (ppm)	4773.98	3399.44	4704.92	454.13	103.94	112.80	n/a	172.85	n/a	n/a	n/a	427.93	850.11	7550.42	2.00
		Standard dev (ppm)	7165.45	3599.18	6270.76	1199.01	232.25	200.04	n/a	257.47	n/a	n/a	n/a	615.90	1165.09	8614.27	1.21
	Mode 1	% of inclusions >LOD	57%	n/a	50%	55%	83%	78%	n/a	77%	n/a	n/a	n/a	56%	42%	40%	n/a
		Min (ppm)	1671.93	n/a	1321.04	41.67	0.09	0.41	n/a	0.33	n/a	n/a	n/a	1.59	1.37	53.94	n/a
		Max (ppm)	8642.89	n/a	5767.74	351.93	76.62	55.20	n/a	136.19	n/a	n/a	n/a	93.04	76.11	97.04	n/a
		Range(ppm)	6970.96	n/a	4446.70	310.26	76.53	54.79	n/a	135.87	n/a	n/a	n/a	91.45	74.74	43.10	n/a
		Average (ppm)	4752.61	n/a	3864.10	152.97	17.72	31.00	n/a	54.78	n/a	n/a	n/a	23.90	22.21	77.87	n/a
		Standard dev (ppm)	2713.19	n/a	2291.27	129.64	25.52	23.96	n/a	58.29	n/a	n/a	n/a	38.86	31.01	19.65	n/a
	Mode 2	% of inclusions >LOD	35%	n/a	n/a	n/a	n/a	n/a	n/a	n/a	n/a	n/a	n/a	n/a	33%	40%	n/a
		Min (ppm)	32.82	n/a	n/a	n/a	n/a	n/a	n/a	n/a	n/a	n/a	n/a	n/a	242.13	9027.91	n/a
		Max (ppm)	82.61	n/a	n/a	n/a	n/a	n/a	n/a	n/a	n/a	n/a	n/a	n/a	584.74	15568.41	n/a
		Range(ppm)	49.79	n/a	n/a	n/a	n/a	n/a	n/a	n/a	n/a	n/a	n/a	n/a	342.61	6540.50	n/a
		Average (ppm)	62.91	n/a	n/a	n/a	n/a	n/a	n/a	n/a	n/a	n/a	n/a	n/a	475.60	11401.27	n/a
		Standard dev (ppm)	19.17	n/a	n/a	n/a	n/a	n/a	n/a	n/a	n/a	n/a	n/a	n/a	157.21	2863.95	n/a
B75C {20} [24%]	All Analyses	% of inclusions >LOD	**100%**	**40%**	**20%**	**60%**	**70%**	**10%**	**n/a**	**55%**	**n/a**	**15%**	**15%**	**40%**	**50%**	**20%**	**20%**
		Min (ppm)	40.70	6.35	8.77	0.71	0.07	0.25	n/a	0.26	n/a	0.08	0.11	1.94	0.95	22.79	0.29
		Max (ppm)	18374.74	3267.73	252.55	782.66	192.56	64.91	n/a	240.73	n/a	5.85	19.36	835.86	1157.64	31197.60	269.27
		Range(ppm)	18334.03	3261.38	243.78	781.96	192.50	64.66	n/a	240.47	n/a	5.77	19.25	833.92	1156.69	31174.81	268.98
		Average (ppm)	4898.97	628.05	85.71	291.39	43.14	n/a	n/a	56.90	n/a	n/a	n/a	194.43	201.01	8944.50	68.68
		Standard dev (ppm)	5913.25	1182.64	113.42	252.99	59.34	n/a	n/a	75.84	n/a	n/a	n/a	325.06	363.79	14983.13	133.73
	Mode 1	% of inclusions >LOD	40%	75%	75%	58%	43%	n/a	n/a	36%	n/a	n/a	n/a	63%	70%	n/a	n/a
		Min (ppm)	40.70	6.35	8.77	283.33	22.36	n/a	n/a	85.39	n/a	n/a	n/a	1.94	0.95	n/a	n/a
		Max (ppm)	82.61	75.07	60.78	782.66	110.11	n/a	n/a	105.41	n/a	n/a	n/a	17.70	49.32	n/a	n/a
		Range(ppm)	41.91	68.72	52.02	499.33	87.74	n/a	n/a	20.02	n/a	n/a	n/a	15.77	48.37	n/a	n/a
		Average (ppm)	64.96	42.58	30.10	462.86	68.28	n/a	n/a	93.30	n/a	n/a	n/a	8.51	23.06	n/a	n/a
		Standard dev (ppm)	16.96	25.95	27.24	177.87	36.81	n/a	n/a	9.76	n/a	n/a	n/a	7.51	21.90	n/a	n/a
	Mode 2	% of inclusions >LOD	25%	n/a	n/a	n/a	n/a	n/a	n/a	n/a	n/a	n/a	n/a	n/a	n/a	n/a	n/a
		Min (ppm)	6193.47	n/a	n/a	n/a	n/a	n/a	n/a	n/a	n/a	n/a	n/a	n/a	n/a	n/a	n/a
		Max (ppm)	11640.56	n/a	n/a	n/a	n/a	n/a	n/a	n/a	n/a	n/a	n/a	n/a	n/a	n/a	n/a
		Range(ppm)	5447.09	n/a	n/a	n/a	n/a	n/a	n/a	n/a	n/a	n/a	n/a	n/a	n/a	n/a	n/a
		Average (ppm)	8870.16	n/a	n/a	n/a	n/a	n/a	n/a	n/a	n/a	n/a	n/a	n/a	n/a	n/a	n/a
		Standard dev (ppm)	2014.67	n/a	n/a	n/a	n/a	n/a	n/a	n/a	n/a	n/a	n/a	n/a	n/a	n/a	n/a

Footwall

Inclusions type { # of analyzed inclusions } [% of inclusions analyzed within a group]			Na	K	Fe	Cu	Sr	Ba	Au	Pb	Mo	Cs	Rb	Zn	Mn	Ca	Sn
B15D {20} [21%]	All Analyses	% of inclusions >LOD	**100%**	**40%**	**20%**	**60%**	**60%**	**10%**	n/a	**10%**	**5%**	**10%**	**35%**	**15%**	**10%**	**25%**	**25%**
		Min (ppm)	1114.38	1120.53	2799.86	226.13	2.16	21.27	n/a	31.45	65.85	3.59	10.72	178.48	136.65	4735.78	99.22
		Max (ppm)	21767.47	75681.06	6282.93	9279.66	142.21	44.15	n/a	56.94	65.85	14.27	86.52	837.57	588.71	25371.55	899.69
		Range(ppm)	20653.09	74560.53	3483.07	9053.53	140.05	22.88	n/a	25.49	0.00	10.69	75.80	659.09	452.06	20635.78	800.47
		Average (ppm)	12185.73	20679.20	4560.43	3589.96	36.73	n/a	n/a	n/a	n/a	n/a	30.64	414.54	n/a	25371.55	899.69
		Standard dev (ppm)	5805.63	26852.64	1989.21	3287.10	36.01	n/a	n/a	n/a	n/a	n/a	28.73	367.17	n/a	7737.25	368.94
	Mode 1	% of inclusions >LOD	40%	50%	n/a	33%	n/a	n/a	n/a	n/a	n/a	n/a	n/a	n/a	n/a	n/a	n/a
		Min (ppm)	15205.79	3104.68	n/a	3049.41	n/a	n/a	n/a	n/a	n/a	n/a	n/a	n/a	n/a	n/a	n/a
		Max (ppm)	17954.64	4450.76	n/a	4628.12	n/a	n/a	n/a	n/a	n/a	n/a	n/a	n/a	n/a	n/a	n/a
		Range(ppm)	2748.85	1346.08	n/a	1578.70	n/a	n/a	n/a	n/a	n/a	n/a	n/a	n/a	n/a	n/a	n/a
		Average (ppm)	16342.33	3941.81	n/a	3848.71	n/a	n/a	n/a	n/a	n/a	n/a	n/a	n/a	n/a	n/a	n/a
		Standard dev (ppm)	825.30	627.88	n/a	659.28	n/a	n/a	n/a	n/a	n/a	n/a	n/a	n/a	n/a	n/a	n/a
B15C {23} [28%]	All Analyses	% of inclusions >LOD	**100%**	**48%**	**22%**	**17%**	**87%**	**22%**	**4%**	**4%**	**9%**	**9%**	**39%**	**22%**	**17%**	**35%**	**26%**
		Min (ppm)	27.38	9.90	120.64	0.46	0.06	0.82	0.07	156.17	0.49	0.03	0.06	4.40	0.38	94.59	7.49
		Max (ppm)	35544.30	86392.40	1431.17	8927.42	183.73	58.39	0.07	156.17	45.23	1.14	43.64	5487.18	942.21	98488.42	3397.68
		Range(ppm)	35516.92	86382.50	1310.53	8926.96	183.66	57.57	n/a	0.00	44.73	1.11	43.57	5482.78	941.83	98393.83	3390.19
		Average (ppm)	5961.53	16713.69	625.92	2260.81	39.24	26.38	n/a	n/a	n/a	n/a	10.17	1192.72	261.37	17439.81	805.56
		Standard dev (ppm)	9708.03	25500.54	590.35	4444.52	57.89	23.73	n/a	n/a	n/a	n/a	13.91	2401.84	455.97	32996.45	1452.28
	Mode 1	% of inclusions >LOD	35%	n/a	n/a	n/a	61%	n/a	n/a	n/a	n/a	n/a	n/a	n/a	n/a	n/a	n/a
		Min (ppm)	3464.62	n/a	n/a	n/a	0.06	n/a	n/a	n/a	n/a	n/a	n/a	n/a	n/a	n/a	n/a
		Max (ppm)	6602.99	n/a	n/a	n/a	24.45	n/a	n/a	n/a	n/a	n/a	n/a	n/a	n/a	n/a	n/a
		Range(ppm)	3138.37	n/a	n/a	n/a	24.39	n/a	n/a	n/a	n/a	n/a	n/a	n/a	n/a	n/a	n/a
		Average (ppm)	4915.22	n/a	n/a	n/a	5.68	n/a	n/a	n/a	n/a	n/a	n/a	n/a	n/a	n/a	n/a
		Standard dev (ppm)	1271.53	n/a	n/a	n/a	8.82	n/a	n/a	n/a	n/a	n/a	n/a	n/a	n/a	n/a	n/a
	Mode 2	% of inclusions >LOD	35%	n/a	n/a	n/a	n/a	n/a	n/a	n/a	n/a	n/a	n/a	n/a	n/a	n/a	n/a
		Min (ppm)	27.38	n/a	n/a	n/a	n/a	n/a	n/a	n/a	n/a	n/a	n/a	n/a	n/a	n/a	n/a
		Max (ppm)	82.61	n/a	n/a	n/a	n/a	n/a	n/a	n/a	n/a	n/a	n/a	n/a	n/a	n/a	n/a
		Range(ppm)	55.23	n/a	n/a	n/a	n/a	n/a	n/a	n/a	n/a	n/a	n/a	n/a	n/a	n/a	n/a
		Average (ppm)	61.65	n/a	n/a	n/a	n/a	n/a	n/a	n/a	n/a	n/a	n/a	n/a	n/a	n/a	n/a
		Standard dev (ppm)	18.89	n/a	n/a	n/a	n/a	n/a	n/a	n/a	n/a	n/a	n/a	n/a	n/a	n/a	n/a

REFERENCES

Anderson, C.A., Scholz, E.A., and Strobell, J.D., 1955, Geology and Ore Deposits of the Bagdad area, Yavapai County, Arizona: USGS Professional Paper 278, p. 103.

Bodnar, R.J., Reynolds, T.J., and Kuehn, C.A., 1985, Fluid Inclusion Systematics in Epithermal Systems: *In* Society of Economic Geologists, Reveiws in Economic Geology, 2, Geology and Geochemistry of Epithermal Systems, Berger, B.R., and Bethke, P.M., eds., 73-98.

Bodnar, R.J., and Vityk, M.O., 1994, Interpretation of Microthermometric data for H_2O-NaCl Fluid Inclusions, *in* DeVivo, B., and Frezzotti, M.L., eds., Fluid Inclusions in Minerals: Methods and Applications: Blacksburg, VA, Virginia Polytechnic Institute and State University, p. 117-130.

Bowers, T.S., and Helgeson, H.C., 1983, Calculation of the Thermodynamic and Geochemical Consequences of Nonideal Mixing in the System H_2O-CO_2-NaCl on Phase Relations in Geologic Systems: Equation of State for H_2O-CO_2-NaCl fluids at High Pressures and Temperatures: Geochimica et Cosmochimica Acta, v. 47, p. 1247-1275.

Brown, P. E., and Hagemann, S. G., 1994, MacFlinCor and its Application to Fluids in Archean Lode-gold Deposits: Geochimica et Cosmochimica, v.59, no. 19, p. 3943-3952.

Brown, P.E., 1989, FLINCOR: A Microcomputer Program for the Reduction and Investigation of Fluid-Inclusion Data: American Mineralogist: Software Notice, v.74, p. 1390-1393.

Candela, P.A., and Holland, H.D., 1986, A Mass Transfer Model for Copper and Molybdenum in Magmatic Hydrothermal Systems: The Origins of Porphyry-Type Ore Deposits. Economic Geology, v. 81, pp. 1-19.

Cline, J.S., and Bodnar. R.J., 1991, Can Economic Porphyry Mineralization be Generated by a Typical Calc-alkaline Melt?: Journal of Geophysical Research, v.96, p. 8113-8126.

Cloos, M., Sepiie, B., 2013, Porphyry Copper Deposits: Strike-slip Faulting and Throttling Cupolas: International Geology Review, v.55, no.1, 43-65.

Dale, V.B., 1961, Tungsten Deposits of Gila, Yavapai, and Mohave Counties, Arizona: United States Bureau of Mines Information Circular I.C. 8078, p. 71-94.

Goldstein, R.H., and Reynolds, J.T., 1994, Systematics of Fluid Inclusions in Diagenetic Minerals: Society of Sedimentary Geology, SEPM Short Course 31, p.199

Guilbert, J.M., Park, C.F., 1986. Waveland press, The geology of Ore Deposits: p405-434

Guillong, M., Heinrich, C.A., 2007, Sensitivity Enhancement in Laser Ablation ICP-MS Using Small Amounts of Hydrogen in the Carrier Gas: Journal of Analytical Atomic Spectrometry, v.22, p. 1488-1494.

Guillong, M., Meier D. M., Allan M. M., Heinrich C. A. and Yardley B., 2008, SILLS: A MATLAB-Based Program for the Reduction of Laser Ablation ICP–MS Data of Homogeneous Materials and Inclusions: Mineralogical Association of Canada Short Course 40, Vancouver, B.C., pp. 328–333.

Gustafson, L. B., Hunt, J.P., 1975. The Porphyry Copper Deposit at El Salvador, Chile. Economic Geology, v. 70, pp. 857-912.

Hedenquist, J.W., Arribas, A., Reynolds, J.T., 1998, Evolution of an intrusion- centered hydrothermal system: Far Southeast-Lepanto porphyry and epithermal Cu-Au deposits, Philippines: Economic Geology, v. 93, p. 373–404.

Heinrich, C.A., Günther, D., Audétat, A., Ulrich, T., and Frischknecht, R., 1999, Metal fractionation between magmatic brine and vapor, determined by micro-analysis of fluid inclusions: Geology, v. 27, p. 755–758.

Hedenquist, J.W., Lowenstern, J.B., 1994, The Role of Magmas in Hydrothermal Ore Deposits. Nature, v.370, p. 519-526

Heinrich, C.A., Driesner, T., Stefánsson, A., Seward, T.M., 2004, Magmatic Vapor Contraction and the Transport of Gold from the Porphyry Environment to Epithermal Ore Deposits: Geological Society of America, v. 32, no. 9. P. 761-764.

Lecumberri-Sanchez, P., Steele-MacInnis, M., Weis, P., Driesner, T., Bodnar, R.J., 2015, Salt Precipitation in magmatic-hydrothermal systems Associated with Upper-Crustal Plutons: Unpublished manuscript

John, D.A., Ayuso, R.A., Barton, M.D., Blakely, R.J., Bodnar, R.J., Dilles, J.H., Gray, Floyd, Graybeal, F.T., Mars, J.C., McPhee, D.K., Seal, R.R., Taylor, R.D., Vikre, P.G., 2010, Porphyry copper deposit model, chap. B of Mineral deposit models for resource assessment: U.S. Geological Survey Scientific Investigations Report 2010–5070–B, p. 169.

Landtwing, M.R., Furrer, C., Redmond, P.B., Pettke, T., Guillong, M., Heinrich, C.A., 2010, The Bingham Canyon Porphyry Cu-Mo-Au Deposit. III. Zone Copper-Gold Ore Deposition by Magmatic Vapor Expansion: Economic Geology, v. 105, p. 91-118.

Lang, J.R., and Eastoe, C.J., 1988, Relationship Between a Porphyry Cu-Mo Deposit, Base and Precious Metal Veins, and Laramide Intrusions, Mineral Park, Arizona: Economic Geology, v. 83, p. 551-567.

Lowell, J. D., Guilbert, J.M., 1970. Lateral and Vertical Alteration-Mineralization Zoning in Porphyry Ore Deposits. Economic Geology, v. 65, pp. 373-408.

Maher, D.J., 2008, Reconstruction of middle tertiary extension and Laramide porphyry copper systems, east-central Arizona: University of Arizona, ProQuest, UMI Dissertations Publishing

Muntean, J.L., and Einaudi, M.T., 2001, Porphyry Gold Deposits of the Refugio District, Maricunga Belt, Northern Chile: Economic Geology, v. 95, p. 1445-1472.

Reynolds, J.T., and Beane, R.E., 1985, Evolution of hydrothermal Fluid Characteristics at the Santa Rita, New Mexico, Porphyry Copper Deposit: Economic Geology, v. 80, p.1328-1347.

Rusk, B.G., Reed, M.H., Dilles, J.H., Klemm, L.M., Heinrich, C.A., 2004, Compositions of Magmatic Hydrothermal Fluids Determined by LA-ICP-MS of Fluid Inclusions from the Porphyry Copper-Molybdnum Deposit at Butte, MT: Chemical Geology, v. 210, p. 173-199.

Rusk, B.G., Reed, M.H., Dilles, J.H., 2008, Fluid Inclusion Evidence for Magmatic-Hydrothermal Fluid Evolution in the Porphyry Copper-Molybdenum Deposit at Butte, Montana: Economic Geology, v. 103, p. 307-334.

Schrader, F.C., 1909, Mineral Deposits of the Cerbat Range, Black Mountains and Grand Wash Cliffs, Mohave County, Arizona: USGS bulliten 397, p. 226

Seedorff, E, Dilles, J.H., Proffett, J.M., Jr., Einaudi, M.T., Zurcher, L., Stavast, W.J.A., Johnson, D.A., and Barton, M.D., 2005, Porphyry deposits-Characteristics and origin of hypogene features: Society of Economic Geologists, Economic Geology 100th anniversary Volume, 1905-2005, p. 251-298

Seedorff, E., Barton, M. D., Stavast, W. J. A., Maher., D. J., 2008. Root Zones of Porphyry Systems: Extending the Porphyry System to Depth. Economic Geology, v. 103, pp. 939-956.

Selby, D., Nesbitt, B.E., Muehlenbachs, K., Prochaska, W., 2000, Hydrothermal Alteration and Fluid Chemistry of the Endako Porphyry Molybdenum Deposit, British Columbia: Economic Geology, v. 95, p. 183-202.

Sillitoe, R. H., 1973. The Tops and Bottoms of Porphyry Copper Deposits: Economic Geology, v. 68, pp. 799-815

Sillitoe, R. H., 2010. Porphyry Copper Systems: Economic Geology, v. 105, pp.3-41.

Stavast, W. J. A., 2006, Three Dimensional Evolution of Magmatic Hydrotherm Systems, Schultze Granite and Ruby Star Granodiortie, Arizona: University of Arizona Ph.D dissertation

Sterner, S.M., and Bodnar, R.J., 1984, Synthetic Fluid Inclusions in Natural Quartz. I. Compositional Types Synthesized and Applications to Experimental Geochemistry: Geochimica et Cosmochimica Acta, v. 48, p. 2659-2668.

Sterner, M., 1992, Homogenization of Fluid Inclusions to the Vapor Phase: The Apparent Homogenization Phenomenon: Economic Geology, v. 87, p. 1616-1623.

Tattitch, B.C., Candela, P.A., Piccoli, P.M., Bodnar, R.J., 2015, Copper partitioning between felsic melt and H_2O-CO_2 bearing saline fluids: Geochimica et Cosmochimica Acta, v. 148, p. 81-99.

Titley S. R. and Anthony E. Y., 1989, Laramide mineral deposits in Arizona. Geologic Evolution of Arizona: Arizona Geological Society Digest, v. 17, p.485–514.

Ulrich, T., Gunther, D., Heinrich, C.A., 2001, The Evolution of a Porphyry Cu-Au Deposit, Based on LA-ICP-MS Analysis of Fluid Inclusions: Bajo de la Alumbrera, Argentina: Economic Geology, v. 96, p. 1743-1774.

Vuich, J.S., 1974, A geologic reconnaissance and mineral evaluation, Wheeler Wash area, Hualpai Mountains, Mohave County, Arizona: Tucson, University of Arizona, Unpub. M.S. thesis, 77 p., 6 sheets, scales 1:12,000, 1:24,000, and 1:125,000.

Wang, X., Chou, I., Hu, W., Burruss, R.C., Sun, Q., Song, Y., 2011, Raman Spectroscopic Measurments of CO_2 Density: Experimental Calibration with High-Pressure Optical Cell (HPOC) and Fused Silica Capillary Capsule (FSCC) with Application to Fluid Inclusion Observations: Geochimica et Cosmochimica Acta, v. 75, p. 4080-4093.

Zajacz, Z., Candela, P.A., Piccoli, P.M., Wälle, M., and Sanchex-Valle, C., 2012, Gold and Copper inVolatile Saturated Mafic to Intermediate Magmas: Solubilities, Partitioning, and Implications for Ore Deposit Formation: Geochimica et Cosmochimica Acta, v. 91, p. 140-159.

CURRICULUM VITAE

Graduate College
University of Nevada, Las Vegas

Wyatt M. Bain
bainw1@unlv.nevada.edu

Degrees:

Bachelors of Science, Geology and Geophysics, 2012
University of Wisconsin, Madison, WI

Testing Established Models of Hydrothermal Fluid Distribution Around Porphyry Deposits: The Application of Fluid Inclusion Research to Porphyry Deposit Exploration

Thesis Examination Committee

Chairperson, Jean S. Cline, Ph.D.

Committee Member, Rodney M. Metcalf, Ph.D.

Committee Member, Minghua Ren, Ph.D.

Graduate Faculty Representative, Barbara Luke, Ph. D.